Utrecht University
Faculty of Geosciences
Department of Earth Sciences

Jimmy de Rooij – Bringing fossils back to life

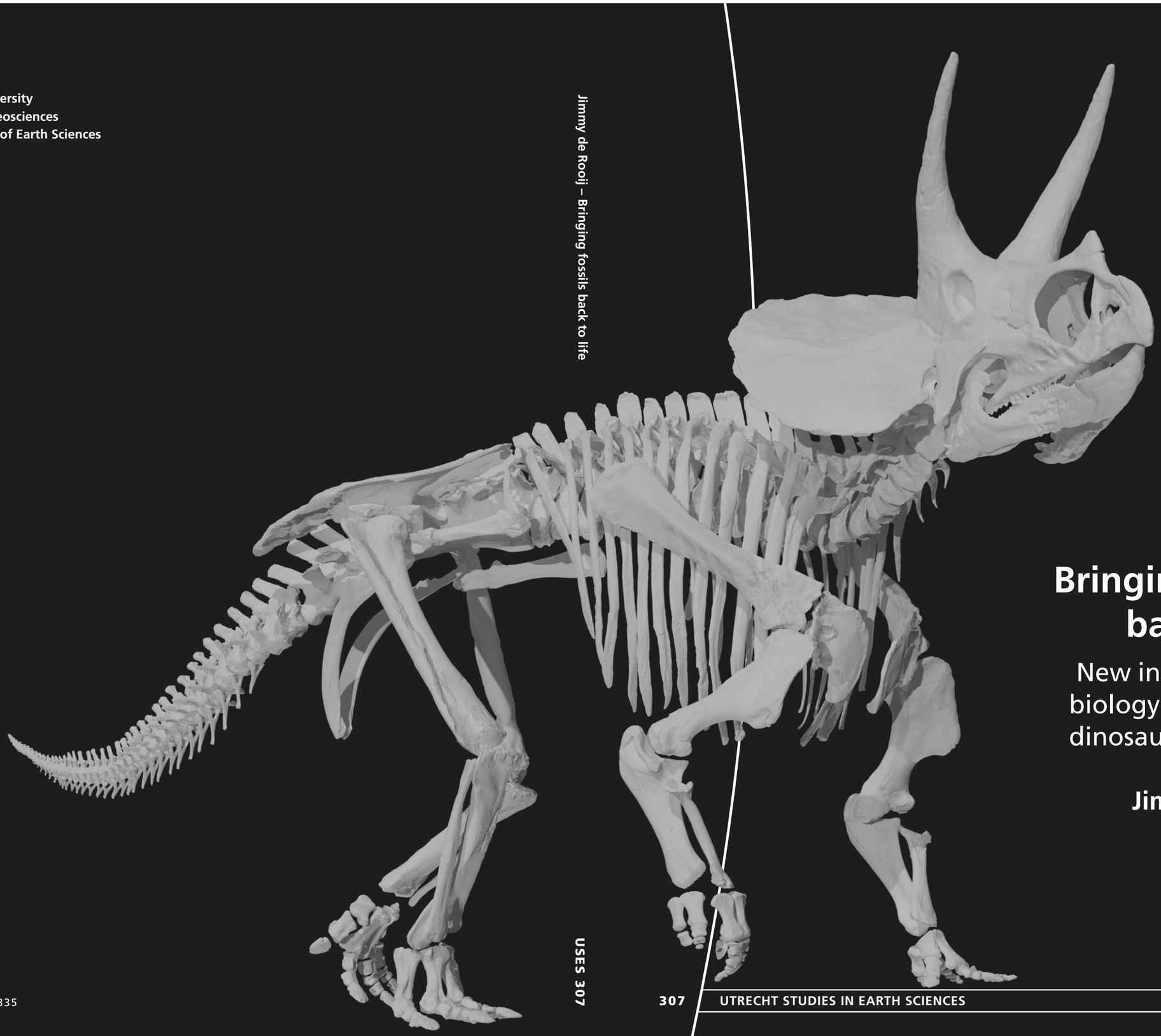

Bringing fossils back to life

New insights on the biology of the iconic dinosaur *Triceratops*

Jimmy de Rooij

ISSN 2211-4335

USES 307

307 UTRECHT STUDIES IN EARTH SCIENCES

USES-307_A4 Cover de Rooij.indd 1 05-03-2024 08:02

Bringing fossils back to life - New insights on the biology of the iconic dinosaur *Triceratops*

© Jimmy de Rooij (2024). Bringing fossils back to life – New insights on the biology of the iconic dinosaur *Triceratops*

PhD thesis at Naturalis Biodiversity Center & Utrecht University

ISBN: 978-90-6266-680-5

Utrecht Studies in Earth Sciences: 307

ISSN: 2211-4335

Cover: 'Individual 3', the third reconstructed *Triceratops* skeleton from the 'Darnell *Triceratops* Bonebed' representing the smallest and youngest individual (by Colijn Dijkers).

Title page image: Life reconstruction of 'Dirk' the *Triceratops,* a *Triceratops* discovered in close proximity to the 'Darnell *Triceratops* Bonebed' and the first *Triceratops* to be on display at Naturalis (by Ydnas Louisa).

Palaeoart Chapter 6: Digital art reconstruction of the formation of the 'Darnell *Triceratops* Bonebed' (by Nadia de Waal).

Photographs chapter covers: Anne S. Schulp (Ch. 1, 4 and 5), Hanneke Jacobs (Ch. 2), Dirk Cornelissen (Ch. 3), Oeki Verhage (Ch. 6), Yanell Braumuller (Closing chapter)

Printed by: Ipskamp Printing

Bringing fossils back to life – New insights on the biology of the iconic dinosaur *Triceratops*

Het tot leven wekken van fossielen – Nieuwe inzichten over de biologie van de iconische dinosaurus *Triceratops*
(met een samenvatting in het Nederlands)

Proefschrift

ter verkrijging van de graad van doctor aan de
Universiteit Utrecht
op gezag van de
rector magnificus, prof. dr. H.R.B.M. Kummeling,
ingevolge het besluit van het college voor promoties
in het openbaar te verdedigen op

woensdag 27 maart 2024 des middags te 2.15 uur

door

Jimmy de Rooij

geboren op 12 juni 1995
te Haarlem

Promotor:
Prof. dr. A.S. Schulp

Copromotor:
Dr. H.J.L. van der Lubbe

Beoordelingscommissie:
Prof. dr. L.P.A.M. Claessens
Prof. dr. C.A. Forster
Dr. F.M. Holwerda
Prof. dr. ir. J.C.A. Joordens
Prof. dr. J.W.F. Reumer

Dit proefschrift werd mede mogelijk gemaakt met financiële steun van de Nederlandse Organisatie voor Wetenschappelijk Onderzoek (NWO, ALW Open Programme ALWOP.633)

Table of contents

Summary **1**
Samenvatting **3**
Chapter 1. Introduction **6**
1.1 General background 6
1.2 Research context: introducing the Bonebed Toolkit 10
References 15
Chapter 2. The taphonomy of the Darnell *Triceratops* bonebed **24**
Abstract 24
2.1 Introduction 24
2.2 Material and methods 26
2.3 Results 31
2.4 Discussion 36
2.5 Supplementary data 40
Acknowledgements 59
References 60
Chapter 3. Stable isotope record of *Triceratops* from a mass accumulation (Lance Formation, Wyoming, USA) provides insights into *Triceratops* behaviour and ecology **70**
Abstract 70
3.1 Introduction 70
3.2 Background 71
3.3 Material and methods 73
3.4 Results 77
3.5 Discussion 83
3.6 Conclusion 92
3.7 Supplementary data 93
Acknowledgements 96
References 97
Chapter 4. Exploring the ceratopsid growth record: a comprehensive osteohistological analysis of *Triceratops* (Ornithischia: Ceratopsidae) and its implications for growth and ontogeny **106**
Abstract 106
4.1 Introduction 106
4.2 Material and methods 107
4.3 Results 112
4.4 Discussion 129
4.5 Conclusion 139
4.6 Supplementary data 141
Acknowledgements 163
References 163
Chapter 5. Quantification of bone surface textures: exploring a new method of ontogenetic ageing **171**
Abstract 171
5.1 Introduction 171
5.2 Material and methods 172

5.3 Results 175
5.4 Discussion 178
5.5 Conclusion 180
5.6 Supplementary data 181
Acknowledgements 184
References 185
Chapter 6. Synthesis 188
6.1 Combining multiple independent lines of evidence to reveal the behaviour of extinct animals 188
6.2 Potential mechanisms for bonebed preservation and gregarious behaviour in ceratopsids 195
6.3 Future perspectives 197
References 197
Acknowledgements 205
Curriculum vitae 206
Relevant work experience 206
School and study career 206
Outreach 206
Publications 206

Summary

Non-avian dinosaurs walked the Earth for nearly 160 million years. As a group, they represent an ideal candidate to study evolutionary drivers and mechanisms that shape lineages in the fossil record. *Triceratops* was amongst the last (non-avian) dinosaur species to survive, and is known from a large number of fossils. However, despite its status as a relatively iconic dinosaur, only little is actually known about its biology. Current *Triceratops* life reconstructions only provide a very limited view on preferred living habitats, migration, diet, growth patterns and (social) behaviour. Current records of *Triceratops* fossils have mostly been limited to cranial material, but the recent addition of more unique post-cranial material warrants a thorough analysis of *Triceratops* palaeobiology.

This thesis presents the 'Darnell *Triceratops* Bonebed' (DTB) from Wyoming, USA, the world's largest *Triceratops* bonebed to date, and aims to unravel its origin through a multidisciplinary approach applying established methods in geology and biology. In doing so, this work answers unresolved questions on *Triceratops* palaeobiology and create the most accurate (i.e., parsimonious) life reconstruction based on multiple independent lines of evidence. Bonebeds may often present a unique case study in archaeology and palaeontology alike, but it is crucial to distinguish between true mass death assemblages and time-accumulated assemblages, especially when considering the palaeobiological implications. We combined high-resolution grain size analyses, bone histological descriptions and stable isotope geochemistry – culminating in the 'Bonebed Toolkit' – to provide an in-depth analysis on *Triceratops* palaeobiology, including potential social behavioural patterns.

Grain size analyses on the bone-bearing layers that contain a minimum of five *Triceratops* individuals help to better understand the depositional environment of the DTB. Our results reveal very fine-grained particles pertaining to a low energy depositional environment and limited post-mortem transportation of the carcasses (**Chapter 2**). This is further corroborated by the bone modification data, indicating exceptional preservation as well as lack of scavenging and trample marks across the majority of the discovered material. However, two crevasse splay events – as evidenced by peripheral influx of coarse-grained material – disarticulated and redeposited the material at an early stage during fossilisation. The sedimentological and taphonomic data provide strong evidence in favour of a single event that killed and buried the group of *Triceratops*.

Identifying the isotopic fingerprint of the DTB provides additional insights on the potential provenance of the fossil material and elucidates *Triceratops* palaeoecology. The carbon and oxygen isotope signal of the DTB revealed no signs of significant reworking or introduction of exogenous fossil material (**Chapter 3**). Carbon and oxygen isotope signatures from the *Triceratops* remains overlap with those of the local environment such as indicated by isotope values from freshwater choristoderes and lepisosteids. Moreover, extensive chemical pretreatment of the fossil teeth, bones and scales showed homogenous diagenetic effects across all the sampled material, and our isotope dataset suggests that the different *Triceratops* from the DTB share the same taphonomic history. The carbon and oxygen isotope signals revealed for the first time patterns in *Triceratops* migration and living habitat, showing that *Triceratops* inhabited more widespread areas than previously established, extending from coastal floodplains to inland river systems.

The histological data such as primary bone tissue and vascular organisation sheds light on the relative age classes of all the *Triceratops* individuals from the DTB (**Chapter 4**). This helps to establish accurate mortality profiles and reconstruct potential age profiles of the living population which provide insights on the origin of the DTB. The DTB individuals represent actively growing subadults and

skeletally mature young adults conforming to a catastrophic death assemblage, and complementing both the sedimentological and isotopic datasets. Furthermore, the histological preservation was similar across all the studied bones, corroborating the taphonomic interpretation. The assessment of histological ontogenetic stages and skeletochronological markers reveals a unique bone histology for *Triceratops.* Changes in primary bone tissue show that skeletal maturity coincides with the final cranial ontogenetic stage. This has enabled the correlation of the ontogenetic changes in cranial morphology to the changes in histology, which helps to resolve the taxonomic synonymity between *Triceratops* and *Torosaurus*.

An alternative method of ontogenetic ageing relies on the changes in bone surface texture that occur with increasing age. Formation of specific bone surface roughness profiles relates to the number of blood vessels that penetrate the bone tissue and open at the bone surface. This phenomenon is observed in the majority of extant and fossil animals. 3D digital microscopy on the limb bones of extant Canada goose (*Branta canadensis*) and grey herons (*Ardea cinerea*) shows that quantitative roughness profiles accurately capture changes in bone surface texture correlated to ontogenetic age (**Chapter 5**). Previous analyses have been limited to qualitative texture classes, but applying digital microscopy allows for more accurate comparisons between roughness profiles. While not directly related to the large-scale analysis of the DTB discussed in this thesis, the identification of quantitative roughness profiles can be applied to fossil material in the future to better understand ontogenetic growth trajectories of extinct animals. Moreover, this technique is easily applied on disarticulated and fragmented material, which is common for the majority of the available fossil material.

Behaviour of extinct animals can only be indirectly inferred from fossil bones, trackways or through comparison with extant analogues, making true accurate testing of hypotheses more complex. However, the results of each applied method presented in this thesis provide a robust dataset to inform on *Triceratops* behaviour, inspiring an accurate and truthful life reconstruction. The Bonebed Toolkit – especially when combined with available theoretical data – provides strong support in favour of *Triceratops* gregarious behaviour. As such, the application of previously established methods combined in a multidisciplinary framework breathes new life into an iconic taxon, and offers an innovative framework for the analysis of bonebeds.

Samenvatting

Triceratops was een van de laatste vertegenwoordigers van een bijzondere, zeer diverse groep van gehoornde dinosaurussen. Hiermee vormt deze soort de perfecte kandidaat om de evolutionaire mechanismen te onderzoeken die over een tijdsspanne van 160 miljoen jaar de dinosaurussen vorm gaven. Ondanks dat *Triceratops* één van de meest iconische dinosaurussen is, is er maar weinig bekend over zijn biologie. Bestaande reconstructies van *Triceratops* bieden maar weinig zicht in hun leefgebied, migratie, dieet, groeipatroon en (sociaal) gedrag. De huidig beschikbare *Triceratops*-fossielen zijn vooral beperkt tot schedelonderdelen, maar recente ontdekkingen van meer post-craniaal materiaal maken een meer diepgaand onderzoek mogelijk naar de biologie van deze uitgestorven soort.

Dit promotieonderzoek biedt een uitgebreide beschrijving van het 'Darnell *Triceratops* Bonebed' (DTB), 's werelds grootste *Triceratops*-vindplaats uit Wyoming, VS. Het onderzoek volgt een multidisciplinaire aanpak waarbij biologische en geologische technieken gebruikt worden om beter te begrijpen hoe de rijke opeenhoping van fossielen is ontstaan. De combinatie van deze verschillende bewijsstukken leert ons iets over het leven van uitgestorven dinosaurussen, en stelt ons in staat een zo natuurgetrouw mogelijk beeld van *Triceratops* te reconstrueren. Fossiele verzamelingen bieden op deze manier vaak een unieke kijk in het leven van uitgestorven dieren, maar het is cruciaal om onderscheid te maken tussen een werkelijke massasterfte of een accumulatie van materiaal over tijd. Dit is vooral belangrijk wanneer we aannames doen over het gedrag van de betreffende soorten. In dit werk combineren we sedimentologische korrelgrootte-analyses, histologische beschrijvingen van botweefsel en geochemie van stabiele isotopen – dat samen de 'Bonebed Toolkit' vormt – om nieuwe kennis op te doen over de biologie van *Triceratops*, inclusief mogelijk sociaal gedrag.

De bottenlaag dateert van 67 miljoen jaar geleden gebaseerd op de stratigrafische positie binnen de geologische formaties, en bevat de overblijfselen van vijf verschillende *Triceratops*-individuen. De korrelgrootte-analyse van het sediment rondom de vijf skeletten uit het DTB bieden inzicht in het toen heersende afzettingsmilieu van de vindplaats. Het fijne sediment wijst op een lage energie. Het water zal dus geen grote rol hebben gespeeld in het transport van de karkassen (**Hoofdstuk 2**). Ook de uitmuntende conserveringstoestand van de skeletten wijst hierop, net als de afwezigheid van tandafdrukken van aaseters. Echter, twee zogenaamde 'crevasse splays' – de influx van grofkorrelig sediment aan de randen van de groeve – hebben de fossielen omgewoeld in de vroege stadia van fossilisatie. De sedimentologische en tafonomische informatie bieden overtuigend bewijs dat de *Triceratops*-groep op één moment gezamenlijk is gestorven en begraven.

De isotopensamenstelling van de bottenlaag biedt aanvullende mogelijkheden om de herkomst van de fossielen te achterhalen, en biedt inzicht in de ecologische rol van *Triceratops*. Ook de stabiele koolstof- en zuurstofisotoop-signatuur van de fossielen laat zien dat de fossielen niet 'reworked' zijn, en dat er geen materiaal van elders is ingespoeld (**Hoofdstuk 3**). Het koolstof- en zuurstofisotopensignaal van alle *Triceratops*-individuen overlapt met het signaal van zoetwaterreptielen en -vissen, met andere woorden: het signaal van het lokale afzettingsmilieu. Uitgebreide chemische voorbehandelingsmethoden op de onderzochte fossiele tanden, botten en schubben laten zien dat al het materiaal dezelfde diagenetische effecten heeft ondergaan, en onze isotopendata suggereert dat de *Triceratops*-individuen de zelfde tafonomische (fossilisatie) geschiedenis delen. Daarnaast biedt de chemische samenstelling van de *Triceratops*-tanden nieuwe inzichten in mogelijke migratiepatronen en leefomgeving van deze soort. De schommelingen in koolstof- en zuurstofisotopen laten zien dat *Triceratops* voorkwam in meer verschillende

leefomgevingen dan gedacht. *Triceratops* leefde niet alleen in kustgebieden maar ook in riviersystemen meer landinwaarts.

Het histologische beeld wordt omschreven als de structuur van het primaire botweefsel en de organisatie van het bloedvatenstelsel, en biedt inzicht in de relatieve leeftijden van de individuen uit de groep (**Hoofdstuk 4**). Deze leeftijdsschatting geeft een beeld van de populatieopbouw, en geeft daarmee meer duidelijkheid over het ontstaan van deze fossiele accumulatie. De *Triceratops*-individuen zijn onder te verdelen in late adolescenten en jongvolwassenen wat een sterke aanwijzing is voor een zogenaamde 'catastrofale massasterfte'. Dit betekent dat kwetsbare individuen zoals heel jonge of heel oude dieren ontbreken, wat erop wijst dat de massasterfte acuut genoeg moet zijn geweest om ook de sterkste groepsleden om het leven te brengen. Deze informatie is in lijn met de resultaten uit de sedimentologie en de stabiele isotopen. Bovendien is de preservatie van het microscopische botweefsel van alle fossielen identiek, en ook dat bevestigt de gezamenlijke fossilisatiegeschiedenis uit het sedimentologische onderzoek. De benadering van 'histologische ontogenetische klassen' en skeletochronologische structuren laten zien dat *Triceratops* gekarakteriseerd wordt door een unieke bothistologie en bevestigt dat de ontwikkeling van de schedels samenvalt met de ontwikkeling van lichaamsgrootte. Dit stelt ons ook in staat om taxonomische misvattingen tussen *Torosaurus* en *Triceratops* te verhelderen.

Karakterisering van de ruwheid van het botoppervlak biedt een aanvullende methode om tot een leeftijdsschatting te komen. De aanwezigheid van specifieke ruwheidspatronen heeft te maken met de hoeveelheid bloedvaten aan het botoppervlakte. Dit fenomeen is leeftijdsafhankelijk en is terug te vinden in bestaande en uitgestorven dieren. Middels digitale microscopie is aangetoond dat de Canadese gans (*Branta canadensis*) en de blauwe reiger (*Ardea cinerea*) een sterke correlatie laten zien tussen kwantitatieve ruwheidsprofielen en leeftijd (**Hoofdstuk 5**). Voorgaande studies hebben zich vooral gefocust op kwalitatieve ruwheidsklassen, maar de toepassing van digitale microscopie biedt meer nauwkeurige kwantitatieve ruwheidsmetingen die onderling vergeleken kunnen worden. Ondanks dat deze nieuwe bevindingen niet direct gelinkt zijn aan de grootschalige analyse van de *Triceratops*-massasterfte, bieden de resultaten wel nieuwe mogelijkheden voor toepassing op fossiel materiaal om een beter begrip te krijgen over de leeftijdsklassen en groei van uitgestorven dieren. Bovendien leent deze nieuwe methode zich uitstekend voor gebruik op verspoeld of fragmentarisch materiaal.

Het gedrag van uitgestorven dieren kan enkel indirect worden afgeleid van fossiele overblijfselen, sporenfossielen of door vergelijking met bestaande diersoorten. Hypotheses kunnen dus nooit daadwerkelijk op de proef worden gesteld, en conclusies blijven vaak beperkt tot een (nauwe) benadering van de waarheid. Maar als we de resultaten van alle toegepaste methoden combineren, ontstaat er een robuust en overkoepelend beeld. Op die manier bouwen we een zo natuurgetrouw mogelijke reconstructie van het leven en gedrag van *Triceratops*. De toepassing van een combinatie van bewezen technieken in een multidisciplinaire aanpak levert nieuwe inzichten op, en biedt hiermee een innovatieve strategie voor onderzoek naar complexe fossiele samenstellingen binnen de paleontologie en archeologie.

1

Chapter 1. Introduction

1.1 General background

1.1.1 Horned dinosaurs through time

Dinosaurs are among the most perplexing extinct organisms and continue to amaze children, adults and scientists alike. Since the onset of palaeontology in the 18th and 19th century, over 600 (and counting) different species of dinosaur have been officially named based on (near-)complete skeletal remains (Wang & Dodson, 2006). Putative species erected based only on fragmentary material add an additional ~1000 species (Starrfelt & Liow, 2016). The total number of dinosaur species in the Mesozoic is estimated between 1500 and 2500 (Starrfelt & Liow, 2016). Thus, the currently available fossils only represent a small portion of past dinosaur ecosystems. Non-avian dinosaurs roamed the planet for more than 160 million years, with the earliest discoveries from the Late Triassic approximately 230 million years ago up to the end of the Cretaceous 66 million years ago (Benton, 2015). During this period, they were able to globally disperse, achieving a world-wide distribution. Fossil discoveries of dinosaurs are known from all of the major landmasses including Europe, Asia, North- and South America, Oceania, Afro-Arabia and even Antarctica (Chiarenza et al., 2022; Dunhill et al., 2016; O'Donovan et al., 2018; Upchurch et al., 2002). Palaeontologists have become significantly better equipped since the onset of palaeontology to reconstruct a detailed picture of Earth's past life (Currie, 2023). New techniques combined with a continuously growing fossil record consistently produce new theories on dinosaur palaeobiology. The following work adds to this database by describing the 'Darnell *Triceratops* Bonebed' (DTB), a large multigenerational monospecific mass death assemblage preserving a large number of cranial as well as postcranial remains of five *Triceratops* individuals, an iconic horned dinosaur from the Late Cretaceous of North America.

Some of the most enigmatic taxa are found among the horned dinosaurs (Ceratopsia). Ceratopsians are characterized by the disproportionally large parietal and squamosal bones of the skull, producing a bony frill that extends across the back of the head and neck. Furthermore, all ceratopsians possess a lateromedially flattened beak at the snout as part of its feeding apparatus, and more derived taxa develop elaborate facial horns (Figure 1) (Nabavizadeh, 2023). Ceratopsians comprise an extremely speciose group and their fossil record yielded 60 to 70 established genera so far, of which many contain numerous species (Dodson, 2013). Initial discoveries, during the late 1800s and large parts of the 1900s, were restricted to large derived quadrupedal ceratopsids in North America such as *Triceratops* and *Centrosaurus* (Dodson, 2013; Hatcher et al., 1907). It long remained a question how these dinosaurs evolved their characteristic cranial ornamentation and gigantic body size. Later expeditions to Mongolia in 1923 led to the discovery of *Psittacosaurus* and *Protoceratops*, two basal ceratopsians taking the place as outgroup to the Neoceratopsia and Ceratopsoidae, respectively (Figure 1) (Granger et al., 1923; Osborn, 1923; Sereno, 2010). It was not until the late 1990s and early 2000s that additional basal ceratopsians were discovered, including the earliest ceratopsian *Yinlong downsi* dating back to approximately 160 million years (Xu et al., 2006). *Y. downsi* still possessed traits observed in the sister taxa including pachycephalosaurids and heterodontosaurids and – as the most basal member of Ceratopsia – is evidence for an Asian origin of the clade (Lee et al., 2011; Xu et al., 2006). One other noteworthy basal member is *Aquilops americanus,* a neoceratopsian discovered from the

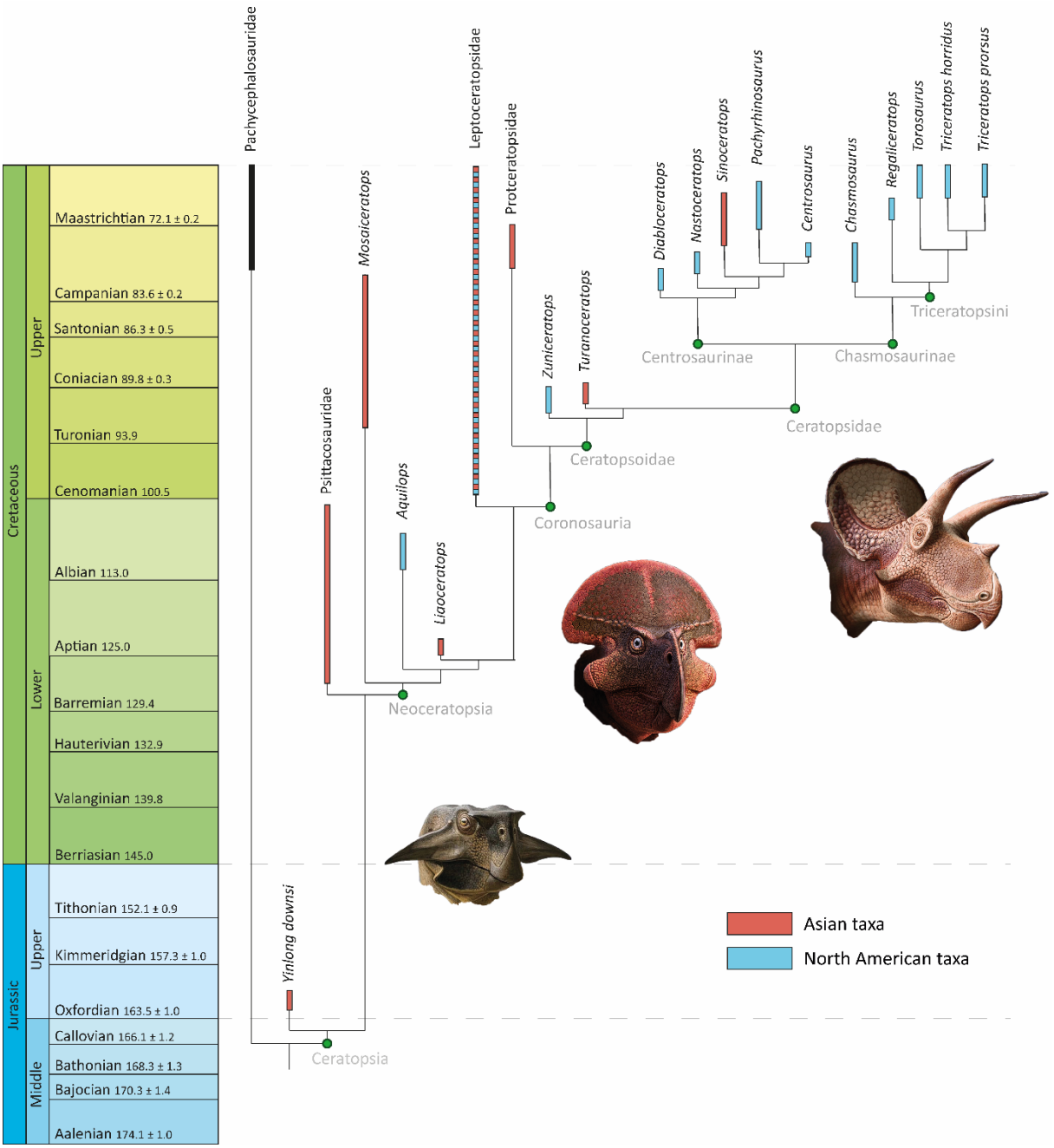

Figure 1. Ceratopsian phylogenetic tree showing relevant taxa. The outgroup is represented by Pachycephalosauridae (in black). The more basal ceratopsians occur mostly in Asia, while the derived ceratopsids are almost limited to North America. Note the development of the horns and frill through evolutionary time from *Psittacosaurus* (left) to *Protoceratops* (middle) and ending at *Triceratops* (right). Phylogenetic relationships and age ranges for each group are based on literature data (Lee et al., 2011; Mallon et al., 2016; Sampson and Loewen, 2010; Sereno, 2010; Sues and Averianov, 2009a,b; Wolfe and Kirkland, 1998; Zheng et al., 2015). Palaeoart of *Psittacousaurus*, *Protoceratops* and *Triceratops* by Andrey Atuchin (used with permission).

Cloverly Formation in North America (Farke et al., 2014). This discovery provided evidence that ceratopsians dispersed to North America, most likely by crossing the Beringian Seaway, and were already present on the continent around 106 million years ago (Farke et al., 2014).

Upon arriving and dispersing across North America, the ceratopsians rapidly evolved and experienced a strong radiation towards larger body size and increasingly more elaborate craniofacial features (Sampson & Loewen, 2010). One of the first ceratopsoid, and outgroup of all other derived

ceratopsids, is represented by *Zuniceratops christopheri* from the Turonian of New Mexico, USA, dating back to approximately 90 million years ago (Wolfe & Kirkland, 1998). *Zuniceratops* represents a transitional taxon between the small-bodied basal neoceratopsians and the large-bodied derived ceratopsids. *Zuniceratops* only possesses a portion of derived characters defining the Ceratopsidae, but already bore an enlarged frill and horns identical to its evolutionary descendants, corroborating the North American origin and radiation of the late ceratopsids. However, later expeditions discovered another member of the basal ceratopsoids and described *Turanoceratops tardabilis* from the Turonian of Uzbekistan (Sues & Averianov, 2009b). As the exact placement of *Turanoceratops* in the ceratopsian phylogenetic tree remains debated, current hypotheses suggest that *Turanoceratops* and *Zuniceratops* are closely associated taxa (Farke et al., 2009; Sues & Averianov, 2009b, 2009a; Xu et al., 2010).

The presumed absence of ceratopsids in Asia has been a curious issue, especially considering that horned dinosaurs originally came from Asia (Lee et al., 2011; Sereno, 2010; Zheng et al., 2015). So far, only one undisputed ceratopsid from China, *Sinoceratops zhuchengensis*, is known from the Asian continent, opposed to over a dozen ceratopsid taxa described from North America (Xu et al., 2010). The current view is that, after the initial migration to North America, ceratopsian evolution involved multiple dispersal events as evidenced by the occurrence of basal neoceratopsians, ceratopsoids as well as derived ceratopsids on both the North American and Asian continent. However, there is still a clear biogeographical division between the basal taxa in Asia and the derived taxa in North America. The derived ceratopsians are divided between centrosaurines and chasmosaurines and – besides *S. zhuchengensis* – are exclusively found in North America. Centrosaurines are characterized by relatively large nasal horns and distinct ornamentation of the frill, while chasmosaurines generally show relatively large postorbital horns, a smaller nasal horn and little ornamentation. Together, these two groups contribute the most to the number of ceratopsian species (Dodson, 2013). This enormous diversity of derived ceratopsians in North America only spans a period of approximately 90 to 66 million years ago and could be a result of the high degree of endemism among this group (Sampson et al., 2010) and/or suitable paleo-environments being limited to this continent (Xu et al., 2010).

1.1.2 *Triceratops* – the three-horned dinosaur

Triceratops is a chasmosaurine ceratopsian and was one of the largest horned dinosaurs to ever have lived, but showed limited cranial ornamentation when compared to other derived ceratopsids. Their skull had two large brow horns that were extensions of the postorbital bones, and their snout possessed a smaller horn that was an outgrowth of the nasal bone. The characteristic ceratopsian frill formed by the parietosquamosal complex was relatively short and unornamented (Figure 1 and Figure 2). Having been restricted to strata dating back to the Late Cretaceous only 68 to 66 million years ago (Scannella et al., 2014), *Triceratops* represents the most derived ceratopsian and belongs to one of the last surviving dinosaur genera moments before their extinction. Curiously, previous *Triceratops* discoveries have largely been limited to cranial material. While the exact reasons for this preservational bias remains unclear, it is most likely a combination of preferential reworking of smaller elements, collection bias, skull morphology and predator or scavenger behaviour (Brown et al., 2013, 2022; Ryan et al., 2010). Therefore, the cranial morphology of *Triceratops* has extensively been studied and is well understood (Figure 2) (Goodwin et al., 2006; Horner & Goodwin, 2006, 2008; Horner & Lamm, 2011). Juvenile *Triceratops* did not possess the large facial horns seen in adults, but showed relatively large and distinct bony ornamentation called epoccipitals lining the frill margin. During ontogeny, the postorbital horns showed significant growth in anterodorsal direction while the epoccipitals became more inconspicuous and were slowly resorbed into the frill margin. Senescent *Triceratops* were

characterized by smooth frill margins and anteriorly-inclined postorbital horns as well as near-complete fusion of the skull bones.

The group of Centrosaurinae and Chasmosaurinae evolved and radiated in a relatively short time, and there has been much debate about ceratopsian phylogeny, cladistics and species resolution (Forster, 1996b, 1996a; Longrich & Field, 2012; Mallon et al., 2016; Scannella & Horner, 2010, 2011). The large variety of intra- and interspecific cranial ornamentation seen among derived ceratopsids led to description of many new genera and species, especially during the early stages of palaeontological research in the late nineteenth century. Subtle variations in cranial morphology of newly discovered ceratopsian skulls were quickly used as the basis for new taxa. As a result, since *Triceratops* was erected as a new genus in 1889 by O. C. Marsh, a total of sixteen species had been named based on observed differences in cranial morphology (Forster, 1996b). However, more than a century later, an in-depth study on *Triceratops* species resolution using cladistics and morphometric shape analyses showed that only two valid species exist: *Triceratops horridus* and *Triceratops prorsus*, that are separated in time (Forster, 1996b; Scannella et al., 2014). The remaining taxa were deemed as morphotypes, individual variations and/or ontogenetic stages of these two acknowledged species.

1.1.3 Aim of this thesis

Triceratops can be considered as well-known dinosaurs among the general public, and certain aspects have been intensely studied for this specific taxon. However, even more than a century after its discovery, only very limited research has focussed on unravelling the palaeobiology of *Triceratops*. Current life reconstructions of *Triceratops* have largely been based on fragmentary material, comparative data of extinct relatives and/or extant taxa that are presumed to share similar life histories and niche occupations. This thesis aims to provide for the first time a detailed overview of *Triceratops* palaeobiology through the investigation of the 'Darnell *Triceratops* Bonebed' (DTB) from the Lance Formation of Wyoming, USA. The relatively high number of postcranial elements provide a wealth of new material to study *Triceratops* palaeobiology in unprecedented detail. Combining techniques in histology, stable isotope and trace element geochemistry as well as sedimentology, this thesis tries to uncover the exact origin of the DTB while simultaneously providing a renewed and updated life reconstruction of *Triceratops* growth, development, ecology and taxonomy. In doing so, this multidisciplinary approach – constructed from the 'Bonebed Toolkit' – provides an integrated scheme that will help reconstruct the most accurate and parsimonious scenario possible for the formation of one of the largest *Triceratops* bonebeds (Figure 3).

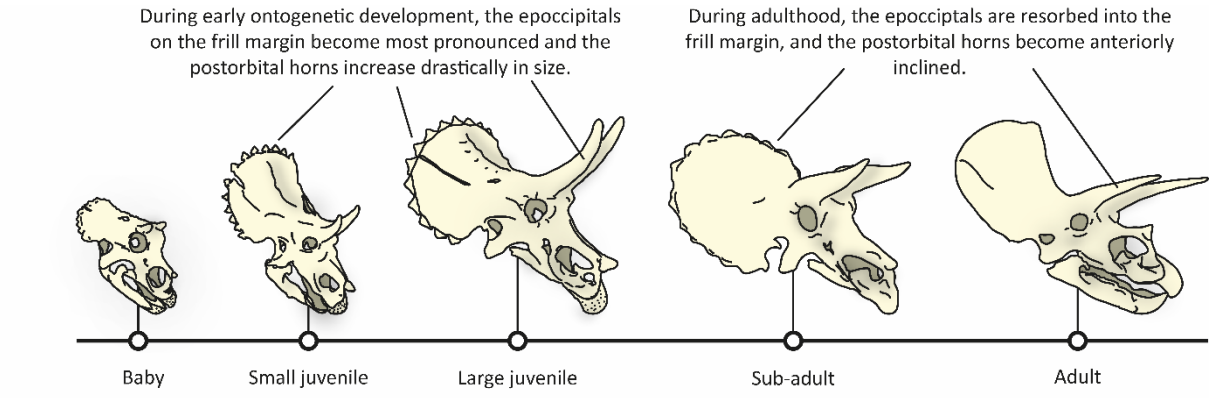

Figure 2. *Triceratops* cranial ontogeny showing the major cranial changes during ontogenetic development. From left to right, drawings based on UCMP 154452 (baby), MOR 1199 (small juvenile), MOR 1110 (large juvenile), MOR 1120 (sub-adult) and TMP1982.006.0001 (adult).

1.2 Research context: introducing the Bonebed Toolkit

1.2.1 Sedimentology and taphonomy

The inclusion of geological data in palaeontological research is crucial for the complete understanding of biological and ecological signals deduced from fossil organisms. Geological analyses reveal relevant information on the depositional setting and taphonomy of fossil specimens, which is especially relevant when dealing with large mass death assemblages (Rogers et al., 2007). While it goes beyond the scope of this thesis to cover the full extent of geological surveys often applied in bonebed analyses, some principles play a more relevant role in the Bonebed Toolkit than others and warrant some additional context. One purely sedimentological analysis that may yield insightful data during bonebed research is grain size analysis. Grain size analyses rely on the measurement and quantification of clastic sediment particles. Sediment samples from any specific fossil locality can be analysed to not only reveal the size of clastic particles, but also provide data on size distribution, relative size proportions as well as shape characteristics of sediment particles (López, 2017). The set of characteristics that defines particle size and shape in a given sediment setting is a result of past environmental factors, especially the type of transporting agents as well as the duration of transport experienced prior to final deposition (Stanley-Wood, 1992). Accordingly, the physical properties of fine-grained sediments allow for preservation

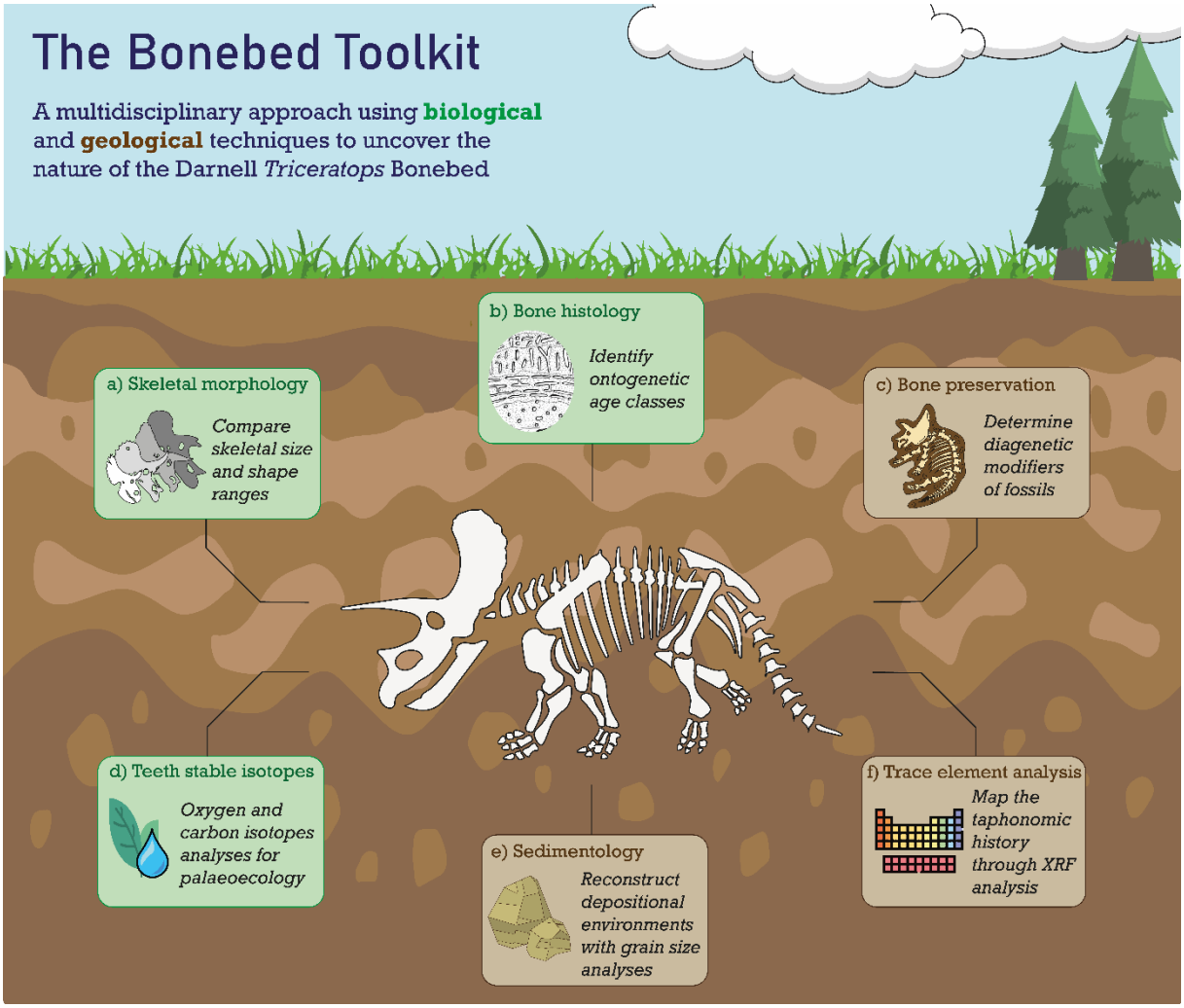

Figure 3. The Bonebed Toolkit showing the relevant areas of research applied in this thesis. Multiple independent lines of evidence should allow for the most accurate reconstruction of a large *Triceratops* bonebed while simultaneously providing new information on *Triceratops* palaeobiology.

almost exclusively in near-stagnant water bodies, while the prevalence of coarse-grained sediments indicates stronger palaeocurrents (López, 2017). Hence, grain size data of the fossiliferous matrix provides insights on past hydrodynamic conditions that prevailed during the deposition and fossilisation of animal remains, and helps in palaeoenvironmental and- ecological reconstructions that focus on transport and provenance of the material.

Complementary to sedimentological surveys such as grain size analyses is the taphonomical assessment of fossil material. Taphonomy studies the complete process of fossilisation and tries to identify relevant parameters that play a significant role during the incorporation of animal remains into the fossil record (Behrensmeyer, 1988; Lyman, 1994; Rogers et al., 2007). Identification of relevant taphonomic/diagenetic factors are crucial for the correct interpretation of large mass death assemblages, and may reveal whether a bonebed represents a single catastrophic event or is merely an accumulation over time (Rogers et al., 2007). Taphonomic signals inform about the degree of preservation and include assemblage, spatial and bone modification data. General assemblage data may simply focus on the taxonomic representation, minimum number of individuals and/or body size distribution within a fossil bonebed. Furthermore, skeletal sorting and articulation may reveal preservation bias towards smaller or larger elements. The spatial orientation of fossil bones and density of accumulation per unit of area may indicate post-mortem displacement and reburial of fossil bones. Additionally, modifications in bone quality such as breakage, weathering, abrasion or tooth marks all inform on the duration of pre- and post-mortem surface exposure, rate of burial and reburial events. Thus, there is a wide array of bonebed parameters that yield important information on its taphonomic history. Moreover, combining observations on taphonomic modifications with sedimentological data creates a powerful tool for reconstructing the depositional environment, and is paramount when aiming for accurate palaeobiological reconstructions (Rogers et al., 2007).

Recently, important contributions of taphonomic analyses have also come from micro-X-ray fluorescence (μXRF). μXRF entails the quantification of different trace elements, such as rare earth elements (REEs), contained within specific samples. This practice is commonly applied in (geo)chemistry (Renjith et al., 2021; Richards, 2019), material science (Dhara & Misra, 2019; Misra & Singh Mudher, 2002), archaeology (Gallello et al., 2019; Shackley, 2011) and forensic sciences (Pringle et al., 2022; Ulrich et al., 2004), but recent advances have yielded promising results in the context of invertebrate and vertebrate palaeontology (de Winter et al., 2016, 2020, 2021). The exact pathways through which trace elements enter the living organism are still unresolved, but the current consensus states that trace elements are incorporated through food and drinking water, as well as through the ingestions of soil and dust (Kohn et al., 2013). Thus, trace elements are mobilized through similar pathways as stable isotopes (see below), and as such, also must answer to chemical diagenesis during fossilisation. Taphonomical processes introduce exogenous trace elements from the embedding sediment into the material during different stages of fossilisation and is dependent on the composition of diagenetic fluid such as percolating groundwater, prevalent redox state and lithology (Herwartz et al., 2011; Picard et al., 2002; Trueman et al., 2003). Thus, animal remains acquire a unique elemental fingerprint during fossilisation related to their depositional environment (Tütken et al., 2011). While the original signal may be lost through different pathways, trace elemental composition of fossils can still provide invaluable data in provenance studies. Fossil material traces its own taphonomic history, and may record possible events such as post-mortem transport or reburial. As a result, detailed analysis of trace element compositions of fossil bonebeds provide insights on the postmortem history of the fossil assemblage, allowing to better reconstruct its taphonomic history (Botfalvai et al., 2023; Mclain et al., 2021).

1.2.2 Stable isotopes

Stable isotope analyses focus on extracting isotopic information from vertebrate hard tissue in order to reconstruct past ecosystems, animal behaviour and physiology (Clementz, 2012; Cullen et al., 2019, 2022, 2023; Fricke et al., 2008, 2009; Fricke & Pearson, 2008; Fricke & Rogers, 2000; Terrill et al., 2020). The two most commonly studied stable isotope systems in vertebrate palaeontology are carbon and oxygen, which provide information on diet and temperature, respectively (Cerling & Harris, 1999; Passey et al., 2005; Pecquerie et al., 2010; Rey et al., 2017). However, an increasing portion of research has expanded focus to other elements (Clementz, 2012; Martin et al., 2017), including nitrogen for trophic level reconstructions (Leichliter et al., 2022; Leichliter et al., 2021), sulphur for past changes in ecosystems and biomes (Nehlich, 2015), calcium for assessing dietary shifts and organismal physiology (Tacail et al., 2020) and strontium for migration and provenance (Terrill et al., 2020). Fossil hard tissue such as bone and teeth are commonly used in stable isotope research. Animals may move around within their home range or migrate long distances covering a large variety of food and water sources. Stable isotopes from the environment, such as carbon or oxygen, are taken up during feeding and drinking and are incorporated in the tooth enamel. This way, newly formed teeth that show incremental growth of enamel mobilise a time-record of ingested isotope signatures which is directly related to the animal's behavioural patterns as well as ecology (Figure 4). However, a thorough understanding of the prehistoric processes that may potentially have shaped the isotopic landscape is paramount to the interpretation of stable isotope data from extinct animals.

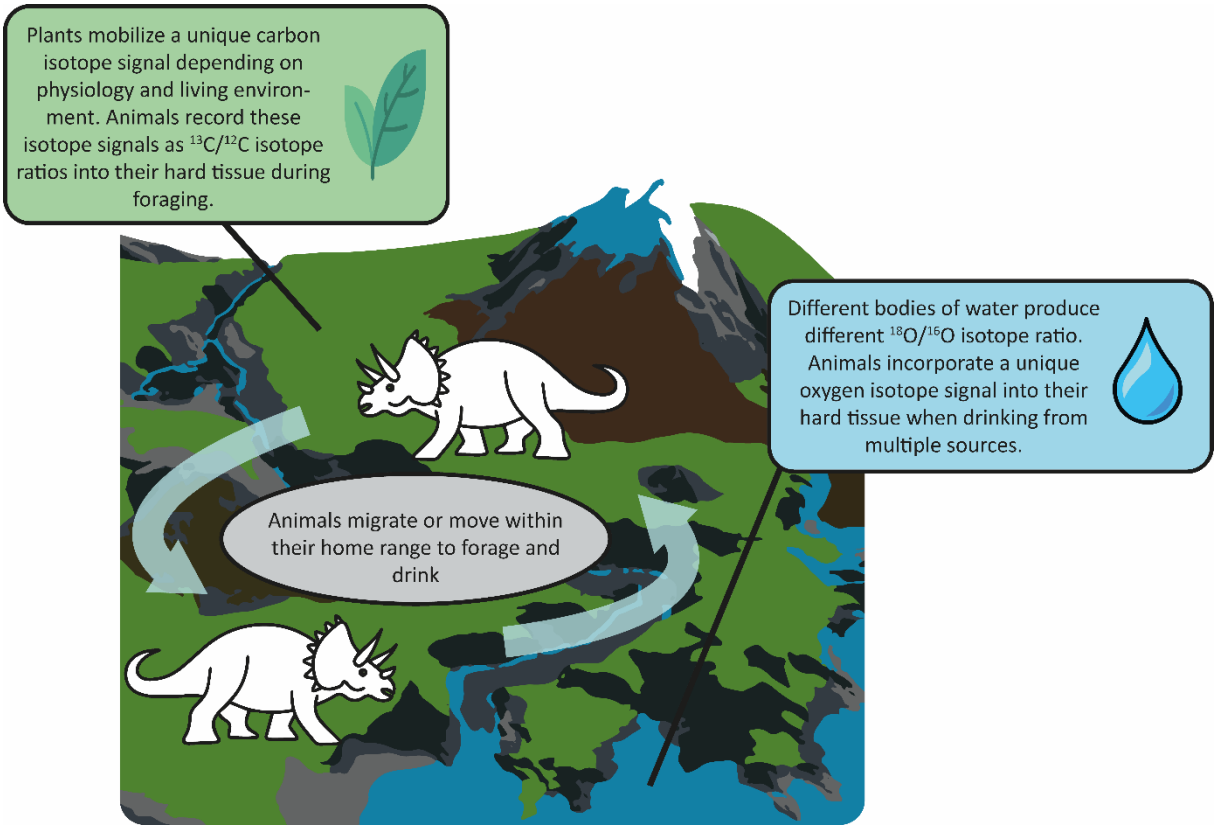

Figure 4. Schematic landscape showing how oxygen and carbon isotopes from the environment are taken up by animals when they migrate or move through their habitat, creating a time-accumulated isotope record to be studied for (palaeo-)ecology and (palaeo-)biology.

The preservation of an original isotope signature entirely depends on the degree of preservation of the studied material. Taphonomic effects may significantly alter the stable isotope composition during fossilisation by introducing exogenous material that overprints the original chemical signature (Kohn et al., 1999). Different types of bioapatite tissues such as bone or teeth show varying degrees of resistance against diagenetic overprinting during fossilisation. Bone and tooth dentine are relatively more organic-rich and porous due to the less dense organisation of their mineral (bioapatite) crystal lattice. Their bioapatite crystals generally preserve a larger surface area for exchange with minerals from surrounding sediment and groundwater, leading to overprinting and loss of the original isotopic fingerprint acquired during life (Glimcher, 2006; Kendall et al., 2018; Schwarcz, 2015). On the other hand, especially dense biominerals such as tooth enamel in fossils may more likely preserve the original isotopic fingerprint from when the animal was still alive. Enamel is an inorganic biomineral with highly organized large bioapatite crystals and is thus practically non-porous. Therefore, chemical alteration by means of mineral substitution during fossilisation is significantly less pronounced in tooth enamel, making it the preferred tissue for stable isotope analyses (Fricke et al., 2008; Trueman et al., 2003). The results of stable isotope analyses must always be considered in the larger framework of diagenesis, and the identification of relevant taphonomic processes that potentially could affect isotopic preservation is crucial when testing palaeoecological and- biological hypotheses.

1.2.3 Bone histology

Bone histology describes the study of (fossil) bone microstructure (Bailleul et al., 2019; Buffrénil et al., 2021). Bones can be sectioned to reveal microscopic histological markers such as bone tissue types, vascular canals, growth marks, osteocytes and bone remodelling patterns (De Boef & Larsson, 2007). The combination of different observed histological markers provides information on the growth and development of many vertebrates (Figure 5) (Buffrénil et al., 2021). Bone histology has been applied to many different extant and extinct taxa to inform about different life history parameters such as longevity and sexual and skeletal maturity, but have also played a major role in growth rate reconstructions and study of metabolism and physiology (Botha et al., 2022; Cullen et al., 2020; D'Emic et al., 2023; Horner et al., 1999, 2000; Klein & Sander, 2008; Sander, 2000).

On the most basic level, the organisation of the bone collagen fibres within the primary bone tissue conveys information about relative growth rates. Analysis of different primary bone tissue types in extant animals have succeeded in quantifying and comparing the apposition rates of different bone tissue types, which can now be applied to fossils of extinct taxa (de Margerie et al., 2002, 2004). Well-organized bone tissue often called lamellar bone is associated with periods of relatively slow growth, while so-called woven bone is characterized by highly disorganized collagen fibres related to periods of fast bone growth. Primary bone tissues are also commonly defined by different vascular patterns, in which the numbers and orientation of vascular canals relate to relative growth rates (de Margerie et al., 2002; Montes et al., 2010; Pratt & Cooper, 2018). Similarly, growth lines indicate periods of growth cessation and have become paramount in the analysis of age, longevity and growth rates (Cullen et al., 2021). Initial studies were ambiguous in establishing the major agents that led to the deposition of growth lines, but the current body of research holds that growth lines are annually deposited and occur in almost all major vertebrate groups (Horner et al., 1999; Köhler et al., 2012; Schucht et al., 2021; Tütken et al., 2004; Woodward et al., 2014). The extensive array of histological markers create unique patterns which can be compared among different taxa. For example, a substantial amount of dinosaur histological studies have shown that dinosaurs had relatively high growth rates, contradicting that of crocodiles and rivalling that of extant birds and mammals (Cullen et al., 2020; Padian et al., 2001;

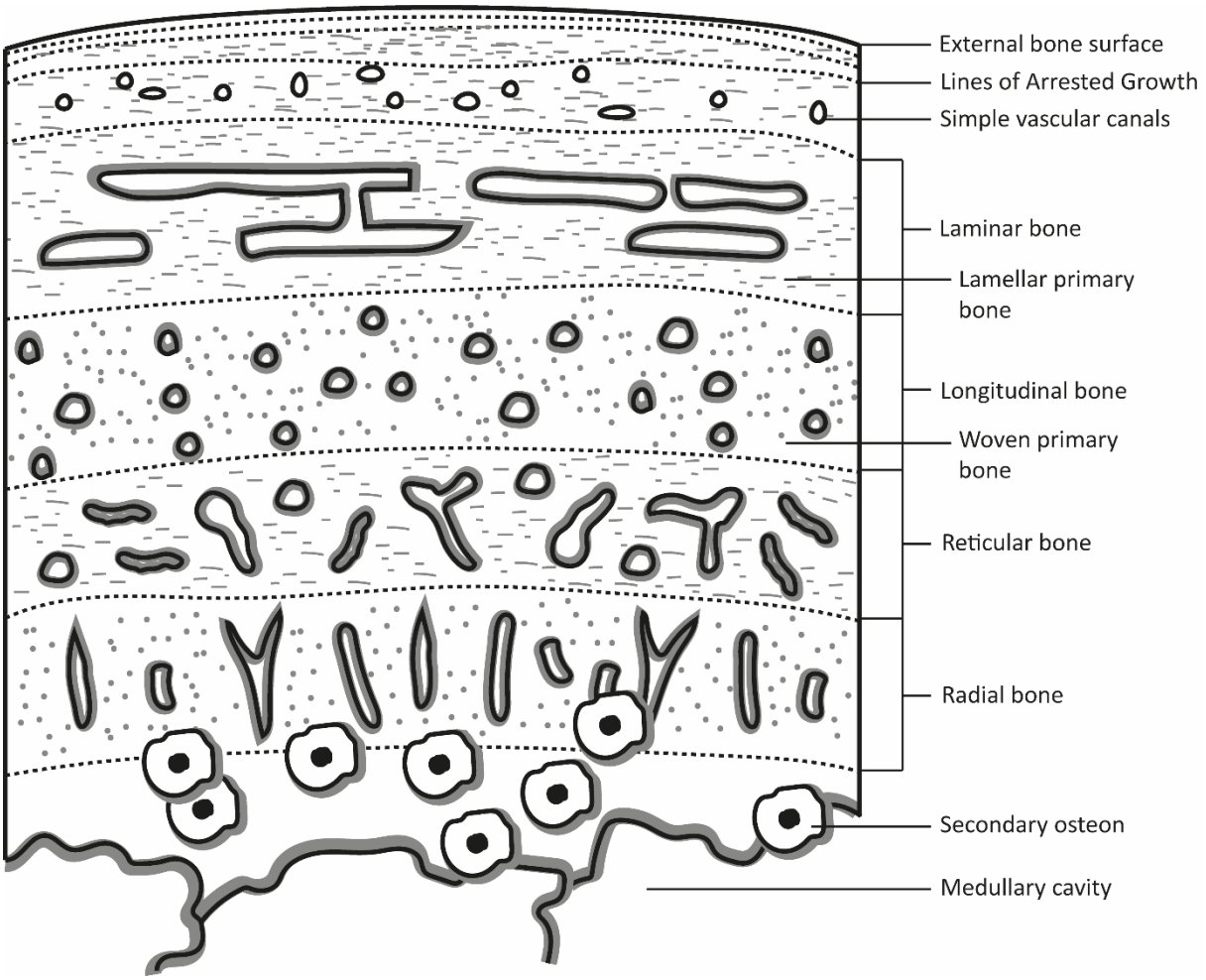

Figure 5. Schematic representation of a collection of the most relevant histological markers that can be observed in any bone histological section. Commonly studied markers include the orientation of primary osteons (indicated by grey outlines representing lamellar bone tissue surrounding the canal, opposed to simple vascular canals) and organisation of the primary bone tissue (slow growing lamellar vs. fast growing woven bone). Hypothetically, any combination of osteon and tissue organisation may occur, but some combinations appear more often in association. Different zones of bone are sometimes separated by lines of arrested growth. Secondary osteons advance from the medullary cavity towards the bone surface, overprinting any original primary bone tissue. When combined, these markers provide information about the (relative) age and growth of an (extinct) animal.

Sander, 2000). This provides a better understanding of metabolic and physiological thermoregulatory strategies (Grigg et al., 2022; Köhler et al., 2012; Rezende et al., 2020; Wiemann et al., 2022). Accordingly, bone histology of fossil vertebrates provides an essential method to study the palaeobiology of extinct organisms, especially when comparative data of related taxa is available.

Put into the larger framework of bonebed analyses, bone histology remains the only tool to create accurate mortality profiles and reconstruct age distributions of large mass death assemblages. Deciphering age profiles of bonebeds may provide insights on its formation and deposition, especially when studied through multiple ontogenetic characters. Bonebeds are generally categorized by attritional or catastrophic age profiles (R. G. Klein, 1982; Rogers et al., 2007). Attritional bonebeds preserve individuals that are most susceptible to various smaller scale mortality events and are generally characterized by animals that are either very young (i.e., juveniles) or very old (Rogers et al., 2007). These bonebeds may therefore form over time. In contrast, catastrophic bonebeds are formed after a single large-scale mortality event in which there is no age-selective mortality. Catastrophic

bonebeds more closely reflect the age distribution of the living population, where each ontogenetic stage gradually decreases in number (Rogers et al., 2007; Snyder et al., 2020). Thus, age profiles established through bone histological data shed light on the formation of fossil assemblages, and are especially valuable when complementing taphonomic, sedimentological and geochemical datasets.

1.2.4 Thesis outline

This thesis aims to unravel the origin of the Darnell *Triceratops* Bonebed by combining the aforementioned techniques in the multidisciplinary framework of the Bonebed Toolkit and – in doing so – create a better understanding of *Triceratops* ecology and behaviour. Each chapter focusses on a single method which combines in a Bonebed Toolkit unique for the analysis of the DTB.

Chapter 2 provides an in-depth analysis on the sedimentology and lithology of the DTB including high resolution grain-size and µXRF analyses. Furthermore, this chapter identifies the most relevant taphonomic modifiers that shaped the skeletal material in the DTB during its fossilization, and investigates multiple scenarios to reconstruct its depositional environment.

Chapter 3 focusses on identifying the stable carbon and oxygen isotope signature of fossil *Triceratops* teeth from the DTB. The preservation of the stable isotope record is evaluated through multiple analytical pathways of which the results extend upon and complement the hypotheses tested in Chapter 2. Moreover, characterisation of stable oxygen and carbon records allow for accurate palaeoecological and behavioural reconstructions of *Triceratops*.

Chapter 4 describes the bone histology of the DTB *Triceratops* in detail to identify ontogenetic age classes for large-bodied ceratopsian dinosaurs. This chapter employs multiple histological analyses to investigate age-related changes in bone microstructure, and puts the acquired data on growth and development in an evolutionary framework.

Chapter 5 extends on methods of ontogenetic ageing (such as bone histology) by attempting to quantify bone textural patterns of extant birds. This chapter complements previously established methods of textural ageing, and investigates whether bone surfaces can be quantified using established surface roughness parameters in digital microscopy.

Chapter 6 summarizes the most relevant findings of this thesis and serves as an evaluation of the Bonebed Toolkit to answer palaeobiological questions. Do all the multiple lines of evidence support the same hypothesis? Or in other words: **Does the Darnell *Triceratops* Bonebed represent a true social group, and thus provide evidence for gregarious behaviour in this taxon?**

References

Bailleul, A.M., O'Connor, J., Schweitzer, M.H., 2019. Dinosaur paleohistology: review, trends and new avenues of investigation. PeerJ 7, e7764. https://doi.org/10.7717/peerj.7764

Behrensmeyer, A.K., Hill, A.P. (Eds.), 1988. Fossils in the making: vertebrate taphonomy and paleoecology. The University of Chicago press, Chicago.

Benton, M.J. (Ed.), 2015. Vertebrate palaeontology, fourth edition. Wiley Blackwell, Chichester, West Sussex ; Hoboken, NJ.

Botfalvai, G., Kocsis, L., Szabó, M., Király, E., Sebe, K., 2023. Preliminarily report on rare earth element taphonomy of a Miocene mixed age fossil vertebrate assemblage (Pécs-Danitzpuszta, Mecsek Mts., Hungary): uptake mechanism and possible separation of palaeocommunities. Historical Biology 35, 498–517. https://doi.org/10.1080/08912963.2022.2049771

Botha, J., Choiniere, J.N., Benson, R.B.J., 2022. Rapid growth preceded gigantism in sauropodomorph evolution. Current Biology 32, 4501-4507.e2. https://doi.org/10.1016/j.cub.2022.08.031

Brown, C.M., Campione, N.E., Wilson Mantilla, G.P., Evans, D.C., 2022. Size-driven preservational and macroecological biases in the latest Maastrichtian terrestrial vertebrate assemblages of North America. Paleobiology 48, 210–238. https://doi.org/10.1017/pab.2021.35

Brown, C.M., Evans, D.C., Campione, N.E., O'Brien, L.J., Eberth, D.A., 2013. Evidence for taphonomic size bias in the Dinosaur Park Formation (Campanian, Alberta), a model Mesozoic terrestrial alluvial-paralic system. Palaeogeography, Palaeoclimatology, Palaeoecology 372, 108–122. https://doi.org/10.1016/j.palaeo.2012.06.027

Buffrénil, V. de, Ricqlès, A. de, Zylberberg, L., Padian, K. (Eds.), 2021. Vertebrate skeletal histology and paleohistology. CRC Press, Boca Raton.

Cerling, T.E., Harris, J.M., 1999. Carbon isotope fractionation between diet and bioapatite in ungulate mammals and implications for ecological and paleoecological studies. Oecologia 120, 347–363. https://doi.org/10.1007/s004420050868

Chiarenza, A.A., Mannion, P.D., Farnsworth, A., Carrano, M.T., Varela, S., 2022. Climatic constraints on the biogeographic history of Mesozoic dinosaurs. Current Biology 32, 570-585.e3. https://doi.org/10.1016/j.cub.2021.11.061

Clementz, M.T., 2012. New insight from old bones: stable isotope analysis of fossil mammals. Journal of Mammalogy 93, 368–380. https://doi.org/10.1644/11-MAMM-S-179.1

Cullen, T.M., Brown, C.M., Chiba, K., Brink, K.S., Makovicky, P.J., Evans, D.C., 2021. Growth variability, dimensional scaling, and the interpretation of osteohistological growth data. Biology Letters 17, 20210383. https://doi.org/10.1098/rsbl.2021.0383

Cullen, T.M., Canale, J.I., Apesteguía, S., Smith, N.D., Hu, D., Makovicky, P.J., 2020. Osteohistological analyses reveal diverse strategies of theropod dinosaur body-size evolution. Proceedings of the Royal Society B 287, 20202258. https://doi.org/10.1098/rspb.2020.2258

Cullen, T.M., Longstaffe, F.J., Wortmann, U.G., Goodwin, M.B., Huang, L., Evans, D.C., 2019. Stable isotopic characterization of a coastal floodplain forest community: a case study for isotopic reconstruction of Mesozoic vertebrate assemblages. Royal Society Open Science 6, 181210. https://doi.org/10.1098/rsos.181210

Cullen, T.M., Longstaffe, F.J., Wortmann, U.G., Huang, L., Evans, D.C., 2023. Anomalous ^{13}C enrichment in Mesozoic vertebrate enamel reflects environmental conditions in a "vanished world" and not a unique dietary physiology. Paleobiology 1–15. https://doi.org/10.1017/pab.2022.43

Cullen, T.M., Zhang, S., Spencer, J., Cousens, B., 2022. Sr-O-C isotope signatures reveal herbivore niche-partitioning in a Cretaceous ecosystem. Palaeontology 65. https://doi.org/10.1111/pala.12591

Currie, P.J., 2023. Celebrating dinosaurs: their behaviour, evolution, growth, and physiology. Canadian Journal of Earth Sciences 60, 263–293. https://doi.org/10.1139/cjes-2022-0131

De Boef, M., Larsson, H.C.E., 2007. Bone microstructure: quantifying bone vascular orientation. Canadian Journal of Zoology 85, 63–70. https://doi.org/10.1139/z06-195

de Margerie, E., Cubo, J., Castanet, J., 2002. Bone typology and growth rate: testing and quantifying 'Amprino's rule' in the mallard (*Anas platyrhynchos*). Comptes Rendus Biologies 325, 221–230. https://doi.org/10.1016/S1631-0691(02)01429-4

de Margerie, E., Robin, J.-P., Verrier, D., Cubo, J., Groscolas, R., Castanet, J., 2004. Assessing a relationship between bone microstructure and growth rate: a fluorescent labelling study in the king penguin chick (*Aptenodytes patagonicus*). Journal of Experimental Biology 207, 869–879. https://doi.org/10.1242/jeb.00841

de Winter, N.J., Dämmer, L.K., Falkenroth, M., Reichart, G.-J., Moretti, S., Martínez-García, A., Höche, N., Schöne, B.R., Rodiouchkina, K., Goderis, S., Vanhaecke, F., van Leeuwen, S.M., Ziegler, M.,

2021. Multi-isotopic and trace element evidence against different formation pathways for oyster microstructures. Geochimica et Cosmochimica Acta 308, 326–352. https://doi.org/10.1016/j.gca.2021.06.012

de Winter, N.J., Snoeck, C., Claeys, P., 2016. Seasonal cyclicity in trace elements and stable isotopes of modern horse enamel. PLoS ONE 11, e0166678. https://doi.org/10.1371/journal.pone.0166678

de Winter, N.J., Ullmann, C.V., Sørensen, A.M., Thibault, N., Goderis, S., Van Malderen, S.J.M., Snoeck, C., Goolaerts, S., Vanhaecke, F., Claeys, P., 2020. Shell chemistry of the boreal Campanian bivalve *Rastellum diluvianum* (Linnaeus, 1767) reveals temperature seasonality, growth rates and life cycle of an extinct Cretaceous oyster. Biogeosciences 17, 2897–2922. https://doi.org/10.5194/bg-17-2897-2020

D'Emic, M.D., O'Connor, P.M., Sombathy, R.S., Cerda, I., Pascucci, T.R., Varricchio, D., Pol, D., Dave, A., Coria, R.A., Curry Rogers, K.A., 2023. Developmental strategies underlying gigantism and miniaturization in non-avialan theropod dinosaurs. Science 379, 811–814. https://doi.org/10.1126/science.adc8714

Dhara, S., Misra, N.L., 2019. Elemental characterization of nuclear materials using total reflection X-ray fluorescence spectrometry. Trends in Analytical Chemistry 116, 31–43. https://doi.org/10.1016/j.trac.2019.04.017

Dodson, P., 2013. Ceratopsia increase: history and trends. Canadian Journal of Earth Sciences 50, 294–305. https://doi.org/10.1139/cjes-2012-0085

Dunhill, A.M., Bestwick, J., Narey, H., Sciberras, J., 2016. Dinosaur biogeographical structure and Mesozoic continental fragmentation: a network-based approach. Journal of Biogeography 43, 1691–1704. https://doi.org/10.1111/jbi.12766

Farke, A.A., Maxwell, W.D., Cifelli, R.L., Wedel, M.J., 2014. A ceratopsian dinosaur from the Lower Cretaceous of Western North America, and the biogeography of Neoceratopsia. PLoS ONE 9, e112055. https://doi.org/10.1371/journal.pone.0112055

Farke, A.A., Sampson, S.D., Forster, C.A., Loewen, M.A., 2009. *Turanoceratops tardabilis*—sister taxon, but not a ceratopsid. Naturwissenschaften 96, 869–870. https://doi.org/10.1007/s00114-009-0543-8

Forster, C.A., 1996a. Species resolution in *Triceratops* : cladistic and morphometric approaches. Journal of Vertebrate Paleontology 16, 259–270. https://doi.org/10.1080/02724634.1996.10011313

Forster, C.A., 1996b. New information on the skull of *Triceratops*. Journal of Vertebrate Paleontology 16, 246–258. https://doi.org/10.1080/02724634.1996.10011312

Fricke, H.C., Pearson, D.A., 2008. Stable isotope evidence for changes in dietary niche partitioning among hadrosaurian and ceratopsian dinosaurs of the Hell Creek Formation, North Dakota. Paleobiology 34, 534–552. https://doi.org/10.1666/08020.1

Fricke, H.C., Rogers, R.R., 2000. Multiple taxon–multiple locality approach to providing oxygen isotope evidence for warm-blooded theropod dinosaurs. Geology 28, 799. https://doi.org/10.1130/0091-7613(2000)28<799:MTLATP>2.0.CO;2

Fricke, H.C., Rogers, R.R., Backlund, R., Dwyer, C.N., Echt, S., 2008. Preservation of primary stable isotope signals in dinosaur remains, and environmental gradients of the Late Cretaceous of Montana and Alberta. Palaeogeography, Palaeoclimatology, Palaeoecology 266, 13–27. https://doi.org/10.1016/j.palaeo.2008.03.030

Fricke, H.C., Rogers, R.R., Gates, T.A., 2009. Hadrosaurid migration: inferences based on stable isotope comparisons among Late Cretaceous dinosaur localities. Paleobiology 35, 270–288. https://doi.org/10.1666/08025.1

Gallello, G., Ferro-Vázquez, C., Chenery, S., Lang, C., Thornton-Barnett, S., Kabora, T., Hodson, M.E., Stump, D., 2019. The capability of rare earth elements geochemistry to interpret complex archaeological stratigraphy. Microchemical Journal 148, 691–701. https://doi.org/10.1016/j.microc.2019.05.050

Glimcher, M.J., 2006. Bone: nature of the calcium phosphate crystals and cellular, structural, and physical chemical mechanisms in their formation. Reviews in Mineralogy and Geochemistry 64, 223–282. https://doi.org/10.2138/rmg.2006.64.8

Goodwin, M.B., Clemens, W.A., Horner, J.R., Padian, K., 2006. The smallest known *Triceratops* skull: new observations on ceratopsid cranial anatomy and ontogeny. Journal of Vertebrate Paleontology 26, 103–112. https://doi.org/10.1671/0272-4634(2006)26[103:TSKTSN]2.0.CO;2

Granger, W., Gregory, W.K., Berkey, C.P., 1923. *Protoceratops andrewsi*, a pre-ceratopsian dinosaur from Mongolia. American Museum novitates 72.

Grigg, G., Nowack, J., Bicudo, J.E.P.W., Bal, N.C., Woodward, H.N., Seymour, R.S., 2022. Whole-body endothermy: ancient, homologous and widespread among the ancestors of mammals, birds and crocodylians. Biological Reviews 97, 766–801. https://doi.org/10.1111/brv.12822

Hatcher, J.B., Lull, R.S., Marsh, O.C., Osborn, H.F., 1907. The Ceratopsia,. Govt. Print. Off., Washington,. https://doi.org/10.5962/bhl.title.60500

Herwartz, D., Tütken, T., Münker, C., Jochum, K.P., Stoll, B., Sander, P.M., 2011. Timescales and mechanisms of REE and Hf uptake in fossil bones. Geochimica et Cosmochimica Acta 75, 82–105. https://doi.org/10.1016/j.gca.2010.09.036

Horner, J.R., De Ricqlès, A., Padian, K., 2000. Long bone histology of the hadrosaurid dinosaur *Maiasaura peeblesorum* : growth dynamics and physiology based on an ontogenetic series of skeletal elements. Journal of Vertebrate Paleontology 20, 115–129. https://doi.org/10.1671/0272-4634(2000)020[0115:LBHOTH]2.0.CO;2

Horner, J.R., de Ricqlès, A., Padian, K., 1999. Variation in dinosaur skeletochronology indicators: implications for age assessment and physiology. Paleobiology 25, 295–304. https://doi.org/10.1017/S0094837300021308

Horner, J.R., Goodwin, M.B., 2008. Ontogeny of cranial epi-ossifications in *Triceratops*. Journal of Vertebrate Paleontology 28, 134–144. https://doi.org/10.1671/0272-4634(2008)28[134:OOCEIT]2.0.CO;2

Horner, J.R., Goodwin, M.B., 2006. Major cranial changes during *Triceratops* ontogeny. Proceedings of the Royal Society B 273, 2757–2761. https://doi.org/10.1098/rspb.2006.3643

Horner, J.R., Lamm, E.-T., 2011. Ontogeny of the parietal frill of *Triceratops*: A preliminary histological analysis. Comptes Rendus Palevol 10, 439–452. https://doi.org/10.1016/j.crpv.2011.04.006

Kendall, C., Eriksen, A.M.H., Kontopoulos, I., Collins, M.J., Turner-Walker, G., 2018. Diagenesis of archaeological bone and tooth. Palaeogeography, Palaeoclimatology, Palaeoecology 491, 21–37. https://doi.org/10.1016/j.palaeo.2017.11.041

Klein, N., Sander, M., 2008. Ontogenetic stages in the long bone histology of sauropod dinosaurs. Paleobiology 34, 247–263. https://doi.org/10.1666/0094-8373(2008)034[0247:OSITLB]2.0.CO;2

Klein, R.G., 1982. Age (Mortality) Profiles as a Means of Distinguishing Hunted Species from Scavenged Ones in Stone Age Archeological Sites. Paleobiology 8, 151–158.

Köhler, M., Marín-Moratalla, N., Jordana, X., Aanes, R., 2012. Seasonal bone growth and physiology in endotherms shed light on dinosaur physiology. Nature 487, 358–361. https://doi.org/10.1038/nature11264

Kohn, M.J., Morris, J., Olin, P., 2013. Trace element concentrations in teeth – a modern Idaho baseline with implications for archeometry, forensics, and palaeontology. Journal of Archaeological Science 40, 1689–1699. https://doi.org/10.1016/j.jas.2012.11.012

Kohn, M.J., Schoeninger, M.J., Barker, W.W., 1999. Altered states: effects of diagenesis on fossil tooth chemistry. Geochimica et Cosmochimica Acta 63, 2737–2747. https://doi.org/10.1016/S0016-7037(99)00208-2

Lee, Y.-N., Ryan, M.J., Kobayashi, Y., 2011. The first ceratopsian dinosaur from South Korea. Naturwissenschaften 98, 39–49. https://doi.org/10.1007/s00114-010-0739-y

Leichliter, J., Lüdecke, T., Foreman, A., Bourgon, N., Duprey, N., Vonhof, H., Souksavatdy, V., Bacon, A.-M., Sigman, D., Tütken, T., Martinez-Garcia, A., 2022. Nitrogen isotopic composition of tooth enamel organic matter records trophic position in modern and fossil ecosystems (preprint). In Review. https://doi.org/10.21203/rs.3.rs-1942250/v1

Leichliter, J.N., Lüdecke, T., Foreman, A.D., Duprey, N.N., Winkler, D.E., Kast, E.R., Vonhof, H., Sigman, D.M., Haug, G.H., Clauss, M., Tütken, T., Martínez-García, A., 2021. Nitrogen isotopes in tooth enamel record diet and trophic level enrichment: Results from a controlled feeding experiment. Chemical Geology 563, 120047. https://doi.org/10.1016/j.chemgeo.2020.120047

Longrich, N.R., Field, D.J., 2012. *Torosaurus* Is Not *Triceratops*: Ontogeny in Chasmosaurine Ceratopsids as a Case Study in Dinosaur Taxonomy. PLoS ONE 7, e32623. https://doi.org/10.1371/journal.pone.0032623

López, G.I., 2017. Grain Size Analysis. In: Gilbert, A.S. (Ed.), Encyclopedia of Geoarchaeology, Encyclopedia of Earth Sciences Series. Springer Netherlands, Dordrecht, pp. 341–348. https://doi.org/10.1007/978-1-4020-4409-0_18

Lyman, R.L., 1994. Vertebrate Taphonomy, 1st ed. Cambridge University Press, Cambridge. https://doi.org/10.1017/CBO9781139878302

Mallon, J.C., Ott, C.J., Larson, P.L., Iuliano, E.M., Evans, D.C., 2016. *Spiclypeus shipporum* gen. et sp. nov., a boldly audacious new chasmosaurine ceratopsid (Dinosauria: Ornithischia) from the Judith River Formation (Upper Cretaceous: Campanian) of Montana, USA. PLoS ONE 11, e0154218. https://doi.org/10.1371/journal.pone.0154218

Martin, J.E., Tacail, T., Balter, V., 2017. Non-traditional isotope perspectives in vertebrate palaeobiology. Palaeontology 60, 485–502. https://doi.org/10.1111/pala.12300

Mclain, M.A., Ullmann, P.V., Ash, R.D., Bohnstedt, K., Nelsen, D., Clark, R.O., Brand, L.R., Chadwick, A.V., 2021. Independent confirmation of fluvial reworking at a Lance Formation (Maastrichtian) bonebed by traditional and chemical taphonomic analyses. Palaios 36, 193–215. https://doi.org/10.2110/palo.2020.064

Misra, N.L., Singh Mudher, K.D., 2002. Total reflection X-ray fluorescence: A technique for trace element analysis in materials. Progress in Crystal Growth and Characterization of Materials 45, 65–74. https://doi.org/10.1016/S0960-8974(02)00029-3

Montes, L., Castanet, J., Cubo, J., 2010. Relationship between bone growth rate and bone tissue organization in amniotes: first test of Amprino's rule in a phylogenetic context. Animal Biology 60, 25–41. https://doi.org/10.1163/157075610X12610595764093

Nabavizadeh, A., 2023. How *Triceratops* got its face: An update on the functional evolution of the ceratopsian head. The Anatomical Record ar.25196. https://doi.org/10.1002/ar.25196

Nehlich, O., 2015. The application of sulphur isotope analyses in archaeological research: A review. Earth-Science Reviews 142, 1–17. https://doi.org/10.1016/j.earscirev.2014.12.002

O'Donovan, C., Meade, A., Venditti, C., 2018. Dinosaurs reveal the geographical signature of an evolutionary radiation. Nature Ecology and Evolution 2, 452–458. https://doi.org/10.1038/s41559-017-0454-6

Osborn, H.F., 1923. Two Lower Cretaceous dinosaurs of Mongolia. American Museum novitates 95.

Padian, K., de Ricqlès, A.J., Horner, J.R., 2001. Dinosaurian growth rates and bird origins. Nature 412, 405–408. https://doi.org/10.1038/35086500

Passey, B.H., Robinson, T.F., Ayliffe, L.K., Cerling, T.E., Sponheimer, M., Dearing, M.D., Roeder, B.L., Ehleringer, J.R., 2005. Carbon isotope fractionation between diet, breath CO_2, and bioapatite in different mammals. Journal of Archaeological Science 32, 1459–1470. https://doi.org/10.1016/j.jas.2005.03.015

Pecquerie, L., Nisbet, R.M., Fablet, R., Lorrain, A., Kooijman, S.A.L.M., 2010. The impact of metabolism on stable isotope dynamics: a theoretical framework. Philosophical Transactions of the Royal Society B 365, 3455–3468. https://doi.org/10.1098/rstb.2010.0097

Picard, S., Lécuyer, C., Barrat, J.-A., Garcia, J.-P., Dromart, G., Sheppard, S.M.F., 2002. Rare earth element contents of Jurassic fish and reptile teeth and their potential relation to seawater composition (Anglo-Paris Basin, France and England). Chemical Geology 186, 1–16. https://doi.org/10.1016/S0009-2541(01)00424-7

Pratt, I.V., Cooper, D.M.L., 2018. The effect of growth rate on the three-dimensional orientation of vascular canals in the cortical bone of broiler chickens. Journal of Anatomy 233, 531–541. https://doi.org/10.1111/joa.12847

Pringle, J.K., Jeffery, A.J., Ruffell, A., Stimpson, I.G., Pirrie, D., Bergslien, E., Madden, C., Oliver, I., Wisniewski, K.D., Cassella, J.P., Lamont, N., Gormley, S., Partridge, J., 2022. The use of portable XRF as a forensic geoscience non-destructive trace evidence tool for environmental and criminal investigations. Forensic Science International 332, 111175. https://doi.org/10.1016/j.forsciint.2022.111175

Renjith, R.A., Rejith, R.G., Sundararajan, M., 2021. Evaluation of coastal sediments. In: Rani, M., Seenipandi, K., Rehman, S., Kumar, P., Sajjad, H. (Eds.), Remote Sensing of Ocean and Coastal Environments. Elsevier, pp. 99–116. https://doi.org/10.1016/B978-0-12-819604-5.00007-X

Rey, K., Amiot, R., Fourel, F., Abdala, F., Fluteau, F., Jalil, N.-E., Liu, J., Rubidge, B.S., Smith, R.M., Steyer, J.S., Viglietti, P.A., Wang, X., Lécuyer, C., 2017. Oxygen isotopes suggest elevated thermometabolism within multiple Permo-Triassic therapsid clades. eLife 6, e28589. https://doi.org/10.7554/eLife.28589

Rezende, E.L., Bacigalupe, L.D., Nespolo, R.F., Bozinovic, F., 2020. Shrinking dinosaurs and the evolution of endothermy in birds. Science Advances 6, eaaw4486. https://doi.org/10.1126/sciadv.aaw4486

Richards, M.J., 2019. Realising the potential of portable XRF for the geochemical classification of volcanic rock types. Journal of Archaeological Science 105, 31–45. https://doi.org/10.1016/j.jas.2019.03.004

Rogers, R.R., Eberth, D.A., Fiorillo, A.R. (Eds.), 2007. Bonebeds: genesis, analysis, and paleobiological significance. University of Chicago Press, Chicago.

Ryan, M.J., Chinnery-Allgeier, B.J., Eberth, D.A. (Eds.), 2010. New perspectives on horned dinosaurs: the Royal Tyrrell Museum Ceratopsian Symposium. Indiana University Press, Bloomington.

Sampson, S.D., Loewen, M.A., 2010. Unraveling a radiation: a review of the diversity, stratigraphic distribution, biogeography, and evolution of horned dinosaurs (Ornithischia: Ceratopsidae). In: Ryan, M.J. Chinnery-Allgeier, B.J. Eberth, D.A. (Eds.), New Perspectives on Horned Dinosaurs: The

Royal Tyrrell Museum Ceratopsian Symposium. Indiana University Press, Bloomington, pp. 405–427.

Sampson, S.D., Loewen, M.A., Farke, A.A., Roberts, E.M., Forster, C.A., Smith, J.A., Titus, A.L., 2010. New horned dinosaurs from Utah provide evidence for intracontinental dinosaur endemism. PLoS ONE 5, e12292. https://doi.org/10.1371/journal.pone.0012292

Sander, P.M., 2000. Longbone histology of the Tendaguru sauropods: implications for growth and biology. Paleobiology 26, 466–488. https://doi.org/10.1666/0094-8373(2000)026<0466:LHOTTS>2.0.CO;2

Scannella, J.B., Fowler, D.W., Goodwin, M.B., Horner, J.R., 2014. Evolutionary trends in *Triceratops* from the Hell Creek Formation, Montana. Proceedings of the National Academy of Science U.S.A. 111, 10245–10250. https://doi.org/10.1073/pnas.1313334111

Scannella, J.B., Horner, J.R., 2011. '*Nedoceratops*': An example of a transitional morphology. PLoS ONE 6, e28705. https://doi.org/10.1371/journal.pone.0028705

Scannella, J.B., Horner, J.R., 2010. *Torosaurus* Marsh, 1891, is *Triceratops* Marsh, 1889 (Ceratopsidae: Chasmosaurinae): synonymy through ontogeny. Journal of Vertebrate Paleontology 30, 1157–1168. https://doi.org/10.1080/02724634.2010.483632

Schucht, P.J., Klein, N., Lambertz, M., 2021. What's my age again? On the ambiguity of histology-based skeletochronology. Proceedings of the Royal Society B. 288, 20211166. https://doi.org/10.1098/rspb.2021.1166

Schwarcz, H.P., 2015. The ultrastructure of bone as revealed in electron microscopy of ion-milled sections. Seminars in Cell & Developmental Biology 46, 44–50. https://doi.org/10.1016/j.semcdb.2015.06.008

Sereno, P.C., 2010. Taxonomy, cranial morphology, and relationships of parrot-beaked dinosaurs (Ceratopsia: *Psittacosaurus*). In: Ryan, M.J. Chinnery-Allgeier, B.J. Eberth, D.A. (Eds.), New Perspectives on Horned Dinosaurs: The Royal Tyrrell Museum Ceratopsian Symposium. Indiana University Press, Bloomington, pp. 21-58.

Shackley, M.S. (Ed.), 2011. X-Ray Fluorescence Spectrometry (XRF) in Geoarchaeology. Springer New York, New York. https://doi.org/10.1007/978-1-4419-6886-9

Snyder, K., McLain, M., Wood, J., Chadwick, A., 2020. Over 13,000 elements from a single bonebed help elucidate disarticulation and transport of an *Edmontosaurus* thanatocoenosis. PLoS ONE 15, e0233182. https://doi.org/10.1371/journal.pone.0233182

Stanley-Wood, N.G. (Ed.), 1992. Particle size analysis: the proceedings of the 25th Anniversary Conference organised by the Particle Characterisation Group of the Analytical Division of the Royal Society of Chemistry, 17th - 19th September 1991, University of Technology, Loughborough, Special publication / Royal Society of Chemistry. Presented at the Particle Size Analysis Conference, Royal Soc. of Chemistry, Cambridge.

Starrfelt, J., Liow, L.H., 2016. How many dinosaur species were there? Fossil bias and true richness estimated using a Poisson sampling model. Philosophical Transactions of the Royal Society B 371, 20150219. https://doi.org/10.1098/rstb.2015.0219

Sues, H.-D., Averianov, A., 2009a. *Turanoceratops tardabilis*—the first ceratopsid dinosaur from Asia. Naturwissenschaften 96, 645–652. https://doi.org/10.1007/s00114-009-0518-9

Sues, H.-D., Averianov, A., 2009b. Phylogenetic position of *Turanoceratops* (Dinosauria: Ceratopsia). Naturwissenschaften 96, 871–872. https://doi.org/10.1007/s00114-009-0552-7

Tacail, T., Le Houedec, S., Skulan, J.L., 2020. New frontiers in calcium stable isotope geochemistry: Perspectives in present and past vertebrate biology. Chemical Geology 537, 119471. https://doi.org/10.1016/j.chemgeo.2020.119471

Terrill, D.F., Henderson, C.M., Anderson, J.S., 2020. New application of strontium isotopes reveals evidence of limited migratory behaviour in Late Cretaceous hadrosaurs. Biology Letters 16, 20190930. https://doi.org/10.1098/rsbl.2019.0930

Trueman, C., Chenery, C., Eberth, D.A., Spiro, B., 2003. Diagenetic effects on the oxygen isotope composition of bones of dinosaurs and other vertebrates recovered from terrestrial and marine sediments. Journal of the Geological Society 160, 895–901. https://doi.org/10.1144/0016-764903-019

Tütken, T., Pfretzschner, H.-U., Vennemann, T.W., Sun, G., Wang, Y.D., 2004. Paleobiology and skeletochronology of Jurassic dinosaurs: implications from the histology and oxygen isotope compositions of bones. Palaeogeography, Palaeoclimatology, Palaeoecology 206, 217–238. https://doi.org/10.1016/j.palaeo.2004.01.005

Tütken, T., Vennemann, T.W., Pfretzschner, H.-U., 2011. Nd and Sr isotope compositions in modern and fossil bones – Proxies for vertebrate provenance and taphonomy. Geochimica et Cosmochimica Acta 75, 5951–5970. https://doi.org/10.1016/j.gca.2011.07.024

Ulrich, A., Moor, C., Vonmont, H., Jordi, H.-R., Lory, M., 2004. ICP-MS trace-element analysis as a forensic tool. Analytical and Bioanalytical Chemistry 378, 1059–1068. https://doi.org/10.1007/s00216-003-2434-8

Upchurch, P., Hunn, C.A., Norman, D.B., 2002. An analysis of dinosaurian biogeography: evidence for the existence of vicariance and dispersal patterns caused by geological events. Proceedings of the Royal Society of London B 269, 613–621. https://doi.org/10.1098/rspb.2001.1921

Wang, S.C., Dodson, P., 2006. Estimating the diversity of dinosaurs. Proceedings of the National Academy of Science U.S.A. 103, 13601–13605. https://doi.org/10.1073/pnas.0606028103

Wiemann, J., Menéndez, I., Crawford, J.M., Fabbri, M., Gauthier, J.A., Hull, P.M., Norell, M.A., Briggs, D.E.G., 2022. Fossil biomolecules reveal an avian metabolism in the ancestral dinosaur. Nature 606, 522–526. https://doi.org/10.1038/s41586-022-04770-6

Wolfe, D.G., Kirkland, J.I., 1998. *Zuniceratops christopheri* n. gen. & n. sp., a ceratopsian dinosaur from the Moreno Hill Formation (Cretaceous, Turonian) of west-central New Mexico. Lower and Middle Cretaceous terrestrial ecosystems 14, 303–318.

Woodward, H.N., Horner, J.R., Farlow, J.O., 2014. Quantification of intraskeletal histovariability in *Alligator mississippiensis* and implications for vertebrate osteohistology. PeerJ 2, e422. https://doi.org/10.7717/peerj.422

Xu, X., Forster, C.A., Clark, J.M., Mo, J., 2006. A basal ceratopsian with transitional features from the Late Jurassic of northwestern China. Proceedings of the Royal Society B 273, 2135–2140. https://doi.org/10.1098/rspb.2006.3566

Xu, X., Wang, K., Zhao, X., Li, D., 2010. First ceratopsid dinosaur from China and its biogeographical implications. Chinese Science Bulletin 55, 1631–1635. https://doi.org/10.1007/s11434-009-3614-5

Zheng, W., Jin, X., Xu, X., 2015. A psittacosaurid-like basal neoceratopsian from the Upper Cretaceous of central China and its implications for basal ceratopsian evolution. Scientific Reports 5, 14190. https://doi.org/10.1038/srep14190

2

Chapter 2. The taphonomy of the Darnell *Triceratops* bonebed

To be submitted as:
Pim Kaskes, Jimmy de Rooij, Dylan Bastiaans, Oeki Verhage, Roeland Emaus, Leonie Portanger, Martijn Guliker, Yasmin Grooters, Maarten Prins, Philippe Claeys, Anne Schulp. Gregarious behavior in chasmosaurine dinosaurs: evidence from a large *Triceratops* bonebed.

Abstract

The iconic horned dinosaur *Triceratops* is one of the most abundant non-avian dinosaurs of Late Cretaceous western North America. While extensively studied from more material than for most other dinosaurs, its biology still remains poorly known. Vertebrate bonebeds can provide unique snapshots in the paleobiology of non-avian dinosaurs, including gregarious behavior. Here, we present the monodominant 'Darnell *Triceratops* Bonebed' from the Lower Lance Formation in eastern Wyoming. This site represents the largest chasmosaurine bonebed found to date with >700 identifiable fossil elements preserved within a thin, fine-grained stratum of approximately 0.8 meter thick. This includes a large fraction of rare postcranial material (>30%) and encompasses a minimum number of five individuals of *Triceratops horridus*. Osteohistology hint towards a multigenerational assemblage, both with adult and subadult individuals. This is based on the presence of unornamented and ornamented frills, fused and unfused skull parts, and pristine preservation of both fast-growing circumferential bone and slower growing woven-parallel bone. Grain-size, thermogravimetric, X-ray fluorescence, petrographic and paleobotanical analyses show that the sediments entombing the skeletons represent organic-rich clay to fine siltstones, covered by two distinct very fine sandstone intervals, of which one is enriched in CaO content. Intra-bone trace element patterns throughout the bonebed reveal overall homogeneous low REE contents and steep declines in light REE concentrations with increasing cortical depth, implying a shared taphonomic history excluding an attritional bonebed scenario. Hence, the most parsimonious taphonomic scenario that matches these lines of evidence entails miring of multiple *Triceratops* individuals in paludal conditions within a residual river channel setting, possibly as a group. This phase is followed by rapid burial by two separate crevasse splay events, causing a slight lateral displacement and disarticulation of the bone elements but preventing scavenging and still allowing the rare preservation of small postcranial elements. We interpret that the Darnell *Triceratops* Bonebed therefore provides a unique snapshot in possible gregarious behavior of *Triceratops horridus*, which might have been common in earlier chasmosaurine dinosaurs as well.

2.1 Introduction

Triceratops (Dinosauria, Ceratopsia, Chasmosaurinae) is one of the most well-known and most abundant dinosaur taxa from the uppermost Cretaceous of western North America (1, 2). This iconic horned dinosaur represents the end of an evolutionary lineage of an incredibly successful and diverse group of megaherbivores (Ceratopsidae) that formed an important part of terrestrial ecosystems in Laramidia during the Campanian and Maastrichtian (3). Remains of *Triceratops* have been found in a variety of Maastrichtian-aged geological formations in the Western Interior of the USA (Hell Creek, Lance and Denver Formation (Fm.)) and Canada (Scollard and Frenchman Fm.), which covered a range of paludal, fluvial and coastal depositional environments (3–5). *Triceratops* has a well-defined stratigraphic range with specimens found in strata dating back from ~67 Ma up to the Cretaceous-

Paleogene (K-Pg) boundary, ~66 Ma (1, 6, 7). Dinosaur census recorded during the Hell Creek Project in northern Montana (1999-2009) showed that *Triceratops* (n = 73) was the most encountered large-bodied dinosaur comprising ~40% of the assemblage (2). A more recent dinosaur census study, covering associated and articulated specimens from museum and private collections of both the Hell Creek Fm. (Montana, North-Dakota and South-Dakota) and Lance Fm. (Wyoming), showed that ceratopsians (n = 335) encompass even 51% of the dinosaur assemblage, most of them positively identified as *Triceratops* (8).

Despite this abundant fossil record, collections of *Triceratops* consist predominantly of cranial material, recovered mostly from the Hell Creek and Lance Fm. (9–12). Associated specimens of *Triceratops* comprising both cranial and postcranial elements remain relatively rare. Horner et al. (2011) (2) attributed this rarity to a historical collecting bias influenced by facies and taphonomic factors or due to the effect of how extensive a fossil quarry is excavated after a *Triceratops* skull is collected. The lack of adequate postcranial material available for study can be considered as a major caveat in the paleobiological knowledge of the genus *Triceratops*, or even the Chasmosaurinae as a whole. Our current osteological understanding of the skeleton of *Triceratops* is mostly based on historical accounts with only a handful of reference specimens available to date (10). Partially as a result of this, the ontogeny and even taxonomy of *Triceratops* remains poorly constrained to date, and scientific debate on these topics has emerged in recent years. For example, Scanella & Horner (2010), based on studies on parietal fenestrae and squamosal elongation, claimed that *Torosaurus* should not be considered as a separate coeval chasmosaurine genus but as a very mature ontogenetic stage of *Triceratops* (13). On the other hand, Longrich & Field (2012) claimed that *Torosaurus* was indeed a valid separate genus based on difference in e.g., cranial ornamentation (14). Both of these studies based their main findings solely on cranial material. New discoveries of associated or articulated Chasmosaurinae specimens with both cranial and post-cranial material preserved, are therefore of fundamental importance to provide more insights into the complex taxonomy and anatomy of this group of horned dinosaurs, but also into their paleobiology such as their growth, locomotion, and behavior.

Fossil vertebrate bonebeds can provide such a unique window into the paleobiology and paleoecology of large-bodied dinosaurs, since they preserve multi-individual mortality in a close spatial and temporal proximity (15). Numerous sizeable ceratopsian bonebeds have been described in literature, but these are strongly dominated by centrosaurine assemblages (indicated on the map of Fig. 1A). These include the taxa *Centrosaurus* (16–19), *Avaceratops* (20), *Albertaceratops* (21), *Styracosaurus* (22), *Pachyrhinosaurus* (23), *Wendiceratops* (24), *Achelousaurus* and *Einiosaurus* (25, 26). Many of these centrosaurine assemblages contain large amounts of specimens (>1000 in the case of *Centrosaurus* from the Hilda mega-bonebed in Alberta; (17)), relatively high numbers of postcranial elements (27), and have in many cases been subject to thorough taphonomic analyses (e.g., (17)).

To date, the availability of such published datasets is lacking in chasmosaurines due to the prevalence of isolated finds and almost complete absence of large bonebed assemblages containing numerous individuals (27). Chasmosaurine bonebeds (Fig. 1A) are so far only known for *Agujaceratops* ("*Chasmosaurus mariscalensis*" (28, 29)), *Anchiceratops* (30), *Torosaurus* (31), *Utahceratops* (32), *Coahuilaceratops* (33), and *Triceratops* (34, 35). The scarcity of these bonebeds for chasmosaurines as well as their relatively lower minimum number of individuals (MNI) cannot easily be explained by differences in depositional environment between Chasmosaurinae and Centrosaurinae as they shared similar Laramidian lowlands during the Late Cretaceous (27, 32, 36). However, the rarity of taphonomically well-described chasmosaurine bonebeds, inhibits a large-scale comparative study on

both paleoenvironmental and paleobiological preferences of both clades, including potential gregarious behavior (27).

Here, we present the 'Darnell *Triceratops* bonebed' (DTB), a new, large *Triceratops* assemblage from the lower Lance Formation in eastern Wyoming (Fig. 1B-E; Fig. S1-S2), that can shed light on this conundrum. This well-preserved chasmosaurine bonebed represents the first detailed description of a multigenerational monodominant assemblage for the genus *Triceratops* from the Lance Fm. The other two *Triceratops* bonebeds described in literature are derived from overbank deposits from the Hell Creek Fm. of southeastern Montana (the Homer Bonebed; (34)) and northern Montana (the Quittin' Time Bonebed; (35)), respectively. Both bonebeds display a MNI of three, a disarticulated assemblage dominated by juvenile to young adult individuals, and a relatively low number of total bone numbers of 92 (35) and 130 (34), respectively. In this study, we describe in detail the complex three-dimensional taphonomy of the DTB, based on a novel, multi-proxy approach integrating geological and paleontological field observations with high-resolution sedimentological and geochemical analyses, together with paleobotany, osteology, bone histology, and a quantitative assessment of bone quality (see Methods). Hereby we aim to unravel the depositional environments throughout the bonebed and to establish taphonomic models explaining the fossilization and preservation of this *Triceratops* assemblage. Solid taphonomic scenarios are crucial to eludicate the paleobiological implications of this site, including potential gregarious behavior of these dinosaurs.

2.2 Material and methods

2.2.1 Field expeditions, mapping and sampling

The Darnell *Triceratops* Bonebed was discovered in 2012 on the private land of Donley and Nancy Darnell, after whom the bonebed is named. Naturalis Biodiversity Center (NBC), the national natural history museum of the Netherlands, started excavations in spring 2013 and returned to the site in the summers of 2015-2019 with a large group of volunteers and assistance of the Black Hills Institute (BHI). Initial assessment of the site revealed two disarticulated but associated specimens of *Triceratops*, but this number rapidly increased in 2015 when more overburden was removed and a new upper bonebed level was discovered, approximately 4 m above the original, lower main bonebed (Fig. S3). This chapter describes the details of the lower main bonebed (see also section 2.3).

We followed the multi-proxy procedures outlined in Rogers et al. (2007) regarding bonebed analysis by integrating high-resolution analyses of stratigraphy (litho & chronostratigraphy), sedimentology (sedimentary structures/geometries and host facies grain-size, mineralogy, geochemistry and (micro)fossil content) and taphonomy (assemblage data, spatial data, and bone modification data) (15). To document the lateral and vertical complexity of the bonebed throughout different years of excavation, a novel bonebed documentation was applied that replaced the traditional 2D grid mapping of bonebeds. The DTB quarry and the individual bone elements were documented and visualized in x, y, and z by terrestrial LiDAR (Faro Focus laser scanner) in combination with drone photogrammetry (using a DJI Mavic Pro) and with Differential GPS Base and Rover and Total Station (Sokkia) surveys of ground control points (100). Rendering, processing and georeferencing of the 3D data occurred with Agisoft Photoscan, ArcGIS and Quantum GIS. This resulted in a fully three-dimensional, georeferenced database with a global accuracy of 15 mm, allowing a high-resolution lateral and vertical correlation between individual bones and sedimentary strata. Size and orientation data of individual bones is stored in this GIS database as well, allowing the production of averaged size distributions per bone element type (Fig. S4) and rose diagrams (Fig. 1E), similar to recent work done

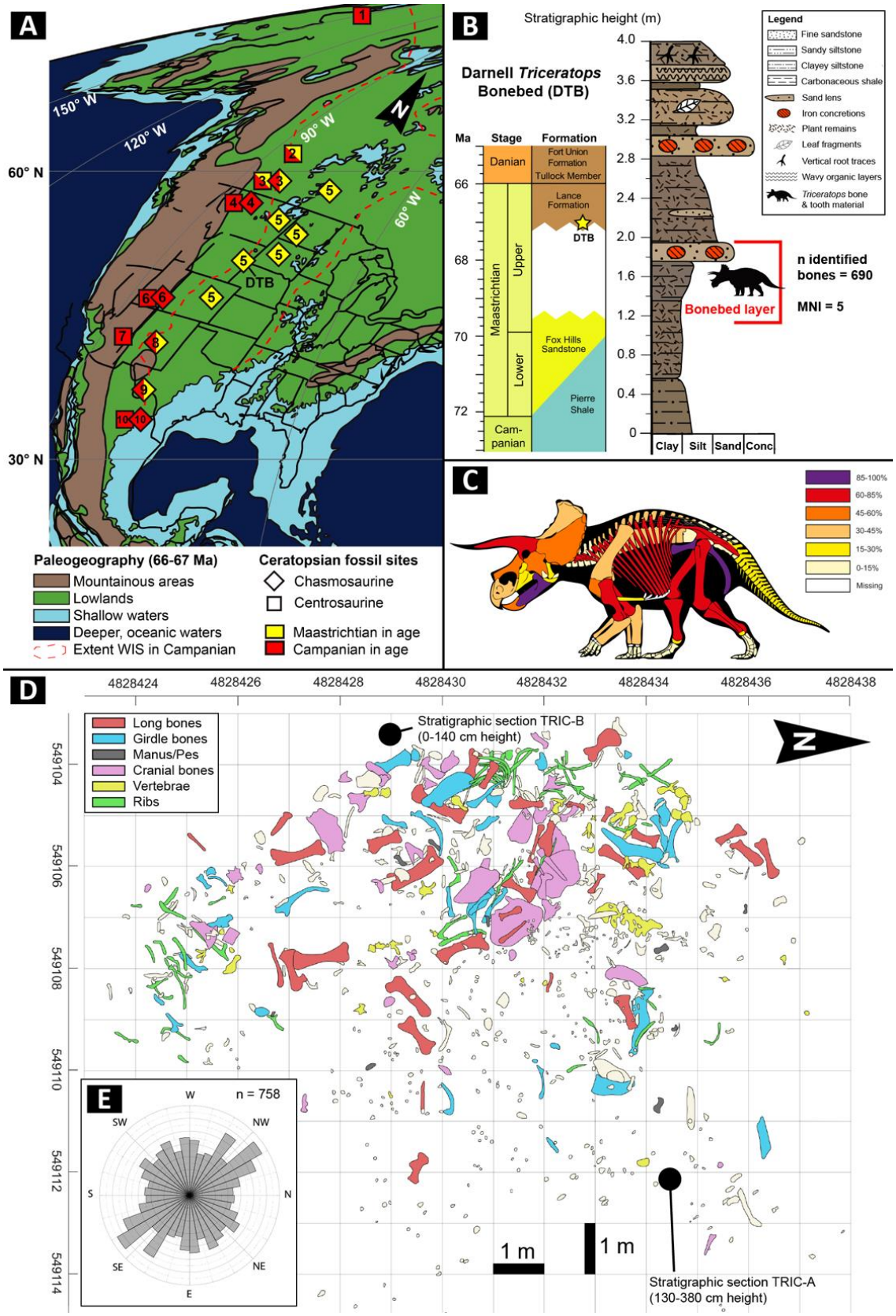

by Brown et al. (2021) (101). In addition, an independent lithostratigraphic framework was created at the bonebed site and at adjacent exposures (including sections named Sunburn Creek and Turtle Hill) to cover a c. 35 m thick regional stratigraphy (Fig. S3). Measuring took place using a Jacob's Staff and Brunton Pocket Transit and sample positions were incorporated in the 3D outcrop model by means of drone photogrammetry. Geological samples (~20 cc) were taken at a vertical resolution of 10 cm and

Figure 1. The Darnell *Triceratops* Bonebed (DTB). (A) Paleogeography of the Late Cretaceous (following Scotese, 2020) showing the distribution of main ceratopsian (chasmosaurine and centrosaurine) bonebeds. A paleogeographic map of the Late Maastrichtian is shown, together with the extent of the Western Interior (WIS) during the Campanian to show the Laramidian landmass. The associated numbers (1-10) of ceratopsian-bearing formations are discussed in the Supplementary Information. (B) Simplified chronostratigraphy and lithostratigraphy of the DTB, details can be found in Figs. S1-S3. (C) Heatmap showing the skeletal completeness for the DTB based on a MNI of 5. Only elements of the gastralia and the carpals and tarsals are not represented in the lower DTB. For each corresponding skeletal element, values were obtained by dividing the total number of occurrences by the expected amounts for five individual skeletons. (D) Quarry bone map of the DTB, highlighting the 2D distribution of long bones, girdle bones, manus/pes elements, cranial parts, vertebrae and ribs, together with the position of the main stratigraphic sections (see Fig. 3). (E) Rose diagram showing the orientation of bones from the DTB, showing a slight preference of SE-NW oriented elements.

at regular lateral positions throughout the deposit to analyze grain-size, organic and carbonate content, and elemental composition (see results in Table S3), in order to map the heterogeneity of the sediments surrounding the bones to decipher the paleoenvironmental conditions.

2.2.2 Sedimentological and paleobotanical analyses

To better understand the nature and mineralogy of the DTB deposit, 18 polished thin sections (30 µm thick) were produced of representative lithofacies and bone-sediment contacts (Table S3). All thin sections were examined under plane and cross-polarized light with a Zeiss (Carl Zeiss GmbH, Jena, Germany) Axioscope 5 TL/RL Polarizing microscope equipped with a Zeiss Axiocam 208 camera available at the Vrije Universiteit Brussel (VUB).

To gain quantitative insights in the energy level of and the physical and biological components within the sedimentary system through time, a combination of laser-diffraction grain-size analysis (GSA) and thermogravimetric analysis (TGA) was carried out on 413 sediment samples in the Sedimentology Lab of the Vrije Universiteit Amsterdam (VUA), listed in Table S3. The Sympatec HELOS/KR laser diffraction particle-size analyser, accommodated with an advanced wet dispersing system QUIXEL, was used to obtain grain-size distributions with a size range of 0.12 µm to 2000 µm. Prior to laser diffraction, the sediment samples were prepared following the procedure of Konert & Vandenberghe (1997) to ensure solely the lithogenic fraction was measured (102). Approximately 200 mg of pure clay samples and 10 g of pure sand samples were added to attain a beam obscuration of 15 to 25% on the HELOS device. The samples were treated with 5 - 10 ml of 30% hydrogen peroxide (H_2O_2) and subsequently heated to boiling point to ensure all organic matter was oxidized. After leaving the suspension standing overnight and decantating down to c. 50 ml, all carbonate material was removed by adding 5 - 10 ml of 10% hydrochloric acid (HCl) and subsequent heating to boiling point. To prevent clumping of clay minerals to agglomerates and thereby biased laser diffraction results, 300 mg of sodium pyrophosphate ($Na_4P_2O_7 \cdot 10H_2O$) was added to the suspension, followed again by heating until the boiling point. After cooling, the samples in suspension could be measured in the HELOS sensor device with the resulting pure lithogenic grain-size distribution data expressed in volume percentage (vol %). Subsequently, the lithogenic grain-size distribution dataset (n = 248) was used as input for an End Member Modelling Algorithm (EMMA) (103). With this technique it becomes possible to unmix a large particle population into several dominant, geologically meaningful components which is a powerful tool to better understand sediment provenance and to distinguish different depositional processes (104). End-member modelling followed procedures described by Van Hateren et al. (2018) (103).

Quantifying organic and carbonate content was achieved by performing thermogravimetric analysis with a LECO TGA701 instrument that measured weight loss as a function of temperature in a

controlled environment and with a precise internal balance (105). Prior to analyses, sediment samples were gently crushed with mortar and pestle. The homogeneous powders were dried overnight at 50°C to remove moisture, before 1-2 g of material was added to a ceramic crucible inside the carousel of the LECO TGA701. Step-wise heating with a ramp rate of 10°C/min took place allowing the determination of moisture (quantified at 105 °C), organic matter (quantified at 330 and 550 °C) and total carbonate content (at 1000 °C), expressed as weight percentage (wt%) of dry mass. In addition, by studying the first derivative of weight loss per temperature step per sample), a discrimination between different clay minerals (e.g., montmorillonite, kaolinite, illite and muscovite) and carbonate minerals (aragonite, siderite, dolomite, calcite and aragonite) becomes possible (105).

Additional information on the depositional environment and paleoecology of the DTB was derived from paleobotany. Numerous (n = 43) macrofloral remains, in the form of fossil leaves, stems, fruits and seeds were collected from the DTB (Table S1). These were described following standard procedures from Harris & Harris (1994) (106) and compared with reference literature (107). In addition, 21 palynological slides were produced from a selection of sediment samples throughout the deposit for both (palyno)stratigraphic and paleoenvironmental applications (section GT4b-S at 130-230 cm; BB-ST-S at 110-160 cm; TRIC-A at 330, 480 and 530 cm; see Table S3). Pollen preparation at the VUA followed standard techniques described by Faegri & Iversen (1998) of removal of clay, leaching, acetolysis and separation of palynomorphs by using heavy liquids (108). The identifying, counting and documenting of the fossil pollen and spores occurred with a Carl Zeiss Primo Star light microscope at VUB, equipped with an Axiocam 105 camera and using magnifications of 4x, 10x, 40x and 100x and oil immersion if necessary. Palynomorph taxa were morphologically identified using reference literature of Nichols (2002) and Bercovici et al. (2009) (109, 110).

2.2.3 Geochemical analyses

Homogenized powders from the same intervals used for both GSA and TGA, were analyzed for bulk major and trace element composition by using energy-dispersive micro X-ray fluorescence (µXRF) analysis. We used a Bruker (Bruker nano GmbH, Berlin, Germany) M4 Tornado benchtop µXRF surface scanner available at the VUB equipped with a Rh tube as X-ray source and two XFlash 430 Silicon Drift detectors. This novel technique offers the possibility to obtain accurate major and trace element compositions by means of spot-analysis as well as high resolution elemental distributions by scanning flat sample surfaces, such as polished thick and thin sections, in a rapid, non-destructive and cost-efficient way (111). The µXRF spot measurements were performed with two detectors and maximized X-ray source energy settings (50 kV and 600 µA, without any filter) and were carried out under near vacuum conditions (20 mbar) with a spotsize of 25 µm and an integration time of 120 s. After manual inspection of the spectra and assigning all the visible peaks to the correct elements, a standardless fundamental parameters method (112) was applied to quantify a normalized bulk composition (111) (Table S3). In addition, high-resolution (25 µm, with an integration time of 1 ms per 25 µm) element mapping was carried out on both bone, sediment slabs and thin sections from the DTB. This approach resulted in qualitative multi-element maps and semi-quantitative single-element heat maps (111), in which the highest spectral peak for one element (i.e., largest number of counts below the – in general – Kα peak) corresponds to the pixel in the sample with the highest possible RGB value (i.e. 255). Finally, bone thick sections were mapped and analyzed using µXRF linescans composed of lines of points drawn perpendicularly from the outer cortical bone inwards to produce quantitative major and trace element profiles, useful to decipher taphonomic and diagenetic processes (113). This follows the procedure of Kaskes et al. (2022) using a spot-size and spatial resolution of 25 µm, and an integration time of 60 s

(114). Subsequently, raw XRF spectra were quantified using a multi-standard, matrix-matched calibration specifically designed for bio-apatites, as outlined in de Winter et al., 2019 (115).

2.2.4 Osteological and histological analyses

The bone list (Table S1) was composed by distinguishing between different categories of skeletal elements including long bones, girdle bones, cranial elements, manus and pes, vertebrae, ribs, tendons and teeth. The remaining material such as trace fossils, indeterminate fragments and plant fossils were omitted to focus on the categories that encompass the most relevant skeletal material preserved in the DTB. Long bones and girdle bones were measured following Chinnery (2004) (116) to determine body size differences and evaluate possible age differences between the preserved *Triceratops* individuals in the DTB, complementing the histological analysis. Morphological characters of the cranial elements were used for the taxonomic identification of the *Triceratops* following (38, 40). An automated size distribution was made based on the field map statistics in ArcGIS, and subsequently verified using maximum length measurements on a selection of bones in the lab following (116).

Tibiae were chosen for histological sectioning as visual inspection indicated that they preserve the thickest cortex with the least degree of taphonomic distortion, thus providing the best preservation of the bone microstructure. The sampling strategy applied here combines the histological coring method (HCM) (117, 118) with medical CT scans. CT imagery prior to sampling as best practice complements the HCM by revealing the most ideal sampling location on each element. Identification of the most suitable sampling area on a specific bone is based on overall preservation such as fractures/cracks and diagenetic infill surrounding the mid-diaphysis. Following these criteria, this strategy ensures standardized sampling locations for both tibiae. CT cross-sections and sampling locations for both tibiae are found in Figure S21. Accordingly, this approach enables homologous sampling important for inter-bone comparisons (119) and provides access to the internal bone microstructure of unique material with minimal impact on its morphology.

Thin-sections were prepared at the palaeohistology laboratory of the Rheinische Friedrich-Wilhelms Universität in Bonn, Germany, conforming to standard methods (120, 121), where each sample was ground by hand until the desired thickness was reached. Sections were studied under normal transmitted and polarized transmitted light using a Leica DMR light microscope housed at Naturalis Biodiversity Center, the national natural history museum of the Netherlands. Photographs were taken using a Nikon DS-Ri2 digital microscope camera mounted on a Nikon Eclipse E600POL polarizing light microscope housed in the Dutch Gemmology Laboratory at Naturalis. Terminology for histological markers follows Buffrénil and Quilhac (2021) (122).

2.2.5 Bone modification scheme

Three authors independently ranked a significantly large bone sample set of the lower main bonebed level (n = 39) from scale 1 to 5 for different criteria of bone modifications. Lower ranks represent more intense modification (i.e., more poorly preserved) and higher ranks are assigned to unmodified elements (i.e., better preserved). The relevant bone modification factors that were assessed follow Rogers et al., (2007) (15) and include weathering, abrasion, fragmentation, distortion/compression, bioerosion and depression pits/marks such as trampling or tooth marks. Detailed explanations on the definition of bone modification data are found in (15). Furthermore, we assessed the intensity of iron encrustation as an additional modification factor due to its prevalence in the DTB fossils. Fossil elements were chosen on the basis of their location within the quarry. The coordinates of all the available fossil elements were plotted and a selection of different datapoints were made so as to make

a selection that represents the entire surface area of the quarry as well as a representative sample of the size distribution within the assemblage. Accordingly, the acquired sample set was based on a random selection of diverse fossil elements that accurately represents the DTB. Each corresponding fossil was assigned a rank, thus providing an average rank for each fossil as well as an average rank for each modification factor across all scored elements (Table S2). The upper bonebed level was sampled for completion but is not discussed further (n = 34) (see 2.3 Results).

2.3 Results

Excavations at the DTB location (43º36'26.1"N, 104º23'29.3"W) amassed >1100 skeletal elements, and with preparation still ongoing, a total number of ~700 skeletal elements were identified and used as the main focus in this study. Based on the collection of 5 left tibiae and 10 ischia (see bone list in supplementary Table 1), this results in an MNI of 5 and thereby making the DTB, to our knowledge, the largest *Triceratops* bonebed found to date. The ~700 identifiable skeletal elements derive from the main bonebed, whereas ~4 meters higher in stratigraphy a secondary bonebed was unearthed with MNI of 2 *Triceratops* (Fig. S3; and see Supplementary Material for more details). The main lower bonebed (referred to as DTB here) is ~0.8 m thick and stretches over an area of ~200 m^2 (Fig. 1C; Fig. S5), displaying disarticulated but associated skeletal remains with little evidence of scavenging. Below we describe in detail the taxonomy, bone preservation, osteohistology, sedimentology, and geochemistry of the main lower bonebed (the DTB). The analysis of the upper bonebed is still pending, and preliminary data is depicted purely for comparison with the main lower bonebed of interest (Table S2, Fig. S3, Fig. S6, Fig. S8, Fig. S13-14).

2.3.1 Taxonomy

Only three ceratopsid genera are known from the Lance Formation: *Triceratops*, *Torosaurus* and *Leptoceratops* (37). The DTB yielded diagnostic material pertaining to *Triceratops horridus* including – but not limited to – two well-preserved squamosals, two parietals, a nasal bone with fused epinasal and two rostrums of which one is fused to the premaxilla (Fig. 2). The squamosals are relatively short and stout with a pronounced dorsally-inclined concave frill margin that constricts the posterior margin of the parietal (Fig. 2A-B), as previously described for *Triceratops* (38). Accordingly, these elements significantly differ from relatively elongated *Torosaurus* squamosals that show more linear lateral frill margins tapering towards the posterior suture with the parietal in lateral view (13, 14, 39). In addition, the discovered parietals from the DTB are unfenestrated and do not show incipient fenestrae such as depressions. The epinasal fused to the nasal bone is relatively short (Fig. 2C) which is characteristic of *T. horridus* opposed to the well-developed nasal horn-core of *T. prorsus* (40). Diagnostic for *T. horridus*, the rostrum is relatively large and elongated (40), especially the dorsally elongated protuberance that drapes and attaches to the anterodorsal region of the premaxilla (Fig. 2D-E). Overall, the elements that make up the nasal region form a relatively longer snout in *T. horridus* than in *T. prorsus* (Fig. 2E) (40) where the anteroposterior attachment of the premaxilla with the nasal bone results in the nasal horn being more posteriorly positioned compared to the rostrum. *T. horridus* and *T. prorsus* both show a different unique configuration of the postorbital, squamosal and jugal bone, in which the jugal forms the dorsal rim of the lower temporal fenestra in *T. horridus*, while in *T. prorsus* the dorsal rim consists mainly of the squamosal (40). The DTB *Triceratops* clearly pertain to the former configuration diagnostic for *T. horridus* (Fig. 2F). Lastly, the lower Hell Creek Formation is known to produce predominantly fossils pertaining to *T. horridus* (12) and the stratigraphic position of the DTB in the time-equivalent lower Lance Fm. (Fig. S2; (6)) corroborates the observed osteological trends. The size

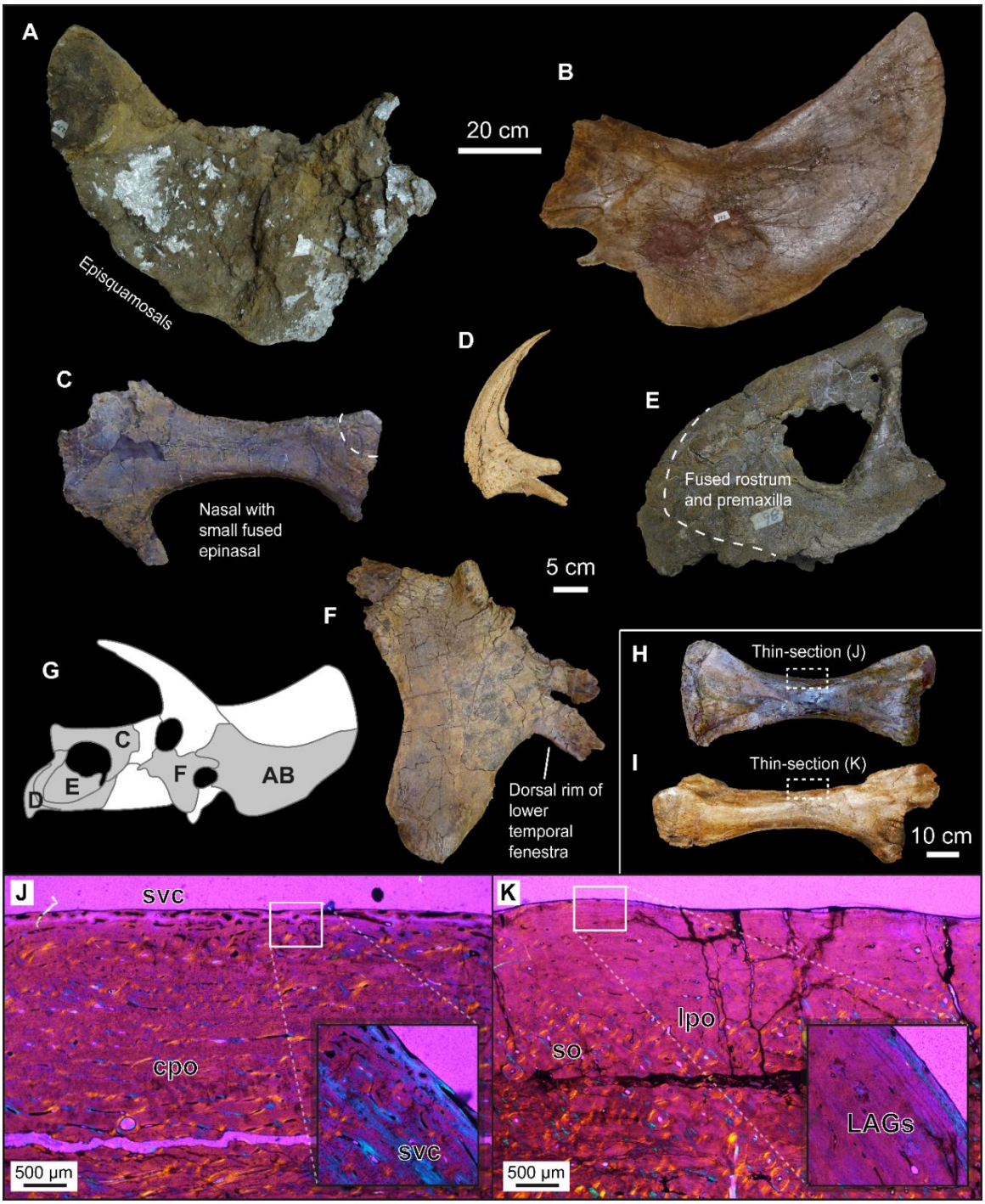

distribution of the bone elements shows a non-selective pattern with all size groups included (Fig. S4), thereby likely excluding an attritional bonebed scenario that is characterized by excluding specific size groups (15, 41).

2.3.2 Bone modification

Complete bone modification data is presented in Supplementary Table 2 alongside an overview of dominant modification patterns of the lower (Fig. S5, S7) and upper (Fig. S6, S8) bone-bearing intervals of the DTB. Independent scorings of the different types of bone modifications revealed an overall lower average degree of preservation for the upper intervals compared to the lower bonebed (Table S2). The largest differences are observed between weathering and abrasion patterns. Fossil material from the upper DTB often do not preserve their original bone surface textures and bone extremities are

Figure 2. Diagram showing material from the DTB relevant for taxonomic identification as well as indicating age-related osteological and histological markers for *Triceratops*. (A) Relatively smaller left squamosal showing developed episquamosals along most of the frill margin. (B) Relatively larger left squamosal showing inconspicuous episquamosals only at the most anterior frill margin. (C) Right nasal bone with a small fused epinasal. (D) Unfused rostrum with relatively elongated dorsal extremity. (E) Fused rostrum and premaxilla elements. The dorsoposterior attachment site for the anterior part of the nasal bone forms a relatively elongated snout. (F) Left jugal showing the dorsal margin of the lower temporal fenestra. (G) Schematic diagram highlighting the anatomical position of elements A to F. The drawing is not to scale. (H) Left smaller tibia that was studied for histology. Inset represents sampling location for sectioning depicted in J. (I) Right larger tibia that was studied for histology. Inset represents sampling location for sectioning depicted in K. (J) Histology of the bone surface of the smaller tibia (H) in cross-polarized light with lambda filter showing high vascular and osteocyte density, circumferential/laminar organisation of the primary osteons and no bone remodelling. The inset shows reticular vascular canals that open to the bone surface, indicating active bone growth at time of death. (K) Histology of the bone surface of the larger tibia (I) in cross-polarized light with lambda filter showing poorly vascularized primary bone, lower densities of osteocytes, longitudinal organisation of the primary osteons and advanced bone remodelling patterns. Moreover, the inset shows two clear lines of arrested growth indicating skeletal maturity. Cross-polarized light with lambda filter provides more details about bone tissue organisation of the histological markers. Scale bar for A-B is 20 cm. Scale bar for C-F is 5 cm. Scale bar for H-I is 10 cm. Scale bar for J-K is 500 µm. cpo, circumferential primary osteon; LAG, line of arrested growth; lpo, longitudinal primary osteons; so, secondary osteon; svc, simple vascular canal.

frequently eroded (Fig. S8). Fragmentation was relatively abundant at both localities and was observed in the majority of the scored elements. Morphological distortion was least observed and the fossils from the DTB have overall well-preserved original morphologies. Scoring of (average) bone modification data from the DTB fossils revealed negligible impact of bioerosion and depression marks (i.e., high ranks). Therefore, we omitted the ranks for bioerosion and depression marks when we calculated the final averages for each fossil element (Table S2). Otherwise, these numbers would increase the average scores significantly even though these categories were never truly observed. Taken altogether, the overall positive bone modification values of the lower bonebed are linked to a depositional environment allowing good preservation without a long-distance transport mechanism.

2.3.3 Ontogenetic and histological age markers

Preliminary osteohistological analysis of the tibiae reveals that the DTB *Triceratops* shows pristine preservation of the bone microstructure. Based on the preserved histological markers, the DTB *Triceratops* can be separated in two distinct age classes. One smaller tibia (704 mm; Bone ID #353 shows well-vascularized primary bone tissue with secondary bone remodelling limited to deeper parts of the cortex. The cortical bone close to the periosteal surface deposits high numbers of simple vascular canals and shows high osteocyte densities indicative of active bone growth (Fig. 2J). The larger tibia (781 mm; #062) preserves poorly vascularized primary bone close to the periosteal surface including the deposition of two clear lines of arrested growth (LAGs) that signify an incipient external fundamental system (EFS) and growth cessation (Fig. 2K). Bone remodelling is extensive with secondary osteons advancing close towards the bone surface. Moreover, the smaller tibia contains large zones of faster growing circumferential woven-parallel bone, while the larger tibia predominantly preserves slower growing longitudinal woven-parallel bone (42, 43). The histological markers show a clear distinction between an ontogenetically younger and older age class. A similar dichotomy is observed between the cranial elements with ornamented and unornamented frills as well as fused and unfused

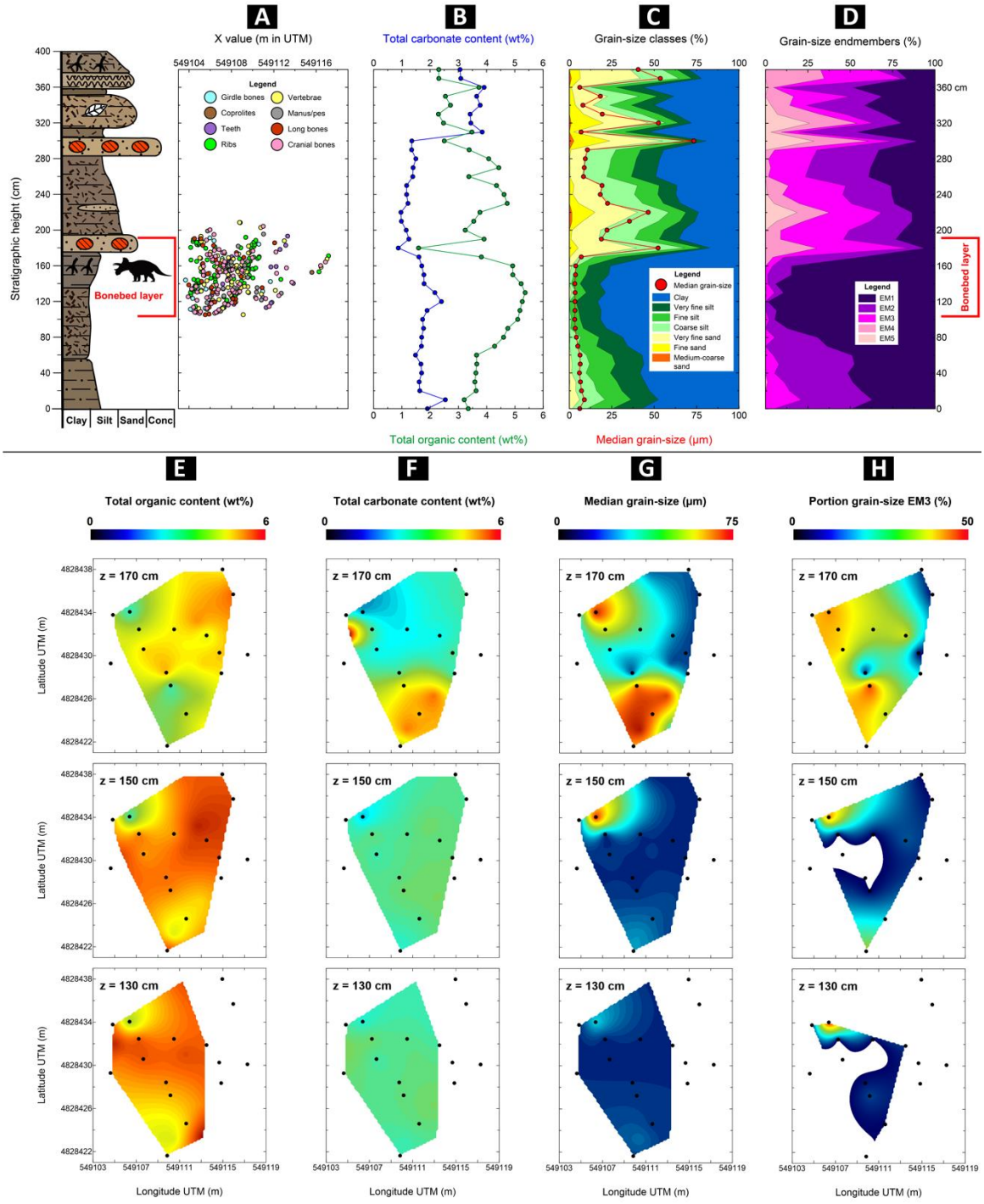

Figure 3. Multi-proxy and multi-dimensional stratigraphy of the DTB. (A) Bone positions expressed as mid-point surface depth versus longitude (n = 377). (B) Total organic and total carbonate content of sections TRIC-A & B. (C) Median grain-size profile with a filled diagram showing the proportions of the grain-size classes. (D) Contributions of each of the five grain-size end-members versus depth. (E-H) 2D surface contourplots of total organic content (E), total carbonate content (F), median grain-size (G) and proportion of grain-size end-member 3, expressed during three different intervals within the bonebed deposition.

skull parts (Fig. 2). Thus, the osteological and histological data strongly support the presence of subadult and adult *Triceratops* in the DTB (11).

2.3.4 Sedimentology

The ~4 m thick lithostratigraphic section at the DTB comprises an alternation of carbonaceous shales, siltstones, and fine-grained sandstones that are, in general, high in total organic content (on average: 3.8 wt%) and low in total carbonate content (on average: 2.0 wt%). The composite section TRIC-A & B can roughly be subdivided in four sedimentary units (Fig. 1B; Fig. 3). The basal layer (0-110 cm stratigraphic height) is a rather homogeneous brown clayey siltstone unit that becomes finer and more organic rich towards its top (Fig. 3B). The overlying unit is the bonebed layer (110-190 cm; Fig. 3A) that yields the remains of five *Triceratops* individuals and that is dominated by a purple-grey carbonaceous claystone (up to 82 vol% clay; Fig. 3C-D; also highlighted in the high proportions of grain-size end-members 1 and 2) characterized by microlaminations (Fig. S11), a high total organic content (up to 5.5 wt%; Fig. 3B) and abundant plant remains. The top part of this interval consists of a thin (10-20 cm thick) layer of a yellowish, coarse silt to very fine sandstone dominated by quartz minerals (Fig. S11) and rich in iron concretions (Fig. 1B). Approximately 10% of the bones extend up into this very fine sandstone layer. The third stratum (190-310 cm) is dominated by a brown sandy siltstone unit rich in sandy lenses and plant remains. Near the top, this unit is characterized by an iron concretion-bearing fine sandstone layer (Fig. 1B). The uppermost unit (>310 cm) consists of alternating dark brown clayey siltstone beds and light brown sandy siltstone beds with wavy organic layers and fossil leaf remains. This unit stands out from the underlying intervals based on a significantly higher total carbonate content (on average 3.5 wt% $CaCO_3$) compared to the three underlying units (on average 1.6 wt% $CaCO_3$; Fig. 2C).

Based on field observations (Fig. S10) the yellowish, very fine sandstone layer on top of the purple-grey claystone (110-190 cm) shows strong variations in structure and lateral thickness throughout the extent of the bonebed. For this reason, we collected additional samples from multiple locations throughout the bonebed area to ensure a correlation based on 10 cm stratigraphic intervals to further decipher the bonebed geometry and the depositional conditions prior, during and after the bonebed formation. The results of organic content, carbonate content, median grain-size and % end-member 3 are displayed in three crucial stratigraphic intervals across the bonebed level (Fig. 3E-H), and show that a large body of a rather homogeneous organic-rich, carbonate-poor claystone transitions into a heterogenous mixture with influx of more sandy material. This first coarse influx arrived from the north, followed 20 cm higher up in stratigraphy by an influx of very fine sand from the south, which is carbonate rich and therefore distinct from the first sandy influx event. The majority of the bones are found in between these two sandy influxes (~0.8 m), resulting in an organic-rich central area (Fig. 3E) in which the sandy bodies are pinching out (Fig. S11). When bone orientations are plotted on the same grain-size contour plots (Fig. S16), it becomes apparent that a preferential orientation is found of NW-SE for the northern region and NE-SW for the southern region, likely steered by these coarser-grained influx events.

2.3.5 Geochemistry

All sediment samples were also analyzed by micro-XRF to obtain bulk major and trace element contents. This resulted in fairly homogeneous compositions throughout the entire DTB stratigraphy dominated by siliciclastic material rich in SiO_2 and Al_2O_3, and with local variations in Fe_2O_3 and CaO (Fig. S13). Micro-XRF linescans of five bone thick sections, selected based on a wide spread of positions

throughout the bonebed, showed overall light rare earth element (REE) values that are low in average concentration, in combination with steeply inclined REE patterns (e.g., in Ce and La) (Fig. S19, S20).

2.4 Discussion

2.4.1 Taphonomy of the Darnell *Triceratops* Bonebed

Based on the multi-dimensional sedimentological, geochemical and paleontological datasets, we propose that the most parsimonious taphonomic scenario for the DTB represents a miring scenario of *Triceratops* individuals which in a later stage was altered by fluvial processes. This taphonomic scenario is outlined in Fig. 4.

The organic content, grain-size classes and end-member data reveal that the DTB is characterized by a very fine-grained interval that represents a very low energy environment with likely stagnant water in paludal conditions (44). This clay-rich, organic-rich and carbonate-poor unit yields the majority of the bones (~90%). Interestingly, the x-y-z values of the bone positions follow a geometry that shows a steep slope near the western part and a gentle slope near the eastern part of the bonebed (Fig. 1C), although erosion might have influenced the pattern on the western side. This morphology resembles a river channel, but since the lithologies are so fine-grained and organic rich, this most likely represents a filled-up residual channel (44). This matches a depositional environment typical for Late Cretaceous lowland and estuarine systems bordering the Western Interior Seaway (45, 46).

The overlying sandy unit displays typical sedimentary features related to a distal crevasse splay event (c.f. Burns et al., 2017 (47)), with grain-sizes in the range of coarse silt to very fine sand. This unit exhibits an undulating lower surface contact with sedimentary features reminiscent to flame structures (Fig. S10). This type of soft-sediment deformation occurs in unconsolidated sediments that are saturated with water, hence the bone-bearing unit was likely heavily waterlogged when it was abruptly covered by the crevasse splay. Interestingly, two crevasse splay units have been discovered, the southern more enriched in CaO content, showing the dynamics of a river channel close by that influenced this residual channel on the floodplain. This crevasse splay event from a nearby river channel likely transported the skeletal remains, causing disarticulation prior to final deposition and burial, but the transport distance was minor as the skeletons are still associated. In addition, the DTB fossil material is overall well-preserved with limited morphological distortion, retention of original bone surfaces, and only minor weathering and erosion damage (Fig. 2 and S7). Absence of evidence of scavenging (e.g., no abundant shed theropod teeth) suggests that exposure of the animal carcasses was limited, and that initial burial by these crevasse splays occurred relatively fast, which is corroborated by the sharp contrast in grain size data between the bone-bearing clay interval and overlying crevasse splay unit (Fig. 3). From a sedimentary geometry perspective, miring is a possibility as there is a fine-grained unit still at least 1 m below the main bonebed, in contrast to a theropod bonebed described by Titus et al. (2021) that disputed the miring scenario based on the absence of a thick underlying fine-grained stratum (48). The sedimentary setting at DTB does also not suggest a large effect of reworking and influence of secondary carbonates such as common with an attritional death assemblage (49). This is corroborated by the fact that the embedding sediment from the bonebed is practically devoid of authigenic carbonates (on average 1.7 wt% $CaCO_3$ in the bonebed layer; Fig. 3B), providing an unlikely scenario for the uptake of secondary carbonates.

The bone size frequency (Fig. S4) shows a pattern that is compatible with a non-selective, catastrophic kill event and not with a long-term attritional mortality scenario that predominantly kills vulnerable young and old members of a population (15, 41). Post-mortem burial histories can further

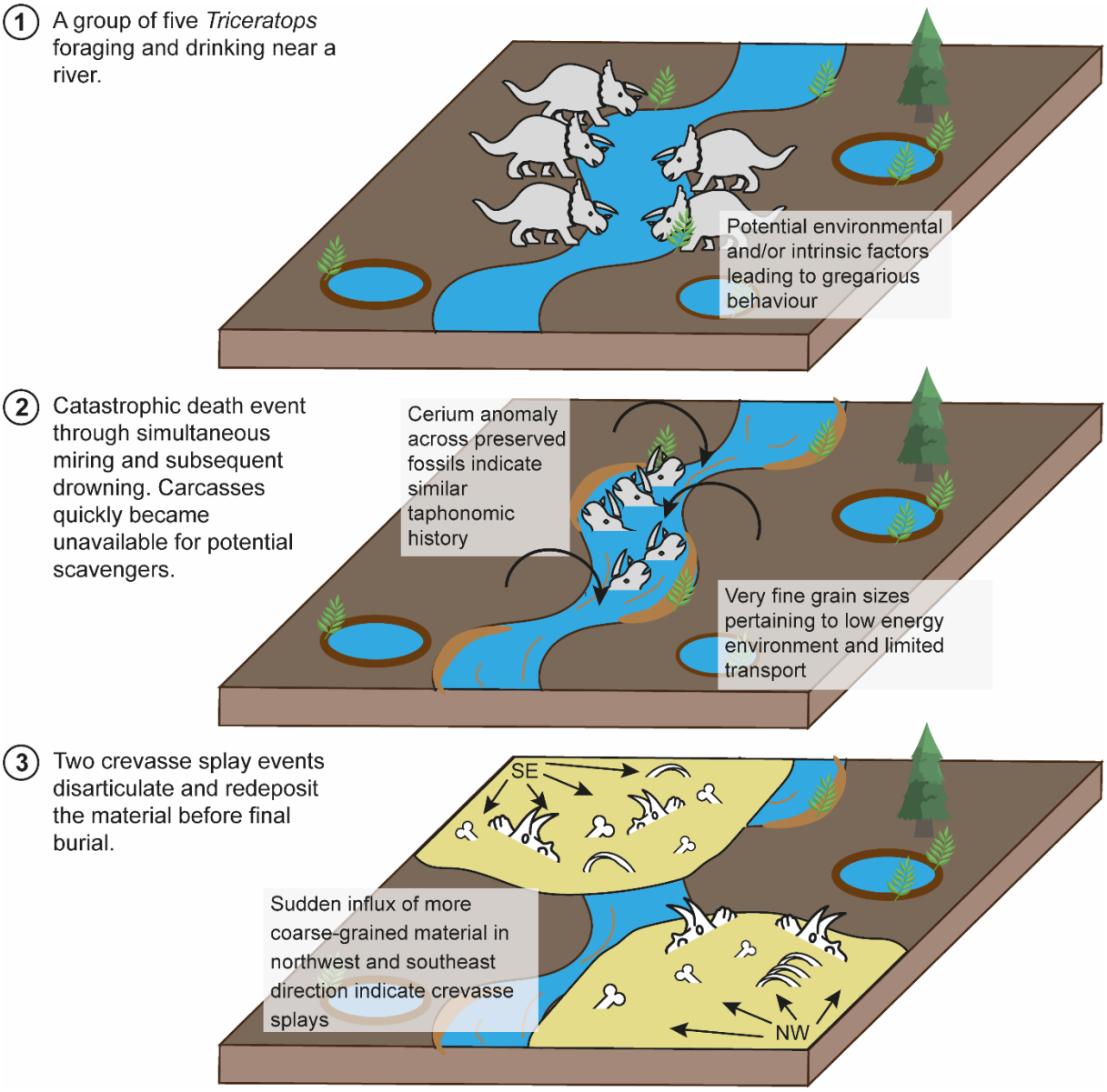

Figure 4. Hypothetical scenario of the formation of the DTB.

modify preserved age and size structures by destructive taphonomic processes. In this case the size frequency resembles a rapid permanent burial scenario as highlighted in (15). This interpretation is also supported by the micro-XRF based trace element patterns in a range of bones throughout the entire extent of the bonebed, which show steep REE gradients towards the cortical surface and low overall REE concentrations, suggesting a similar taphonomic history for these bone elements, and likely individuals. The same REE patterns have been described in a fine-grained, mass-mortality bonebed of *Edmontosaurus* from the Hell Creek Formation in South Dakota (49). This is in stark contrast to a coarse-grained, sand-rich *Edmontosaurus* bonebed in the Lance Fm. of Wyoming (50, 51), that shows much higher total REE contents and much more gentle cortical chemical profiles, hence suggesting a later stage diagenetic process influencing the bone chemistry and most likely allowing an attritional setting to be formed for this other site in the Lance Fm.

In conclusion, the series of sedimentological constraints at the DTB (fine-grained residual channel filling followed by a rapid sandy cover) formed a unique and spatially and temporally well-constrained depositional environment preserving both postcranial and cranial remains of a relatively

large group of *Triceratops*. This provides new opportunities to study its anatomy and biology including ecology, ontogeny and behavior, the latter of which we discuss below.

2.4.2 Implications for gregarious behavior in *Triceratops*

Triceratops fossils are virtually exclusively reported as isolated remains. However, the three currently reported *Triceratops* bonebeds – including the DTB – indicate a more complex social behavior that warrants a reevaluation of potential gregariousness of this iconic taxon. While behavioral patterns are extremely difficult to reconstruct using the fossil record, mass death assemblages can provide a unique window into the paleobiology of extinct taxa. Fossil bonebeds require detailed taphonomic scrutiny to discern between true mass death events and taphonomic or preservational artefacts. Previous studies focused on a combination of conditions to identify such events including taxonomic exclusivity, high numbers of densely clustered skeletal elements and shared taphonomic history among the preserved individuals (50–57). The available taphonomic data of the two previously reported *Triceratops* bonebeds (Homer Site in southern Montana and Quittin Time Bonebed in South Dakota; Fig. S1A) indicate possible log-jam scenarios (34) and asynchronous deposition of different individuals (35), thus providing equivocal evidence for the existence of true mass death assemblages for the genus which leaves current inferences on *Triceratops* paleobiology and gregariousness ambiguous at best. However, the in-depth analysis presented here shows that the DTB preserves high numbers of closely associated skeletal elements exclusively pertaining to a single taxon, embedded in sediments that were rapidly deposited and having overlapping taphonomic history. In addition, the DTB shows different ontogenetic stages and more mature individuals as compared to the other two described *Triceratops* bonebeds. Thus, we argue that the DTB represents a true mass death assemblage and that our analysis provides the hitherto most robust dataset to speculate on potential gregarious behavior in *Triceratops*.

Social behavioral strategies may vary tremendously based on taxonomic and/or environmental factors (58, 59). For example, temporary aggregations of animals may form due to environmental stresses such as food scarcity or prolonged drought periods (25, 52, 60, 61). In this case, conspecifics may tolerate each other's presence irrespective of preferred social behaviour. Additionally, conspecifics may show habitual group formation only during mating seasons (62). On the other end of the spectrum, animals may form permanent herds, here defined as a monospecific socially cohesive group of (related) individuals, with a possible complex hierarchal structure of dominance (59). The extensive sedimentological and taphonomic dataset from the DTB does not explain the concentration of *Triceratops* skeletons preserved at the locality. Instead, some form of sociality, whether environmentally driven or more complex social behavior such as associations or community structures, is underlying this unusual scenario of the DTB. The DTB may represent the first unequivocal evidence of gregarious behavior in this taxon, but more specific insights on potential underlying social structures such as dominance hierarchies, mating strategies or parental care in *Triceratops* remain purely hypothetical at present (63, 64). These monospecific habitual gatherings like the DTB would have enabled more complex social interactions among conspecifics, as further supported by comparisons with extant analogues (64) as well as by the development of the elaborate parietosquamosal frill complex of *Triceratops* (and other ceratopsids), which is hypothesized to serve in socio-sexual signalling, species recognition and/or intraspecific combat (64–72). Moreover, stable isotope work on this bonebed already provided insights on potential migratory movements and provenance of the DTB specimens, revealing significant overlap in isotope signals among the preserved individuals (73). However, additional analyses such as detailed histological (de Rooij et al., 2023), gross morphological descriptions (currently in prep) and 3D geometric morphometric analyses are required to better

understand the ontogenetic and potential sexual dimorphic variability within the DTB and potential social hierarchy. These analyses will provide further support for hypotheses on potential gregarious and social behavior and the formation of relatively small aggregations in *Triceratops*.

Chasmosaurine bonebeds have currently been described for *Agujaceratops* (28, 29), *Anchiceratops* (30), *Coahuilaceratops* (33), *Torosaurus* (Gilmore, 1946), *Triceratops* (34, 35); the DTB described here) and *Utahceratops* (32). Overall, chasmosaurine taxa are less often preserved in bonebeds compared to centrosaurines, and chasmosaurine bonebeds also preserve a relatively low number of individuals despite no clear geographical, temporal or taphonomic differences between the two groups (27, 54, 63). Despite representing the largest *Triceratops* mass death assemblage, the relatively low minimum number of individuals preserved in the DTB, which cannot be explained by taphonomic scenarios, is consistent with currently available data on chasmosaurine bonebeds, and therefore the discrepancy between the number of centrosaurine and chasmosaurine bonebeds most likely represents an inherent biological signal.

Gregariousness evolved relatively early in ceratopsian evolution, as basal taxa such as *Psittacosaurus* (originated ~125 Ma) and *Protoceratops* are often preserved in multigenerational mass death assemblages of over a dozen associated individuals, even indicating more complex social behavior such as potential parental care (56, 74–76). Basal ceratopsoids, such as *Zuniceratops* (~90 Ma), are known from mass death assemblages containing up to five associated skeletons (77), suggesting a significant decrease in potential group size throughout evolutionary time. The earliest occurring centrosaurine *Menefeeceratops* (~83 Ma) (78) and the earliest occurring chasmosaurine *Chasmosaurus* (~77 Ma) have no known report of mass death assemblages (54). The most basal centrosaurine of which bonebeds are reported include *Wendiceratops* (~79 Ma), described from assemblages preserving up to four individuals (24, 79), while more derived taxa such as *Centrosaurus* (~75 Ma) may preserve hundreds of associated skeletons at a single locality (17). The earliest basal chasmosaurine, in contrast, found in bonebed deposits, *Agujaceratops* (~77 Ma), preserves up to 20 individuals (28, 80), while many more derived chasmosaurine bonebeds are characterized by relatively lower numbers of associated skeletons (54, 63). Thus, if we would consider *Zuniceratops* as the last common ancestor of Centrosaurinae and Chasmosaurinae, then it would suggest that many chasmosaurines show the ancestral condition of relatively small group sizes, and some centrosaurines evolved relatively larger group sizes. However, the occurrence of both smaller and larger bonebeds among both taxa as well as the limited taxonomic range of well-described bonebeds hampers any precise testing of hypotheses on the evolution of social behavior in ceratopsids at this time. Instead, the currently available datasets suggest that aggregative behavior evolved early in ceratopsians (24), and that many derived ceratopsids were characterized by diverging patterns in social behavior.

Gregarious and social behavioral strategies in extant animals are often the result of a complex interplay of environmental and ecological factors including predation pressure (81–84) resource distribution (e.g., terrain, vegetation type and cover, water availability) (84–90), home range size (58, 91, 92) and mate accessibility for reproductive success as well as the dominance of male or female hierarchies (92–94). Alternatively, many extant taxa are considered facultatively aggregating, gregarious or social, participating in social hierarchies only during specific seasons, using different sensory cues, or showing completely different social structures per generation or population altogether (95–99). Many of these aspects are extremely difficult to trace in the fossil record, but it is reasonable to assume that similar aspects may have defined group compositions in chasmosaurines and centrosaurines, and that taxa from both groups evolved distinct strategies along the spectrum of aggregative, gregarious and/or social behavioral patterns. Careful taphonomic examination of other

well-constrained ceratopsid bonebeds as well as their specific paleoenvironments and- ecology will shed more light on (the evolution of) ceratopsid socioecology (64). Nonetheless, periodic aggregative behavior in *Triceratops* is substantiated for the first time, making the DTB a unique and highly informative mass mortality bonebed that adds to the current database on ceratopsid social behavior.

2.5 Supplementary data

2.5.1 Geological setting

The Darnell *Triceratops* Bonebed is located in Weston County in eastern Wyoming, ~30 km SW of the town of Newcastle (Fig. 1B; Fig. S1). The bonebed is situated in the southeastern part of the Powder River Basin on the western flank of the Black Hills. The strata at and outcropping around the bonebed are of Upper Maastrichtian age and belong to the continental Lance Formation (124-126). The Lance Fm. is stratigraphically equivalent to the Hell Creek Fm. in Montana (125) and has yielded a wealth of dinosaur fossils over the last 130 years, but detailed studies integrating geological and paleontological datasets are surprisingly limited (127), especially compared to the Hell Creek Fm. in Montana (128), South Dakota and North Dakota (129). The Lance Fm. is composed of siliciclastic continental deposits belonging to high sinuosity fluvial systems (130). Large sandstone channel deposits (>6 m thickness) make up approximately 30% of the Lance Fm., the other 70% consists of more fine-grained floodplain-, lacustrine-, paleosol-, and swamp deposits characterized as siltstones, claystones and carbonaceous shales (125). Paleo-flow direction indicators show that the general flow direction during the Late Cretaceous was in eastward direction indicating the Powder River Basin and Black Hills Uplift were not yet formed (125, 130, 131). The Lance Fm. in this part of the Powder River Basin is estimated to be between ~600 and 760 m thick (Fig. S1B) (132). The DTB is deposited in time much closer to the Fox Hill Sandstone Fm. (Fig. S1B) than to the Fort Union Fm., which is characterized by the K-Pg boundary. Despite the lack of continuous exposures in these badlands, we estimate the DTB to yield a geological age of ~67 Ma, based on its stratigraphic distance from the underlying Fox Hills Fm (only ~1.5 km west from Fox Hills outcrops), and a recent correlation with the time-equivalent Hell Creek Formation in Montana and a corresponding integrated stratigraphic study by Fowler (2017) (126). For an integrated chronostratigraphic overview (including palynostratigraphy and magnetostratigraphy) of the Lance Fm. compiled by the Wyoming State Geological Survey, we refer to Fig. S2.

Table S1. Comprehensive bonelist of the lower DTB showing the distribution of all relevant fossils discovered during field seasons (2015-2019), including percentage completeness when compared to five *Triceratops* individuals.

Category	Taxon	Skeletal element	Left	Right	Total	Completeness
Cranial elements	*Triceratops horridus*	Angular	0	0	1	10%
		Braincase	0	0	2	40%
		Condyle	0	0	1	20%
		Dentary	3	3	9	90%
		Epijugal	0	0	1	10%
		Epoccipital	0	0	7	-
		Exoccipital	0	0	0	-
		Frill	0	0	0	-
		Horn	0	0	11	70%
		Jugal	1	1	11	50%
		Lachrymal	0	1	5	20%
		Maxilla	0	1	2	30%
		Nasal	2	1	3	50%
		Palatine	1	1	5	20%
		Parietal	0	0	2	40%
		Predentary	2	1	8	60%
		Premaxilla	0	0	3	40%
		Pterygoid	0	0	4	20%
		Quadrate	1	0	2	30%
		Rostrum	2	1	3	40%
		Splenial	0	0	1	50%
		Squamosal	0	1	5	50%
		Surangular	4	0	9	20%
Vertebrae	*Triceratops horridus*	Caudal vertebra	0	0	42	19%
		Centrum	0	0	13	-
		Cervical vertebra	0	0	3	-
		Chevron	0	0	15	21%
		Dorsal vertebra	0	0	22	31%
		Fragment	0	0	0	-
		Lateral spine	0	0	4	-
		Neural spine	0	0	15	-
		Sacral vertebra	0	0	2	-
		Vertebra indet.	0	0	16	-
Ribs	*Triceratops horridus*	Cervical rib	0	0	7	-
		Fragment	0	0	0	-
		Rib	9	4	149	74%
		Sacral rib	0	0	2	-
Girdle bones	*Triceratops horridus*	Coracoid	2	3	6	60%
		Fragment	0	0	0	-
		Ilium	1	4	7	70%
		Ischium	4	5	10	100%
		Pubis	1	3	9	90%
		Scapula	1	2	4	40%
		Sternum	0	0	2	20%
Long bones	*Triceratops horridus*	Femur	3	5	8	80%
		Fibula	2	1	6	60%
		Fragment	0	0	0	-
		Humerus	1	3	7	70%
		Radius	1	2	4	40%
		Tibia	3	4	8	80%
		Ulna	0	2	3	30%
Manus and pes	*Triceratops horridus*	Astragalus	0	1	2	20%
		Carpal	0	0	0	-
		Fragment	0	0	0	-
		Metacarpal	0	0	10	14%
		Metapodial	0	0	1	-
		Metatarsal	0	0	15	22%
		Phalange	0	0	16	6%
		Tarsal	0	0	1	-
***Triceratops* teeth**	*Triceratops horridus*	Tooth	-	-	65	-
Trace fossils	-	Coprolite	-	-	8	-
Misc.	-	Plant	-	-	43	-
	Triceratops horridus	Tendon	-	-	78	-
Associated fauna	*Struthiomimus*	Caudal vertebra	-	-	1	-
	Marsupial	Dentary	-	-	1	-
	Brachychampsa	Dentary	-	-	1	-
	-	Fish	-	-	3	-
	-	Fragment	-	-	0	-
	Champsosaurus	Humerus	-	-	1	-
	Champsosaurus	Osteoderm	-	-	3	-
	Leptoceratops	Rib	-	-	1	-
	Lepisosteid	Scale	-	-	9	-
	Mollusca	Shell	-	-	1	-
	Champsosaurus	Tooth	-	-	7	-

Table S2. Average bone modification values of three independent surveys for each corresponding fossil element for the upper and lower DTB.

Fossil ID	Bonebed	Element	Weathering	Abrasion	Fragmentation	Distortion	Iron Encrustation	Bioerosion	Depression marks	Average
3	Lower	Sternum	3,7	4,0	3,0	5,0	5,0	4,7	5,0	4,1
5	Lower	Dentary	3,0	4,3	2,7	4,7	4,3	5,0	5,0	3,8
7	Lower	Coracoid	3,3	4,0	3,3	5,0	2,3	5,0	5,0	3,6
15	Lower	Predentary	3,7	3,7	2,3	4,0	4,3	4,7	5,0	3,6
17	Lower	Fibula	3,3	4,3	1,3	3,0	2,3	5,0	5,0	2,9
46	Lower	Radius	5,0	5,0	4,0	4,3	4,0	5,0	5,0	4,5
51	Lower	Metatarsal III	4,3	4,7	2,7	4,3	3,3	5,0	5,0	3,9
52	Lower	Maxilla	4,7	4,7	2,7	4,7	3,3	5,0	5,0	4,0
55	Lower	Surangular	4,3	4,7	4,0	5,0	4,7	5,0	5,0	4,5
126	Lower	Fibula	3,0	4,0	2,7	3,3	3,7	5,0	5,0	3,3
133	Lower	Coracoid	4,3	4,7	3,0	5,0	4,0	5,0	5,0	4,2
134	Lower	Cervical rib	5,0	4,7	4,0	5,0	5,0	5,0	5,0	4,7
146	Lower	Articular	3,3	3,7	3,3	4,3	4,0	4,7	5,0	3,7
150	Lower	Ischium	4,0	4,3	3,0	4,7	3,0	5,0	5,0	3,8
157	Lower	Nasal	4,0	4,7	3,7	5,0	4,3	5,0	5,0	4,3
161	Lower	Rostrum	4,7	5,0	4,0	3,3	5,0	5,0	5,0	4,4
170	Lower	Quadrate	4,7	5,0	4,0	5,0	5,0	5,0	5,0	4,7
172	Lower	Rib	4,3	5,0	4,0	4,7	5,0	5,0	5,0	4,6
205	Lower	Ulna	3,0	4,3	2,7	4,3	2,3	5,0	5,0	3,3
216	Lower	Pubis	4,0	4,3	3,0	3,7	3,7	5,0	4,7	3,7
218	Lower	Metatarsal II	4,0	4,7	4,0	4,3	4,7	5,0	5,0	4,3
238	Lower	Coracoid	3,7	3,7	3,7	4,3	3,7	5,0	5,0	3,8
249	Lower	Epijugal	4,3	4,3	4,3	5,0	5,0	5,0	5,0	4,6
264	Lower	Radius	4,5	5,0	2,5	3,5	5,0	5,0	5,0	4,1
273	Lower	Premaxilla	4,0	4,3	3,3	4,0	4,0	5,0	5,0	3,9
275	Lower	Ischium	4,0	3,3	3,7	4,0	4,3	5,0	5,0	3,9
333	Lower	Cervical rib	4,3	5,0	4,0	4,7	4,7	5,0	5,0	4,5
461	Lower	Caudal vertebra	4,3	5,0	4,3	5,0	5,0	4,7	5,0	4,7
495	Lower	Ischium	4,3	5,0	3,3	5,0	5,0	5,0	5,0	4,5
621	Lower	Scapula	3,7	3,7	3,3	4,0	4,3	5,0	5,0	3,8
690	Lower	Pubis	3,0	4,7	3,3	4,3	3,7	4,7	5,0	3,8
729	Lower	Fibula	2,3	4,0	3,0	4,0	4,3	4,7	5,0	3,5
739	Lower	Humerus	2,7	3,7	3,7	4,0	4,7	5,0	5,0	3,7
761	Lower	Premaxilla	4,7	5,0	3,7	4,3	4,7	5,0	5,0	4,5
802	Lower	Condyle	2,3	4,3	5,0	4,7	4,3	4,3	5,0	4,1
821	Lower	Splenial	3,5	4,0	4,0	4,0	3,5	5,0	5,0	3,8
825	Lower	Horn-core	3,7	5,0	4,7	5,0	3,3	4,7	5,0	4,3
904	Lower	Ulna	4,5	4,5	3,0	4,5	4,0	5,0	5,0	4,1
1041	Lower	Jugal	4,7	5,0	4,3	5,0	5,0	4,7	5,0	4,8
B2	Upper	Tibia	3	3	2	4	4	5	5	3,7
B3	Upper	Horn-core	3	4	2	4	2	5	5	3,6
B7	Upper	Squamosal	3	3	2	4	3	5	5	3,6
B9	Upper	Femur	3	4	3	3	3	5	5	3,7
B14	Upper	Ischium	3	4	3	5	4	5	5	4,1
B19	Upper	Scapula	3	4	3	5	3	5	5	4,0
B21	Upper	Ilium	2	4	3	5	3	5	5	3,9
B22	Upper	Ischium	2	4	3	4	5	5	5	4,0
B24	Upper	Ilium	3	4	3	4	3	5	5	3,9
B32	Upper	Pubis	3	5	2	2	4	5	5	3,7
B34	Upper	Humerus	3	3	2	4	4	5	5	3,7
B36	Upper	Nasal	2	4	4	5	5	4	4	4,0
B38	Upper	Dentary	2	4	4	5	5	5	5	4,3
B48	Upper	Humerus	2	5	3	4	3	5	5	3,9
B54	Upper	Pubis	3	5	3	4	5	5	5	4,3
B63	Upper	Femur	3	4	4	4	4	5	5	4,1
B68	Upper	Ulna	2	4	4	4	5	5	5	4,1
B69	Upper	Dentary	3	4	4	5	4	5	5	4,3
B76	Upper	Metatarsal III	3	4	3	5	5	5	5	4,3
B85	Upper	Fibula	4	4	4	3	5	5	5	4,3
B88	Upper	Surangular	5	5	3	4	5	5	5	4,6
B89	Upper	Rostrum	2	4	3	3	5	5	5	3,9
B106	Upper	Tibia	4	5	3	5	4	5	5	4,4
B110	Upper	Radius	2	4	3	5	4	5	5	4,0
B113	Upper	Quadratojugal	2	4	4	5	5	5	5	4,3
B142	Upper	Chevron	4	5	4	5	5	5	5	4,7
B196	Upper	Metatarsal I	2	3	5	5	5	5	5	4,3
B248	Upper	Metatarsal IV	4	4	4	5	5	5	5	4,6
B326	Upper	Metatarsal II	2	2	3	5	5	5	5	3,9
B339	Upper	Astragalus	3	2	4	3	5	5	5	3,9
B344	Upper	Phalange	2	5	5	5	5	5	3	4,3
B347	Upper	Fibula	2	3	3	5	5	5	5	4,0
B358	Upper	Radius	2	4	3	2	3	5	5	3,4
B389	Upper	Nasal	2	3	3	5	5	5	4	3,9
Average Lower			**3,9**	**4,4**	**3,4**	**4,4**	**4,1**	**4,9**	**5,0**	**4,1**
Average Upper			**2,7**	**3,9**	**3,3**	**4,3**	**4,3**	**5,0**	**4,9**	**4,0**

Table S3. Raw sedimentological data of the lower DTB showing distribution of grain-size classes.

Full sample ID	Year	X	Y	Z	Ymin	Z_10	LOI550 (wt%)	CaCO3tot (wt%)	Median grainsize (um)	%Clay	%Silt	%Very Fine Silt	%Fine Silt	%Coarse Silt	%Sand	%Very Fine Sand	%Fine Sand	%Middle Coarse Sand	%Coarse Sand	%Very Coarse Sand
TRIC-A0	2015	549111,345	4828437,915	1248,9	-4828437,915	200	5,36	1,769	3,33	78,84	20,04	11,21	5,82	3	1,13	1,06	0,07	0	0	0
TRIC-A1	2015	549111,345	4828437,915	1249	-4828437,915	201	5,218	1,785	3,18	82,13	17,87	11,52	5,25	1,1	0	0	0	0	0	0
TRIC-A2	2015	549111,345	4828437,915	1249,1	-4828437,915	202	4,923	1,779	3,59	76,94	22,99	13,38	7,13	2,49	0,07	0,07	0	0	0	0
TRIC-A3	2015	549111,345	4828437,915	1249,2	-4828437,915	203	4,918	1,704	3,69	75,91	22,81	12,72	6,71	3,38	1,28	1,27	0,01	0	0	0
TRIC-A4	2015	549111,345	4828437,915	1249,3	-4828437,915	204	3,811	1,602	6,98	53,45	41,1	17,19	14,89	9,01	5,45	5,04	0,41	0	0	0
TRIC-A5	2015	549111,345	4828437,915	1249,4	-4828437,915	205	1,59	0,8747	52,26	17,23	43,11	5,07	9,78	28,27	39,66	34,5	5,16	0	0	0
TRIC-A6	2015	549111,345	4828437,915	1249,5	-4828437,915	206	3,907	1,248	18,86	35,54	47,11	11,48	14,48	21,15	17,35	16,41	0,94	0	0	0
TRIC-A7	2015	549111,345	4828437,915	1249,6	-4828437,915	207	3,241	1,154	22,16	32,83	48,79	11,14	14,59	23,06	18,38	16,91	1,47	0	0	0
TRIC-A8	2015	549111,345	4828437,915	1249,7	-4828437,915	208	3,542	0,9828	35,4	26,09	43,75	8,7	12,64	22,41	30,16	22,38	6,24	0,98	0,57	0
TRIC-A9	2015	549111,345	4828437,915	1249,8	-4828437,915	209	3,762	0,9676	46,44	23,88	35,86	7,44	10,02	18,41	40,26	25,18	13,55	1,39	0,13	0
TRIC-A10	2015	549111,345	4828437,915	1249,9	-4828437,915	210	4,725	1,216	22,47	34,6	40,92	9,96	12,29	18,68	24,48	19,08	5,4	0	0	0
TRIC-A11	2015	549111,345	4828437,915	1250	-4828437,915	211	4,615	1,168	18,19	37,26	44,98	10,59	13,82	20,58	17,76	15,71	2,05	0	0	0
TRIC-A12	2015	549111,345	4828437,915	1250,1	-4828437,915	212	4,347	1,169	19,22	36,55	43,07	10,48	12,91	19,69	20,38	17,69	2,68	0	0	0
TRIC-A13	2015	549111,345	4828437,915	1250,2	-4828437,915	213	3,369	1,386	8,29	49,17	43,47	14,3	14,52	14,65	7,36	7,19	0,18	0	0	0
TRIC-A14	2015	549111,345	4828437,915	1250,3	-4828437,915	214	4,428	1,397	8,75	48,03	43,32	13,84	14,51	14,97	8,64	8,15	0,5	0	0	0
TRIC-A15	2015	549111,345	4828437,915	1250,4	-4828437,915	215	4,071	1,495	9,36	46,72	44,76	13,76	14,9	16,09	8,52	8,33	0,19	0	0	0
TRIC-A16	2015	549111,345	4828437,915	1250,5	-4828437,915	216	3,38	1,346	10,58	44,47	44,36	13,46	14,62	16,28	11,17	10,33	0,84	0	0	0
TRIC-A17	2015	549111,345	4828437,915	1250,6	-4828437,915	217	2,5	1,353	73,31	19,37	25,59	6,18	7,23	12,17	55,04	31,32	21,05	2,06	0,61	0
TRIC-A18	2015	549111,345	4828437,915	1250,7	-4828437,915	218	3,476	3,841	6,89	53,27	36,7	13,75	13,23	9,72	10,03	7,45	2,58	0	0	0
TRIC-A19	2015	549111,345	4828437,915	1250,8	-4828437,915	219	2,473	3,44	52,47	28,14	25,45	7,49	7,76	10,2	46,41	26,47	18,84	0,89	0,21	0
TRIC-A20	2015	549111,345	4828437,915	1250,9	-4828437,915	220	2,293	3,415	19,36	37,44	32,53	9,87	10,01	12,65	30,02	21,72	8,28	0,02	0	0
TRIC-A21	2015	549113,045	4828436,037	1251	-4828436,037	221	2,719	3,77	7,95	50,14	36,01	13,27	12,84	9,9	13,85	10,35	3,49	0,01	0	0
TRIC-A22	2015	549113,045	4828436,037	1251,1	-4828436,037	222	2,54	3,644	18,26	38,53	39	9,65	10,82	18,53	22,48	19,94	2,53	0	0	0
TRIC-A23	2015	549113,045	4828436,037	1251,2	-4828436,037	223	3,726	3,91	6,09	56,73	38,21	15,73	14,78	7,71	5,06	3,94	1,12	0	0	0
TRIC-A24	2015	549113,045	4828436,037	1251,3	-4828436,037	224	2,307	3,084	53,58	22,27	35,92	5,62	7,52	22,78	41,81	35,44	5,19	0,25	0,92	0,01
TRIC-A25	2015	549113,045	4828436,037	1251,4	-4828436,037	225	2,305	3,057	40,51	29,54	34,73	7,18	8,67	18,88	35,74	29,76	5,98	0	0	0

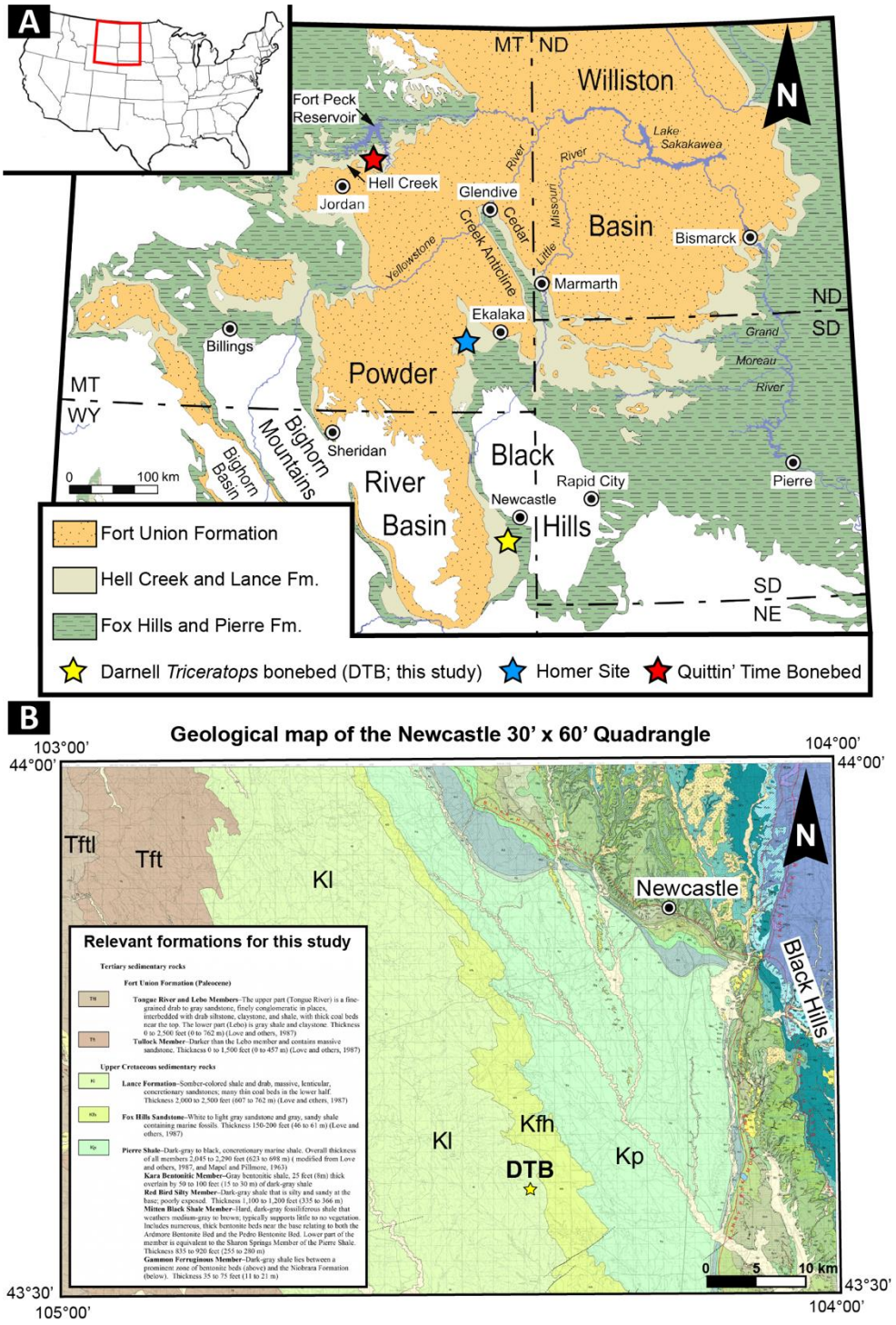

Figure S1. (A) Geological overview map of the northern Great Plains (Wyoming, Montana, North- and South Dakota) showing the distribution of Upper Cretaceous and Paleocene deposits (modified from 133-134). The DTB site in the Powder River Basin of eastern Wyoming (this study) is indicated, as well as the other two described bonebed with *Triceratops* individuals. These are the Homer Site (135) close to Ekalaka in SE Montana and the Quittin' Time Bonebed close to Jordan in the Hell Creek Fm. prime area (136). (B) Detailed geological map of the Newcastle 30' x 60' Quadrangle from the Wyoming State Geological Survey showing the DTB site within the lower Lance Fm (137).

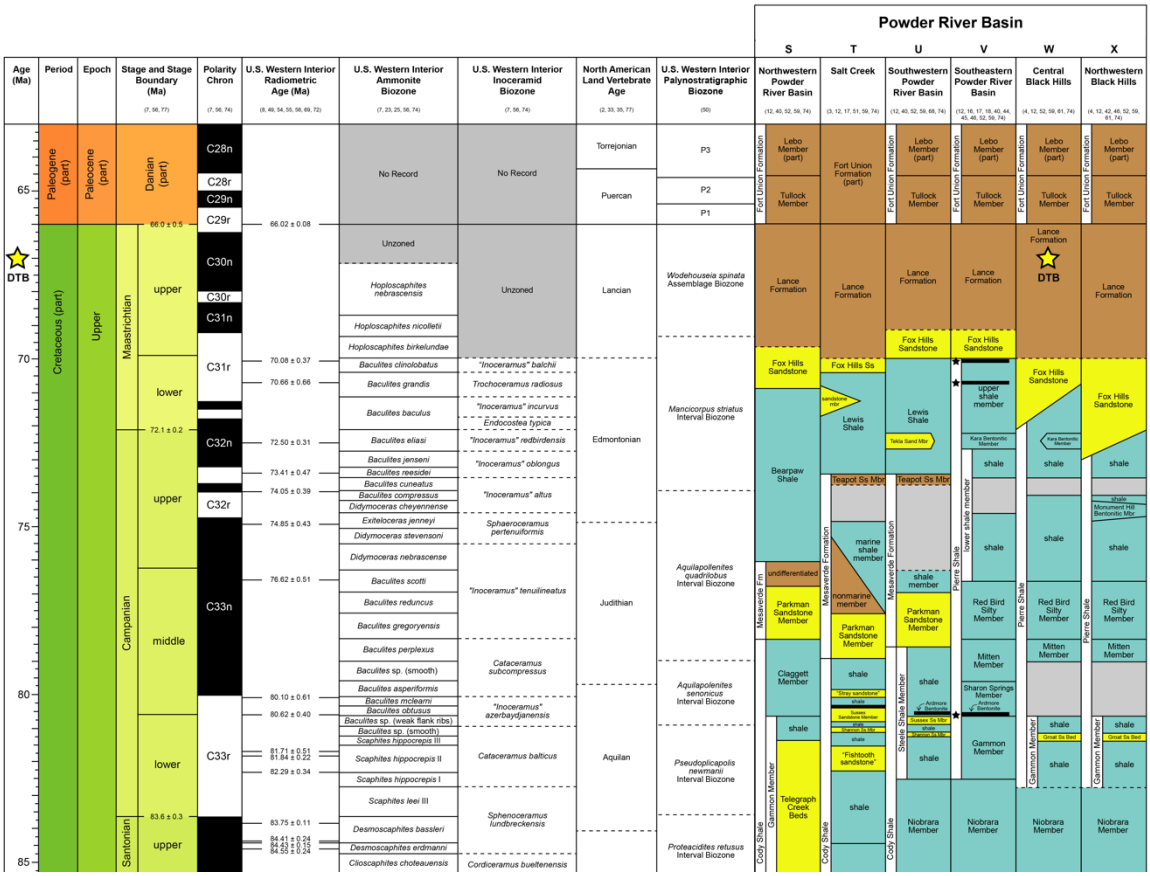

Figure S2. Chronostratigraphic overview of the DTB site, based on a compilation of the Wyoming State Geological Survey (138). The DTB is located in between the regions of the Central Black Hills and the Southeastern Powder River Basin. Note that the hiatus between the Fox Hills Fm. and the overlying Lance Fm. is not well constrained (126).

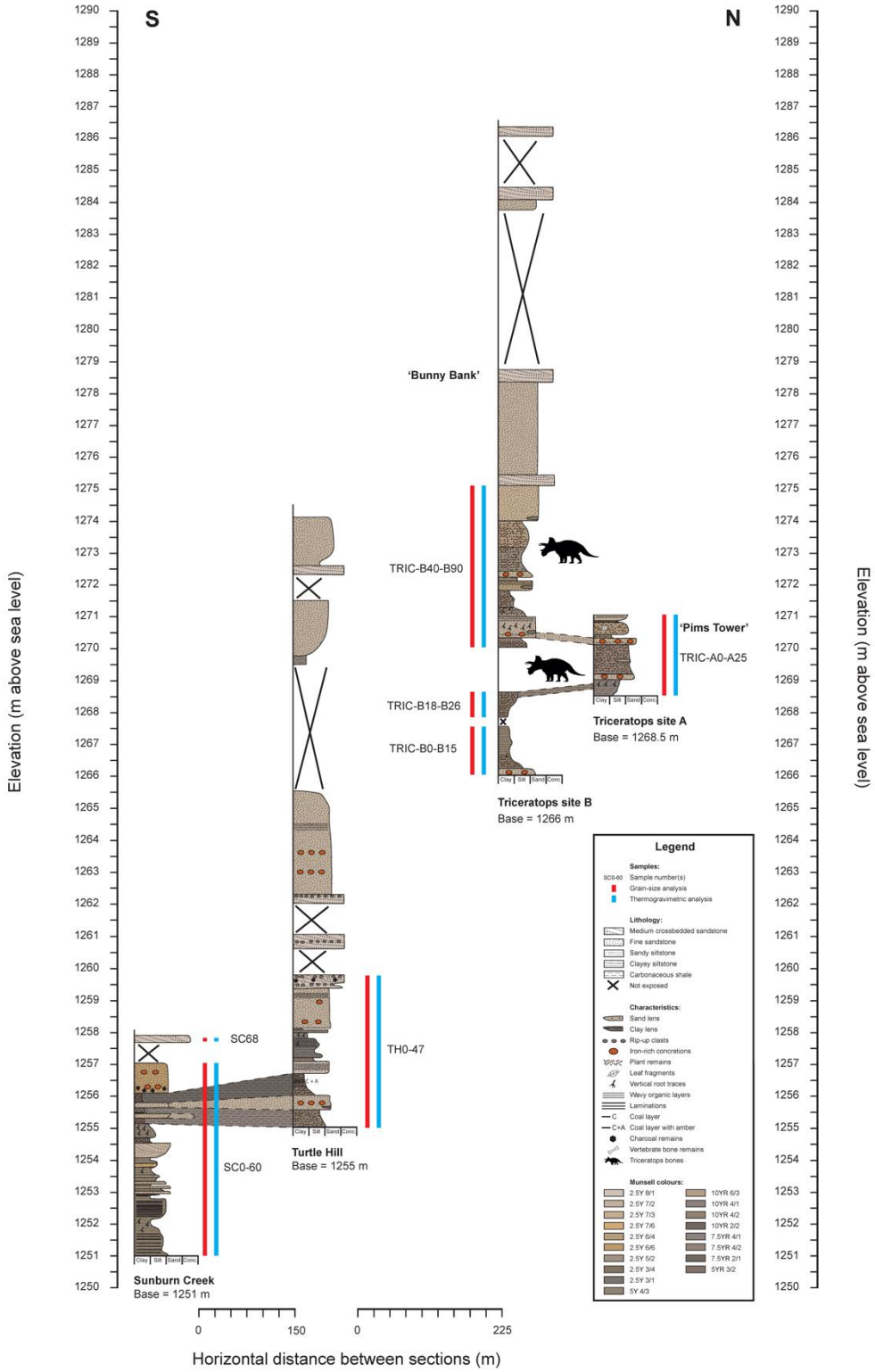

Figure S3. Field correlation between DTB and surrounding sites (Sunburn Creek, Turtle Hill).

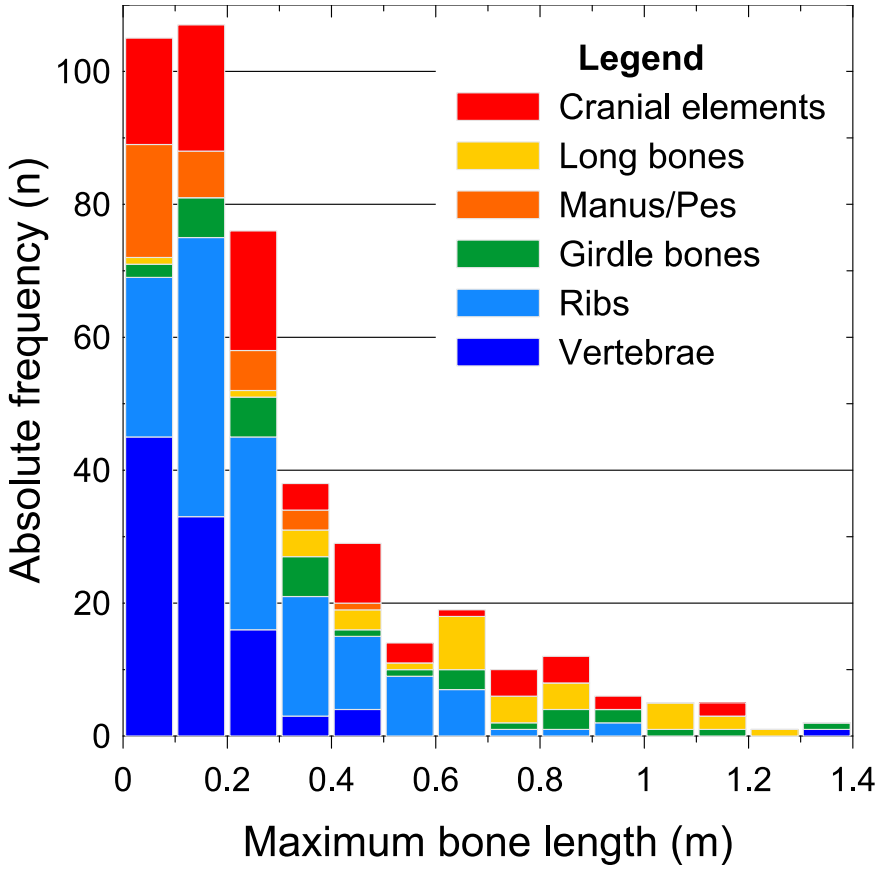

Figure S4. Size frequency plot of bone elements from the main bonebed at DTB (n = 794). This distribution is based on maximum bone length measurements established through a GIS database of the field site, and verified with lab measurements of a selection of bones. This size frequency shows a pattern that is compatible with a non-selective, catastrophic kill event and not with a long-term attritional mortality scenario that predominantly kills vulnerable young and old members of a population (138-140). Post-mortem burial histories can further modify preserved age and size structures by destructive taphonomic processes. In this case the size frequency resembles a rapid permanent burial scenario as highlighted in Eberth et al., 2007 (140).

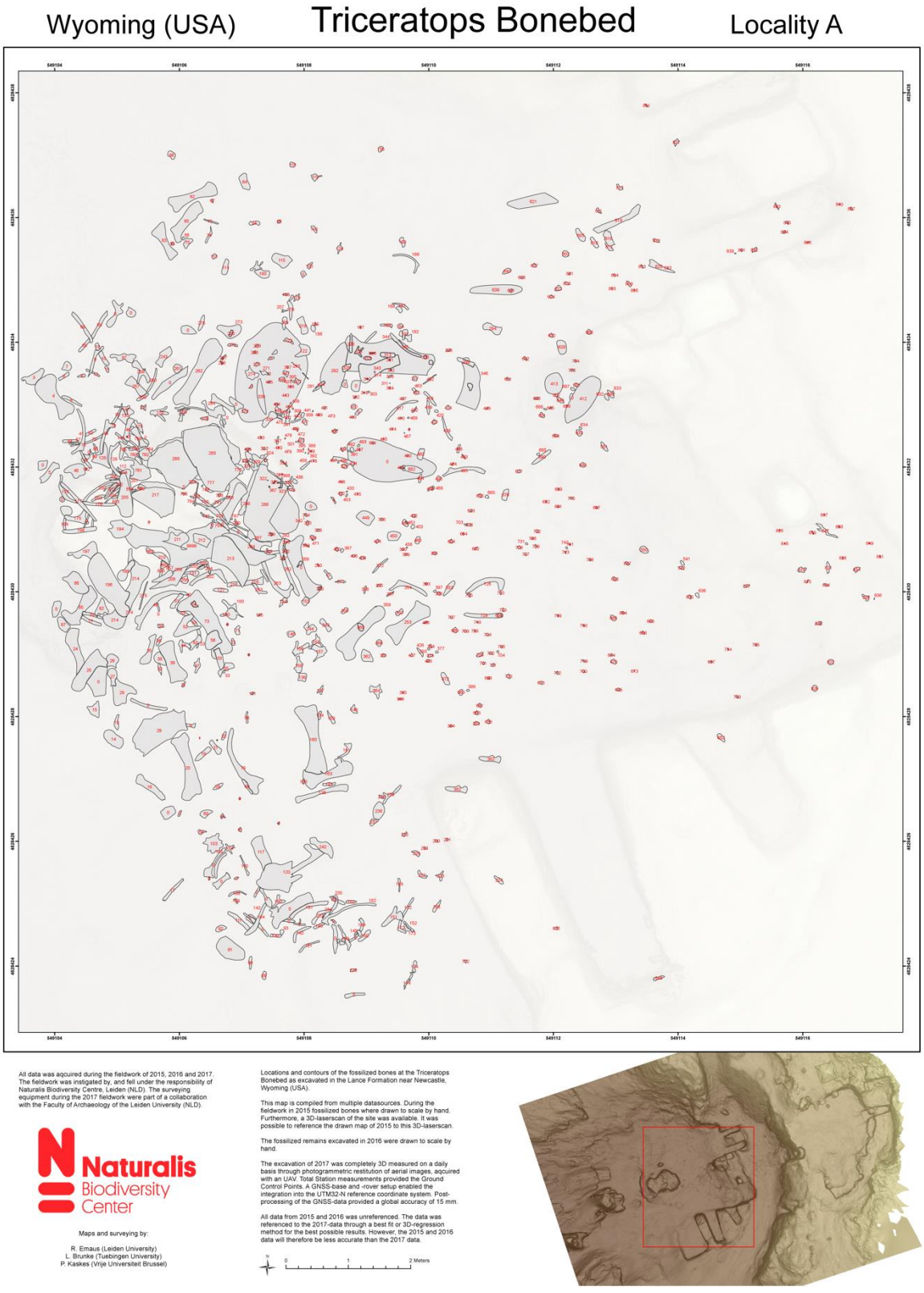

Figure S5. Bonemap of Lower Bonebed of the DTB site. Plotted on top of a shaded relief.

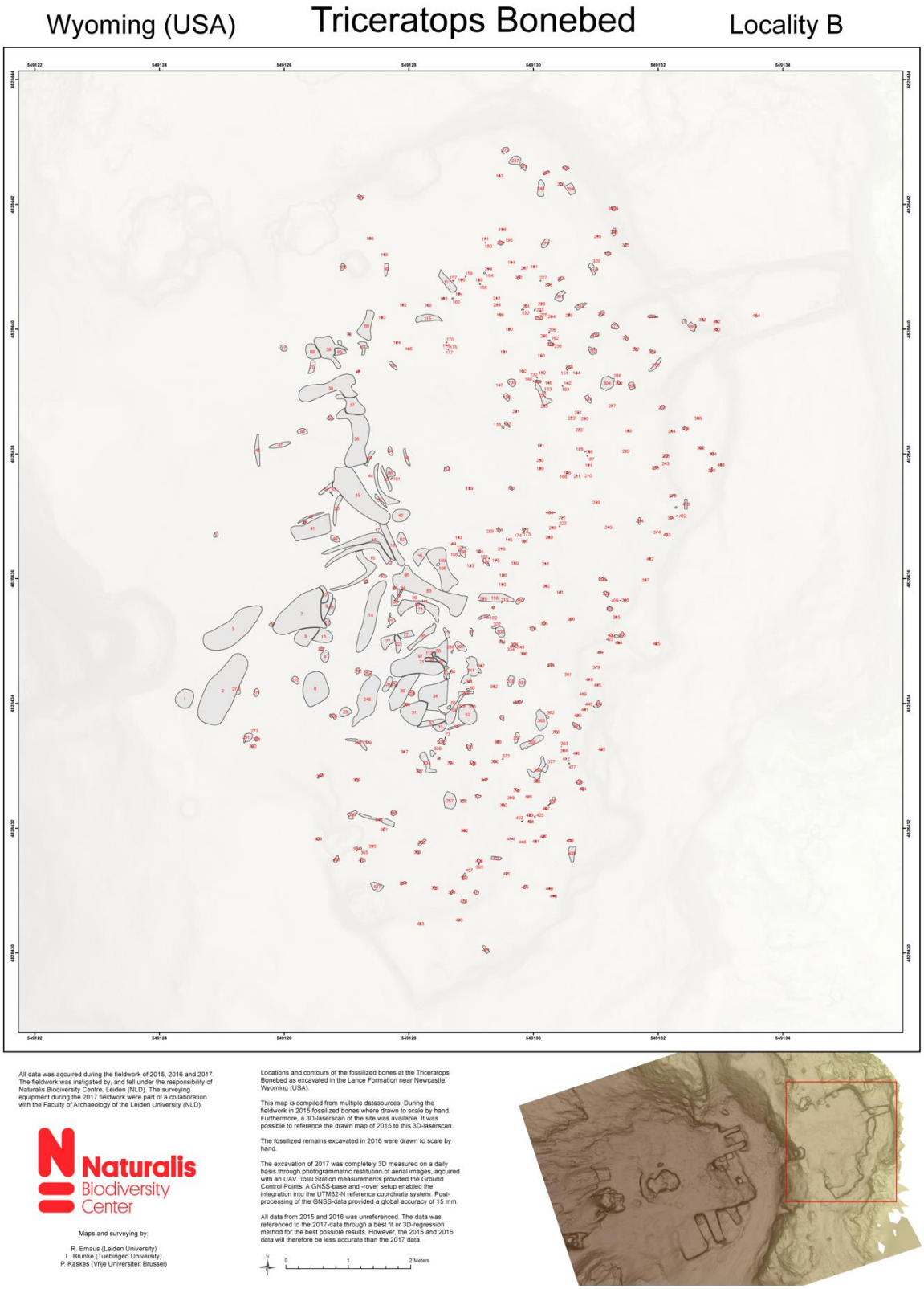

Figure S6. Bonemap of Upper Bonebed of the DTB site. Plotted on top of a shaded relief.

Figure S7. Selected overview of fossil material from the lower DTB showing the most dominant bone modification patterns. (A) Complete left humerus showing minor fragmentation as well as large areas of iron encrustation on the proximal condyle. (B) Left maxilla with multiple teeth still preserved showing some degree of fragmentation. The proximal protuberance that forms the infraorbital foramen is slightly distorted posteriorly. (C) Left tibia with well-preserved bone surface textures and very little fragmentation. Note that the proximal condyle is still significantly distorted approximately 90 degrees. (D) Left coracoid showing abrasion effects on the anterior and medial margins. (E) Well-preserved rostrum with only minor iron encrustation damage near the most anterior apex. (F) Broken right humerus that experienced high degrees of weathering. Note the difference between the dark-brown surface area on the midshaft representing the original bone surface and light-coloured surface on the remaining areas. Nevertheless, distortion is extremely limited. (G) Completely fragmented and broken fibula. The original bone surface is still present. (H) Right ulna showing a heavily fragmented and iron-encrusted proximal half. (I) Exceptionally preserved quadrate showing only minor breakage. (J) Extremely fragmented but undistorted left squamosal element.

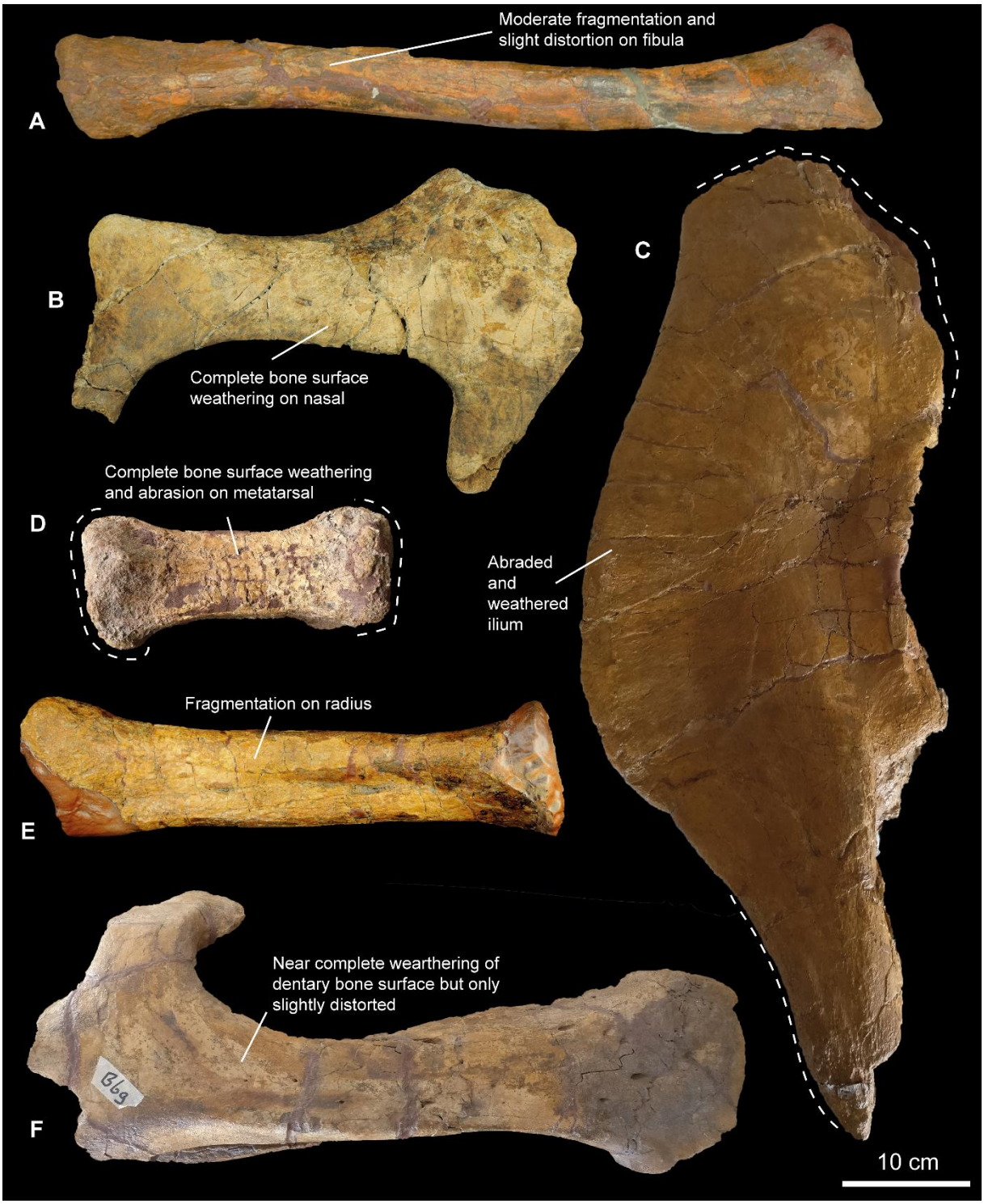

Figure S8. Selected overview of fossil material from the upper DTB showing representative bone modification patterns. Note the lighter coloration and rugose textures typical of the fossils from the upper DTB due to loss of the original bone surface through weathering and abrasion. (A) Fibula showing significant fragmentation and distortion. (B) Left nasal bone with fused epinasal that completely lost its original bone surface and has abraded bone margins. (C) Right ilium with large patches of weathered bone surface and highly abraded proximal region (lower part in photo). (D) Metatarsal showing complete loss of the original bone surface. (E) Fragmented and weathered radius with abraded condyles. (F) Completely weathered right dentary, but showing an otherwise good preservation.

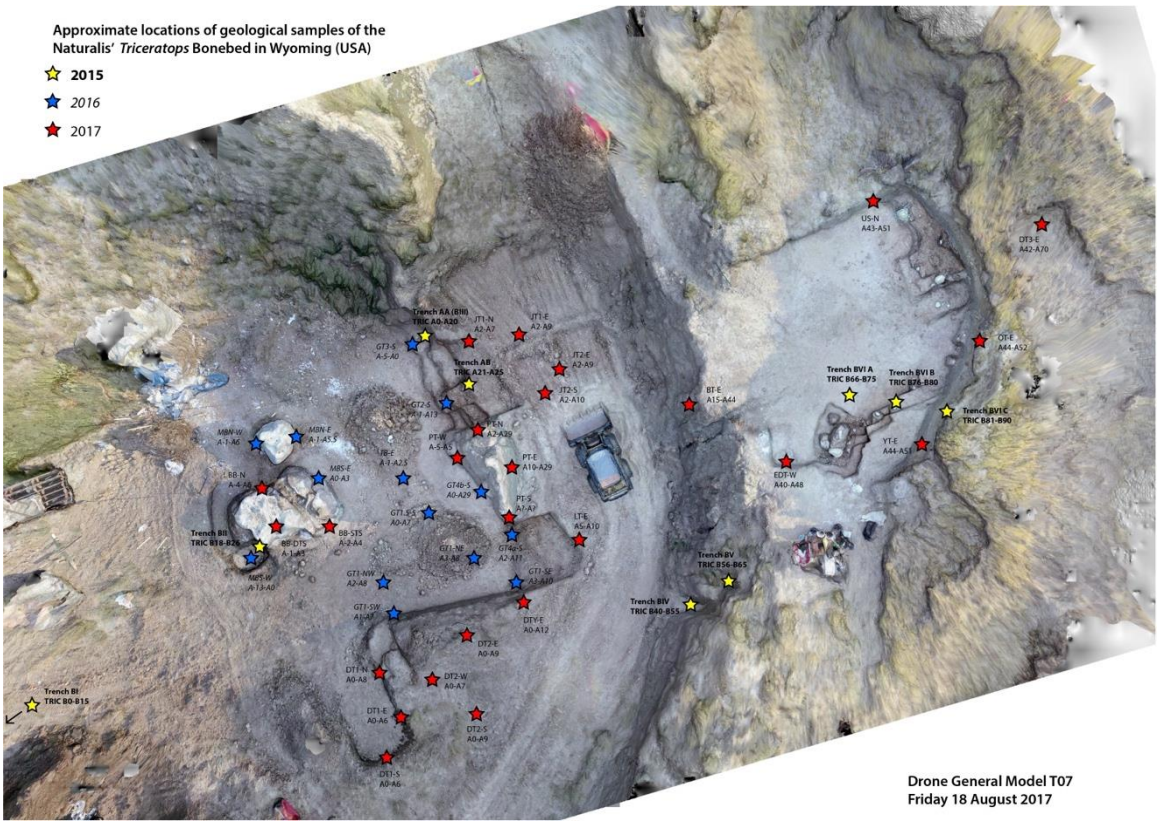

Figure S9. DTB drone orthomosaic with the approximate positions of the sections that comprises geological samples used in this study.

Figure S10. Representative field photos of the sedimentary structures preserved at DTB.

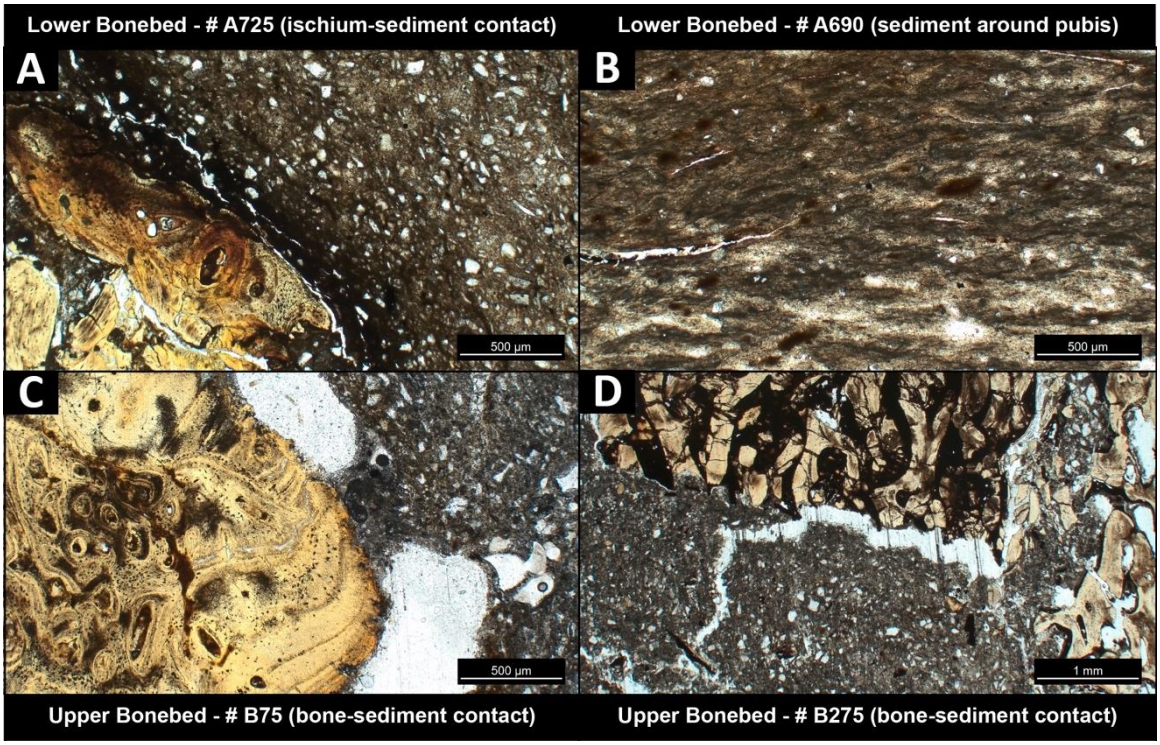

Figure S11. Representative DTB thin section photographs (all in plane polarized light) of bone and sediment from the Lower Bonebed (A-B) and Upper Bonebed (C-D).

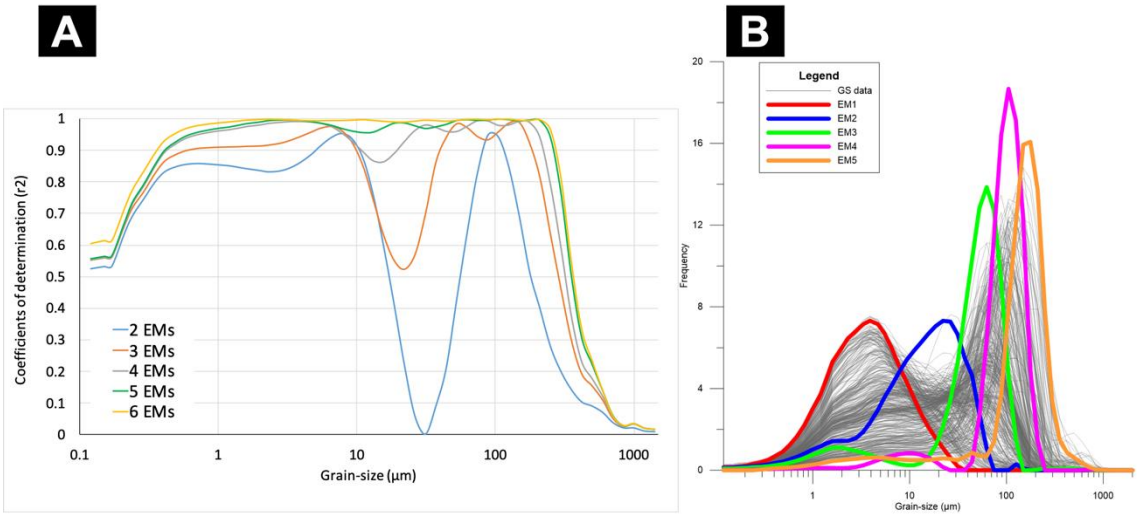

Figure S12. Grain-size end-member statistics. (A) R^2 values versus grain-size, showing that 5 end-members result in >90% coverage of the grain-size variations. (B) Full dataset of the grain-size distribution curves overlain by the five modelled grain-size end-member distributions.

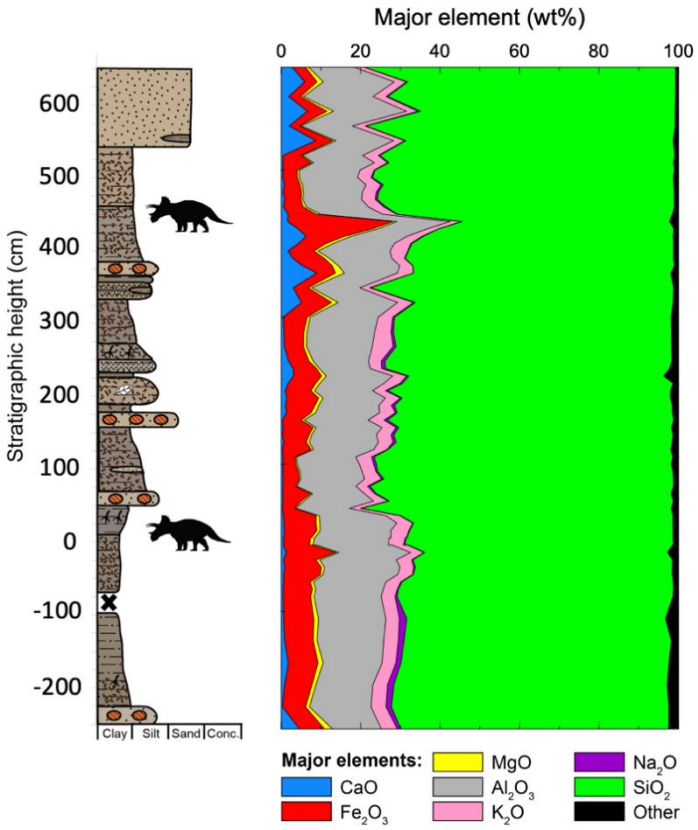

Figure S13. Micro-XRF based major element plot of the full section at DTB, containing subsections TRIC-A and TRIC-B.

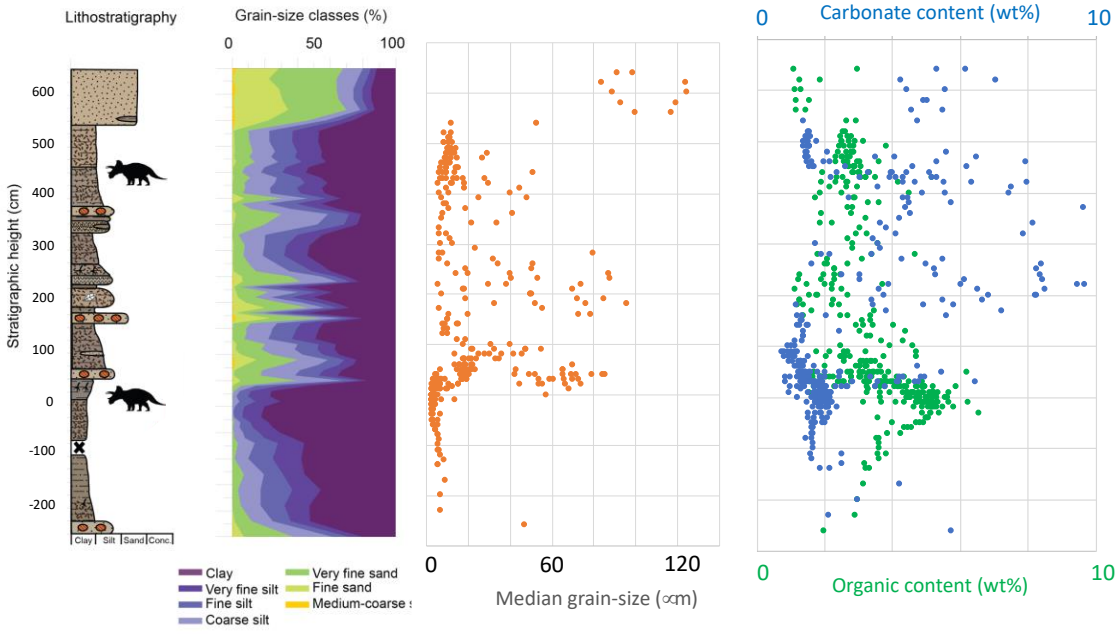

Figure S14. Full 1D multiproxy plot of c. 9 meters containing also the upper bonebed from the DTB site, showing of all measured subsections the % grain-size classes, median grain-size, total organic content, and total carbonate content.

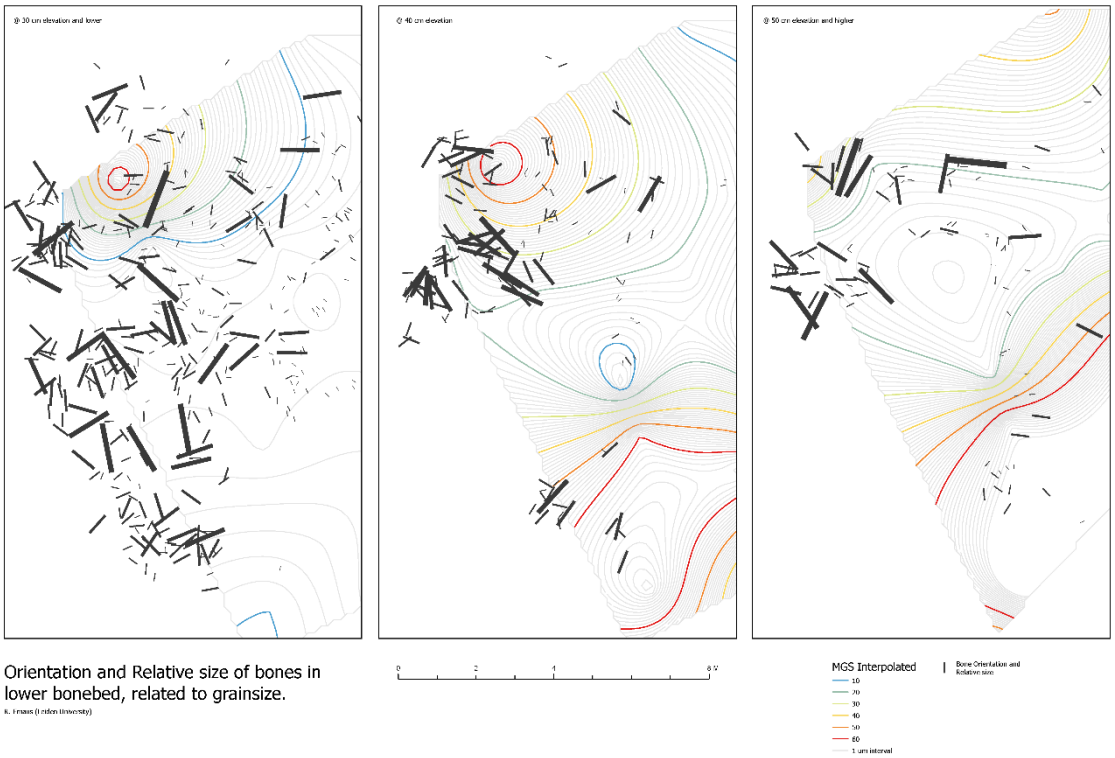

Figure S16. Bone orientation and relative size of the DTB, plotted on top of a median grain-size contourplot of depths 130,140 and 150 cm.

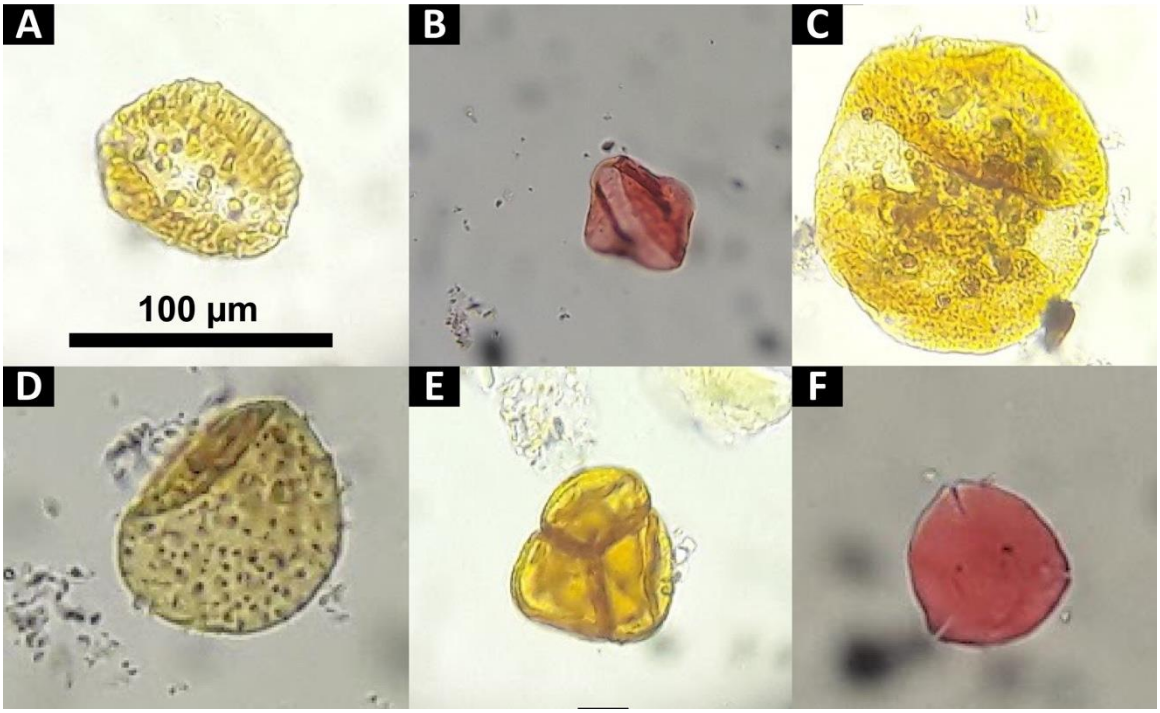

Figure S17. Palynological overview of the DTB with representative palynomorph species found in organic rich sediments surrounding the *Triceratops* bones. All photos taken at a magnification of 40x. (A) *Wodehouseia spinata*, a stratigraphic angiosperm index fossil (Fig. S2). (B) *Aquilapollenites* spp., angiosperm. (C) *Pityosporites* spp., gymnosperm. (D) *Pandanites typicus*, angiosperm. (E) *Inaperturotetradites scabrates,* gymnosperm. (F) *Kurtzipites circularis,* angiosperm (Beugelink, 2019).

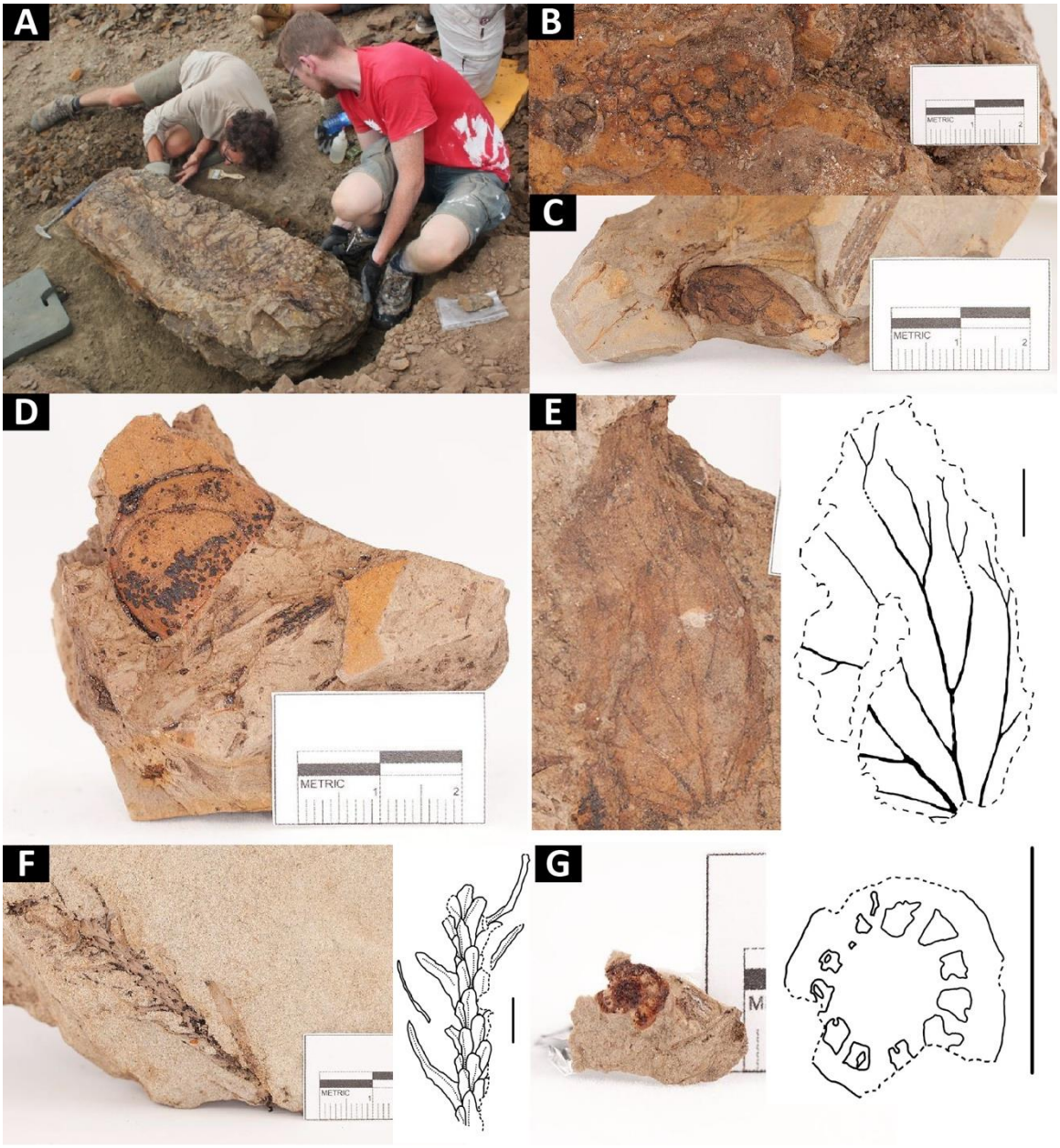

Figure S18. Paleobotanical overview showing representative Cretaceous macrofloral remains of the DTB (Verwijs, 2018). (A) Excavated palm tree within the main bonebed. (B) Pine-cone like pattern preserved in host rock (# A715), most likely the female cone of the pine tree *Pinophyta.* (C) A flattened elliptic-ovoid shaped seed or fruit (# A346c), unidentifiable. (D) Fragment of an ovoid shaped fruit (# A667), most likely belonging to the monocotyledon (palm) angiosperm *Spinifructus antiquus* (141). (E) Fragmentary fossil leaf (# T11), venation visible but too incomplete to be identified. Scale bar of the drawing equals 1 cm. (F) Imprint of a piece of conifer branch (# A890), most likely from the family of *Auracariaceae* (142). Scale bar of the drawing equals 0.5 cm. (G) Cross section of a stem of a species of *Equisetopsida*, most likely the horsetail *Equisetum sp.,* derived from the upper bonebed (# B19a). Scale bar of the drawing equals 0.5 cm.

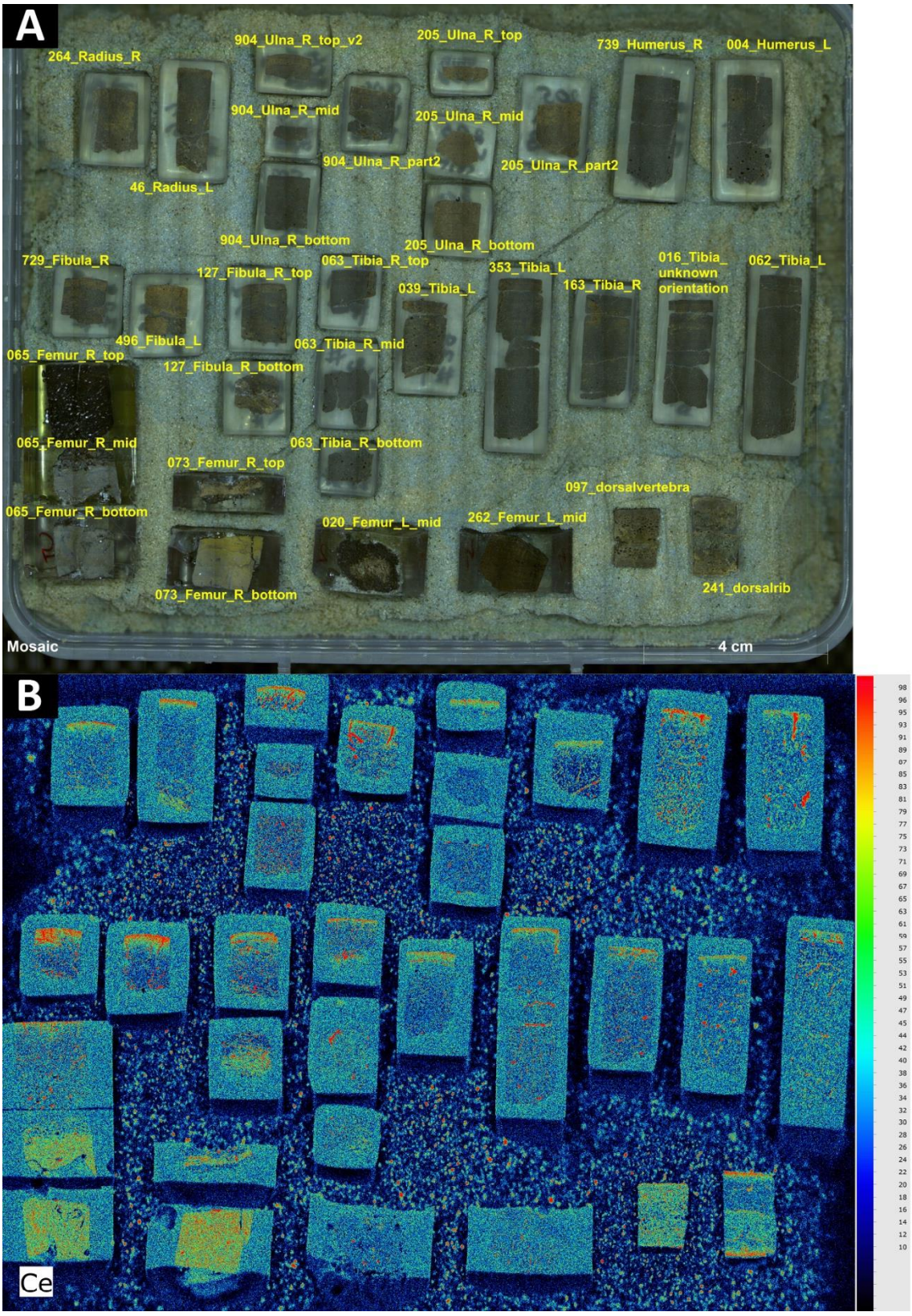

Figure S19. Micro-XRF mapping results of DTB bones. (A) Photoscan mosaic of the analysed thick sections. (B) Single-element micro XRF heatmap of cerium showing the relative, semi-quantitative Ce distribution across the bone surfaces, with a clear enrichment near the outer cortical bone.

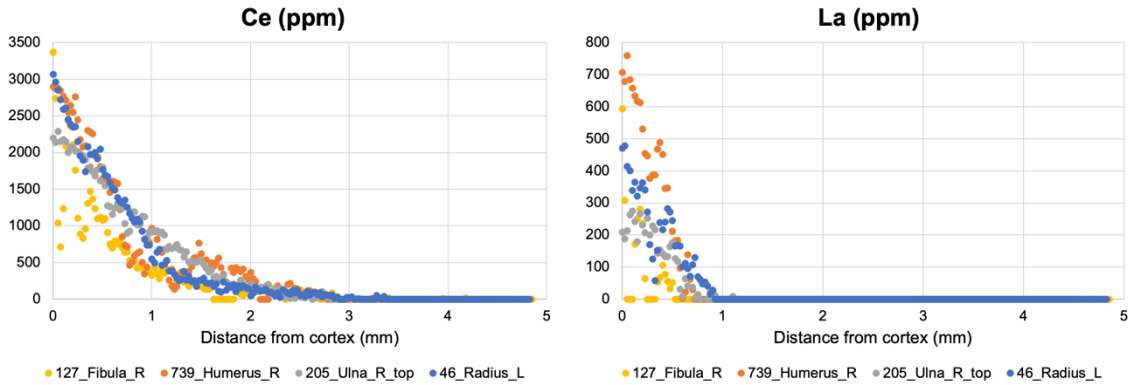

Figure S20. High-resolution trace element profiles of five selected bone thick sections (see Fig. S19A for a photo overview of the different samples) throughout the DTB, using micro-XRF point-linescans. Both Ce and La show steep profiles from outer cortical bone towards trabecular bone, with the remark that La reached below the limit of detection c. > 50 ppm, indicative of a shared taphonomic history characterized by limited diagenetic alteration due to likely rapid burial.

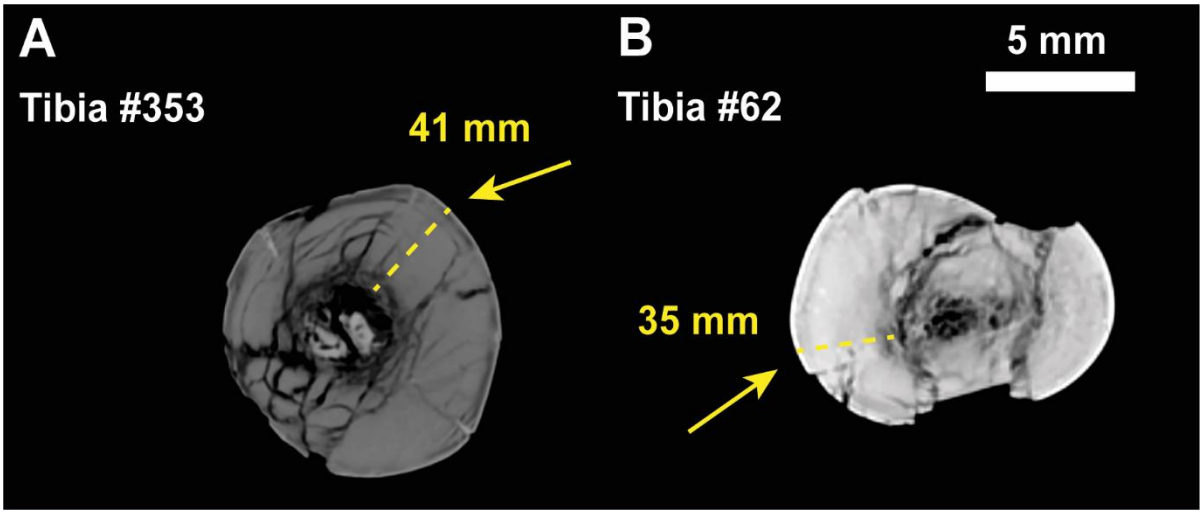

Figure S21. CT images of the tibia #353 and #62 of which histological samples are available (Figure 2J,K) showing intra-bone preservation and cortical depth of the acquired drill-core (in yellow). Sampling location of both tibiae was on the posteromedial midshaft.

Acknowledgements

We thank Donley and Nancy Darnell for access to the DTB site. Black Hills Institute is thanked for logistical support. We are grateful to numerous volunteers of the Dinolab at Naturalis for putting their time and energy in excavating and preparing the *Triceratops* bones. PK thanks the financial support by Research Foundation - Flanders (FWO) PhD fellowship 11E6621N. AS & JR thank the Dutch Research Council (NWO) for financial support through the ALW Open Programme (ALWOP.633). PC thanks the FWO - Hercules Program for financing the µXRF instrument at the VUB. Partial data from this study were generated during the BSc and MSc thesis projects of JR, OV and LP (at VU Amsterdam and Universiteit Utrecht, in collaboration with Naturalis). We thank Martine Hagen and Unze van Buuren (VUA) for assistance with grain-size and thermogravimetric analyses. We thank Janna Verwijs, Yorick Beugelink, Michael Field, Erica van Hees and Corrie Bakels (Leiden University) for paleobotanical and palynological analyses.

References

1. J. B. Scannella, D. W. Fowler, M. B. Goodwin, J. R. Horner, Evolutionary trends in *Triceratops* from the Hell Creek Formation, Montana. Proceedings of the National Academy of Sciences U.S.A. 111, 10245–10250 (2014).
2. J. R. Horner, M. B. Goodwin, N. Myhrvold, Dinosaur census reveals abundant *Tyrannosaurus* and rare ontogenetic stages in the upper Cretaceous Hell Creek Formation (Maastrichtian), Montana, USA. PLoS ONE 6 (2011).
3. P. Dodson, C. A. Forster, S. D. Sampson, "Ceratopsidae" in The Dinosauria, 2nd Ed., P. Dodson, D. B. Weishampel, H. Osmólska, Eds. (University of California Press, 2004), pp. 494–514.
4. D. Fowler, The Hell Creek Formation, Montana: A Stratigraphic Review and Revision Based on a Sequence Stratigraphic Approach. Geosciences 10, 1–59 (2020).
5. T. R. Lyson, N. R. Longrich, Spatial niche partitioning in dinosaurs from the latest cretaceous (Maastrichtian) of North America. Proceedings of The Royal Society B Biological Sciences 278, 1158–1164 (2011).
6. D. W. Fowler, Revised geochronology, correlation, and dinosaur stratigraphic ranges of the Santonian-Maastrichtian (Late Cretaceous) formations of the Western Interior of North America. PloS one 12, e0188426 (2017).
7. R. A. DePalma, et al., A seismically induced onshore surge deposit at the KPg boundary, North Dakota. Proceedings of the National Academy of Sciences U.S.A. 116, 8190–8199 (2019). https:/doi.org/10.1073/pnas.1817407116.
8. W. W. Stein, Taking count: A census of dinosaur fossils recovered from the Hell Creek and Lance Formations (Maastrichtian). The Journal of Paleontological Sciences, 1–42 (2019).
9. O. C. Marsh, Notice of new American Dinosauria. American Journal of Science 3, 331–336 (1889).
10. J. B. Hatcher, The Ceratopsia (United States Geological Survey, 1907).
11. J. R. Horner, M. B. Goodwin, Major cranial changes during *Triceratops* ontogeny. Proceedings of the Royal Society B Biological Sciences 273, 2757–2761 (2006).
12. J. B. Scannella, D. W. Fowler, M. B. Goodwin, J. R. Horner, Evolutionary trends in *Triceratops* from the Hell Creek Formation, Montana. Proceedings of the National Academy of Sciences U.S.A. 111, 10245–10250 (2014).
13. J. B. Scannella, J. R. Horner, *Torosaurus* Marsh, 1891, is *Triceratops* Marsh, 1889 (Ceratopsidae: Chasmosaurinae): synonymy through ontogeny. Journal of Vertebrate Paleontology 30, 1157–1168 (2010).
14. N. R. Longrich, D. J. Field, *Torosaurus* Is Not *Triceratops*: Ontogeny in chasmosaurine ceratopsids as a case study in dinosaur taxonomy. PLoS ONE 7, e32623 (2012).
15. R. R. Rogers, D. A. Eberth, A. R. Fiorillo, Eds. Bonebeds: genesis, analysis, and paleobiological significance (University of Chicago Press, 2007).
16. L. M. Lambe, On the squamoso-parietal crest of the horned dinosaurs *Centrosaurus apertus* and *Monoclonius canadensis* from the Cretaceous of Alberta. Ottawa Naturalist 18, 81–84 (1904).
17. D. A. Eberth, D. B. Brinkman, V. Barkas, "A centrosaurine mega-bonebed from the Upper Cretaceous of Southern Alberta: Implications for behavior and death events" in New Perspectives on Horned Dinosaurs: The Royal Tyrrell Museum Ceratopsian Symposium, M. J. Ryan, B. J. Chinnery-Allgeier, D. A. Eberth, Eds. (Indiana University Press, 2010), pp. 495–508.
18. K. Chiba, et al., Taphonomy of a monodominant *Centrosaurus apertus* (Dinosauria: Ceratopsia) bonebed from the Upper Oldman Formation of Southeastern Alberta. Palaios 30, 655–667 (2015).

19. M. J. Ryan, et al., The taphonomy of a *Centrosaurus* (Ornithischia : Ceratopsidae) bone bed from the Dinosaur Park Formation (Upper Campanian), Alberta, Canada, with comments on cranial ontogeny. Palaios 16, 482–506 (2001).
20. P. Dodson, *Avaceratops lammersi*: a new ceratopsid from the Judith River Formation of Montana. Proceedings of the Academy of Natural Sciences of Philadelphia, 305–317 (1986).
21. M. J. Ryan, A new basal centrosaurine ceratopsid from the Oldman Formation, southeastern Alberta. Journal of Paleontology 81, 376–396 (2007).
22. L. M. Lambe, A new genus and species of Ceratopsia from Belly River Formation of Alberta. Ottawa Naturalis 27, 109–116 (1913).
23. C. M. Sternberg, *Pachyrhinosaurus canadensis*, representing a new family of the Ceratopsia, from southern Alberta. National Museum of Canada Bulletin 118, 109–120 (1950).
24. S. H. W. Scott, M. J. Ryan, D. C. Evans, Postcranial description of *Wendiceratops pinhornensis* and a taphonomic analysis of the oldest monodominant ceratopsid bonebed. The Anatomical Record 306, 1824–1841 (2023).
25. R. R. Rogers, Taphonomy of three dinosaur bone beds in the Upper Cretaceous Two Medicine Formation of Northwestern Montana: Evidence for drought-related mortality. Palaios 5, 394–413 (1990).
26. S. D. Sampson, Two new horned dinosaurs from the Upper Cretaceous Two Medicine Formation of Montana; with a phylogenetic analysis of the Centrosaurinae (Ornithischia: Ceratopsidae). Journal of Vertebrate Paleontology 15, 743–760 (1995).
27. M. J. Ryan, B. J. Chinnery-Allgeier, D. A. Eberth, P. E. Ralrick, Eds., New Perspectives on Horned Dinosaurs: The Royal Tyrrell Museum Ceratopsian Symposium (Indiana University Press, 2010).
28. T. M. Lehman, *Chasmosaurus mariscalensis* , sp. nov., a new ceratopsian dinosaur from Texas. Journal of Vertebrate Paleontology 9, 137–162 (1989).
29. S. G. Lucas, R. M. Sullivan, A. P. Hunt, Re-evaluation of *Pentaceratops* and *Chasmosaurus* (Ornithischia: Ceratopsidae) in the Upper Cretaceous of the Western Interior. New Mexico Museum of Naturalis History and Science Bulletin 35 (2006).
30. B. Brown, *Anchiceratops*, a new genus of horned dinosaurs from the Edmonton Cretaceous of Alberta ; with Discussion of the origin of the ceratopsian crest and the brain casts of *Anchiceratops* and *Trachodon*. Bulletin of the American Museum of Natural History 33 (1914).
31. C. W. Gilmore, Reptilian fauna of the North Horn formation of central Utah (United States Geological Survey, 1946).
32. S. D. Sampson, et al., New horned dinosaurs from Utah provide evidence for intracontinental dinosaur endemism. PLoS ONE 5, 1–12 (2010).
33. M. A. Loewen, et al., “Horned dinosaurs (Ornithischia: Ceratopsidae) from the Upper Cretaceous (Campanian) Cerro del Pueblo Formation, Coahuila, Mexico” in New Perspectives on Horned Dinosaurs: The Royal Tyrrell Museum Ceratopsian Symposium, M. J. Ryan, B. J. Chinnery-Allgeier, D. A. Eberth, Eds. (Indiana University Press, 2010), pp. 99–116.
34. J. C. Mathews, S. L. Brusatte, S. A. Williams, M. D. Henderson, The first *Triceratops* bonebed and its implications for gregarious behavior. Journal of Vertebrate Paleontology 29, 286–290 (2009).
35. S. W. Keenan, J. B. Scannella, Paleobiological implications of a *Triceratops* bonebed from the Hell Creek Formation, Garfield County, northeastern Montana. Geological Society of America Special Papers 503, 349–364 (2014).
36. J. R. Horner, D. J. Varricchio, M. B. Goodwin, Marine transgressions and the evolution of Cretaceous dinosaurs. Nature 358, 59–61 (1992).

37. J. H. Ostrom, *Leptoceratops gracilis* from the Lance Formation of Wyoming. Journal of Paleontology, 697–704 (1978).
38. C. A. Forster, New information on the skull of *Triceratops*. Journal of Vertebrate Paleontology 16, 246–258 (1996).
39. A. A. Farke, K. Carpenter, "Cranial osteology and phylogenetic relationships of the chasmosaurine ceratopsid *Torosaurus latus*" in Horns and beaks: Ceratopsian and ornithopod dinosaurs, K. Carpenter, Ed. (Indiana University Press, 2006), pp. 235–257.
40. C. A. Forster, Species resolution in *Triceratops*: cladistic and morphometric approaches. Journal of Vertebrate Paleontology 16, 259–270 (1996).
41. M. R. Voorhies, Taphonomy and population dynamics of an early Pliocene vertebrate fauna, Knox County, Nebraska. Contributions to Geology (1969).
42. E. de Margerie, J. Cubo, J. Castanet, Bone typology and growth rate: testing and quantifying 'Amprino's rule' in the mallard (*Anas platyrhynchos*). Comptes Rendus Biologies 325, 221–230 (2002).
43. E. de Margerie, et al., Assessing a relationship between bone microstructure and growth rate: a fluorescent labelling study in the king penguin chick (*Aptenodytes patagonicus*). Journal of Experimental Biology 207, 869–879 (2004).
44. A. Miall, Ed., Fluvial Depositional Systems (Springer Cham, 2014) https:/doi.org/10.1007/978-3-319-00666-6.
45. R. M. Jerrett, G. D. Price, S. T. Grimes, A. T. Dawson, A paleoclimatic and paleoatmospheric record from peatlands accumulating during the Cretaceous-Paleogene boundary event, Western Interior Basin, Canada. Bulletin of the Geological Society of America 127, 1564–1582 (2015).
46. H. C. Fricke, B. Z. Foreman, J. O. Sewall, Integrated climate model-oxygen isotope evidence for a North American monsoon during the Late Cretaceous. Earth and Planetary Science Letters 289, 11–21 (2010).
47. C. E. Burns, N. P. Mountney, D. M. Hodgson, L. Colombera, Anatomy and dimensions of fluvial crevasse-splay deposits: Examples from the Cretaceous Castlegate Sandstone and Neslen Formation, Utah, U.S.A. Sedimentary Geology 351, 21–35 (2017).
48. A. L. Titus, et al., Geology and taphonomy of a unique tyrannosaurid bonebed from the upper Campanian Kaiparowits Formation of southern Utah: Implications for tyrannosaurid gregariousness. PeerJ 9 (2021).
49. P. V Ullmann, D. E. Grandstaff, R. D. Ash, K. J. Lacovara, Geochemical taphonomy of the Standing Rock Hadrosaur Site: Exploring links between rare earth elements and cellular and soft tissue preservation. Geochimica et Cosmochimica Acta 269, 223–237 (2020).
50. K. Snyder, M. McLain, J. Wood, A. Chadwick, Over 13,000 elements from a single bonebed help elucidate disarticulation and transport of an *Edmontosaurus thanatocoenosis*. PLOS ONE 15, e0233182 (2020).
51. M. A. McLain, et al., Independent confirmation of fluvial reworking at a Lance Formation (Maastrichtian) bonebed by traditional and chemical taphonomic analyses. Palaios 36, 193–215 (2021).
52. G. Botfalvai, E. Prondvai, A. Ősi, Living alone or moving in herds? A holistic approach highlights complexity in the social lifestyle of Cretaceous ankylosaurs. Cretaceous Research 118, 104633 (2021).
53. S. D. Capaldo, C. R. Peters, Skeletal inventories from wildebeest drownings at Lakes Masek and Ndutu in the Serengeti ecosystem of Tanzania. Journal of Archaeological Science 22, 385–408 (1995).
54. D. A. Eberth, M. A. Getty, "Ceratopsian bonebeds: occurrence, origins, and significance" in Dinosaur Provincial Park: A spectacular ancient ecosystem revealed, P. J. Currie, E. B. Koppelhus, Eds. (Indiana University Press, 2005), pp. 501–536.

55. G. Haynes, Mass deaths and serial predation: Comparative taphonomic studies of modern large mammal death sites. Journal of Archaeological Science 15, 219–235 (1988).
56. Z. Qi, P. M. Barrett, D. A. Eberth, Social behaviour and mass mortality in the basal ceratopsian dinosaur *Psittacosaurus* (Early Cretaceous, People's Republic of China). Palaeontology 50, 1023–1029 (2007).
57. W. D. Turnbull, D. M. Martill, Taphonomy and preservation of a monospecific titanothere assemblage from the Washakie formation (Late Eocene), southern Wyoming. An ecological accident in the fossil record. Palaeogeography, Palaeoclimatology, Palaeoecology 63, 91–108 (1988).
58. F. H. Pough, C. M. Janis, J. B. Heiser, Eds., Vertebrate life, 9th ed (Pearson, 2013).
59. N. Tinbergen, Ed., Social behaviour in animals: With special reference to vertebrates (Springer Netherlands, 1990).
60. R. M. H. Smith, J. Botha, P. A. Viglietti, Taphonomy of drought afflicted tetrapods in the Early Triassic Karoo Basin, South Africa. Palaeogeography, Palaeoclimatology, Palaeoecology 604, 111207 (2022).
61. D. J. Varricchio, Taphonomy of Jack's Birthday Site, a diverse dinosaur bonebed from the Upper Cretaceous Two Medicine Formation of Montana. Palaeogeography, Palaeoclimatology, Palaeoecology 114, 297–323 (1995).
62. J. N. Fenner, Occasional Hunts or Mass Kills? Investigating the Origins of Archaeological Pronghorn Bonebeds in Southwest Wyoming. American Antiquity 74, 323–350 (2009).
63. R. K. Hunt, A. A. Farke, "Behavioral Interpretations from Ceratopsid Bonebeds" in New Perspectives on Horned Dinosaurs: The Royal Tyrrell Museum Ceratopsian Symposium, M. J. Ryan, B. J. Chinnery-Allgeier, D. A. Eberth, Eds. (Indiana University Press, 2010), pp. 447–455.
64. S. D. Sampson, "Speculations on the socioecology of ceratopsid dinosaurs (Ornithischia: Neoceratopsia)" in Mesozoic Vertebrate Life, D. H. Tanke, K. Carpenter, Eds. (Indiana University Press, 2009), pp. 263–276.
65. R. D'Anastasio, et al., Histological and chemical diagnosis of a combat lesion in *Triceratops.* Scientific Reports 12, 3941 (2022).
66. A. A. Farke, E. D. S. Wolff, D. H. Tanke, Evidence of Combat in *Triceratops*. PLoS ONE 4, e4252 (2009).
67. J. O. Farlow, P. Dodson, The Behavioral Significance of Frill and Horn Morphology in Ceratopsian Dinosaurs. Evolution 29, 353 (1975).
68. D. W. E. Hone, D. Naish, I. C. Cuthill, Does mutual sexual selection explain the evolution of head crests in pterosaurs and dinosaurs?: Ornithodiran mutual sexual selection. Lethaia 45, 139–156 (2012).
69. D. E. Hone, D. Wood, R. Knell, Positive allometry for exaggerated structures in the ceratopsian dinosaur *Protoceratops andrewsi* supports socio-sexual signaling. Palaeontologia Electronica (2016) https:/doi.org/10.26879/591.
70. A. Knapp, R. J. Knell, A. A. Farke, M. A. Loewen, D. W. E. Hone, Patterns of divergence in the morphology of ceratopsian dinosaurs: sympatry is not a driver of ornament evolution. Proceedings of the Royal Society B Biological Sciences 285, 20180312 (2018).
71. A. Nabavizadeh, How *Triceratops* got its face: An update on the functional evolution of the ceratopsian head. The Anatomical Record, ar.25196 (2023).
72. K. Padian, J. R. Horner, The evolution of 'bizarre structures' in dinosaurs: biomechanics, sexual selection, social selection or species recognition? Journal of Zoology 283, 3–17 (2011).

73. J. De Rooij, et al., Stable isotope record of *Triceratops* from a mass accumulation (Lance Formation, Wyoming, USA) provides insights into *Triceratops* behaviour and ecology. Palaeogeography, Palaeoclimatology, Palaeoecology 607, 111274 (2022).
74. G. M. Erickson, P. J. Makovicky, B. D. Inouye, C.-F. Zhou, K.-Q. Gao, A life table for *Psittacosaurus lujiatunensis*: Initial insights into ornithischian dinosaur population biology. The Anatomical Record: Advances in Integrative Anatomy and Evolutionary Biology 292, 1514–1521 (2009).
75. D. E. Fastovsky, et al., A nest of *Protoceratops andrewsi* (Dinosauria, Ornithischia). Journal of Paleontology 85, 1035–1041 (2011).
76. Q. Meng, J. Liu, D. J. Varricchio, T. Huang, C. Gao, Parental care in an ornithischian dinosaur. Nature 431, 145–146 (2004).
77. D. G. Wolfe, J. I. Kirkland, *Zuniceratops christopheri* n. gen. & n. sp., a ceratopsian dinosaur from the Moreno Hill Formation (Cretaceous, Turonian) of west-central New Mexico. Lower and Middle Cretaceous terrestrial ecosystems 14, 303–318 (1998).
78. S. G. Dalman, S. G. Lucas, S. E. Jasinski, A. J. Lichtig, P. Dodson, The oldest centrosaurine: a new ceratopsid dinosaur (Dinosauria: Ceratopsidae) from the Allison Member of the Menefee Formation (Upper Cretaceous, early Campanian), northwestern New Mexico, USA. PalZ 95, 291–335 (2021).
79. D. C. Evans, M. J. Ryan, Cranial anatomy of *Wendiceratops pinhornensis* gen. et sp. nov., a centrosaurine ceratopsid (Dinosauria: Ornithischia) from the Oldman Formation (Campanian), Alberta, Canada, and the evolution of ceratopsid nasal ornamentation. PLOS ONE 10, e0130007 (2015).
80. T. Lehman, "Growth and population age structure in the horned dinosaur *Chasmosaurus*" in Horns and beaks: Ceratopsian and ornithopod dinosaurs, K. Carpenter, Ed. (Indiana University Press, 2006).
81. A. B. Avila, et al., Capybara responses to varying levels of predation risk. Animal Behaviour 190, 1–9 (2022).
82. M. J. Childress, M. A. Lung, Predation risk, gender and the group size effect: does elk vigilance depend upon the behaviour of conspecifics? Animal Behaviour 66, 389–398 (2003).
83. G. Shannon, L. S. Cordes, R. Slotow, C. Moss, K. McComb, Social disruption impairs predatory threat assessment in African elephants. Animals 12, 495 (2022).
84. E. Sorato, P. R. Gullett, S. C. Griffith, A. F. Russell, Effects of predation risk on foraging behaviour and group size: adaptations in a social cooperative species. Animal Behaviour 84, 823–834 (2012).
85. J. M. Gómez, E. W. Schupp, P. Jordano, The ecological and evolutionary significance of effectiveness landscapes in mutualistic interactions. Ecology Letters 25, 264–277 (2022).
86. C. Iribarren, B. P. Kotler, Foraging patterns of habitat use reveal landscape of fear of Nubian ibex *Capra nubiana*. Wildlife Biology 18, 194–201 (2012).
87. D. D. P. Johnson, R. Kays, P. G. Blackwell, D. W. Macdonald, Does the resource dispersion hypothesis explain group living? Trends in Ecology & Evolution 17, 563–570 (2002).
88. B. Koger, et al., Quantifying the movement, behaviour and environmental context of group-living animals using drones and computer vision. Journal of Animal Ecology, 1365-2656.13904 (2023).
89. F. Lesmerises, C. J. Johnson, M.-H. St-Laurent, Landscape knowledge is an important driver of the fission dynamics of an alpine ungulate. Animal Behaviour 140, 39–47 (2018).
90. P. Monaghan, N. B. Metcalfe, Group foraging in wild brown hares: effects of resource distribution and social status. Animal Behaviour 33, 993–999 (1985).
91. F. A. Campos, et al., Drivers of home range characteristics across spatiotemporal scales in a Neotropical primate, *Cebus capucinus*. Animal Behaviour 91, 93–109 (2014).

92. S. D. Gehrt, E. K. Fritzell, Resource distribution, female home range dispersion and male spatial interactions: group structure in a solitary carnivore. Animal Behaviour 55, 1211–1227 (1998).
93. L. R. Dougherty, Meta-analysis shows the evidence for context-dependent mating behaviour is inconsistent or weak across animals. Ecology Letters 24, 862–875 (2021).
94. A. M. Roth, et al., Sexual selection and personality: Individual and group-level effects on mating behaviour in red junglefowl. Journal of Animal Ecology 90, 1288–1306 (2021).
95. J. S. Brashares, P. Arcese, Role of forage, habitat and predation in the behavioural plasticity of a small African antelope. Journal of Animal Ecology 71, 626–638 (2002).
96. W. Jędrzejewski, et al., Collaborative behaviour and coalitions in male jaguars (*Panthera onca*)—evidence and comparison with other felids. Behavioral Ecology and Sociobiology 76, 121 (2022).
97. J. Jenikejew, B. Chaignon, S. Linn, M. Scheumann, Proximity-based vocal networks reveal social relationships in the Southern white rhinoceros. Scientific Reports 10, 15104 (2020).
98. C. S. Menz, A. W. Goldizen, S. P. Blomberg, N. J. Freeman, E. C. Best, Understanding repeatability and plasticity in multiple dimensions of the sociability of wild female kangaroos. Animal Behaviour 126, 3–16 (2017).
99. D. Réale, N. J. Dingemanse, "Personality and individual social specialisation" in Social Behaviour: Genes, Ecology and Evolution, T. Székely, A. J. Moore, J. Komdeur, Eds. (Cambridge University Press, 2010).
100. P. Kaskes, L. Brunke, R. Emaus, D. Bastiaans, A. S. Schulp, A novel 3D visualization of dinosaur bonebeds: integrating geology, paleontology and archaeology in Geological Society of America Abstracts with Programs, (2017) https:/doi.org/10.1130/abs/2017AM-306574.
101. C. M. Brown, S. Herridge-Berry, K. Chiba, A. Vitkus, D. A. Eberth, High-resolution (centimetre-scale) gps/gis-based 3D mapping and spatial analysis of in situ fossils in two horned-dinosaur bonebeds in the dinosaur park formation (Upper Cretaceous) at Dinosaur Provincial Park, Alberta, Canada. Canadian Journal of Earth Sciences 58, 225–246 (2021).
102. M. Konert, J. Vandenberghe, Comparison of laser grain size analysis with pipette and sieve analysis: a solution for the underestimation of the clay fraction. Sedimentology 44, 523–535 (1997).
103. J. A. van Hateren, M. A. Prins, R. T. van Balen, On the genetically meaningful decomposition of grain-size distributions: A comparison of different end-member modelling algorithms. Sedimentary Geology 375, 49–71 (2018).
104. M. A. Prins, G. J. Weltje, End-member modeling of siliciclastic grain-size distributions: the late Quaternary record of eolian and fluvial sediment supply to the Arabian Sea and its paleoclimatic significance. SEPM Special Publication 63, 91–111 (1999).
105. M. Konert, C. J. Beets, Simultaneous analysis of organic matter and carbonates in sediments with a thermo-gravimetric analyzer (TGA): comparison to classical analytical techniques. Submitted.
106. J. G. Harris, M. W. Harris, Eds., Plant identification terminology: an illustrated glossary (Spring Lake Publishing Utah, 1994).
107. K. R. Johnson, Megaflora of the Hell Creek and lower Fort Union Formations in the western Dakotas: Vegetational response to climate change, the Cretaceous-Tertiary boundary event, and rapid marine transgression. The Hell Creek Formation and the Cretaceous-Tertiary boundary in the northern Great Plains: An integrated continental record of the end of the Cretaceous: Boulder, Colorado, Geological Society of America Special Paper 361, 329–391 (2002).
108. K. Faegri, J. Iversen, Textbook of Pollen Analysis, revised by Faegri K., Kaland P.E., Krzywinski K. J Eds. (Wiley, 1989).

109. D. J. Nichols, K. R. Johnson, Palynology and microstratigraphy of Cretacous/Tertiary boundary sections in southwestern North Dakota. Geological Society of America Special Papers 361, 95–143 (2002). https:/doi.org/10.1130/0-8137-2361-2.95.
110. A. Bercovici, D. Pearson, D. Nichols, J. Wood, Biostratigraphy of selected K/T boundary sections in southwestern North Dakota, USA: toward a refinement of palynological identification criteria. Cretaceous Research 30, 632–658 (2009).
111. P. Kaskes, T. Déhais, S. J. de Graaff, S. Goderis, P. Claeys, Micro–X-ray fluorescence (μXRF) analysis of proximal impactites: High-resolution element mapping, digital image analysis, and quantifications. Geological Society of America Special Paper 550, 171–206 (2021).
112. J. Sherman, The theoretical derivation of fluorescent X-ray intensities from mixtures. Spectrochimica Acta 7, 283–306 (1955).
113. D. Herwartz, T. Tütken, K. P. Jochum, P. M. Sander, Rare earth element systematics of fossil bone revealed by LA-ICPMS analysis. Geochimica et Cosmochimica Acta 103, 161–183 (2013).
114. P. Kaskes, et al., "High-Resolution Chemostratigraphy of the Cretaceous-Paleogene (K-Pg) Boundary Interval in the US Western Interior: Implications for Chicxulub Impact Ejecta Dynamics" in 53rd Lunar and Planetary Science Conference, (Lunar and Planetary Institute, 2022), pp. 1–2.
115. N. J. de Winter, C. Snoeck, R. Schulting, T. Fernández-Crespo, P. Claeys, High-resolution trace element distributions and models of trace element diffusion in enamel of Late Neolithic/Early Chalcolithic human molars from the Rioja Alavesa region (north-central Spain) help to separate biogenic from diagenetic trends. Palaeogeography, Palaeoclimatology, Palaeoecology 532, 109260 (2019).
116. B. Chinnery, Morphometric analysis of evolutionary trends in the ceratopsian postcranial skeleton. Journal of Vertebrate Paleontology 24, 591–609 (2004).
117. P. M. Sander, Longbone histology of the Tendaguru sauropods: implications for growth and biology. Paleobiology 26, 466–488 (2000).
118. K. Stein, P. M. Sander, Histological core drilling: a less destructive method for studying bone histology. Methods in fossil preparation: proceedings of the first annual Fossil Preparation and Collections Symposium 1, 69–80 (2009).
119. T. M. Cullen, et al., Growth variability, dimensional scaling, and the interpretation of osteohistological growth data. Biology Letters 17, 20210383 (2021).
120. A. Chinsamy, M. A. Raath, Preparation of fossil bone for histological examination. Palaeontologia africana 29, 39–44 (1992).
121. E.-T. Lamm, K. Padian, "Preparation and sectioning of specimens" in Bone Histology of Fossil Tetrapods: Advancing Methods, Analysis, and Interpretation, (University of California Press, 2013), pp. 55–160.
122. V. de Buffrénil, A. Quilhac, "Bone tissue types: A brief account of currently used categories" in Vertebrate Skeletal Histology and Paleohistology, V. de Buffrénil, A. J. de Ricqlès, L. Zylberberg, K. Padian, Eds. (CRC Press, 2021), pp. 147–190.
123. C. R. Scotese, C. Dreher, Global Geology. http://www.globalgeology.com/ (2012).
124. J. R. Gill, W. A. Cobban, Stratigraphy and geologic history of the Montana Group and equivalent rocks, Montana, Wyoming, and North and South Dakota. U.S. Government Printing Office Professional Paper 776, p. 37 (1973).
125. C. W. Connor, "The Lance Formation - petrography and stratigraphy, Powder River Basin and nearby basins, Wyoming and Montana" in Evolution of sedimentary basins: Powder River Basin, V. F. Nuccio, P. L. Hansley, W. A. Cobban, C. G. Whitney, Eds. (US Government Printing Office 1992).

126. D. W. Fowler, Revised geochronology, correlation, and dinosaur stratigraphic ranges of the Santonian-Maastrichtian (Late Cretaceous) formations of the Western Interior of North America. PloS one 12, e0188426 (2017).
127. K. Snyder, M. McLain, J. Wood, A. Chadwick, Over 13,000 elements from a single bonebed help elucidate disarticulation and transport of an *Edmontosaurus thanatocoenosis*. PLOS ONE 15, e0233182 (2020).
128. J. R. Horner, "Introduction" in Wilson, G.P., Clemens, W.A., Horner, J.R., and Hartman, J.H., eds., Through the end of the Cretaceous in the type locality of the Hell Creek Formation in Montana and adjacent areas, G. P. Wilson, W. A. Clemens, J. R. Horner, J. H. Hartman, Eds. (Geological Society of America Special Paper 503, 2014) pp. ix–x.
129. K. R. Johnson, D. J. Nichols, J. H. Hartman, Hell Creek Formation: A 2001 synthesis. The Hell Creek Formation and the Cretaceous-Tertiary boundary in the northern Great Plains: An integrated continental record of the end of the Cretaceous: Boulder, Colorado, Geological Society of America Special Paper 361, 503–510 (2002).
130. R. M. Jerrett, G. D. Price, S. T. Grimes, A. T. Dawson, A paleoclimatic and paleoatmospheric record from peatlands accumulating during the Cretaceous-Paleogene boundary event, Western Interior Basin, Canada. Bulletin of the Geological Society of America 127, 1564–1582 (2015).
131. K. Hinaman, Hydrogeologic framework and estimates of groundwater volumes in Tertiary and Upper Cretaceous hydrogeologic units in the Powder River basin, Wyoming. U.S. Geological Survey Scientific Investigation Reports 2005-5008 (2005).
132. J. D. Love, A. C. Christiansen, L. W. McGrew, Geologic map of the Newcastle 1° x 2° quadrangle, northeastern Wyoming and western South Dakota. Wyoming State Geological Survey Map Series 25I (1987).
133. J. H. Hartman, K. R. Johnson, D. J. Nichols, The Hell Creek Formation and the Cretaceous-Tertiary boundary in the northern Great Plains: an integrated continental record of the end of the Cretaceous. Geological Society of America Special Papers 361 (2002).
134. D. E. Fastovsky, A. Bercovici, The Hell Creek Formation and its contribution to the Cretaceous–Paleogene extinction: A short primer. Cretaceous Research 57, 368–390 (2016).
135. J. C. Mathews, S. L. Brusatte, S. A. Williams, M. D. Henderson, The first *Triceratops* bonebed and its implications for gregarious behavior. Journal of Vertebrate Paleontology 29, 286–290 (2009).
136. S. W. Keenan, J. B. Scannella, Paleobiological implications of a *Triceratops* bonebed from the Hell Creek Formation, Garfield County, northeastern Montana. Geological Society of America Special Paper 503, 349–364 (2014).
137. J. F. McLaughlin, A. J. Ver Ploeg, "Geologic map of the Newcastle 30'x 60'quadrangle, Weston and Niobrara counties, Wyoming, and Pennington and Custer counties, South Dakota". Wyoming State Geological Survey Map Series 71 (2006).
138. R. M. Lynds, J. S. Slattery, "Correlation of the Upper Cretaceous strata of Wyoming". Wyoming State Geological Survey Open File Report 2017-3 (2017).
139. M. R. Voorhies, Taphonomy and population dynamics of an early Pliocene vertebrate fauna, Knox County, Nebraska. Contributions to Geology 1 (1969).
140. D. A. Eberth, R. R. Rogers, A. R. Fiorillo, "A practical approach to the study of bonebeds" in Bonebeds: Genesis, analysis, and paleobiological significance, R. R. Rogers, D. A. Eberth, A. R. Fiorillo, Eds. (University of Chicago Press, 2007), pp. 265–331.
141. E. E. McIver, The paleoenvironment of *Tyrannosaurus rex* from southwestern Saskatchewan, Canada. Canadian Journal of Earth Sciences 39, 207–221 (2002).

142. E. Dorf, Upper Cretaceous floras of the Rocky Mountain region: II Flora of the Lance Formation at its type locality, Niobrara County, Wyoming. Carnegie Institution of Washington Publication 508, 79–159 (1942).

3

Chapter 3. Stable isotope record of *Triceratops* from a mass accumulation (Lance Formation, Wyoming, USA) provides insights into *Triceratops* behaviour and ecology

Published as:
de Rooij, J., van der Lubbe, J. H., Verdegaal, S., Hulscher, M., Tooms, D., Kaskes, P., Verhage, O., Portanger, L., Schulp, A. S., 2022. Stable isotope record of *Triceratops* from a mass accumulation (Lance Formation, Wyoming, USA) provides insights into *Triceratops* behaviour and ecology. *Palaeogeography, Palaeoclimatology, Palaeoecology, 607, 111274.* DOI: https://doi.org/10.1016/j.palaeo.2022.111274

Abstract
Our understanding of Late Cretaceous dinosaur ecosystems from North America has considerably improved through stable isotope analyses on fossil bones and teeth. Oxygen and carbon stable isotopic compositions of structurally-bound carbonate in these fossil apatites are commonly used to infer variations of ingested water and food sources, which are in turn related to environmental and climatic conditions. Incremental isotopic records potentially provide insights into seasonality and migratory behaviour. So far, these reconstructions are based on vertebrate remains from spatiotemporally diverse datasets. Here, we present oxygen ($\delta^{18}O$) and carbon ($\delta^{13}C$) isotopic records from a large, spatially and temporally well-constrained, *Triceratops* bonebed from the Upper Maastrichtian Lance Formation (eastern Wyoming. USA). These isotopic compositions allow to elucidate the palaeoecology of these large herbivores and their ecosystem in detail, as well as their habitat use, diet and possible migration. The $\delta^{18}O$ signature from incrementally sampled *Triceratops* teeth reveal relatively low intra-tooth variation (average 1.3 ‰), comparable to contemporaneous dinosaur species as well as modern herbivorous mammals. Average $\delta^{13}C$ values (-5.4 ‰) are somewhat higher than for modern C3 plant grazers, and hint towards complex interactions during carbon uptake by non-avian herbivorous dinosaurs. Calculated $\delta^{18}O$ of drinking water (-14.8 ‰) combined with the local sedimentology of fine-grained siliciclastic deposits with high total organic and low carbonate contents strongly suggest a freshwater environment. Additionally, the combined average $\delta^{18}O$ and $\delta^{13}C$ *Triceratops* isotope signatures indicate a living environment intermediate between inland forests and coastal floodplains, expanding on earlier theories of ornithischian niche partitioning. Our robust dataset provides meaningful tests of habitat and palaeoecological hypotheses for *Triceratops*, and highlights the application of spatiotemporally well-constrained fossil remains.

3.1 Introduction
The iconic ceratopsian dinosaur *Triceratops* is known for its adorned skull and relatively large body size (Goodwin et al., 2006; Horner & Goodwin, 2006). While the *Triceratops* fossil record encompasses numerous well-preserved specimens, especially skulls of different ontogenetic age (Goodwin et al., 2006; Horner & Goodwin, 2006), little focus has been on behavioural and ecological topics including growth, feeding, gregariousness/herding and migration (Farke et al., 2009; Mathews et al., 2009; Erickson et al., 2015; Illies & Fowler, 2020). The discovery of a large well-constrained bonebed (Kaskes et al., 2016, 2019) preserving the remains of at least five *Triceratops* individuals of varying ontogenetic age (sensu Horner & Goodwin, 2006; Bastiaans et al., 2016) in Wyoming, USA, presents a unique

opportunity to elucidate ceratopsian palaeobiology and -ecology. Moreover, the bonebed is characterized by a relatively large proportion of postcranial material, while, in contrast, *Triceratops* finds are normally mainly restricted to the more robust cranial parts (Ryan et al., 2010; Brown et al., 2021). Associated fauna include lepisosteids and aquatic reptiles such as *Brachychampsa* and *Champsosaurus*.

Stable isotopes analyses of bioapatite tissues from modern ecosystems provide information on the behaviour, metabolism, and ecology of extant species (Layman et al., 2012; Hobson & Wassenaar, 2018). Similarly, stable isotopes in fossil bioapatite have improved our understanding of ancient ecosystems, where they provide important insights into the biology and ecology of the Late Cretaceous dinosaur fauna of North America (Stanton Thomas & Carlson, 2004; Fricke & Pearson, 2008; Fricke et al., 2009; Terrill et al., 2020; Burgener et al., 2021). These topics – ranging from ecosystem to individual scale – include niche partitioning and habitat preference (Stanton Thomas & Carlson, 2004; Fricke & Pearson, 2008; Fricke et al., 2009; Cullen et al., 2022), community and food web structure (Ostrom et al., 1993; Cullen et al., 2022), climate (Amiot et al., 2004; Straight et al., 2004), migration (Fricke et al., 2009; Terrill et al., 2020), provenance of fossil material (Dufour et al., 2007; Tütken et al., 2011), (ontogenetic) shifts in feeding habits (Frederickson et al., 2020) and body temperature and metabolism (Barrick 1998; Amiot et al., 2006; Eagle et al., 2011). Until now, stable isotope research on dinosaurs was heavily skewed towards theropods and hadrosaurs (Fricke & Rogers, 2000; Straight et al., 2004; Fricke et al., 2009; Goedert et al., 2016; Terrill et al., 2020) while many other taxa including ceratopsians have received relatively little attention.

Here, we present oxygen and carbon stable isotope analyses on the diverse fossil content of the so-called 'Darnell *Triceratops* Bonebed' (DTB). Isotope analysis of different bioapatite tissues (i.e., bone, dentine, enamel(oid)) among the different fossil taxa helps to evaluate the degree of (geochemical) preservation and isotopic integrity of the studied fossils. Furthermore, in order to explore the habitat preferences, migration and behaviour of *Triceratops,* we conduct histological and stable isotope analyses of accretionary growth trajectories in enamel of multiple teeth to provide constraints on intra- and interannual variability in diet and local hydroclimatic conditions. This new isotopic dataset further allows for direct comparison and integration with other coeval stable isotope datasets, ultimately contributing to a more detailed understanding of Late Cretaceous dinosaur ecosystems of North America. Furthermore, sedimentological analysis of the DTB has been carried out to better constrain its depositional setting and taphonomy.

3.2 Background

3.2.1 Geological background

The DTB is a monospecific multi-generational mass death assemblage discovered in western Wyoming, USA on the south-eastern flank of the Powder River Basin (43°36'26.1"N, 104°23'29.3"W; Kaskes et al., 2016). The bonebed is part of the Upper Maastrichtian terrestrial Lance Formation (Bartos et al., 2021) and is dated at ~67 Ma, based on its stratigraphic proximity to the underlying Fox Hills Formation. Five *Triceratops* individuals are identified as *Triceratops horridus* based on the recovered diagnostic cranial elements (Bastiaans et al., 2016) and relatively lower stratigraphic position in the Lance Formation (Longrich & Field, 2012; Scannella et al., 2014).

3.2.2 Oxygen and carbon stable isotopes in (palaeo-)environmental reconstructions

Biogenic apatite ($Ca_{10}(PO_4)_6(OH)_2$) contains small amounts (< 10%) of structurally-bound carbonate (CO_3^{2-}) from which the carbon and oxygen isotope ratio can be analysed. The oxygen and carbon isotope values (expressed in $\delta^{13}C$ and $\delta^{18}O$ relative to reference standard) of the body pool from which the bioapatite carbonate is precipitated reflects that of the ingested food and water (Cerling & Harris, 1999).

Most of the ingested oxygen (and $\delta^{18}O$) in herbivores is incorporated as free drinking (surface) and/or plant water, which are representatives of local precipitation values (Kohn et al., 1996). The $\delta^{18}O$ value in precipitation is dependent on geographical and climatic factors including air temperature, latitude, altitude, storage in ice sheets as well as the precipitation amount effect (Dansgaard, 1964; Koch, 1998). Precipitation has a relatively low $\delta^{18}O$ signature with increasing latitude and altitude due to the preferential loss of ^{18}O over ^{16}O. Evaporation of surface water and evapotranspiration via plant leaf stomata facilitate the removal of the lighter ^{16}O over the heavier ^{18}O, generating a relative enrichment in ^{18}O relative to the initial rainfall (Barbour 2007). Foraging herbivores hold a unique $\delta^{18}O$ signal as a function of this ingested plant and drinking water, which is further metabolically modified (e.g., homeothermic vs. poikilothermic) by transpiration and body temperature (Pecquerie et al., 2010; Vander Zanden et al., 2015; Rey et al., 2017) as well as habitat use (Amiot et al., 2006; Amiot et al., 2010). The sum of these factors results in a specific $\delta^{18}O$ signal recorded in the bioapatite of a (fossil) animal (i.e., bone, dentine, enamel(oid)) and reflects the climatic conditions of that time interval (Kohn & Cerling, 2002; Fricke & Pearson, 2008).

The carbon isotope ratio ($\delta^{13}C$) stored in vertebrate hard tissues is incorporated from ingested plant material during feeding (Passey et al., 2005). The biochemical pathways of plants involved in the fixation of atmospheric CO_2 during photosynthesis cause a preferential uptake of ^{12}C over ^{13}C. Plants may employ different biochemical pathways to fixate CO_2 during photosynthesis, but temperate C3 plants are most common (Taiz et al., 2015) (C4 plants date back to only 34-24 Ma (Sage, 2004)). Fixation of atmospheric CO_2 by C3 plants result in an offset of on average -19.5 ‰ (Smith & Epstein, 1971; Kohn & Cerling, 2002; Kohn, 2010) with atmospheric $\delta^{13}C$ of -6.5 ‰ (pre-industrial) (Graven et al., 2020). Typical C3 modern plant organic matter thus shows an average $\delta^{13}C$ of -26 ± 2.3 ‰, but covers a wider range of -35 ‰ to -22 ‰ $\delta^{13}C$ (Kohn 2010). This atmospheric carbon fixation may thus further vary depending on the environmental conditions including, but not limited to, air temperature, water or nutrient availability and light intensity (Tieszen, 1991). The isotopic offset between the plant diet and tooth enamel for herbivorous mammals shows an average of 14.1 ± 0.5 ‰ (Cerling & Harris, 1999), but this tropic enrichment factor may show a wider range extending beyond 10 ‰ to 15 ‰ based on interspecific physiological and metabolic differences as well as body size differences (Passey et al., 2005; Tejada-Lara et al., 2018; Rey et al., 2020). On average, this offset between the plant carbon composition and tooth enamel in C3 grazers results in a $\delta^{13}C$ of ~ -12 ‰ for modern mammals. However, the actual offsets within mammal enamel range from -20 ‰ to -4 ‰ depending on the aforementioned animal and plant physiology as well as environmental and climatic factors (Cerling et al., 1997). Ultimately, the preserved carbon isotopes in (fossil) bioapatite provide insights into the animal's feeding habits and shed light on their (palaeo)environment.

3.2.3 Stable isotopes in bioapatite

Preservation of the primary $\delta^{13}C$ and $\delta^{18}O$ signal inside the crystal lattice of bioapatitic tissues strongly varies among each tissue type. For example, bones possess relatively high amounts of organic collagen (~30 %) and miniscule apatite crystals that provide increased surface areas for *in vivo* and post-mortem

isotopic exchange during recrystallisation and/or incorporation of secondary carbonates (Glimcher, 2006; Schwarcz, 2015; Kendall et al., 2018). Additionally, *in vivo* dynamics of bone growth during the development and remodelling of the vertebrate skeleton (de Buffrénil et al., 2021) leads to averaging of the $\delta^{13}C$ and $\delta^{18}O$ over the animal's lifespan. The crystal lattice of tooth dentine possesses comparably sized small apatite crystals but contains significantly less pore spaces and organic collagen. Conversely, tooth enamel and the equivalent ganoine of lepisosteid scales both consist of larger and stable apatite crystals (< 3% organic collagen), providing relatively less surface area for isotopic exchange, allowing enamel and ganoine to better retain the primary isotope signature during/after diagenesis (Trueman et al., 2003; Fricke et al., 2008). Comparison of isotope values in different tissue types allows to evaluate the extent of the geochemical alteration of the original isotope signatures. Paired values of enamel and dentine in individual teeth as well as bioapatitic tissues from various sympatric animals occupying distinct habitats may identify diagenetic overprinting across a single locality (Stanton Thomas & Carlson, 2004; Wang et al., 2008; Terrill et al., 2020).

3.2.4 Sclerochronology

Growth dynamics of various bioapatites follow an accretionary time-related succession (Horner et al., 2000; Tütken et al., 2004; Garcia, 2011; Woodward et al., 2014) such that growth lines are deposited annually in compact bone (Waskow & Sander, 2014; Erickson et al., 2017), whereas dentine and enamel growth lines (lines of von Ebner and Retzius, respectively) are laid down daily (Erickson, 1996; Fitzgerald, 1998; Smith, 2006; Tafforeau et al., 2007). Temporal growth trajectories in bone and dental tissues have extensively been studied (Carlson, 1990; Hwang, 2005; O'Meara et al., 2018) and used to reconstruct the growth and estimate the age of (fossil) vertebrates (Erickson, 1996; Waskow & Sander, 2014; Erickson et al., 2017). Despite ceratopsian dinosaurs having poorly developed lines of Retzius (Sander, 1999), it is reasonable to assume that *Triceratops* showed a similar tooth growth pattern as seen in many other vertebrates and a sequence along the length of the enamel surface thus represents a temporal series (Line, 2000).

3.3 Material and methods

3.3.1 Material for palaeoecological analysis

The DTB yielded fossil tooth material of varying degrees of preservation including 63 disarticulated *Triceratops* teeth, seven *Champsosaurus* teeth and eight lepisosteid scales. The *Champsosaurus* teeth were identified as such based on the presence of a clear carina on the anterior and posterior side (Njau & Blumenschine, 2006) and the presence of diagnostic post-cranial *Champsosaurus* material. Selection of teeth for analysis was made based on the preservation: only elements with intact enamel/ganoine surfaces preserved in sufficient detail to allow for an unambiguous identification were selected for isotope sampling. Based on these criteria, a total of fifteen disarticulated *Triceratops* teeth, three aquatic reptile teeth and six lepisosteid scales were used to explore the isotope profile of the DTB ecosystem. In addition, cortical and cancellous bone of two fossil bone fragments were sampled to map the isotope variation in different apatitic tissues. *Champsosaurus* and lepisosteids are representatives of the local fauna that characterized this locality and their isotope signatures inform on the overall palaeoecology of this assemblage.

3.3.2 Tooth microscopy

In addition, one fully intact *Triceratops* tooth (RGM.1333602) was transversely sectioned to further evaluate the preservation of the studied material. Thin-sectioning was performed following standard procedure by mounting on a glass plate and grinding until the desired thickness for optical microscopy was reached. The thin-section was studied to check for any (taphonomic) damage such as infill of fractures and cavities overprinting the original enamel and dentine part, and photographed using a Nikon Eclipse 50i POL Polarizing Microscope.

3.3.3 Isotopic signal of the Darnell *Triceratops* Bonebed

Prior to sampling, the material was cleaned with acetone to remove any possible traces of finger grease, glue residue and other exogenous material. The *Triceratops* teeth were sampled with a diamond-tipped drill bit (1.6 mm diameter) mounted on a Proxxon Micromot hand-held drill. All fourteen *Triceratops* teeth were sampled for their enamel and dentine content. A total of seven teeth preserving a complete crown were used for serial sampling. All serial-sampled teeth belong to adult individuals based on size. However, the sample selection is represented by unworn and worn teeth, providing a transect in tooth size and difference in sample area for each individual tooth (see Supplements Figure S3 for overview). Serial samples were taken along the growth axis of each, resulting in three samples for the smallest tooth and eight samples for the largest tooth. The other remaining seven teeth were too small or too fragmented for serial sampling and are represented only by one single sample. These samples were acquired only from areas with intact enamel. The thin-sectioned tooth provided guidance on the ideal drilling depth based on the enamel thickness and state of preservation (Figure 3), and the enamel was clearly delineated from the dentine based on colour and density. Single samples of the *Champsosaurus* teeth and the lepisosteid scales were acquired using the same method, but their small sizes did not permit serial sampling. Fossil bone samples were also retrieved in singles and are represented by cortical and medullary bone. Powdered samples were collected on weighing paper and transferred into 2.5 ml Eppendorf centrifuge tubes. Prior to sampling, the drill bit was blasted with nitrogen gas to remove possible adhering sample powder. Each collected powder sample was ~0.7 mg.

A selection of samples was leached according to the protocol described in Koch et al. (1997). It has been shown that different pretreatment strategies may cause a shift in isotopic data due to removal of exogenous (i.e., diagenetic) material from (dental) bioapatite such as enamel and dentine (Lee-Thorp & van der Merwe, 1987, 1991; Krueger, 1991; Wang & Cerling, 1994; Koch et al., 1997). Bioapatite powder samples of three *Triceratops* teeth, a *Triceratops* bone fragment, two *Champsosaurus* teeth and three lepisosteid scales retrieved during sampling were split to explore the impact of different pretreatment protocols (Figure 1). Selected samples were either first soaked overnight in sodium hypochlorite (NaOCl) for oxidation or left untreated. Both groups were then rinsed three times with MilliQ water, and soaked overnight in either 0.1 M acetic acid or 1 M acetic acid buffered with calcium acetate creating additional aliquots (Koch et al., 1997). Finally, all groups were rinsed three times again with MilliQ water and dried at 60 °C. Proportions were kept constant between apatite sample powder and fluids during leaching and oxidation (0.04 ml/mg) to avoid imbalanced reactions (Koch et al., 1997). The samples were left for 24 h to react overnight.

After drying, isotope samples were transferred to exetainer vials with pierceable endcaps and flushed with pure helium and subsequently digested through a Thermo Scientific Gasbench II in 100 % water-free phosphoric acid. The formed CO_2 from the structural carbonate part was then analysed for their carbon and oxygen isotope signature by a Finnigan MAT253 Isotope Ratio Mass Spectrometer

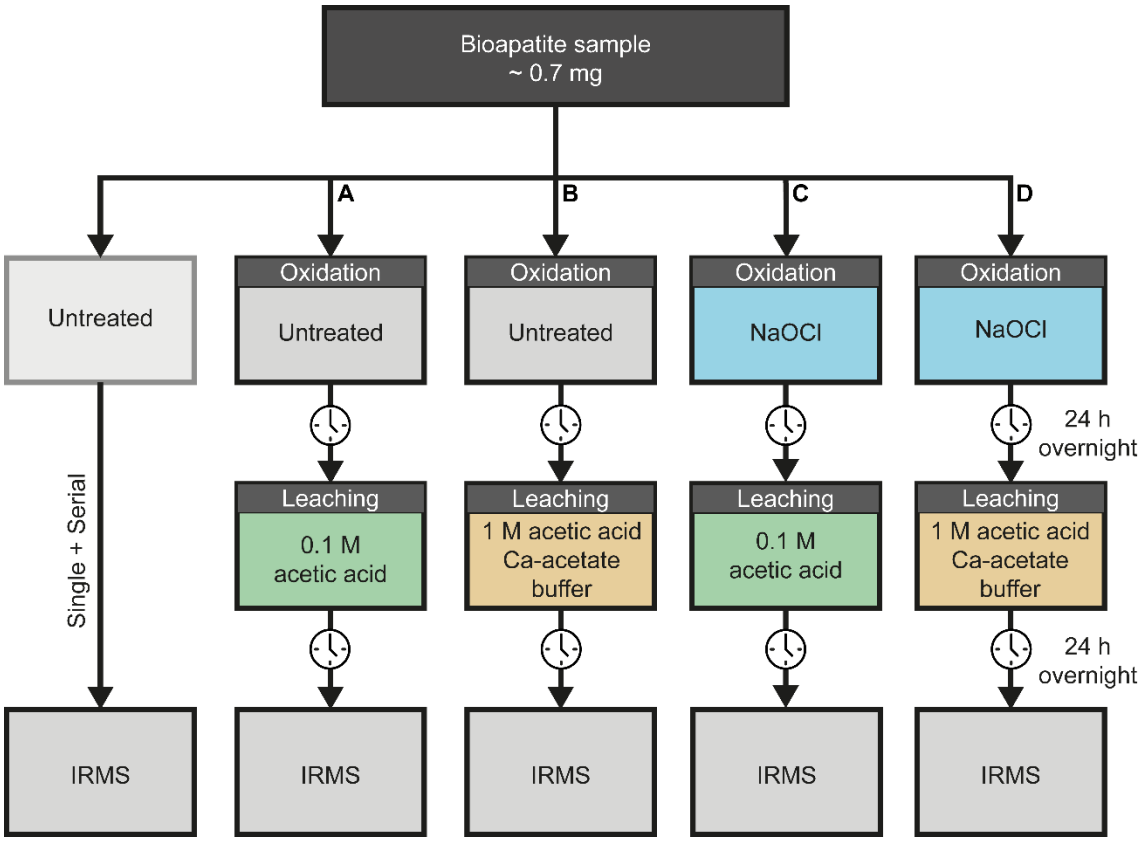

Figure 1. Overview of the four different pretreatment protocols applied to the bioapatite samples. Treatments were applied as a combination of different oxidation and leaching steps.

(IRMS) housed at the Earth Sciences Stable Isotope Laboratory at the Faculty of Science at the Vrije Universiteit (VU) in Amsterdam, the Netherlands. Different amounts of the VU Internal Carbonate Standard (VICS) have been analysed in each run for correction of the so-called sample amount effect. In each run, the IAEA-603 standard (2.49 ± 0.07 ‰ for $\delta^{13}C$ and -2.40 ± 0.07 ‰ for $\delta^{18}O$ (1σ, n = 17)) was routinely analysed as an independent control standard with internationally accepted $\delta^{13}C$ and $\delta^{18}O$ values of 2.46 ± 0.01 ‰ and -2.37 ± 0.04 ‰, respectively (Assonov et al., 2020). The inter-laboratorial apatite standard Ag-lox is also analysed in each run providing mean $\delta^{13}C$ and $\delta^{18}O$ values of -11.62 ± 0.07 ‰ and -0.94 ± 0.22 ‰ (n = 11), respectively, in agreement with the long-term means of -11.62 ‰ and -0.99 ‰ at 45°C (n = 95, VU). In contrast to the $\delta^{13}C$ values, ~0.5 ‰ lower $\delta^{18}O$ values were obtained at 70 °C (Vonhof et al., 2020), which can be attributed to the temperature-dependent fractionation factor between the generated CO_2 and structurally-bound carbonate in apatite during acid digestions that may slightly differ from that of the standards that were used for the linearity corrections (LSVEC and BCT for $\delta^{13}C$, and NBS-18 and BCT for $\delta^{18}O$ (Kim et al., 2015)). Its long-term precision of the apatite standard measurements was determined <0.1 ‰ for $\delta^{13}C$ and <0.2 ‰ for $\delta^{18}O$. The isotopic compositions were initially expressed in standard notation relative to the international standard Vienna Pee Dee Belemnite (VPDB). Hereafter, the $\delta^{18}O$ values were converted to Vienna Standard Mean Ocean Water (VSMOW) according to Coplen (1988; p. 295, formula [11]) allowing for comparison with previous studies on Late Cretaceous $\delta^{18}O$ datasets. In order to estimate the $\delta^{18}O$ of the local (drinking) water ($\delta^{18}O_w$) from the *Triceratops* enamel structural carbonate ($\delta^{18}O_{sc}$), we applied the formula established for large, water-dependent herbivores by Hoppe et al., (2006) (see section 6.2 for details):

Mean $\delta^{18}O_{sc}$ = 30.32(±1.23) + (0.73(±0.10) * Mean $\delta^{18}O_{w}$) [1]

3.3.4 Diagenetic screening

To evaluate the chemical preservation of the *Triceratops* material and extent of specific leaching effects, remaining subsets of untreated and leached powder samples from the DTB were analysed for their calcium/phosphorous (Ca/P) ratios using scanning electron microscopy (SEM) with Energy Dispersive X-Ray Spectroscopy (EDS) at the VU (see Supplementary Raw Data for sample details). Approximately 0.7 mg of sample powder of each bioapatite tissue type (enamel, dentine and bone) covering three treatment strategies (untreated, 0.1 M acetic acid and 1 M calcium acetate buffer) were applied on a carbon sticker and analysed in vacuum by a JEOL JCM-600 SEM. Additionally, *Triceratops* tooth fragments and the open thick section (Figure 3) were analysed for their elemental composition. Modern human tooth fragments were analysed to provide a modern baseline for bioapatite. Each *Triceratops* sample was measured six times and the average was used for data interpretation. The Ca/P ratio is known to shift during diagenesis of the original bioapatite (Herwartz et al., 2011; Tütken et al., 2011; Herwartz et al., 2012; Trueman, 2013),and comparing the Ca/P of fossil bioapatite to modern bioapatite therefore provides information on the degree of diagenetic alterations.

In addition, Fourier-transform infrared spectroscopy (FTIR) was performed using the KBr-pellet method to better constrain mineralogical changes due to fossilisation and leaching strategies applied here. Like for Ca/P ratios, FTIR analyses were applied to all three bioapatite tissues and pretreatment strategies using material from the DTB. Approximately 7 mg of sample powder was mixed and ground with oven-dried KBr powder in a 1:100 ratio (1%) using an agate mortar and pestle. The resulted powder mix was then pressed into a ~3 mm pellet at 10 ton pressure using a hydraulic press. Pellets were transferred into a holder and measured in a Nicolet 6700 FTIR analyser housed at Utrecht University, Faculty of Geosciences, the Netherlands. The acquired spectra were created and analysed using OMNIC software. Each sample mixture yielded three pellets that were measured and their average spectrum was used as end results. Each new sample was standardized using its own 100% KBr pellet background. Spectra were used to calculate the carbonate:phosphate (C/P) ratios and the infrared splitting factors (IR-SF; i.e., crystallinity index). C/P ratios were quantified by dividing the carbonate absorbance peak at 1415 cm^{-1} and the phosphate absorbance peak at 1035 cm^{-1} (Wright & Schwarcz, 1996). The IR-SF values were obtained by adding the two phosphate absorbance peaks at 605 cm^{-1} and 565 cm^{-1} and dividing by the lowest value between those peaks at 590 cm^{-1} (Weiner & Bar-Yosef, 1990).

3.3.5 Sedimentological analysis

Geological fieldwork and excavations at the DTB by Naturalis Biodiversity Center (2015-2019) included detailed lithostratigraphic analysis of the bone-bearing layer (Figure 2). Sedimentary successions bounding the DTB were sampled at 10 cm resolution to analyse lithogenic grain-size properties, organic and carbonate contents of the sediments (n = 7) with the aim to better understand the palaeoenvironmental and depositional conditions.

Grain size analyses were conducted at the Sediment Laboratory of the Vrije Universiteit (VU) Amsterdam using a Sympatec HELOS KR laser-diffraction particle size analyser. Prior to the grain size analysis, the bulk sediment samples were pretreated to isolate the lithogenic fraction following the procedure by Konert & Vandenberghe (1997). Organic matter and carbonate material was removed by treating the samples with 5 - 10 ml of 30% H_2O_2 and 5 - 10 ml of 10% HCl, respectively.

Total organic and carbonate contents were measured through thermogravimetric analysis using a thermogravimetric analyser (LECO TGA 701) instrument at the Sediment Laboratory of the VU. Sediment samples were carefully grinded with mortar and pestle into a homogeneous powder. Approximately 1-2 g per sample powder was analysed by sequential loss-on-ignition using step-wise heating from 25 to 1000 °C until the sample weights stabilized. The associated weight loss per temperature step is used to determine the total organic content (i.e., at max 550 °C; LOI550) and calcium carbonate content (i.e., at max 1000 °C; LOI1000) within the bulk sediment. All of the used data can be found in the Supplementary Data.

3.4 Results

3.4.1 Sedimentological setting

The ~1.1 m thick stratigraphic section exposed at the DTB comprises an alternation of mudstone, fine-grained sandstone, and siltstone with an average organic and carbonate content of 3.2 wt% and 2.4 wt%, respectively. The section can be divided in three distinct sedimentary units (Figure 2B,C). The basal unit of the DTB (~70 cm) yields the remains of at least five *Triceratops* individuals and is dominated by a purple-grey mudstone with a relatively high organic content (up to 4.6 wt%) due to abundant plant remains. The second unit of the DTB consists of a thin (10-20 cm thick) layer of a yellowish, very fine sandstone. The base of this unit is marked by an erosional contact with convolute lamination and siltstone flame structures (Figure 2B). The third stratum (~20 cm) is dominated by a brown sandy siltstone unit with sandy lenses and plant remains. The $CaCO_3$ content is on average low (2.4 wt%) with maximum values of 3.6 wt% and 4.2 wt% in the sandstone layer.

3.4.2 Tooth microstructure

Visual inspection of the tooth thin-section indicates that the dental material is relatively well-preserved, as all of the histological features seem to remain unchanged (Figure 3). The enamel is clearly visible as a transparent band varying from 0.1 to 0.3 mm on the buccal side and a similar, but thinner band on the lingual side. The enamel thickness is in line with previously established enamel thickness for ceratopsids and *Triceratops* in particular (Sander, 1999; Hwang, 2005) confirming that our sampling approach aiming at the enamel separate from the dentine is feasible. The dentine displays incremental lines of Von Ebner (Von Ebner, 1902), but their visibility and quantity varied throughout the section. At the highest, a total of 91 incremental growth lines are counted (Figure 3), indicating that the sclerochronological record preserved in the tooth covers some three months (Erickson, 1996; Fitzgerald, 1998; Smith, 2006; Tafforeau et al., 2007). Some areas display small localized fractures, but the overall preservation of dental features suggests that most of the apatite tissues did not undergo major post-mortem alteration.

3.4.3 Effects of pretreatment

The pretreatment procedures showed significant effects among the different apatitic tissue samples, but do not display unidirectional offsets between treated and untreated samples for the different leaching procedures (Figure 4). Pretreatment of *Triceratops* enamel resulted in significantly higher $\delta^{18}O$ values than untreated enamel ($p = 0.00$), while $\delta^{13}C$ seemed unaffected ($p = 0.17$). For *Triceratops* dentine, the effects of the pretreatment result in both higher $\delta^{18}O$ and $\delta^{13}C$ values ($p = 0.00$ for both). *Triceratops* bone did not show a shift in $\delta^{18}O$ after leaching ($p = 0.92$), but had significantly increased

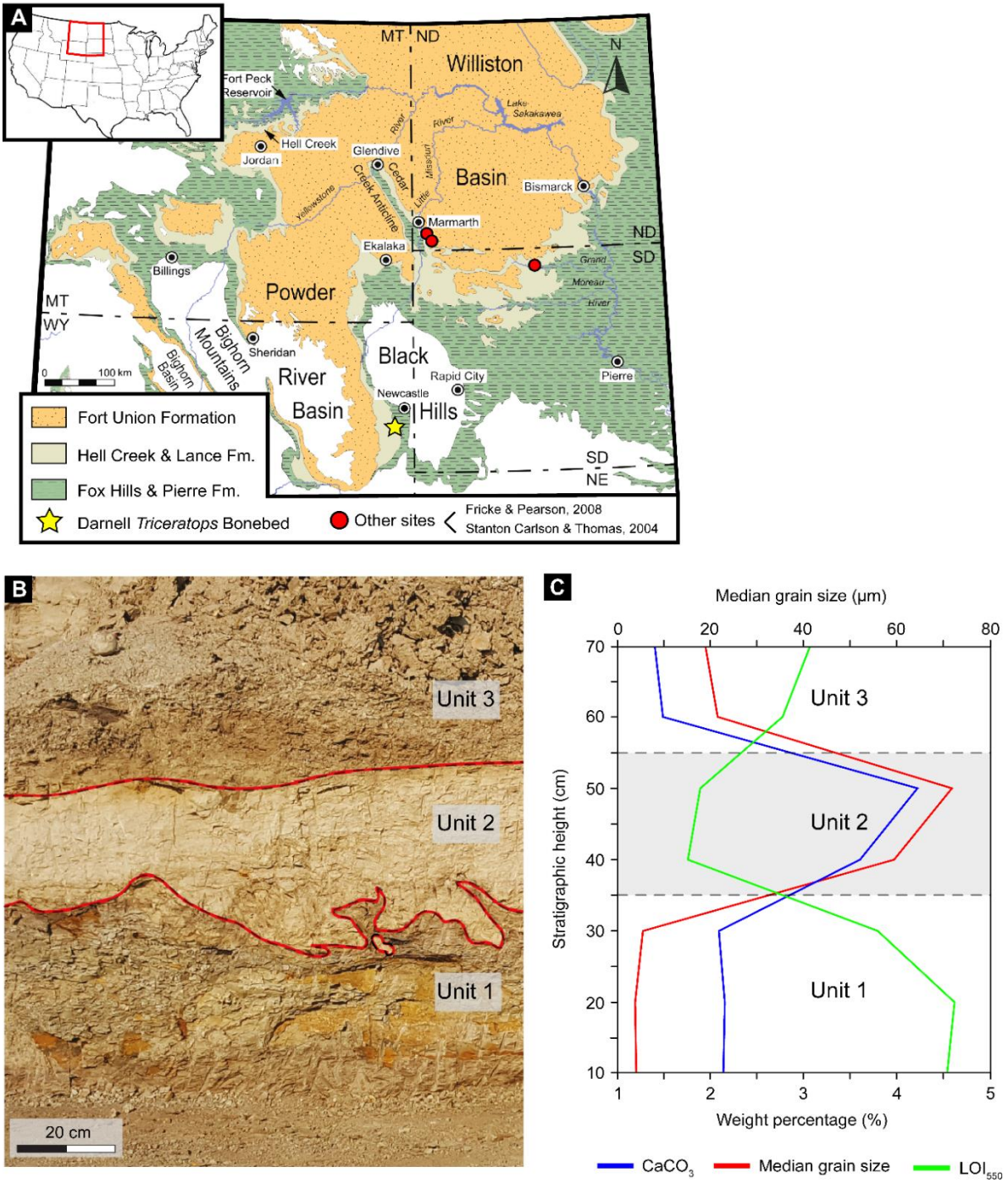

Figure 2. Geography, sedimentology and lithostratigraphy of the sedimentary succession bordering the DTB. A. Geological map of the Williston Basin and Powder River Basin in Wyoming, Montana, South Dakota and North Dakota, displaying the distribution of Upper Cretaceous to Paleocene rock formations (modified from Johnson et al., 2002; Fastovsky & Bercovici, 2016). The Darnell *Triceratops* Bonebed, located in the Lance Formation ~30 km south of Newcastle, is highlighted with a yellow star. Also depicted here are vertebrate sites from the Hell Creek Formation of North Dakota (Fricke & Pearson, 2008) and South Dakota (Stanton Thomas & Carlson, 2008), which datasets are used in this isotopic study as a comparison in Figure 12. B. Field photo depicting the sedimentary succession representing the bonebed layer. C. Total organic content (LOI550, in wt%), median lithogenic grain size (in µm) and carbonate content ($CaCO_3$, in wt%) of the sedimentary succession. Data (C) is plotted against stratigraphic height, and are correlated with the stratigraphy in the field photo (B). Note the marked increase in grain size in the crevasse splay deposit (Unit 2), which is bounded by the red line.

$\delta^{13}C$ values (p = 0.04). Bone is the least affected by pretreatments while dentine shows the strongest shifts between strategies. Strikingly, dentine δ-values became more positive after treatment, diverting from enamel δ-values. This contradicts the assumption that removal of labile material would produce a signal more resembling the enamel δ-values, which are assumed less prone to diagenesis. Treatment of *Champsosaurus* enamel shifted the $\delta^{18}O$ values (p = 0.05), but the $\delta^{13}C$ values did not show a significant change (p = 0.06). *Champsosaurus* dentine $\delta^{18}O$ and $\delta^{13}C$ values on the other hand both increased after the leaching treatment (p = 0.00 and p = 0.04, respectively). Similarly, lepisosteid ganoine $\delta^{18}O$ and $\delta^{13}C$ values were significantly higher for the treated samples (p = 0.01 and p = 0.00, respectively). The data on the sample treatment do not give unanimous results regarding the possible effects of diagenesis on the different tissues and taxa.

Similar trends are observed in the Ca/P ratios of dinosaur bioapatite, which overlap with known modern bioapatite values of ~2.3 (Balter, 2001; Hassler et al., 2018). Moreover, average measured Ca/P ratios of untreated and leached tooth bioapatite overlap with each other and with modern human enamel, and fail to detect any significant differences in the dataset (Figure 5 & Table 1; Kruskal-Wallis test, p = 0.051). Only *Triceratops* bone showed larger spread in their Ca/P ratios, but dentine and enamel closely overlap for each treatment strategy. Additionally, the FTIR analyses provided ambiguous results regarding the effects of the sample pretreatments (Table 1.). Modern bone values are commonly measured at C/P ratio of 0.23 – 0.34 (Wright & Schwarcz, 1996; Nielsen-Marsh & Hedges, 2000; Garvie-Lok et al., 2004; Beasley et al., 2014) and an IR-SF of 2.50 – 3.25 (Berna et al., 2004; Thompson et al., 2009; Beasley et al., 2014). While treated *Triceratops* enamel bioapatite show C/P and IR-SF values more akin to modern bone values, both enamel leached by 0.1 M acetic acid and leached by 1 M calcium buffer fail to fall within modern ranges (Table 1). In fact, leaching with 1 M calcium buffer increased the C/P and IR-SF values far beyond modern ranges. Interestingly, dentine bioapatite shows steady IR-SF values throughout the three treatment strategies. C/P values vary slightly more, but all treatment strategies overshoot modern values. Contradicting to accepted theory on diagenesis, untreated bone seems best preserved, with values most akin to modern values for both C/P ratios and IR-SF data. Both leaching strategies result in greatly increased C/P ratios and IR-SF values, but the change is largest for treatment with 0.1 M acetic acid. Overall, the pretreatment strategies discussed here show no consistent pattern in shifts in C/P and IR-SF data across different bioapatite tissues, and the FTIR spectra indicate only slight diagenetic alteration of *Triceratops* enamel (Figure 6).

While leaching pretreatments could provide more accurate isotope data, it has been found that oxidation and leaching can also have adverse effects (Koch et al., 1997; Lee-Thorp, 2002; Pellegrini et al., 2011; Snoeck & Pellegrini, 2015; Pellegrini & Snoeck, 2016). The samples were left for 24 h to react, which might have induced adverse effects, in particularly $NaOCl_4$ which could promote the (re-)precipitation of secondary carbonate that is equilibrated with atmospheric CO_2 (Zazzo et al., 2004; Snoeck & Pellegrini, 2015; Pellegrini & Snoeck, 2016). On the other hand, it is expected that these secondary carbonates are dissolved during the subsequent leaching step. The non-systematic isotopic responses of the various apatite tissues indicate that not simply labile carbonates and eventual organic matter were stripped, but that complex reactions may have taken place during different pretreatment procedures, doing potentially more harm than good. Furthermore, the sediment matrix of the bonebed is virtually free of $CaCO_3$ (Figure 2), considerably reducing the chance of precipitation of secondary carbonates and isotopic overprint. Considering the overall ambiguous result and nonconformity across the pretreatment data, the Ca/P calculations and the FTIR data, we chose to focus on the untreated data only for the remainder of this paper to represent the bonebed (c.f., Janssen et al., 2016) (see Discussion for more details).

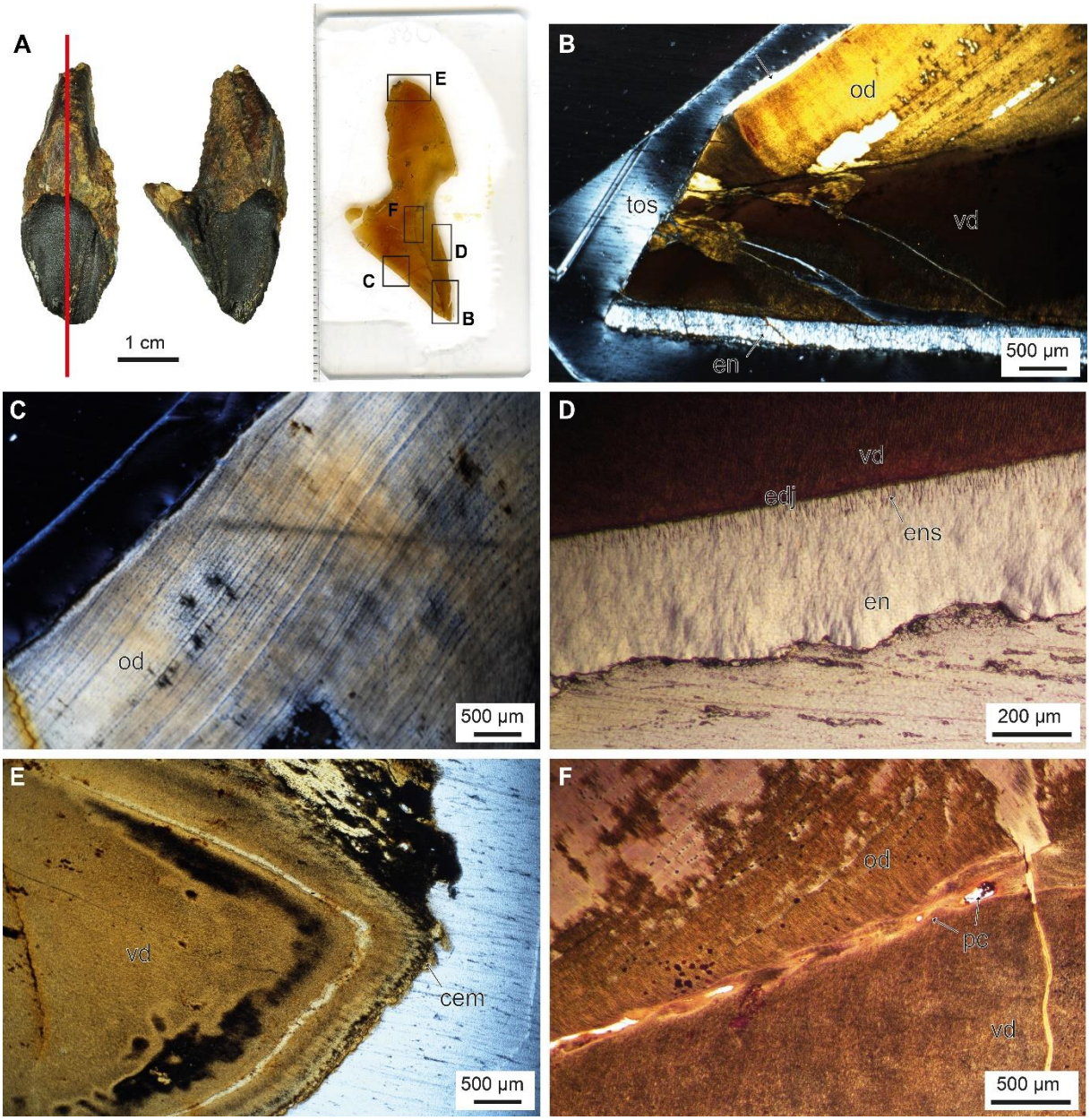

Figure 3. Histology of an adult *Triceratops* tooth. A. Intact *Triceratops* tooth (RGM. 1333602) showing plane of section (red line) and thin-section. B. Tooth apex under cross-polarized light. C. Orthodentine containing Von Ebner lines. D. Closeup of enamel showing enamel spindles protruding from the enamel-dentine junction. E. Tooth root apex with cementum. F. Dentine matrix with pulp cavity. cem, cementum; edj, enamel-dentine junction; en, enamel; ens, enamel spindles; od, orthodentine; pc, pulp cavity; vd, vasodentine.

3.4.4 Isotope systematics amongst different bioapatite tissues

Figure 7 displays the isotope signatures of the different bioapatitic tissues amongst different taxa on all isotopic datasets. Detailed statistical analyses and data exploration are provided in the Supplements (Table S1-S4, Figure S1 & S2). A non-parametric Kruskal-Wallis test with Bonferroni correction did not return a significant difference ($p = 0.15$) between the lower mean $\delta^{18}O$ values of *Triceratops* enamel (19.4 ‰) and the higher *Triceratops* dentine (20.0 ‰, $p = 0.23$). For carbon, the mean *Triceratops* dentine $\delta^{13}C$ values (0.14 ‰) were significantly higher ($p = 0.00$) than those of *Triceratops* enamel (-5.4 ‰). *Triceratops* bone $\delta^{13}C$ values (-3.4 ‰) are significantly lower than those of dentine ($p = 0.00$)

and are markedly higher than mean enamel values (p = 0.02). However, the mean *Triceratops* bone $\delta^{18}O$ value (19.8 ‰) do not seem to differ from enamel and dentine $\delta^{18}O$ (p = 0.26 and p = 1, respectively). Isotopic offsets between bioapatitic tissues are more pronounced in the $\delta^{13}C$ values than $\delta^{18}O$ values. This is further emphasized by the applied paired Kruskal-Wallis test, where mean $\delta^{18}O$ values between apatite groups fall outside the range of significance (p = 0.15) while $\delta^{13}C$ values still show strong significant differences among all apatitic tissue groups (p = 0.00).

Plotting the enamel and dentine isotopic values of the same tooth reveals a similar pattern (Figure 10). For $\delta^{18}O$, differences in enamel and dentine within individual teeth ($\Delta\delta^{18}O_{e\text{-}d}$) were significantly lower than observed for $\delta^{13}C$ ($\Delta\delta^{13}C_{e\text{-}d}$). There is no systematic pattern in the degree of isotopic offset among all the sampled teeth for $\delta^{13}C$ or $\delta^{18}O$ values. However, a general trend is visible within individual teeth showing similar relative changes in $\Delta\delta^{18}O_{e\text{-}d}$ and $\Delta\delta^{13}C_{e\text{-}d}$. In other words, teeth with relatively lower $\Delta\delta^{18}O_{e\text{-}d}$ also show lower $\Delta\delta^{13}C_{e\text{-}d}$. Nevertheless, the preserved isotope systematics are in line with the assumed susceptibility to chemical alteration of fossil bioapatite, where lower δ-values from enamel bioapatite resemble the original signal incorporated into the structurally-bound carbonate during metabolic fractionation. In contrast to enamel, dentine and bone bioapatite values become more positive and average out post-mortem, resulting in an isotope signature more akin to

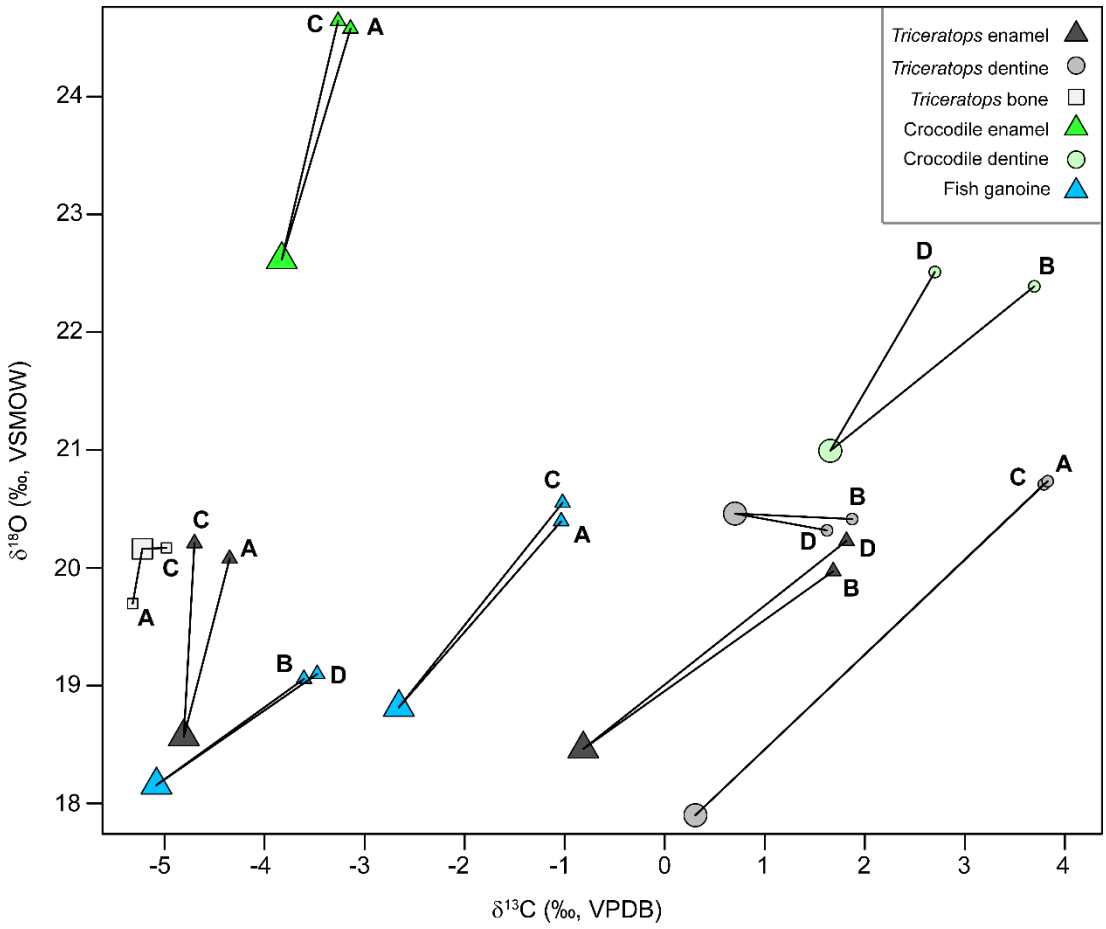

Figure 4. Crossplot showing the effects of the different pretreatment groups across different bioapatite tissues and taxa. The large symbols represent the $\delta^{18}O$ and $\delta^{13}C$ of the untreated bulk data. The connecting smaller symbols associated with the letter 'A', 'B', 'C', or 'D' represent $\delta^{18}O$ and $\delta^{13}C$ values of the same samples but treated by four different combinations of oxidation and leaching steps: A) leached with 0.1 M acetic acid, B) leached with 1 M calcium buffer, C) NaOCl oxidation and leached with 0.1 M acetic acid and D) NaOCl oxidation and leached with 1 M calcium buffer.

the depositional environment (Tütken et al., 2011). This is further emphasized by the larger spread in enamel data ($\delta^{13}C$: 10.8 ‰ and $\delta^{18}O$: 6.5 ‰, n = 60) and the more restricted dentine data ($\delta^{13}C$: 7.5 ‰ and $\delta^{18}O$: 3.1 ‰, n = 21) (Figure 7, 8 and 9). On the other hand, *Champsosaurus* enamel did not significantly differ from *Champsosaurus* dentine for both $\delta^{13}C$ (p = 0.11) and $\delta^{18}O$ (p = 1). This could most likely be attributed to low sample sizes (n = 3 and n = 4), and we do obtain δ-values that overlap those of *Triceratops*. However, rarefying our *Triceratops* enamel $\delta^{13}C$ and $\delta^{18}O$ data (see Supplements Figure S2; recalculating variances based on 1000 random samples of n=5) reveals a markedly lower variance than the original dataset, suggesting unequal variance among taxa, and thus further supports the use of non-parametric Kruskal-Wallis tests.

3.4.5 Oxygen isotopes

Overall, across all sampled material, *Triceratops* enamel $\delta^{18}O$ values (mean 19.4 ‰) show a total range of 6.5 ‰. Dentine $\delta^{18}O$ values of *Triceratops* (mean 20 ‰) have a slightly smaller range of 3.1 ‰ (Figure 8). The three available values for *Champsosaurus* enamel $\delta^{18}O$ (mean 20.5 ‰) show a wider spread of 4.0 ‰, but largely overlap the $\delta^{18}O$ of *Triceratops* enamel. *Champsosaurus* dentine (mean 20.1 ‰) shows a smaller range of 2.8 ‰. The ganoine of lepisosteid scales (mean 18.5 ‰) span a total range of 4.1 ‰ in $\delta^{18}O$ values, but also are within range of both *Triceratops* and *Champsosaurus* enamel $\delta^{18}O$. Non-parametric Kruskal-Wallis test with Bonferroni correction on the enamel/ganoine $\delta^{18}O$ across the three taxa did not return any significant differences (p = 0.19) (Table S4).

The incrementally sampled teeth show extensive overlap in their $\delta^{18}O$ signatures (Figure 11), except for one sample that yields a markedly lower $\delta^{18}O$ value of 15.3 ‰ (RGM.1333595). Variability of $\delta^{18}O$ within the individual teeth for *Triceratops* enamel ranges from 0.4 ‰ to 4.8 ‰, with the majority having intra-tooth variability lower than 1 ‰. On average, intra-tooth $\delta^{18}O$ variability for *Triceratops* enamel is 0.8 ‰. The inter-tooth variability of $\delta^{18}O$ enamel of all serial-sampled *Triceratops* teeth is 5.9 ‰ (15.3 ‰ to 21.2 ‰). This range is on average higher than is observed for sampled *Champsosaurus* enamel (4.0 ‰) and lepisosteids ganoine (4.1 ‰).

Table 1. Overview of carbonate/phosphorus (C/P) and IR-SF values from *Triceratops* enamel, dentine and bone samples. Enamel samples are represented by RGM.1333589, dentine samples are represented by RGM.1333596 and bone samples are represented by unnumbered cortical femur fragments from the Darnell *Triceratops* Bonebed.

Enamel leached with 0.1 M acetic acid	0.22	3.76
Enamel leached with 1 M calcium acetate buffer	0.74	6.19
Enamel untreated	-0.87	1.23
Dentine leached with 0.1 M acetic acid	2.14	3.26
Dentine leached with 1 M calcium acetate buffer	1.02	3.40
Dentine untreated	2.01	3.43
Bone leached with 0.1 M acetic acid	1.55	2.72
Bone leached with 1 M calcium acetate buffer	1.45	2.19
Bone untreated	0.3	2.48

3.4.6 Carbon isotopes

The complete isotope analysis returned a total range of 10.8 ‰ for *Triceratops* enamel $\delta^{13}C$ (mean -5.4 ‰) and a smaller range of 7.5 ‰ for dentine $\delta^{13}C$ (mean 0.14 ‰) (Figure 9). *Champsosaurus* enamel $\delta^{13}C$ shows a spread of 2.0 ‰ with a mean value of -4.5 ‰. *Champsosaurus* dentine $\delta^{13}C$

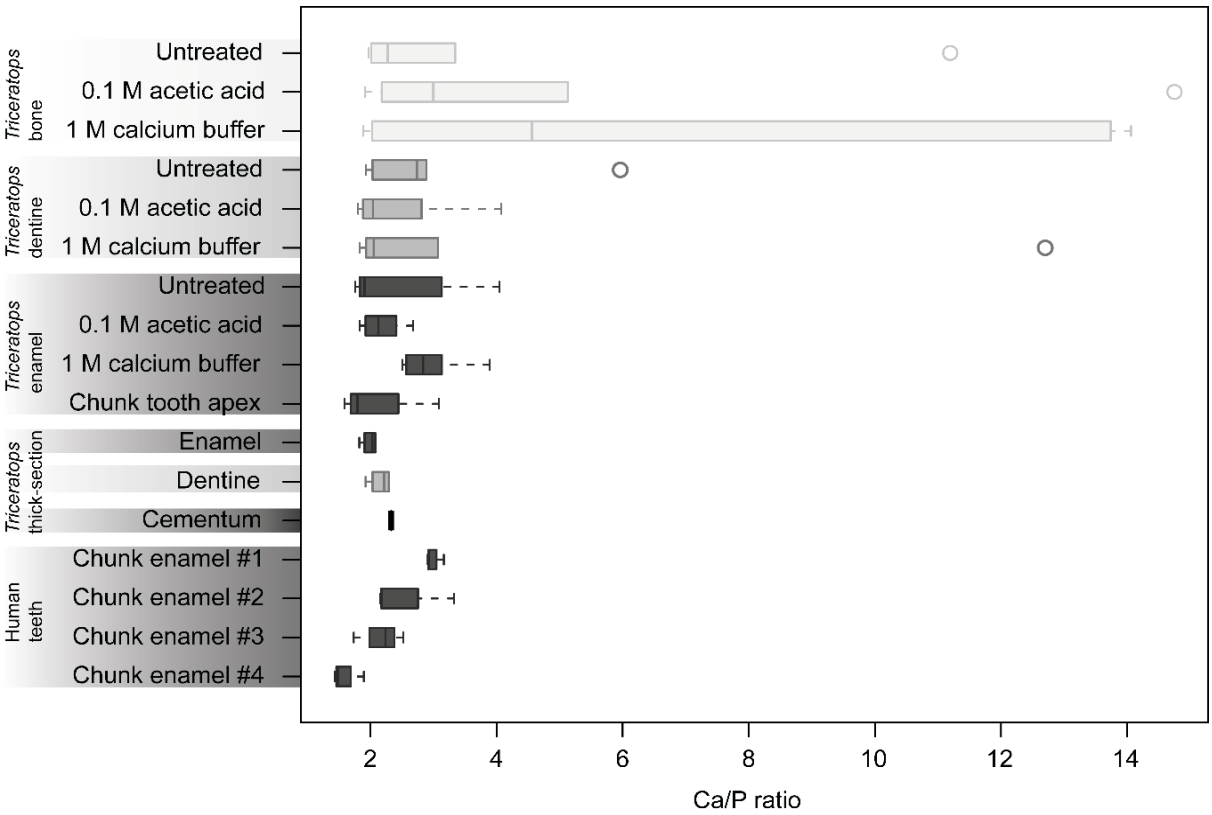

Figure 5. Boxplots showing the spread in Ca/P ratios across different bioapatite tissues and different pretreatment strategies. Across all sampled material, there is no significant difference in Ca/P ratio between fossil and modern specimens. *Triceratops* bone shows greater spread, most probably because bone is more sensitive to diagenetic effects. See Supplementary Raw Data file for all individual Ca/P measurements.

(mean 0.2 ‰) showed a greater range of 3.1 ‰. Lepisosteid ganoine $\delta^{13}C$ (mean -3.0 ‰) values spanned a total range of 4.8 ‰. The $\delta^{13}C$ in the enamel/ganoine of the three taxa are overlapping, but a Kruskal-Wallis test returned a significant difference ($p = 0.01$). Subsequent post-hoc paired Mann-Whitney U tests with Bonferroni correction indicated that only *Triceratops* enamel was significantly different from the lepisosteid ganoine (Table S4).

The incrementally sampled teeth show an overlapping range of enamel $\delta^{13}C$ values and show slightly stronger fluctuations compared to $\delta^{18}O$ increments (Figure 11). The same sample that yielded an unusually low $\delta^{18}O$ value also produced a similarly low $\delta^{13}C$ value (RGM.1333595). Intra-tooth variability among all teeth ranges from 0.6 ‰ to 4.6 ‰ with mean intra-tooth variability calculated at 2.5 ‰. Inter-tooth $\delta^{13}C$ variability calculated among all the serial sampled *Triceratops* enamel is 8.1 ‰. The same pattern emerges here as with $\delta^{18}O$ values, where *Triceratops* inter-tooth enamel $\delta^{13}C$ variability is higher than in *Champsosaurus* and lepisosteids (2.0 ‰ and 4.8 ‰, respectively), although we acknowledge the small dataset for the latter two species.

3.5 Discussion

3.5.1 Depositional setting

The organic rich, carbonate poor, fine-grained siliciclastic sediment that embeds the fossil material matches a depositional environment representing a floodplain setting typical for the Late Cretaceous fluvial systems bordering the Western Interior Seaway (Crystal et al., 2019). The organic rich fine-grained basal unit can be interpreted as a residual channel infill deposited in a low energy terrestrial

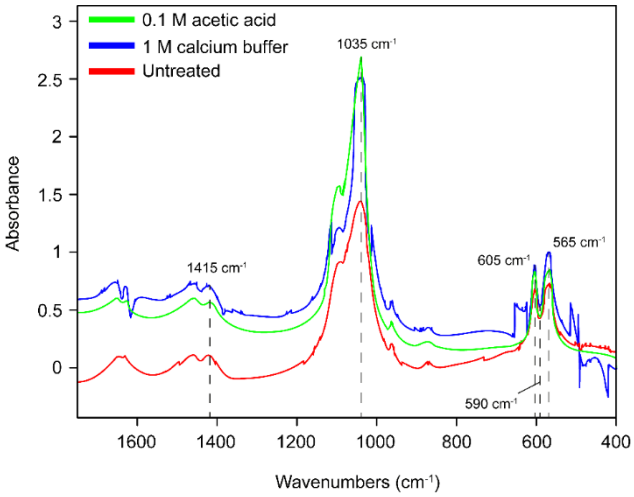

Figure 6. FTIR spectrum showing *Triceratops* enamel across three different treatment strategies. The indicated peaks are used to calculate C/P ratios (1415/1035) and IR-SF values ((605+565)/590).

environment. The overlying sandy unit displays typical sedimentary features related to a crevasse splay event (c.f. Burns et al. 2017). The DTB fossil material is well-preserved with limited morphological distortion, retention of original bone surfaces, and only minor weathering and erosion damage. Absence of evidence of scavenging suggests that exposure of the animal carcasses was limited, and that initial burial occurred relatively fast, which is corroborated by the grain size data (Figure 2C).

3.5.2 Extent of diagenesis

While there is no single test capable of providing conclusive evidence against (significant) diagenetic alteration, a combination of insights can help to understand the post-mortem alteration of fossil bioapatite for this bonebed. A clear (absolute) offset exists between the tooth-specific isotope content of enamel and dentine bioapatite for both oxygen (mean $\Delta\delta^{18}O_{e\text{-}d}$ of 0.87 ‰) and carbon (mean $\Delta\delta^{13}C_{e\text{-}d}$ of 5.54 ‰) for the *Triceratops* from the DTB (Figure 10) (c.f. Stanton Carlson & Thomas, 2004). Hence, the observed isotope systematics of the DTB – especially the difference in enamel and dentine values – indicate some degree of isotopic alteration. Given the low concentration of dissolved inorganic carbon (DIC) compared to oxygen in fluids, the $\delta^{13}C$ values are generally less sensitive to isotopic alteration than the coexisting $\delta^{18}O$ values (c.f. van Baal et al., 2013). This could explain the larger spread in carbon data opposed to oxygen data observed in the dataset discussed here. However, although the absolute $\delta^{18}O$ values might be altered, the relative variability is expected to be preserved within and between specimens.

The sedimentary matrix in the bonebed remained practically devoid of authigenic carbonates (on average 2.4 wt% $CaCO_3$ in the bonebed layer; Figure 2C), providing an unlikely scenario for the uptake of secondary carbonates by the apatitic fossils. In this scenario, the pretreatment procedures aiming to remove secondary carbonates may have had adverse effects. While it might be too early to conclude that these *Triceratops* individuals are part of a biological (social) group, the rapid burial of multiple individuals suggest that the *Triceratops* lived and died at approximately the same time. In any event, they foraged and drank across similar geographical locations and have overlapping or homogenous diagenetic bone alterations due to the shared taphonomic history. This means that even partial preservation of an original isotope signature yields valuable information, as relative changes in $\delta^{18}O$ and $\delta^{13}C$ across the bonebed are comparable. While pretreatment protocols – and subsequent checks through C/P and FTIR – do provide shifts in isotope data, they remain inconsistent relating to the degree of diagenesis in this study. It agrees with the partial preservation of original isotope signatures, and we believe that the data compared and discussed for this specific bonebed provides meaningful results on dinosaur isotope systems.

3.5.3 Local water conditions and *Triceratops* habitat

Intra -and inter-tooth $\delta^{18}O$ variability of the DTB *Triceratops* is comparable to the variability in other dinosaurs as well as modern herbivorous mammals (Kohn et al., 1998; Stanton Carlson & Thomas,

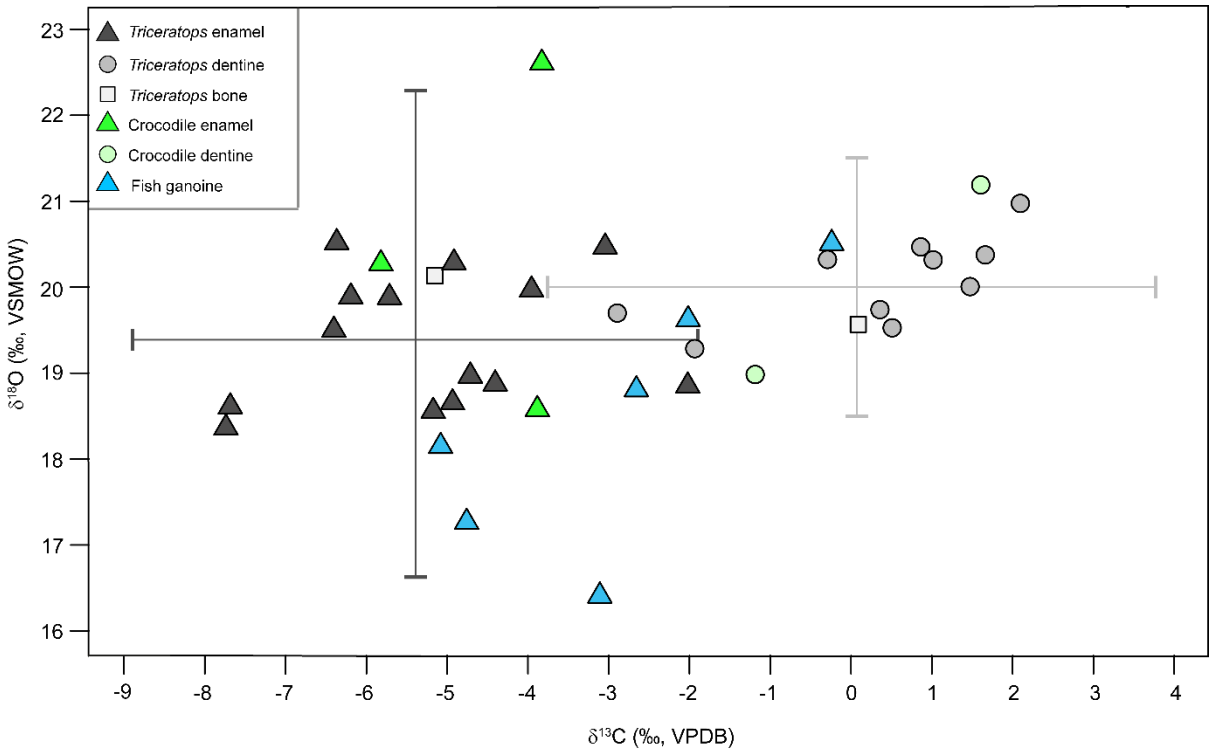

Figure 7. Crossplot diagram showing the total overview (single and incrementals) of $\delta^{18}O$ and $\delta^{13}C$ isotope values across different taxa of the Darnell *Triceratops* Bonebed. Each point represents the average value of a single tooth/scale. Note the more positive values and tighter spread of the dentine values compared to enamel and ganoine. Bone values plot in-between enamel and dentine values. The two crosses represent the spread (±2σ) for enamel and dentine.

2004). The differences in the $\delta^{18}O$ variability among the three taxa possibly reflects the relationship between the animal's physiology and ambient water, where lepisosteids and *Champsosaurus* $\delta^{18}O$ are more in isotopic equilibrium with their surrounding local water compared to free-roaming *Triceratops* $\delta^{18}O$, which shows the highest variability likely due to larger home ranges and access to different water sources.

Given their huge body volume, *Triceratops* can be considered at least gigantothermic and/or even endothermic, maintaining elevated body temperatures as proposed for other large-bodied non-avian dinosaurs (Amiot et al., 2006; Eagle et al., 2011; Erickson 2014; Laskar et al., 2020). Based on $\delta^{18}O$ from phosphate and calculated $\delta^{18}O$ of body water, it has been shown that different taxa of dinosaurs – including ornithischians – show similar physiologies as mammals and are considered true endotherms (Amiot et al., 2006). This implies that *Triceratops* at least precipitated their apatite at elevated temperatures compared to ambient (air) temperatures. Therefore, the $\delta^{18}O$ variability in the *Triceratops* bioapatite likely reflects changes in the $\delta^{18}O$ of body water rather than body temperature. The $\delta^{18}O$ of the body water of herbivores mainly depends on ingested drinking water and to a lesser extent on water that is ingested via plant food (Cerling & Harris, 1999), and is subsequently related to climatic parameters such as the $\delta^{18}O$ value of the local meteoric water, air temperature and humidity (Kohn et al., 1998; Kohn & Cerling, 2002; Fricke & Pearson, 2008). The $\delta^{18}O$ values in herbivores that drink large amounts of surface water and experience high water turnover rates – such as ungulates and elephants – generally track the $\delta^{18}O$ values of local water sources. On the contrary, if most of the ingested water is sourced from the plant food, the $\delta^{18}O$ in herbivores would be more strongly influenced by the local humidity (Kohn et al., 1996). Modelling experiments demonstrate that with

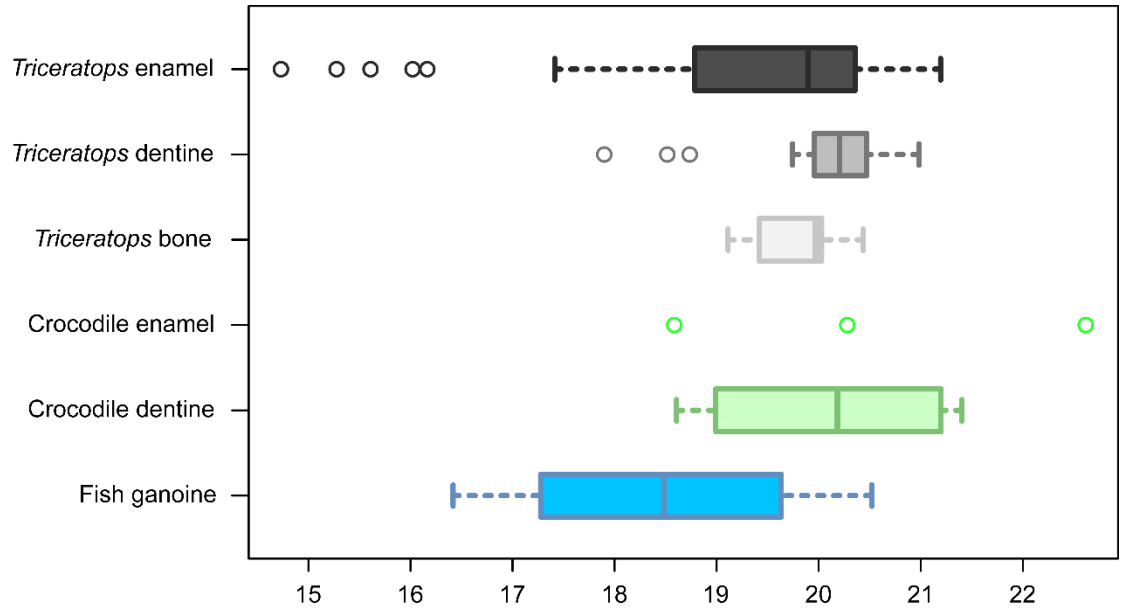

Figure 8. Boxplots showing the range and spread in $\delta^{18}O$ of bioapatite tissues from *Triceratops*, *Champsosaurus* and lepisosteids. *Champsosaurus* enamel is represented by three samples only.

increasing body size the amount of oxygen that is derived via the uptake of food and atmospheric O_2 decreases proportionally to the amount of oxygen taken up as free-drinking water (Bryant and Froehlich, 1995). As a consequence, the $\delta^{18}O$ in teeth of *Triceratops* likely tracked changes in the $\delta^{18}O$ of the local surface drinking water ($\delta^{18}O_w$), and we posit that the $\delta^{18}O$ isotope signature in *Triceratops* enamel corroborates earlier inferences about the $\delta^{18}O$ body water – which is a function of both local water sources and air temperature – and therefore informs on *Triceratops* behaviour and living environments.

Assuming a mammal-like physiology with relatively elevated and constant body temperatures for *Triceratops*, the $\delta^{18}O_w$ might be approximated from the *Triceratops* structural carbonate $\delta^{18}O$

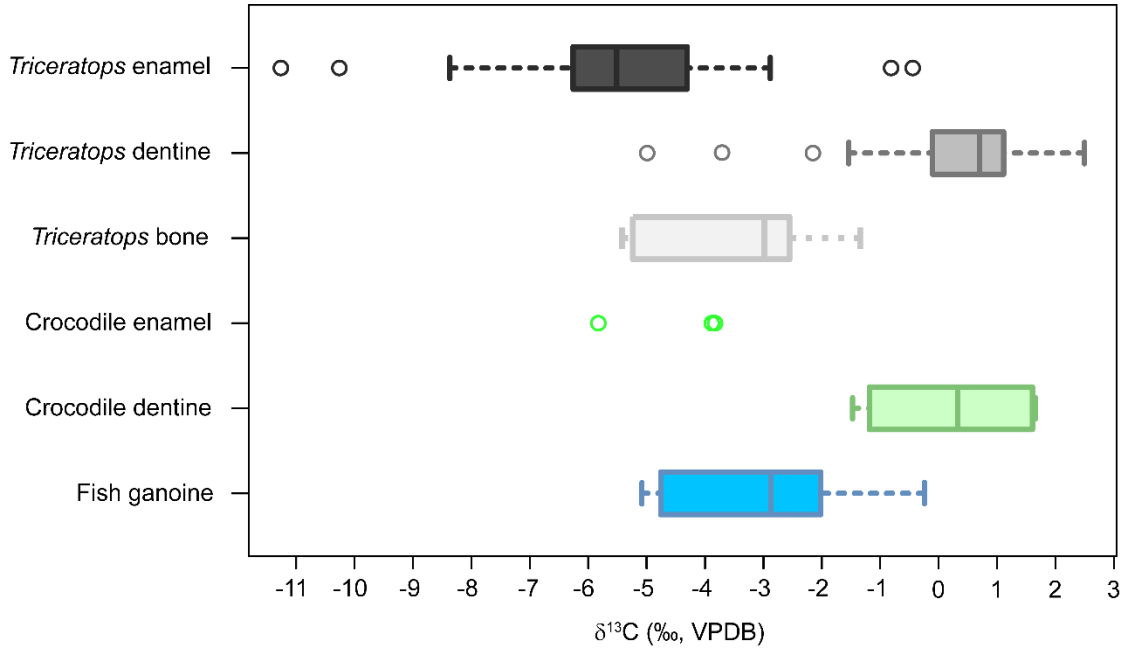

Figure 9. Boxplots showing the range and spread in $\delta^{13}C$ of bioapatite tissues from *Triceratops*, *Champsosaurus* and lepisosteids. *Champsosaurus* enamel is represented by three samples.

($\delta^{18}O_{sc}$) using the formula established for large, water-dependent herbivores by Hoppe et al. (2006). All the *Triceratops* teeth of which enamel $\delta^{18}O$ was available produced an average $\delta^{18}O_w$ of -14.8 ‰ (total range -16.4 to -13.5 ‰, n = 12) by inserting the corresponding $\delta^{18}O$ in formula [1]. This relatively low value coincides with inland freshwater systems ($\delta^{18}O_w$ < ~-11 ‰) according to multiple independent $\delta^{18}O_w$ datasets on Late Cretaceous bivalves – specifically the Hell Creek and Lance Formation (Dettman & Lohmann, 2000; Tobin et al., 2014; Petersen et al., 2016). Bivalves store $\delta^{18}O$ in equilibrium with the surrounding water and have shown to express a bimodal distribution in their $\delta^{18}O$ signature (Tobin et al., 2014). Lower $\delta^{18}O$ values represent freshwater rivers while higher values may be associated with brackish to saltwater coastal floodplain settings (Petersen et al., 2016). This observation of lower oxygen values agrees with the sedimentological setting and hypothesized freshwater floodplain depositional environment for the Darnell *Triceratops* Bonebed.

Since the fossil remains did not undergo long-distance transport after death and deposition, the calculated $\delta^{18}O_w$ of -14.8 ‰ from formula [1] can be interpreted as the local hydrological conditions unique to this fossil assemblage, and – combined with the sedimentological context – provides evidence that these dinosaurs lived in very close vicinity of fluvial settings. *Triceratops* most probably ingested drinking water from rivers and channels and foraged for food around these types of areas. Previous assumptions on *Triceratops* habitat show that they were often placed in more forested settings or open marsh/floodplain habitats based on $\delta^{18}O$ isotope signatures, while contemporaneous hadrosaurs would occupy these river settings more commonly (Fricke & Pearson, 2008). Similar observations have been reported by Lyson & Longrich (2011) who compared dinosaur taxa between mudstone and sandstone deposits from the Hell Creek Formation and other Maastrichtian-aged formations in North America. Mudstone deposits – which reflect floodplain settings – showed the highest representation of ceratopsian dinosaurs, suggesting that their preferred habitat lies in these types of areas. The DTB is interpreted as a mudstone deposit, but closely associated with more inland freshwater environments opposed to brackish or saltwater coastal floodplains. Based on isotope data presented here, the *Triceratops* of the DTB allows to expand the previously assumed habitat range for this species. Instead, *Triceratops* was not restricted to specific habitats, but seems to have occupied a more diverse set of habitats than previously thought (see section 6.4 for more details).

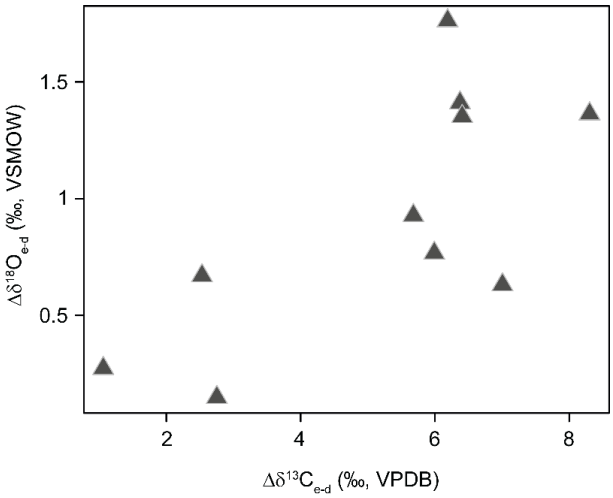

Figure 10. Scatterplot of tooth-specific $\Delta\delta^{18}O_{e\text{-}d}$ and $\Delta\delta^{13}C_{e\text{-}d}$ values. Each point represents a single tooth (n = 9) of which both enamel and dentine samples were measured for their isotope content. These points depict the differences in oxygen and carbon values between enamel and dentine. Teeth that have higher/lower $\Delta\delta^{18}O_{e\text{-}d}$, generally have similar $\Delta\delta^{13}C_{e\text{-}d}$, suggesting that diagenesis at least was uniform across $\delta^{18}O$ and $\delta^{13}C$ values.

Considering an intra-annual variability in the enamel bioapatite, the average $\delta^{18}O$ range within all incrementally sampled *Triceratops* teeth of 1.3 ‰ can serve as a proxy for seasonal shifts. Von Ebner line counts (Figure 3) reveal that this observed variation spans ~90 days. This range is slightly lower than is observed for contemporaneous hadrosaurs from the Late Cretaceous that showed an average intra-tooth $\delta^{18}O$ value of 1.8 ‰ in incrementally sampled teeth (Stanton Carlson & Thomas, 2004). The relatively small variation in the observed $\delta^{18}O$

time series of single teeth of *Triceratops* is thus comparable to records from other dinosaur sites (Stanton Carlson & Thomas, 2004; Fricke & Pearson, 2008; Fricke et al., 2008) and modern herbivorous mammals (Kohn et al., 1998). Migrating dinosaurs may have spent their life in different environments resulting in variable isotope intake. On the other hand, they are expected to follow areas with ideal ambient temperature ranges and food sources, which is theorized to homogenize $\delta^{18}O$ isotopic – and seasonal – variability over time (Stanton Carlson & Thomas, 2004). However, considering the limited variability and presence of unique isotopic environments (Fricke et al., 2008), we argue that the $\delta^{18}O$ signature here represents local seasonal variation and/or movement within a home range, implying restricted migratory behaviour. This interpretation agrees with previous studies on hadrosaur migration, where it is postulated that Late Cretaceous hadrosaurs showed limited dispersal in relatively restricted home ranges (Fricke et al., 2009; Terrill et al., 2020; Cullen et al., 2020; Cullen et al., 2022).

3.5.4 Interactions during carbon uptake

Triceratops would have exclusively fed on C3 plants since there is no evidence for C4 plants from the Late Cretaceous. The average $\delta^{13}C$ of all sampled *Triceratops* enamel is -5.4 ‰ (total $\delta^{13}C$ range -11.3 to -0.4 ‰). This represents the higher end of the distribution for modern C3 grazers and largely overlaps with mixed C3/C4 feeders. Notably, the *Triceratops* from the DTB show considerable overlap in their $\delta^{13}C$ signatures with other contemporaneous herbivorous dinosaurs (Stanton Carlson & Thomas, 2004; Fricke & Pearson, 2008). For putative C3 browsers, hadrosaurs from the Hell Creek

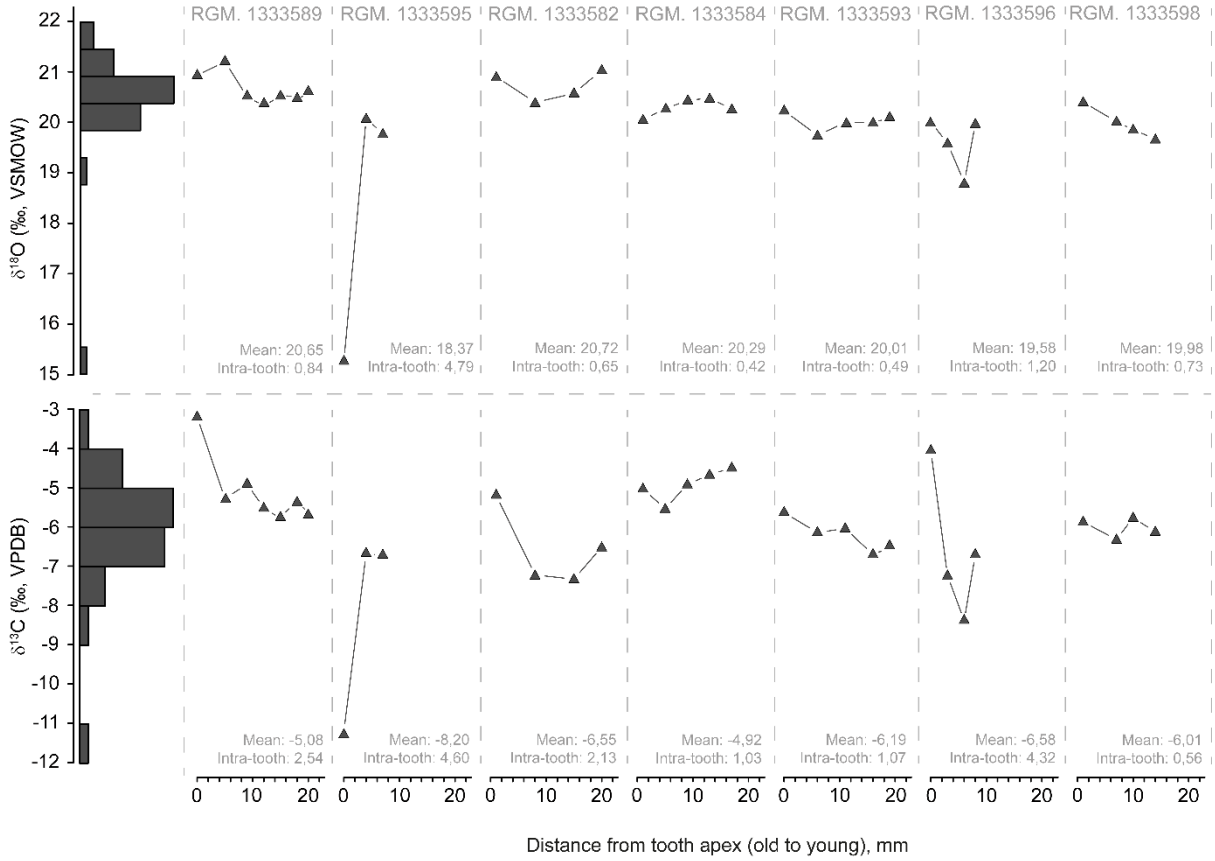

Figure 11. $\delta^{18}O$ and $\delta^{13}C$ isotope values from the seven serial sampled *Triceratops* teeth. Note that, while the graphs are positioned in series, the teeth are considered to be independent and do not come from the same tooth battery or individual. Positioning of the graphs are based on random order. The distance from the tooth apex is oldest to youngest enamel. The histogram on the y-axis represents the total spread of the incremental data for $\delta^{18}O$ and $\delta^{13}C$.

Formation showed a comparably higher mean enamel $\delta^{13}C$ of -3.9 ‰ (Stanton Carlson & Thomas, 2004). Fricke & Pearson (2008) analysed five sites (within ~50 km proximity) from the Hell Creek Formation of southern North-Dakota and obtained similar mean $\delta^{13}C$ values for hadrosaurs and ceratopsians (Figure 12). Corresponding mean hadrosaur enamel $\delta^{13}C$ is -5.9 ‰ with a range of -6.0 to -5.8 ‰, while mean ceratopsian enamel $\delta^{13}C$ was -6.3 ‰ and had a larger range of -8.1 to -3.9 ‰ (Fricke & Pearson, 2008). Thus, $\delta^{13}C$ data from these Late Cretaceous dinosaur sites show extensive overlap with each other, and all seem to point to a relatively high $\delta^{13}C$ value when compared to modern C3 feeders.

Differences in $\delta^{13}C$ of atmospheric CO_2 over geological time may have contributed to the observed higher dinosaur isotope signatures. However, during the Late Maastrichtian, the estimated $\delta^{13}C$ of atmospheric CO_2 was only slightly higher (-6.1 ‰ (Barral et al., 2017)) compared to more recent (pre-industrial) values (~ -6.5 ‰), and therefore cannot explain the significantly higher $\delta^{13}C$ observed in dinosaur bioapatite alone (Stanton Carlson & Thomas, 2004; Fricke & Pearson, 2008).

Preliminary analysis of macrofloral remains indicate that the DTB yielded relatively high amounts of gymnosperm fossils compared to angiosperms. It has been suggested that gymnosperms have more positive $\delta^{13}C$ values than angiosperms (by 2-3 ‰ (Hare & Lavergne, 2021)), and recent studies have indicated that small but consistent offsets in $\delta^{13}C$ between different plant types may vary strongly depending both on the plant species and prevailing climatic and environmental conditions (e.g., up to 2-3 ‰ for halophytes (Wei et al., 2008; Sheldon et al., 2020; Hare & Lavergne, 2021)). Although specific studies on *Triceratops* feeding are lacking, it is proposed that ceratopsians were able to efficiently process fibrous plant material such as gymnosperms using their sharp beak and tooth batteries (Ostrom, 1966; Mallon & Anderson, 2014). A diet shifted more towards gymnosperms and/or halophytes may have led to higher $\delta^{13}C$ values.

One other explanation for elevated $\delta^{13}C$ values is that *Triceratops* and other herbivorous dinosaurs possibly had different $\delta^{13}C$ fractionation offset between ingested plant food and their bioapatite. While the mean $\delta^{13}C$ fractionation for herbivore mammals is ~14 ‰ (Cerling & Harris, 1999), the fractionation factors cover a range from 10 ‰ to 15 ‰ among different taxa, presumably as a result of physiological and metabolic differences (Passey et al., 2005; Rey et al., 2020). Data on carbon fractionation in herbivorous reptiles is scarce but the existing literature shows that they have similar $\delta^{13}C$ isotopic offsets of ~12 ‰ between the ingested plant material and their bioapatite (Biasatti, 2004) However, these observations must be interpreted with care as isotope fractionation in marine reptiles is also affected by diving behaviour (McConnaughey et al., 1997; Biasatti, 2004; Schulp et al., 2013). Birds such as modern ratites have a similar degree of carbon fractionation with ranges comparable to those observed in herbivorous mammals (13 ‰ to 16 ‰ (Johnson et al., 1988; Ségalen & Lee-Thorp, 2009)).

Fricke et al. (2008) and Fricke & Pearson (2008) compared bulk sedimentary organic matter with the $\delta^{13}C$ of ceratopsian and hadrosaurs across a large range of Late Cretaceous dinosaur localities and inferred a $\delta^{13}C$ offset of ~18 ‰ between dinosaur bioapatite and corresponding organic matter (remnants of local plant material). Such offset is higher than the average ~14 ‰ for extant herbivores and would suggest a plant food $\delta^{13}C$ of -23.4 ‰ for the DTB *Triceratops* (mean enamel $\delta^{13}C$ of -5.4‰), which corresponds to the higher tail end of known modern C3 plant distriubtions (-35 ‰ to -22 ‰ (Kohn 2010)). Carbon isotope data on Late Cretaceous herbivore dinosaurs consistently yield an offset of ~18 ‰ and numerous authors have postulated the idea of a dinosaur-specific feeding physiology (Stanton Carlson & Thomas, 2004; Fricke et al., 2008; Fricke & Pearson, 2008; Tütken, 2011; Zhao et al., 2021).

While specialized digestive tracts as seen in ruminant mammals most probably did not evolve in dinosaurs (Smith et al., 2000), one can only speculate on ideas such as dinosaurs possessing single large-chambered stomachs in which food was digested over relatively longer periods (Hummel et al., 2008). In modern herbivores, the intraspecific differences in carbon fractionation partially result from differences in the gut microbiome and methane production by methanogens (Passey et al., 2005). Longer retention times of ingested food combined with a unique intestinal microbiome in dinosaurs could reasonably produce similar variations in carbon isotope systematics as found in modern herbivorous taxa. Additionally, recent research found a relationship between body size and enamel-diet $\delta^{13}C$ offsets in extant mammals, where smaller (micromammals) and larger (megaherbivores) taxa show a difference as much as 7 ‰ (Tejada-Lara et al., 2018). Non-avian dinosaurs being the largest terrestrial herbivores to have ever existed could equally show an offset higher than the average 14 ‰. Adding these animal-specific factors to the sum as well as the earlier proposed environmental factors – such as elevated $\delta^{13}C$ in atmospheric CO_2 and specific plant physiologies – may explain the observed elevated carbon isotope signature in herbivorous dinosaurs (Stanton Thomas & Carlson, 2004). Nevertheless, there is need for a better understanding of the interplay between extant animals, their environments and their food nutrients during incorporation and fixation of specific (carbon) isotope signals to provide unequivocal evidence regarding dinosaur physiology (Tejada-Lara et al., 2020).

3.5.5 Niche partitioning

Time-equivalent hadrosaurs and ceratopsians from the Hell Creek Formation have shown consistent differences in combined $\delta^{18}O$ and $\delta^{13}C$ values (Fricke & Pearson, 2008). These offsets were interpreted as niche partitioning, whereby relatively high $\delta^{18}O$ and $\delta^{13}C$ values are associated with open marsh settings and lower values represent more inland forested areas (Fricke & Pearson, 2008). Additionally, ceratopsians show relatively higher and lower $\delta^{13}C$ values than fish in marsh and forest settings, respectively (Fricke & Pearson, 2008). Interestingly, the mean $\delta^{18}O$ of 19.4 ‰ and mean $\delta^{13}C$ of -5.4 ‰ of the DTB *Triceratops* fall roughly between these two clusters, which may suggest that these *Triceratops* individuals had lived in a transitional area between more open marsh settings and inland forests, such as fluvial systems. Moreover, the spread of the *Triceratops* isotope data discussed here is relatively small which corroborates our interpretation of the DTB as a single event responsible for the death and rapid burial of a large group of *Triceratops*. This becomes especially evident when the DTB is compared to sites characterized by a diverse range of fossil material that is likely concentrated due to reworking, erosion and/or attritional processes over a longer time period (Figure 2A). Earlier hypotheses on ornithischian niche partitioning and habitat occupation were based on isotope data sampled on isolated material from multiple taphonomically-concentrated sites (Pearson et al., 2002; Fricke & Pearson, 2008). While these sites provided a novel view into dinosaur ecosystems, comparison of these multiple individual sites reveal that there is still much isotopic overlap (i.e., higher spread) between hadrosaurs and ceratopsians, particularly when each site is plotted and evaluated separately (Figure 12). Based on more narrow constrained bonebeds, such as the DTB discussed here, isotope data suggest that both taxa were coexisting to a larger degree than previously thought. Additionally, multi-taxon isotope analyses on other well-constrained Late Cretaceous floodplain systems revealed similar significant overlap between the isotope signatures of ornithischian dinosaurs overall (Cullen et al., 2020). It appears that niche partitioning – as preserved in the DTB – among large-bodied herbivorous dinosaurs is more complex than previously thought, if they were partitioning at all. These may include (a combination of) diet specialisation, feeding height stratification and temporal separation (e.g.,

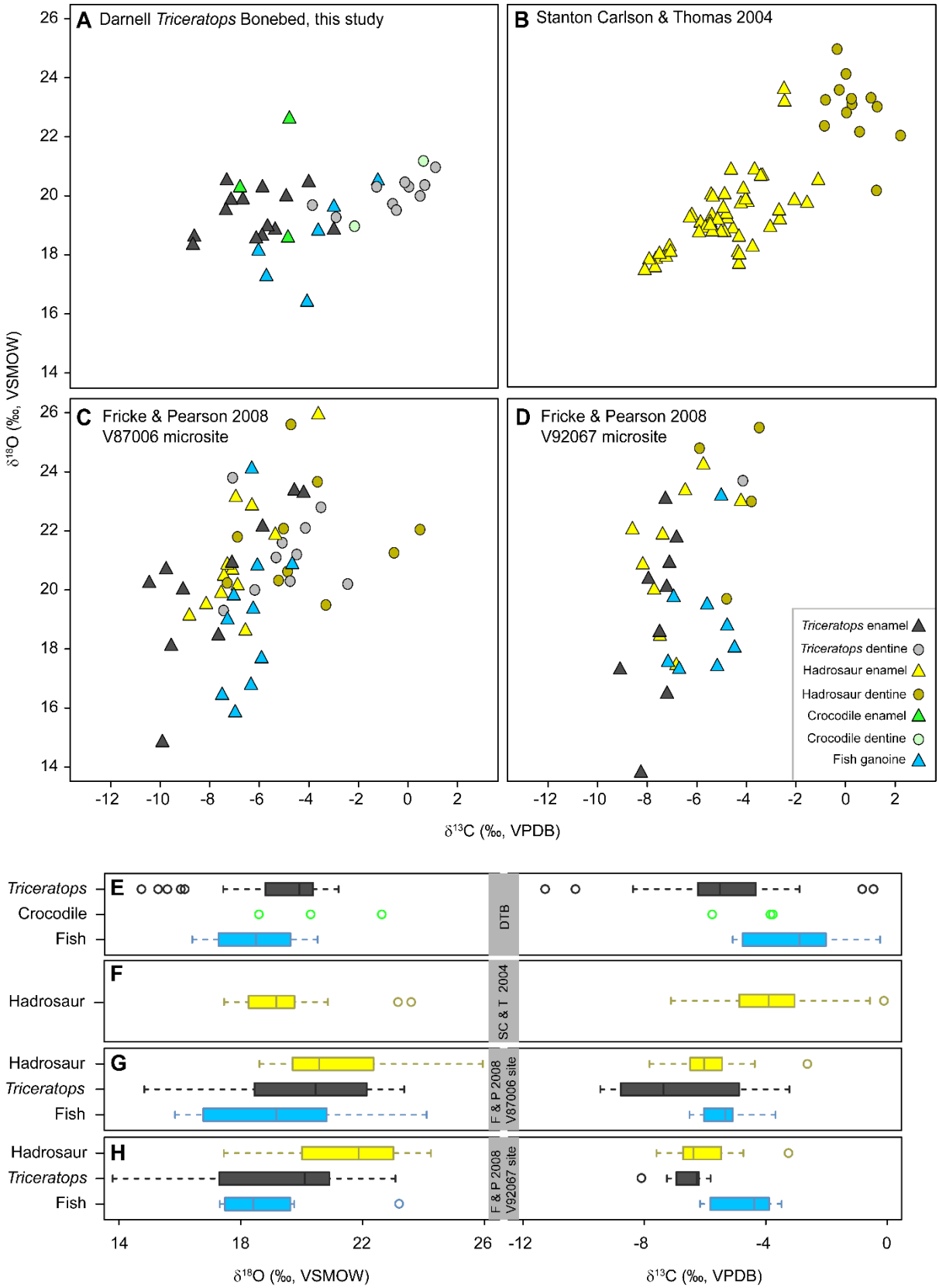

Figure 12. Comparison of $\delta^{18}O$ and $\delta^{13}C$ data from this study with other contemporaneous Late Cretaceous dinosaur sites of which data was available (Figure 1A). Upper part shows cross plots of four different dinosaur sites (A to D) and their respective $\delta^{18}O$ and $\delta^{13}C$ isotope systematics. Lower part focusses on the spread and range of the enamel $\delta^{18}O$ and $\delta^{13}C$ values of the same sites (E to H). Note the larger spread in the spatially less-constrained sites.

seasonal changes in habitat use, diurnal vs. nocturnal), all of which may be difficult to infer with currently available isotope analyses.

The DTB expands the envelope of herbivorous dinosaur niche partitioning (Fricke & Pearson, 2004; Lyson & Longrich 2011), and might even suggest that niche partitioning happened to a significantly lesser degree, at least in this part of the Lance Formation. Instead, Late Cretaceous herbivores could have inhabited specific areas not based on spatial setting, but with competition as actual limiting factor. This line of reasoning does not limit a taxon to a specific habitat, but creates a dynamic system in which areas are inhabited based mainly on the presence of other taxa or even conspecifics. Isotopic research on wider set of local bonebeds could shed more light on this assumption.

Nevertheless, our results demonstrate the application of spatially well-constrained dinosaur sites in stable isotope research. Many earlier studies on dinosaur isotope systems are based on aforementioned (micro-)sites with generally poorly constrained depositional setting, diagenetic conditions, stratigraphy and taphonomy. These taphonomically-concentrated fossils provide a space- and time-averaged isotope signal of a specific ecosystem that creates an understanding of large-scale palaeo-ecosystem dynamics. On the other hand, the chemical fingerprint of bonebeds with well-constrained fossil material represents a more accurate baseline of the local ecology of that specific environment and/or species, such as the DTB studied here. Combining data from both types of assemblages helps in understanding more broader biological implications such as niche partitioning and animal movement.

3.6 Conclusion

Isotopic analysis of the Darnell *Triceratops* Bonebed in eastern Wyoming provides a unique window in studying dinosaur ecosystems of Late Cretaceous North America. There is a significant difference in the $\delta^{18}O$ and $\delta^{13}C$ values between the enamel and dentine of aquatic reptiles and *Triceratops* from the Darnell *Triceratops* Bonebed. These differences are markedly stronger for the $\delta^{13}C$ isotope system. Contrary to previous studies, bone showed less deviation from enamel than dentine, despite its more porous matrix. Moreover, pretreatment effects from leaching and oxidation on enamel, dentine, and bone returned ambiguous results. Diagenesis may have affected the studied material here, but these effects are expected to be uniform and thus the observed $\delta^{18}O$ and $\delta^{13}C$ isotope signatures allow for inferences on *Triceratops* palaeoecology. This is corroborated by the lack of authigenic carbonates in the organic-rich claystone embedding the fossils and the rapid burial of the well-preserved fossils by a very fine sandstone layer. This strengthens the notion that diagenetic overprint may vary per locality and should be checked on a case-by-case basis.

This study provides novel insights on *Triceratops* behaviour and ecology by examining the seasonal patterns in incrementally sampled $\delta^{18}O$ from tooth enamel. In addition, the $\delta^{13}C$ isotope signatures revealed possible feeding habits, and corroborate earlier observations of dinosaur-specific carbon fractionation rates. The stable isotope data from multiple sympatric species in a spatially and temporally well-constrained fossil assemblage allowed for a detailed assessment of a local Late Cretaceous ecosystem, that could be placed in the framework of previously studied dinosaur isotope systematics. The stable isotope dataset presented here shows both the importance and limitations of stable isotopes as local indicator of habitat and home ranges as opposed to time-averaged localities. Future stable isotope analyses on dinosaur remains should combine data from locally well-constrained sites and taphonomically-concentrated sites to better understand diet, habitat preferences, and possible niche partitioning in dinosaur (palaeo-)ecosystems.

3.7 Supplementary data

3.7.1 Check for normality and explorative statistics

All statistical analyses were carried out using R and R-Studio. The majority of the parametric tests assume that the isotopic data come from normally distributed populations. Graphical data visualisation (QQ-plots and density histograms), data transformation and Shapiro-Wilk tests for normality (test statistic: W = 0 to 1, significance level: $p < 0.05$) were used to explore the $\delta^{18}O$ and $\delta^{13}C$ values for normality across the different taxa and bioapatite tissue types (Table S1). The $\delta^{13}C$ and $\delta^{18}O$ dataset for *Triceratops* enamel (n = 60) showed a significant deviation from the normal distribution ($p = 0.01$ and $p = 0.00$ respectively). Shapiro-Wilk tests on log transformed $\delta^{13}C$ and $\delta^{18}O$ values for *Triceratops* enamel also did not return a significant normal distribution ($p = 0.00$ for both). Normality tests on both the $\delta^{13}C$ and $\delta^{18}O$ isotope values of *Triceratops* dentine (n = 21) returned a non-normal distribution for the datasets ($p = 0.00$ for $\delta^{13}C$ and $p = 0.00$ for $\delta^{18}O$). Log transformation of the dentine dataset deviated even further from a normal distribution ($p = 0.000$ for both $\delta^{13}C$ and $\delta^{18}O$). However, for *Triceratops* bone, both the $\delta^{13}C$ and $\delta^{18}O$ values were normally distributed ($p = 0.17$ and $p = 0.21$, respectively). Normality checks on the isotope data on *Champsosaurus* and fish were also performed. However, the $\delta^{13}C$ and $\delta^{18}O$ from the material of *Champsosaurus* and fish is represented by only a few datapoints. Lower sample sizes may often fail to detect any deviations from normality (Le Boedec, 2016), so the statistical output is interpreted with care. *Champsosaurus* enamel $\delta^{13}C$ and $\delta^{18}O$ (n = 3) showed no significant deviation from a normal distribution ($p = 0.05$ and $p = 0.83$, respectively). Similarly, the $\delta^{13}C$ and $\delta^{18}O$ for *Champsosaurus* dentine (n = 6) do not seem to differ from a normal distribution ($p = 0.15$ and $p = 0.50$, respectively). Fish ganoine $\delta^{13}C$ and $\delta^{18}O$ showed no significant deviations from normality ($p = 0.77$ and $p = 0.98$). Given the smaller dataset for *Champsosaurus* and fish as well as the larger *Triceratops* dataset clearly showing deviations from a normal distribution, we resort to non-parametric tests when comparing the population means of the different taxa and their bioapatite tissues in this study (Table S2, Table S3 and Table S4). These include the Mann-Whitney U test (non-parametric equivalent of the Student's t-test) and the Kruskal Wallis rank test of equal medians (non-parametric equivalent of the one-way ANOVA). The Kruskal-Wallis test was combined with post-hoc paired Mann-Whitney U tests using Bonferroni correction to mitigate the problem of multiple comparisons.

Table S1. Results of Shapiro-Wilk normality tests. The larger dataset on *Triceratops* enamel and dentine showed clear deviations from a normal distribution as opposed to smaller datasets of aquatic reptiles and fish.

Group	**p-value (α = 0,05)**
Triceratops enamel δ^{18}O n = 60	0.00 ***
Triceratops enamel δ^{13}C n = 60	0.01 **
Triceratops dentine δ^{18}O n = 21	0.00 ***
Triceratops dentine δ^{13}C n = 21	0.00 ***
Triceratops bone δ^{18}O n = 9	0.21
Triceratops bone δ^{13}C n = 9	0.17
Champsosaurus enamel δ^{18}O n = 3	0.83
Champsosaurus enamel δ^{13}C n = 3	0.05
Champsosaurus dentine δ^{18}O n = 4	0.5
Champsosaurus dentine δ^{13}C n = 4	0.15
Lepisosteid ganoine δ^{18}O n = 6	0.98
Lepisosteid ganoine δ^{13}C n = 6	0.77

Table S3. Results of the Mann-Whitney U test on *Champsosaurus* enamel and dentine.

Variable 1	**Variable 2**	**p-value (α = 0,05)**
Champsosaurus enamel δ18O n = 3	*Champsosaurus* dentine δ18O n = 4	1
Champsosaurus enamel δ13C n = 3	*Champsosaurus* dentine δ13C n = 4	0.11

Table S2. Statistical output of Kruskal-Wallis tests on the δ^{18}O and δ^{13}C values of *Triceratops* enamel, dentine and bone. The p-value in the upper row represents the results of the Kruskal-Wallis test and the lower numbers are the p-values of post-hoc paired Mann-Whitney tests (incl. Bonferroni corrections) for each possible comparison. The dash (/) separates oxygen and carbon p-values, respectively.

δ^{18}O/δ^{13}C of *Triceratops* enamel, dentine and bone p-value (α=0,05) = 0.15/0.00		
Tissue	Bone	Dentine
Dentine	0.26/0.00	-
Enamel	1.00/0.02	0.23/0.00

Table S4. Statistical output of Kruskal-Wallis tests on the δ^{18}O and δ^{13}C values of enamel across three taxa. The p-value in the upper row represents the results of the Kruskal-Wallis test and the lower numbers are the p-values of post-hoc paired Mann-Whitney tests (incl. Bonferroni corrections) for each possible comparison. The dash (/) separates oxygen and carbon p-values, respectively.

δ^{18}O/δ^{13}C of *Triceratops*, *Champsosaurus* and lepisosteid enamel p-value (α=0,05) = 0.19/0.01		
Taxa	*Champsosaurus*	Lepisosteid
Lepisosteid	0.79/0.79	-
Triceratops	1.00/0.76	0.33/0.01

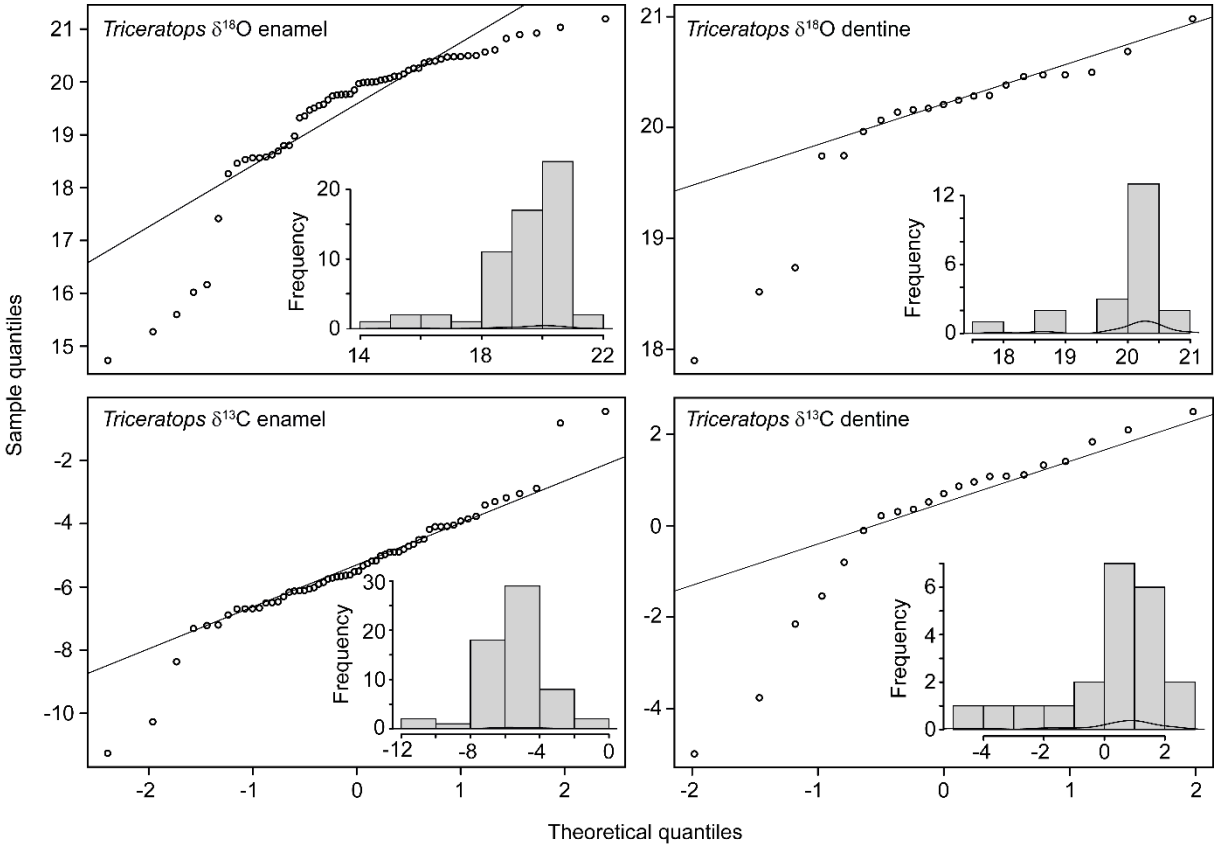

Figure S1. QQ-plots and density histograms of *Triceratops* δ^{18}O and δ^{13}C data.

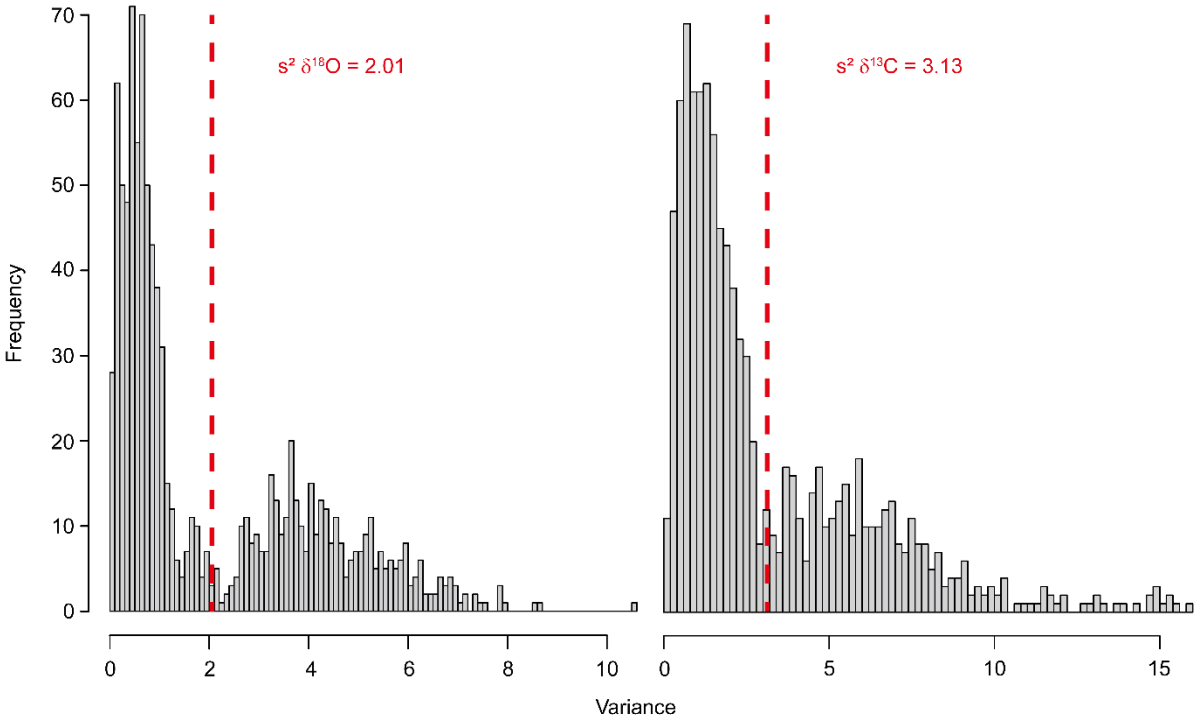

Figure S2. Results of 1000 iterations of random small sampling (n=5; representing the equal amounts of aquatic reptile and fish datapoints) from the *Triceratops* enamel δ^{18}O and δ^{13}C dataset. The red dashed line represents the calculated variance of the entire dataset.

Figure S3. Overview of all the *Triceratops* teeth used for incremental sampling. The majority of the teeth represent unworn adult teeth, but two teeth (RGM. 1333595 and RGM. 1333596) show considerable wear as a result of prolonged food processing during life.

Acknowledgements

We like to express our sincerest gratitude to Donley and Nancy Darnell for their hospitality and help during field seasons. Additionally, we like to thank our team of volunteers for their enthusiasm and efforts in recovering the fossil material. Thanks to Bouke Lacet (Faculty of Science, Earth Sciences, VU Amsterdam) for making the thin-sections and to Natasja den Ouden (Naturalis Biodiversity Center) for streamlining access to the material and handling of the destructive sampling requests. In addition, we owe gratitude to Martijn Guliker, Yasmin Grooters and their team of volunteers (Naturalis Biodiversity

Center) for the preparation of the material presented in this study. We are further thankful for the technical support by Thom Claessen from Utrecht University, Faculty of Geosciences in Utrecht. Martine Hagen, Unze van Buuren, Maarten Prins en Kay Beets (VU Amsterdam) are thanked for their assistance during the laser-diffraction particle size and thermogravimetric analyses. Additionally, we like to thank Lisette Kootker from the VU Amsterdam for providing us with samples on modern human enamel. The project is funded by the Dutch Research Council (NWO) through ALW Open Programme (ALWOP.633). We like to acknowledge Dylan Bastiaans (PIMUZ, Switzerland) for his valuable contributions and input in developing the initial research plan. Furthermore, our gratitude goes towards the Mondriaan Fonds for their important contribution in sponsoring the field seasons. Last but not least, we like to thank the two anonymous reviewers and associated editor Howard Falcon-Lang for their time in carefully reading the manuscript and for providing insightful, constructive comments and suggestions that helped improve the manuscript.

References

Amiot, R., Lécuyer, C., Buffetaut, E., Fluteau, F., Legendre, S., Martineau, F., 2004. Latitudinal temperature gradient during the Cretaceous upper Campanian–Middle Maastrichtian: $\delta^{18}O$ record of continental vertebrates. Earth and Planetary Science Letters 226, 255–272.

Amiot, R., Lécuyer, C., Buffetaut, E., Escarguel, G., Fluteau, F., Martineau, F., 2006. Oxygen isotopes from biogenic apatites suggest widespread endothermy in Cretaceous dinosaurs. Earth and Planetary Science Letters 246, 41–54.

Amiot, R., Buffetaut, E., Lécuyer, C., Wang, X., Boudad, L., Ding, Z., Fourel, F., Hutt, S., Martineau, F., Medeiros, M.A., Mo, J., Simon, L., Suteethorn, V., Sweetman, S., Tong, H., Zhang, F., Zhou, Z., 2010. Oxygen isotope evidence for semi-aquatic habits among spinosaurid theropods. Geology 38, 139–142.

Assonov, S., Groening, M., Fajgelj, A., Hélie, J.F., Hillaire-Marcel, C. 2020. Preparation and characterisation of IAEA-603, a new primary reference material aimed at the VPDB scale realisation for δ13C and δ18O determination. Rapid Communications in Mass Spectrometry 34, e8867.

van Baal, R.R., Janssen, R., Van der Lubbe, H.J.L., Schulp, A.S., Jagt, J.W., Vonhof, H.B., 2013. Oxygen and carbon stable isotope records of marine vertebrates from the type Maastrichtian, The Netherlands and northeast Belgium (Late Cretaceous). Palaeogeography, Palaeoclimatology, Palaeoecology 392, 71–78.

Balter, V., 2001. Were Neandertalians essentially carnivores? Sr and Ba preliminary results of the mammalian palaeobiocoenosis of Saint-Césaire. Comptes Rendus de l'Académie des Sciences - Series 2A – Earth and Planetary Science 332, 59–65.

Barbour, M.M. (2007). Stable oxygen isotope composition of plant tissue: a review. Functional Plant Biology 34, 83–94.

Barral, A., Gomez, B., Legendre, S., Lécuyer, C., 2017. Evolution of the carbon isotope composition of atmospheric CO_2 throughout the Cretaceous. Palaeogeography, Palaeoclimatology, Palaeoecology 471, 40–47.

Barrick, R.E., 1998. Isotope paleobiology of the vertebrates: ecology, physiology, and diagenesis. The Paleontological Society Papers 4, 101–137.

Bartos, T.T., Galloway, D.L., Hallberg, L.L., Deschene, M., Diehl, S. F., Davidson, S.L., 2021. Geologic and hydrogeologic characteristics of the White River Formation, Lance Formation, and Fox Hills

Sandstone, northern greater Denver Basin, southeastern Laramie County, Wyoming. In: U.S. Geological Survey Scientific Investigations Report 2021-5020, pp. 1–242.

Bastiaans, D., Trapman, T., Guliker, M., Kaskes, P., Schulp, A., 2016. Multigenerational assemblage of *Triceratops* from the Newcastle area, Wyoming, USA – An in-depth analysis of cranial and post-cranial ontogenesis. In: Farke, A.A., MacKenzie, A., Miller-Camp, J. (Eds.), Journal of Vertebrate Paleontology, Program and Abstracts, p. 94.

Beasley, M.M., Bartelink, E.J., Taylor, L., Miller, R.M., 2014. Comparison of transmission FTIR, ATR, and DRIFT spectra: implications for assessment of bone bioapatite diagenesis. Journal of Archaeological Science 46, 16–22.

Berna, F., Matthews, A., Weiner, S., 2004. Solubilities of bone mineral from archaeological sites: the recrystallization window. Journal of Archaeological Science 31, 867–882.

Biasatti, D.M., 2004. Stable carbon isotopic profiles of sea turtle humeri: implications for ecology and physiology. Palaeogeography, Palaeoclimatology, Palaeoecology 206, 203–216.

Bryant, J.D., Froelich, P.N., 1995. A model of oxygen isotope fractionation in body water of large mammals. Geochimica et Cosmochimica Acta 59, 4523–4537.

Buffrénil, V. de, Ricqlès, A. de, Zylberberg, L., Padian, K. (Eds.), 2021. Vertebrate Skeletal Histology and Paleohistology. CRC Press, Boca Raton, pp. 229-246.

Burgener, L., Hyland, E., Griffith, E., Mitášová, H., Zanno, L.E., Gates, T.A., 2021. An extreme climate gradient-induced ecological regionalization in the Upper Cretaceous Western Interior Basin of North America. GSA Bulletin 133, 2125–2136.

Burns, C.E., Mountney, N.P., Hodgson, D.M., Colombera, L., 2017. Anatomy and dimensions of fluvial crevasse-splay deposits: Examples from the Cretaceous Castlegate Sandstone and Neslen Formation, Utah, USA. Sedimentary Geology 351, 21–35.

Cerling, T.E., & Harris, J.M., 1999. Carbon isotope fractionation between diet and bioapatite in ungulate mammals and implications for ecological and paleoecological studies. Oecologia 120, 347–363.

Cerling, T.E., Harris, J.M., MacFadden, B.J., Leakey, M.G., Quade, J., Eisenmann, V., Ehleringer, J.R., 1997. Global vegetation change through the Miocene/Pliocene boundary. Nature 389, 153–158.

Crystal, V.F., Evans, E.S., Fricke, H., Miller, I.M., Sertich, J.J., 2019. Late Cretaceous fluvial hydrology and dinosaur behavior in southern Utah, USA: Insights from stable isotopes of biogenic carbonate. Palaeogeography, Palaeoclimatology, Palaeoecology 516, 152–165.

Cullen, T.M., Longstaffe, F.J., Wortmann, U.G., Huang, L., Fanti, F., Goodwin, M.B., Ryan, M.J., Evans, D.C., 2020. Large-scale stable isotope characterization of a Late Cretaceous dinosaur-dominated ecosystem. Geology 48, 546–551.

Cullen, T. M., Zhang, S., Spencer, J., Cousens, B., 2022. Sr-O-C isotope signatures reveal herbivore niche-partitioning in a Cretaceous ecosystem. Palaeontology 65, e12591.

Dansgaard, W., 1964. Stable isotopes in precipitation. Tellus 16, 436–468.

Dettman, D.L., Lohmann, K.C., 2000. Oxygen isotope evidence for high-altitude snow in the Laramide Rocky Mountains of North America during the Late Cretaceous and Paleogene. Geology 28, 243–246.

Dufour, E., Holmden, C., Van Neer, W., Zazzo, A., Patterson, W.P., Degryse, P., Keppens, E., 2007. Oxygen and strontium isotopes as provenance indicators of fish at archaeological sites: the case study of Sagalassos, SW Turkey. Journal of Archaeological Science 34, 1226–1239.

Eagle, R.A., Tütken, T., Martin, T.S., Tripati, A.K., Fricke, H.C., Connely, M., Cifelli R.L., Eiler, J.M., 2011. Dinosaur body temperatures determined from isotopic (^{13}C-^{18}O) ordering in fossil biominerals. Science 333, 443–445.

Ebner, V. von, 1902. Histologie der Zähne mit Einschluss der Histogenese. In: Handbuch der Zahnheilkunde. Scheff, J. (Ed.), pp. 243–299

Erickson, G.M., 1996. Incremental lines of von Ebner in dinosaurs and the assessment of tooth replacement rates using growth line counts. Proceedings of the National Academy of Sciences 93, 14623–14627.

Erickson, G.M., 2014. On dinosaur growth. Annual Review of Earth and Planetary Sciences 42, 675–697.

Erickson, G.M., Sidebottom, M.A., Kay, D.I., Turner, K.T., Ip, N., Norell, M.A., Sawyer, W.G., Krick, B.A., 2015. Wear biomechanics in the slicing dentition of the giant horned dinosaur *Triceratops*. Science Advances 1, e1500055.

Erickson, G.M., Zelenitsky, D.K., Kay, D.I., Norell, M.A., 2017. Dinosaur incubation periods directly determined from growth-line counts in embryonic teeth show reptilian-grade development. Proceedings of the National Academy of Sciences 114, 540–545.

Farke, A.A., Wolff, E.D., Tanke, D.H., 2009. Evidence of combat in *Triceratops*. PLoS One 4, e4252.

Fastovsky, D.E., Bercovici, A., 2016. The Hell Creek Formation and its contribution to the Cretaceous–Paleogene extinction: A short primer. Cretaceous Research 57, 368–390.

FitzGerald, C.M., 1998. Do enamel microstructures have regular time dependency? Conclusions from the literature and a large-scale study. Journal of Human Evolution 35, 371–386.

Fricke, H.C., Rogers, R.R., 2000. Multiple taxon–multiple locality approach to providing oxygen isotope evidence for warm-blooded theropod dinosaurs. Geology 28, 799–802.

Fricke, H.C., Pearson, D.A., 2008. Stable isotope evidence for changes in dietary niche partitioning among hadrosaurian and ceratopsian dinosaurs of the Hell Creek Formation, North Dakota. Paleobiology 34, 534–552.

Fricke, H.C., Rogers, R.R., Backlund, R., Dwyer, C.N., Echt, S., 2008. Preservation of primary stable isotope signals in dinosaur remains, and environmental gradients of the Late Cretaceous of Montana and Alberta. Palaeogeography, Palaeoclimatology, Palaeoecology 266, 13–27.

Fricke, H.C., Rogers, R.R., Gates, T.A., 2009. Hadrosaurid migration: inferences based on stable isotope comparisons among Late Cretaceous dinosaur localities. Paleobiology 35, 270–288.

Garvie-Lok, S.J., Varney, T.L., Katzenberg, M.A., 2004. Preparation of bone carbonate for stable isotope analysis: the effects of treatment time and acid concentration. Journal of Archaeological Science 31, 763–776.

Glimcher, M.J., 2006. Bone: nature of the calcium phosphate crystals and cellular, structural, and physical chemical mechanisms in their formation. Reviews in mineralogy and geochemistry 64, 223–282.

Goedert, J., Amiot, R., Boudad, L., Buffetaut, E., Fourel, F., Godefroit, P., Kusuhashi, N., Suteethorn, V., Tong, H., Watabe, M., Lécuyer, C., 2016. Preliminary investigation of seasonal patterns recorded in the oxygen isotope compositions of theropod dinosaur tooth enamel. Palaios 31, 10–19.

Goodwin, M.B., Clemens, W.A., Horner, J.R., Padian, K., 2006. The smallest known *Triceratops* skull: new observations on ceratopsid cranial anatomy and ontogeny. Journal of Vertebrate Paleontology 26, 103–112.

Graven, H., Keeling, R.F., Rogelj, J., 2020. Changes to Carbon Isotopes in Atmospheric CO2 over the Industrial Era and into the Future. Global biogeochemical cycles 34, e2019GB006170.

Hassler, A., Martin, J.E., Amiot, R., Tacail, T., Godet, F.A., Allain, R., Balter, V., 2018. Calcium isotopes offer clues on resource partitioning among Cretaceous predatory dinosaurs. Proceedings of the Royal Society B: Biological Sciences 285, 20180197.

Hare, V.J., Lavergne, A., 2021. Differences in carbon isotope discrimination between angiosperm and gymnosperm woody plants, and their geological significance. Geochimica et Cosmochimica Acta 300, 215–230.

Herwartz, D., Tütken, T., Jochum, K.P., Sander, P.M., 2013. Rare earth element systematics of fossil bone revealed by LA-ICPMS analysis. Geochimica et Cosmochimica Acta 103, 161–183.

Herwartz, D., Tütken, T., Münker, C., Jochum, K.P., Stoll, B., Sander, P.M., 2011. Timescales and mechanisms of REE and Hf uptake in fossil bones. Geochimica et Cosmochimica Acta 75, 82–105.

Hobson, K.A., Wassenaar, L.I. (Eds.), 2018. Tracking animal migration with stable isotopes. Academic Press, Cambridge.

Hoppe, K.A., 2006. Correlation between the oxygen isotope ratio of North American bison teeth and local waters: Implication for paleoclimatic reconstructions. Earth and Planetary Science Letters 244, 408–417.

Horner, J.R., Goodwin, M.B., 2006. Major cranial changes during *Triceratops* ontogeny. Proceedings of the Royal Society B: Biological Sciences 273, 2757–2761.

Hummel, J., Gee, C.T., Südekum, K.H., Sander, P.M., Nogge, G., Clauss, M., 2008. In vitro digestibility of fern and gymnosperm foliage: implications for sauropod feeding ecology and diet selection. Proceedings of the Royal Society B: Biological Sciences 275, 1015–1021.

Hwang, S.H., 2005. Phylogenetic patterns of enamel microstructure in dinosaur teeth. Journal of Morphology 266, 208–240.

Illies, M.M. C., Fowler, D.W., 2020. *Triceratops* with a kink: Co-ossification of five distal caudal vertebrae from the Hell Creek Formation of North Dakota. Cretaceous Research 108, 104355.

Janssen, R., Joordens, J.C., Koutamanis, D.S., Puspaningrum, M.R., de Vos, J., Van Der Lubbe, J.H., Reijmer, J.J.G., Hampe, O., Vonhof, H.B., 2016. Tooth enamel stable isotopes of Holocene and Pleistocene fossil fauna reveal glacial and interglacial paleoenvironments of hominins in Indonesia. Quaternary Science Reviews 144, 145–154.

Johnson, B.J., Fogel, M.L., Miller, G.H., 1998. Stable isotopes in modern ostrich eggshell: a calibration for paleoenvironmental applications in semi-arid regions of southern Africa. Geochimica et Cosmochimica Acta 62, 2451–2461.

Johnson, K.R., Nichols, D.J., Hartman, J.H., 2002. Hell Creek Formation: A 2001 synthesis. Geological Society of America Special Papers 361, 503–510.

Kaskes, P., Portanger, L.A., Schulp, A.S., 2016. Unravelling the history of a unique *Triceratops* graveyard from eastern Wyoming, USA. In: Holwerda, F., Madern, A., Voeten, D., van Heteren, A., Liston, J., Meijer, H., den Ouden, N., Spiekman, S., Trapman, T., Miedema, F., Bijl, S., Smeets, M., Kaskes, P., Rietbergen, T., Lubeek, J. (Eds.), Program and Abstracts, European Association of Vertebrate Palaeontologists: XIV Annual Meeting, Haarlem, the Netherlands, p. 192.

Kaskes, P., Bastiaans, D., Verhage, O., de Rooij, J., Guliker, M., Schulp, A.S., 2019. Taphonomy of a unique multigenerational *Triceratops* bonebed from eastern Wyoming (USA): New insights from a multi-proxy perspective. In: Godefroit, P., Stein, K., Smith, T., Lambert, O., Olive, S. (Eds.), Program and Abstracts, European Association of Vertebrate Palaeontologists: XVII Annual Meeting, Brussels, Belgium, 2/07/19, vol. 17. p. 54.

Kendall, C., Eriksen, A.M.H., Kontopoulos, I., Collins, M.J., Turner-Walker, G., 2018. Diagenesis of archaeological bone and tooth. Palaeogeography, Palaeoclimatology, Palaeoecology 491, 21–37.

Kim, S.T., Coplen, T.B., Horita, J. 2015. Normalization of stable isotope data for carbonate minerals: implementation of IUPAC guidelines. Geochimica et Cosmochimica Acta 158, 276–289.

Koch, P.L., Tuross, N., Fogel, M.L., 1997. The effects of sample treatment and diagenesis on the isotopic integrity of carbonate in biogenic hydroxylapatite. Journal of Archaeological Science 24, 417–429.

Koch, P.L., 1998. Isotopic reconstruction of past continental environments. Annual Review of Earth and Planetary Sciences 26, 573–613.

Kohn, M.J., 2010. Carbon isotope compositions of terrestrial C3 plants as indicators of (paleo) ecology and (paleo) climate. Proceedings of the National Academy of Sciences 107, 19691–19695.

Kohn, M.J., Cerling, T.E., 2002. Stable isotope compositions of biological apatite. Reviews in Mineralogy and Geochemistry 48, 455–488.

Kohn, M.J., Schoeninger, M.J., Valley, J.W., 1996. Herbivore tooth oxygen isotope compositions: effects of diet and physiology. Geochimica et Cosmochimica Acta 60, 3889–3896.

Kohn, M.J., Schoeninger, M.J., Valley, J.W., 1998. Variability in oxygen isotope compositions of herbivore teeth: reflections of seasonality or developmental physiology? Chemical Geology 152, 97–112.

Konert, M., Vandenberghe, J.E.F., 1997. Comparison of laser grain size analysis with pipette and sieve analysis: a solution for the underestimation of the clay fraction. Sedimentology 44, 523–535.

Krueger, H.W., 1991. Exchange of carbon with biological apatite. Journal of Archaeological Science 18, 355–361.

Laskar, A.H., Mohabey, D., Bhattacharya, S.K., Liang, M.C., 2020. Variable thermoregulation of Late Cretaceous dinosaurs inferred by clumped isotope analysis of fossilized eggshell carbonates. Heliyon 6, e05265.

Layman, C.A., Araujo, M.S., Boucek, R., Hammerschlag-Peyer, C.M., Harrison, E., Jud, Z.R., Matich, P., Rosenblatt, A.E., Vaudo, J.J., Yeager, L.A., Post, D.M., Bearhop, S., 2012. Applying stable isotopes to examine food-web structure: an overview of analytical tools. Biological Reviews 87, 545–562.

Le Boedec, K., 2016. Sensitivity and specificity of normality tests and consequences on reference interval accuracy at small sample size: a computer-simulation study. Veterinary Clinical Pathology 45, 648–656.

Lee-Thorp, J.A., 2002. Preservation of biogenic carbon isotopic signals in Plio-Pleistocene bone and tooth mineral. In: Ambrose, S.H., Katzenberg, M.A. (Eds.), Biogeochemical approaches to paleodietary analysis. Springer, Boston, pp. 89-115.

Lee-Thorp, J.A., van der Merwe, N.J., 1987. Carbon isotope analysis of fossil bone apatite. South African Journal of Science 83, 712–715.

Lee-Thorp, J.A., van der Merwe, N.J., 1991. Aspects of the chemistry of modern and fossil biological apatites. Journal of Archaeological Science 18, 343–354.

Line, S.R., 2000. Incremental markings of enamel in ectothermal vertebrates. Archives of Oral Biology 45, 363–368.

Longrich, N.R., Field, D.J., 2012. *Torosaurus* is not *Triceratops*: ontogeny in chasmosaurine ceratopsids as a case study in dinosaur taxonomy. PloS one 7, e32623.

Lyson, T.R., Longrich, N.R., 2011. Spatial niche partitioning in dinosaurs from the latest Cretaceous (Maastrichtian) of North America. Proceedings of the Royal Society B: Biological Sciences 278, 1158-1164.

Mallon, J.C., Anderson, J.S., 2014. Implications of beak morphology for the evolutionary paleoecology of the megaherbivorous dinosaurs from the Dinosaur Park Formation (upper Campanian) of Alberta, Canada. Palaeogeography, Palaeoclimatology, Palaeoecology 394, 29–41.

Mathews, J.C., Brusatte, S.L., Williams, S.A., Henderson, M.D., 2009. The first *Triceratops* bonebed and its implications for gregarious behavior. Journal of Vertebrate Paleontology 29, 286–290.

McConnaughey, T.A., Burdett, J., Whelan, J.F., & Paull, C.K., 1997. Carbon isotopes in biological carbonates: respiration and photosynthesis. Geochimica et Cosmochimica Acta 61, 611–622.

Nielsen-Marsh, C.M., & Hedges, R.E., 2000. Patterns of diagenesis in bone I: the effects of site environments. Journal of Archaeological Science 27, 1139–1150.

Njau, J.K., Blumenschine, R.J., 2006. A diagnosis of crocodile feeding traces on larger mammal bone, with fossil examples from the Plio-Pleistocene Olduvai Basin, Tanzania. Journal of Human Evolution 50, 142–162.

O'Meara, R.N., Dirks, W., Martinelli, A.G., 2018. Enamel formation and growth in non-mammalian cynodonts. Royal Society Open Science 5, 172293.

Ostrom, J.H., 1966. Functional morphology and evolution of the ceratopsian dinosaurs. Evolution, 290-308.

Ostrom, P.H., Macko, S.A., Engel, M.H., Russell, D.A., 1993. Assessment of trophic structure of Cretaceous communities based on stable nitrogen isotope analyses. Geology 21, 491–494.

Passey, B.H., Robinson, T.F., Ayliffe, L.K., Cerling, T.E., Sponheimer, M., Dearing, M.D., Roeder, B.L., Ehleringer, J.R., 2005. Carbon isotope fractionation between diet, breath CO_2, and bioapatite in different mammals. Journal of Archaeological Science 32, 1459–1470.

Pearson, D.A., Schaefer, T., Johnson, K.R., Nichols, D.J., Hunter, J.P., 2002. Vertebrate biostratigraphy of the Hell Creek formation in southwestern North Dakota and northwestern South Dakota. Geological Society of America Special Paper 361, 145–167.

Pecquerie, L., Nisbet, R.M., Fablet, R., Lorrain, A., Kooijman, S.A., 2010. The impact of metabolism on stable isotope dynamics: a theoretical framework. Philosophical Transactions of the Royal Society B: Biological Sciences 365, 3455–3468.

Pellegrini, M., Snoeck, C., 2016. Comparing bioapatite carbonate pre-treatments for isotopic measurements: Part 2—Impact on carbon and oxygen isotope compositions. Chemical Geology 420, 88–96.

Pellegrini, M., Lee-Thorp, J.A., Donahue, R.E., 2011. Exploring the variation of the $\delta^{18}O_p$ and $\delta^{18}O_c$ relationship in enamel increments. Palaeogeography, Palaeoclimatology, Palaeoecology 310, 71–83.

Rey, K., Amiot, R., Fourel, F., Abdala, F., Fluteau, F., Jalil, N.E., Liu, J., Rubidge, B.S., Smith, R.M.H., Steyer, J.S., Viglietti, P.A., Wang, X., Lecuyer, C., 2017. Oxygen isotopes suggest elevated thermometabolism within multiple Permo-Triassic therapsid clades. Elife 6, e28589.

Rey, K., Day, M.O., Amiot, R., Fourel, F., Luyt, J., Lécuyer, C., Rubidge, B.S., 2020. Stable isotopes ($\delta^{18}O$ and $\delta^{13}C$) give new perspective on the ecology and diet of *Endothiodon bathystoma* (Therapsida, Dicynodontia) from the late Permian of the South African Karoo Basin. Palaeogeography, Palaeoclimatology, Palaeoecology 556, 109882.

Sage, R.F., 2004. The evolution of C4 photosynthesis. New phytologist 161, 341–370.

Sander, P.M., 1999. The microstructure of reptilian tooth enamel: terminology, function, and phylogeny. Münchner Geowissenschaftliche Abhandlungen A 38, 1–102.

Scannella, J.B., Fowler, D.W., Goodwin, M.B., Horner, J.R., 2014. Evolutionary trends in *Triceratops* from the Hell Creek formation, Montana. Proceedings of the National Academy of Sciences 111, 10245–10250.

Schulp, A.S., Vonhof, H.B., Van der Lubbe, J.H.J.L., Janssen, R., Van Baal, R.R., 2013. On diving and diet: resource partitioning in type-Maastrichtian mosasaurs. Netherlands Journal of Geosciences 92, 165–170.

Schwarcz, H.P., 2015. The ultrastructure of bone as revealed in electron microscopy of ion-milled sections. Seminars in Cell & Developmental Biology 46, 44–50.

Ségalen, L., Lee-Thorp, J.A., 2009. Palaeoecology of late Early Miocene fauna in the Namib based on $^{13}C/^{12}C$ and $^{18}O/^{16}O$ ratios of tooth enamel and ratite eggshell carbonate. Palaeogeography, Palaeoclimatology, Palaeoecology 277, 191–198.

Sheldon, N.D., Smith, S.Y., Stein, R., Ng, M., 2020. Carbon isotope ecology of gymnosperms and implications for paleoclimatic and paleoecological studies. Global and Planetary Change 184, 103060.

Smith, T.M., 2006. Experimental determination of the periodicity of incremental features in enamel. Journal of Anatomy 208, 99–113.

Smith, B.N., Epstein, S., 1971. Two categories of $^{13}C/^{12}C$ ratios for higher plants. Plant Physiology 47, 380–384.

Smith, D.M., Grasty, R.C., Theodosiou, N.A., Tabin, C.J., Nascone-Yoder, N.M., 2000. Evolutionary relationships between the amphibian, avian, and mammalian stomachs. Evolution & Development 2, 348–359.

Snoeck, C., Pellegrini, M., 2015. Comparing bioapatite carbonate pre-treatments for isotopic measurements: Part 1—Impact on structure and chemical composition. Chemical Geology 417, 394–403.

Stanton Thomas, K.J., & Carlson, S.J., 2004. Microscale $\delta^{18}O$ and $\delta^{13}C$ isotopic analysis of an ontogenetic series of the hadrosaurid dinosaur *Edmontosaurus*: implications for physiology and ecology. Palaeogeography Palaeoclimatology Palaeoecology 206, 257–287.

Straight, W.H., Barrick, R.E., Eberth, D.A., 2004. Reflections of surface water, seasonality and climate in stable oxygen isotopes from tyrannosaurid tooth enamel. Palaeogeography, Palaeoclimatology, Palaeoecology 206, 239–256.

Tafforeau, P., Bentaleb, I., Jaeger, J.J., Martin, C., 2007. Nature of laminations and mineralization in rhinoceros enamel using histology and X-ray synchrotron microtomography: potential implications for palaeoenvironmental isotopic studies. Palaeogeography, Palaeoclimatology, Palaeoecology 246, 206–227.

Taiz, L., Zeiger, E., Møller, I. M., Murphy, A., 2015. Plant physiology and development (No. Ed. 6). Sinauer Associates Incorporated, Sunderland.

Tejada-Lara, J.V., MacFadden, B.J., Bermudez, L., Rojas, G., Salas-Gismondi, R., Flynn, J.J. 2018. Body mass predicts isotope enrichment in herbivorous mammals. Proceedings of the Royal Society B 285, 20181020.

Tejada, J.V., Flynn, J.J., Antoine, P.O., Pacheco, V., Salas-Gismondi, R., Cerling, T.E. 2020. Comparative isotope ecology of western Amazonian rainforest mammals. Proceedings of the National Academy of Sciences 117, 26263–26272.

Terrill, D.F., Henderson, C.M., Anderson, J.S., 2020. New application of strontium isotopes reveals evidence of limited migratory behaviour in Late Cretaceous hadrosaurs. Biology Letters 16, 20190930.

Thompson, T.J.U., Gauthier, M., Islam, M. 2009. The application of a new method of Fourier Transform Infrared Spectroscopy to the analysis of burned bone. Journal of Archaeological Science 36, 910–914.

Tieszen, L.L., 1991. Natural variations in the carbon isotope values of plants: implications for archaeology, ecology, and paleoecology. Journal of Archaeological Science 18, 227–248.

Tobin, T.S., Wilson, G.P., Eiler, J.M., Hartman, J.H., 2014. Environmental change across a terrestrial Cretaceous-Paleogene boundary section in eastern Montana, USA, constrained by carbonate clumped isotope paleothermometry. Geology 42, 351–354.

Trueman, C.N., 2013. Chemical taphonomy of biomineralized tissues. Palaeontology 56, 475–486.

Trueman, C., Chenery, C., Eberth, D.A., Spiro, B., 2003. Diagenetic effects on the oxygen isotope composition of bones of dinosaurs and other vertebrates recovered from terrestrial and marine sediments. Journal of the Geological Society 160, 895–901.

Tütken, T., 2011. The diet of sauropod dinosaurs: Implications from carbon isotope analysis of teeth, bones, and plants. In: Klein, N., Remes, C., Gee, C.T., Sander, P.M. (Eds.), Biology of the sauropod dinosaurs: Understanding the life of giants. Indiana University Press, Bloomington, pp. 57-79.

Tütken, T., Pfretzschner, H.U., Vennemann, T.W., Sun, G., Wang, Y.D., 2004. Paleobiology and skeletochronology of Jurassic dinosaurs: implications from the histology and oxygen isotope compositions of bones. Palaeogeography, Palaeoclimatology, Palaeoecology 206, 217–238.

Tütken, T., Vennemann, T.W., Pfretzschner, H.U., 2011. Nd and Sr isotope compositions in modern and fossil bones–Proxies for vertebrate provenance and taphonomy. Geochimica et Cosmochimica Acta 75, 5951–5970.

Vonhof, H.B., De Graaf, S., Spero, H.J., Schiebel, R., Verdegaal, S.J., Metcalfe, B., Haug, G.H. 2020. High-precision stable isotope analysis of <5 μg $CaCO_3$ samples by continuous-flow mass spectrometry. Rapid Communications in Mass Spectrometry 34, e8878.

Wang, Y., Cerling, T.E., 1994. A model of fossil tooth and bone diagenesis: implications for paleodiet reconstruction from stable isotopes. Palaeogeography, Palaeoclimatology, Palaeoecology 107, 281–289.

Wang, Y., Wang, X., Xu, Y., Zhang, C., Li, Q., Tseng, Z.J., Takeuchi, G., Deng, T., 2008. Stable isotopes in fossil mammals, fish and shells from Kunlun Pass Basin, Tibetan Plateau: paleo-climatic and paleo-elevation implications. Earth and Planetary Science Letters 270, 73–85.

Waskow, K., Sander, P.M., 2014. Growth record and histological variation in the dorsal ribs of *Camarasaurus* sp. (Sauropoda). Journal of Vertebrate Paleontology 34, 852–869.

Wei, L.L., Yan, C.L., Ye, B.B., Guo, X.Y., 2008. Relationship between salinity and stable carbon isotope composition of C3 plants. Acta Ecologica Sinica 28, 1270–1278.

Weiner, S., Bar-Yosef, O., 1990. States of preservation of bones from prehistoric sites in the Near East: a survey. Journal of Archaeological Science 17, 187–196.

Wright, L.E., Schwarcz, H.P., 1996. Infrared and isotopic evidence for diagenesis of bone apatite at Dos Pilas, Guatemala: palaeodietary implications. Journal of Archaeological Science 23, 933–944.

Zazzo, A., Lécuyer, C., Mariotti, A., 2004. Experimentally-controlled carbon and oxygen isotope exchange between bioapatites and water under inorganic and microbially-mediated conditions. Geochimica et Cosmochimica Acta 68, 1–12.

Zhao, Y., Yang, Y.B., Guo, Y., Ren, G.Y., Zhang, F.C., 2021. Stable carbon isotope composition of bone hydroxylapatite: significance in paleodietary analysis. Palaeoworld 31, 169–184.

4
379
360

Chapter 4. Exploring the ceratopsid growth record: a comprehensive osteohistological analysis of *Triceratops* (Ornithischia: Ceratopsidae) and its implications for growth and ontogeny

Published as:
de Rooij, J., Lucassen, S. A. N., Furer, C., Schulp, A. S., Sander, P. M., 2023. Exploring the ceratopsid growth record: comprehensive osteohistological analysis of *Triceratops* (Ornithischia: Ceratopsidae) and its implications for growth and ontogeny**.** *Cretaceous Research, 154, 105738*. DOI: https://doi.org/10.1016/j.cretres.2023.105738

Abstract
Ceratopsids represent one of the most iconic groups of non-avian dinosaurs. These large quadrupedal ornithischians are well-known for their bizarre cranial ornamentations, which are distinctive among different ceratopsids. However, only very little data exist on ceratopsid osteohistology and growth rates. Here, we present a detailed osteohistological analysis on *Triceratops horridus* preserved in a relatively large bonebed from the Lance Formation (eastern Wyoming, USA) as well as additional *Triceratops* cf. *prorsus* specimens from Canada. Deciphering the bone microstructure of this iconic dinosaur allows to better understand the growth and development of ceratopsids. The *Triceratops* limb elements show a distinct pattern of slower growing parallel-fibred and faster growing woven-parallel bone tissue that serves as basis for the definition of histologic ontogenetic stages (HOS). Lower (i.e., younger) HOS correspond to woven-parallel tissue while higher (i.e., older) HOS correspond to parallel-fibred tissue. The intraskeletal variation in histology is best explained through the Three-Front Model, indicating significant differences in cortical thickness between different limb bones. The *Triceratops* primary growth record is poorly expressed, and the few growth marks preserved show irregular spacing inconsistent with expected growth patterns. The HOS scheme provides seven stages that correspond to biological age classes and that show a correlation with body size. Our analysis suggests that the taxonomic ambiguity between *Torosaurus* and *Triceratops* cannot be solved based purely on histological data, but requires additional taphonomic, taxonomic and histological analyses. This study expands the current ceratopsian histological database and helps to better understand ceratopsid growth patterns.

4.1 Introduction
Bone histology informs about dinosaur growth patterns, age, longevity, (sexual) maturity, and metabolism (Chinsamy et al., 2012; Erickson, 2014; Horner et al., 1999; Sander, 2000; Waskow and Sander, 2014; Woodward et al., 2020). Almost all major dinosaur groups have received considerable attention in osteohistological analyses, including various species of sauropods (Klein and Sander, 2008; Sander, 2000; Sander et al., 2011; Waskow, 2019), theropods (Cullen et al., 2020; Horner and Padian, 2004), hadrosaurs (Horner et al., 2000; Słowiak et al., 2020) and thyreophorans such as stegosaurs (Redelstorff et al., 2013; Redelstorff and Sander, 2009; Waskow and Mateus, 2017) and ankylosaurs (Stein et al., 2013). However, to date horned dinosaurs have received little attention in osteohistological studies. Especially the osteohistology of more derived quadrupedal ceratopsids from North America remains vastly understudied, despite these comprising one of the most species-rich and well-sampled dinosaur groups.

The few histological analyses conducted on ceratopsians are restricted to more basal taxa such as *Psittacosaurus* (Erickson and Tumanova, 2000; Skutschas et al., 2021; Zhao et al., 2019), *Protoceratops* (Fostowicz-Frelik and Słowiak, 2018) and *Koreaceratops* (Baag and Lee, 2022). Ceratopsid histology has mostly been investigated in unpublished thesis projects and/or conference abstracts (including *Centrosaurus* (Lee, 2007), *Einiosaurus* (Reizner, 2010), *Kosmoceratops* (Levitt, 2013), *Pachyrhinosaurus* (Goldsmith, 2018; Vice, 2020), *Utahceratops* (Levitt, 2013), and *Triceratops* (de Rooij, 2018)). These works hinted at differences in growth rate between more basal and more derived ceratopsids, mostly through histological markers such as remodelling patterns and cyclical growth marks. The limited body of published ceratopsid histology covers *Pachyrhinosaurus* (Erickson and Druckenmiller, 2011), *Avaceratops* (Hedrick et al., 2020), *Yehuecauhceratops* (Hedrick et al., 2020), as well as brief histological descriptions of *Medusaceratops* (Chiba et al., 2018) and *Spiclypeus* (Mallon et al., 2016). In addition, Horner and Lamm (2011) explored the histology of the *Triceratops* parietal frill, while Mallon et al. (2022) described femoral histology of *Torosaurus*. However, the results in these projects provided limited data on ceratopsian growth patterns and were often based on single – and fragmentary – elements. In fact, chasmosaurine and centrosaurine species are almost exclusively identified based on their cranial ornamentation, and limb elements suitable for histological sectioning have been described much less often (Chiba et al., 2018; Chinnery, 2004; Holmes and Ryan, 2013; Maidment and Barrett, 2011; Mallon et al., 2016; Mallon and Holmes, 2010; Scott et al., 2023). As a result, the ceratopsian histological record remains relatively unexplored, and our understanding of ceratopsid growth strategies is still limited.

Here we provide an in-depth osteohistological description of *Triceratops*, an iconic horned dinosaur from the Late Cretaceous of North America. The histological analysis is based on a multi-element approach across multiple individuals to visualize and understand their bone microstructure in as much detail as possible. Comparisons with other dinosaur taxa for which detailed histological data are available allow to better comprehend ceratopsid growth strategies and potential life history parameters. Additionally, the data presented here help constrain the timing of ontogenetic characters well-known for *Triceratops* (Goodwin et al., 2006; Horner and Goodwin, 2006).

4.2 Material and methods

4.2.1 Institutional abbreviations

CMN, Canadian Museum of Nature, Ottawa, Canada; RSM, Royal Saskatchewan Museum, Regina, Canada; RGM, Rijksmuseum voor Geologie en Mineralogie (now NBC, Naturalis Biodiversity Center, Leiden, the Netherlands).

4.2.2 Geological background

The majority of the material used in this study is part of a relatively large monodominant mass death assemblage preserving the remains of at least five individuals belonging to the genus *Triceratops* (see de Rooij et al., 2022 for more details). The bonebed, named the 'Darnell *Triceratops* Bonebed' (DTB), occurs in eastern Wyoming, USA on the south-eastern flank of the Powder River Basin. It is situated in the upper Maastrichtian Lance Formation (Bartos et al., 2021) and – based on its closer proximity to the underlying Fox Hills Formation – dates back to c. 67 Mya. Its stratigraphic position as well as preliminary surveys on preserved cranial elements suggest that the preserved species pertains to *Triceratops horridus* (Bastiaans et a., 2016; Forster, 1996b; Scannella et al., 2014). A low-energy depositional environment combined with rapid burial resulted in overall excellent preservation of the

fossil material (Kaskes et al., 2019; de Rooij et al., 2022). However, subsequent crevasse splay events as evidenced by increase in lithogenic grain size resulted in reburial of the fossil elements and caused high degrees of disarticulation (de Rooij et al., 2022). The DTB is characterized by a relatively large proportion of post-cranial elements including limb and girdle bones, ribs and vertebrae. For the limb bones in particular, it is clear that the material represents only larger individuals close to known maximum body size for *Triceratops*. Morphological distortion is limited, and the majority of the skeletal elements retain their original bone surface, providing for the first time excellent opportunities for histological sectioning of a relatively large group of *Triceratops*.

4.2.3 Specimen selection

Limb bones are the most suitable candidates in histological analyses based on their relatively simple (i.e., symmetrical) morphology and growth pattern, providing a representative image of the developmental history in studied sections (Sander, 2000). Additionally, limb bones provide the best suitable data source for body size reconstructions (Klein and Sander, 2008; Sander, 2000; Sander et al., 2011; Waskow and Sander, 2014). The femur and humerus are frequently studied in dinosaur histological research, as they possess the thickest cortex at midshaft preserving the most complete growth record (Sander, 2000). However, to explore the preservation of the histological record in different limb elements as thoroughly as possible, we selected all three autopodial and zeugopodial forelimb (radius, ulna, humerus) and hindlimb (fibula, tibia, femur) elements to study the *Triceratops* histology.

In addition to the bonebed material, we sampled an additional six *Triceratops* limb elements housed in various Canadian institutes in order to expand the coverage of ontogenetic ranges in our sampling strategy as much as possible. These include material housed in the collections of CMN and RSM. The Canadian specimens were not identified to the species level, but as they were all preserved in the Frenchman Formation, they most likely pertain to *Triceratops prorsus* (Tokaryk, 1986). As such, the complete dataset consists of both *Triceratops* species which could potentially introduce some degree of uncertainty when discussing the histological data. However, considering that the majority of the samples are from a single species and the ontogenetic range is relatively large, we do not expect appreciable offsets in histology as a result of taxonomic differences. Moreover, ceratopsids show a relatively conserved post-cranial skeleton (Chinnery, 2010) which is not expected to translate to significant differences in histology, especially for the two closely related *Triceratops* species which are distinguished based on mostly cranial characteristics (Forster, 1996ab). Nevertheless, we incorporated both taxa in our histological analysis to provide additional context on potential histological and ontogenetic offsets related to taxonomic differences (see section 4.7). The dataset is represented by a total of two radii, three ulnae, six humeri, four fibulae, six tibiae and four femora. Table 1 provides a complete list of all the sampled material and their details, and Figure S2-5 shows photographs of all limb bones sampled for this study.

Additionally, it has been shown that sauropod dinosaurs may preserve a near-complete growth record in their ribs (Waskow, 2019; Waskow and Sander, 2014), but previous work on centrosaurine rib histology returned poorly preserved primary growth records (Hedrick et al., 2020). Thus, to further explore the preservation of the histological record in different skeletal elements, we sampled the axial skeleton of *Triceratops*, including three ribs and neural and transverse vertebral processes. Ribs and vertebrae were selected to cover a wide range of the *Triceratops* anatomy, and include a cervical vertebra, thoracic vertebra, an anteriorly positioned rib and posteriorly positioned rib (position reconstructed based on proximal bend in capitulum).

Table 1. List of specimens sampled and discussed in this study. Where applicable, these include details on the dimensions of the skeletal elements as well as inferred histologic ontogenetic stage (HOS). Percentage maximum lengths are calculated by comparing bone lengths to calculated bone proportions for each limb bone type, based on an associated specimen of *Triceratops horridus* (see section 2.5 and Table S1 for details on calculation). Portions of cortical thickness in sample is calculated by dividing the measured cortical thickness by the length of the core sample. Cortical thickness represents the radius of the bone and was measured from the innermost medullary cavity to the bone surface using the CT scans in Supplements Figure 1. Measurements with an asterisk (*) indicate reconstructed lengths of incomplete limb bones based on scaling and extrapolation of other well-preserved bones.

Collection ID	Species	Element	Side	Length (mm)	% Maximum length	Circumference at plane of sampling (mm)	Cortical thickness at sample site (mm)	Length of core sample (mm)	Portion cortical thickness in core sample	HOS
RGM.1394097	*Triceratops horridus*	Rib	-	-	-	-	-	-	-	-
RGM.1394098	*Triceratops horridus*	Rib	-	-	-	-	-	-	-	-
RGM.1394100	*Triceratops horridus*	Dorsal vertebra	-	-	-	-	-	-	-	-
RGM.1394101	*Triceratops horridus*	Cervical vertebra	-	-	-	-	-	-	-	-
RGM.1394102	*Triceratops horridus*	Humerus	Left	761	99	382	23	24	1.04	6
RGM.1394103	*Triceratops horridus*	Humerus	Right	651*	85	313	22	24	1.09	4
RSM P.2691	*Triceratops* cf. *prorsus*	Humerus	Left	205	27	89	4	18	> 1.00	2
RSM P.3324.6.1	*Triceratops* cf. *prorsus*	Humerus	Left	550	72	-	-	8	< 1.00	3
CMN 9533	*Triceratops* cf. *prorsus*	Humerus	Right	-	-	445	-	31	> 1.00	6
RSM P.1163.9	*Triceratops* cf. *prorsus*	Humerus	Left	803	105	472	-	22	> 1.00	7
RGM.1394104	*Triceratops horridus*	Radius	Left	482	110	219	17	24	1.41	6
RGM.1394105	*Triceratops horridus*	Radius	Right	462	106	212	13	13	1.00	7
RGM.1394106	*Triceratops horridus*	Ulna	Right	680	99	288	29	20	0.69	7
RGM.1394107	*Triceratops horridus*	Ulna	Right	649*	95	265	24	20	0.83	5
RSM P.2095	*Triceratops* sp.	Ulna	Left	613	90	290	-	19	< 1.00	7
RGM.1394108	*Triceratops horridus*	Femur	Right	1125*	10	479	43	44	1.02	6
RGM.1394109	*Triceratops horridus*	Femur	Right	1039	93	469	38	38	1.00	4-5
RGM.1394110	*Triceratops horridus*	Femur	Left	1120	100	408	34	24	0.71	6
RGM.1394111	*Triceratops horridus*	Femur	Right	1004	90	429	37	37	1.00	4
RGM.1394112	*Triceratops horridus*	Tibia	Right	-	-	-	-	24	< 1.00	5
RGM.1394113	*Triceratops horridus*	Tibia	Left	785	102	368	-	18	< 1.00	6
RGM.1394114	*Triceratops horridus*	Tibia	Left	781	101	355	41	37	0.90	6
RGM.1394115	*Triceratops horridus*	Tibia	Right	783*	101	367	34	32	0.94	6
RGM.1394116	*Triceratops horridus*	Tibia	Right	740	96	331	38	23	0.61	5
RGM.1394117	*Triceratops horridus*	Tibia	Left	704	91	324	35	36	1.03	5
RGM.1394118	*Triceratops horridus*	Fibula	Left	645	86	163	15	21	1.40	5
RGM.1394119	*Triceratops horridus*	Fibula	Left	616	85	157	12	11	0.92	7
RGM.1394120	*Triceratops horridus*	Fibula	Right	637	88	157	10	10	1.00	6
CMN.57065	*Triceratops cf.* prorsus	Fibula	-	-	-	206	-	21	> 1.00	7

4.2.4 Histological sampling strategy

Traditional histological sampling and thin-sectioning requires a complete cross-section of limb bones (Chinsamy and Raath, 1992; Stein and Sander, 2009). This approach severely compromises the original morphology of fossils and curators are thus understandably more reluctant to grant access, especially when considering unique and well-preserved material suitable for museum exhibitions. However, well-preserved fossils generally have equally well-preserved internal microstructure suitable for histology, and knowing more about the histology provides additional information to enrich museum exhibitions as well. To minimize the impact on the material, we opted for a different approach. The sampling strategy applied here combines the histological coring method (HCM, Sander, 2000; Stein and Sander, 2009) with medical CT scans (Figure 1). CT imaging prior to sampling as best practice complements the HCM by revealing the ideal sampling location on each element. Identification of the most suitable sampling area on a specific bone is based on overall preservation such as fractures/cracks and diagenetic infill surrounding the mid-diaphysis (see Supplements for details on CT scans). Additionally, each sampling area was only considered if it was available in all bones of the same type. Following these two criteria helped determining standardized sampling locations for each limb bone type. CT cross-sections and sampling locations for each available (limb) bone are found in Figure S1. Accordingly, this approach enables homologous sampling important for inter-bone comparisons (Cullen et al., 2021; Prondvai et al., 2018; Sander, 2000; Woodward et al., 2014), and provides access to the internal bone microstructure of unique material with minimal impact on its morphology.

The two ribs and vertebral processes were sampled without using CT scans as visual inspection yielded sufficient confidence on preservation and ideal sampling location. The axial skeletal elements were sampled following a transect from proximal to distal end (Figure 1), yielding five samples for rib RGM.1394097, three samples for rib RGM.1394098, four samples for dorsal vertebra RGM.1394100 and three samples for cervical vertebra RGM.1394101. The rib sections did not cover the entire length

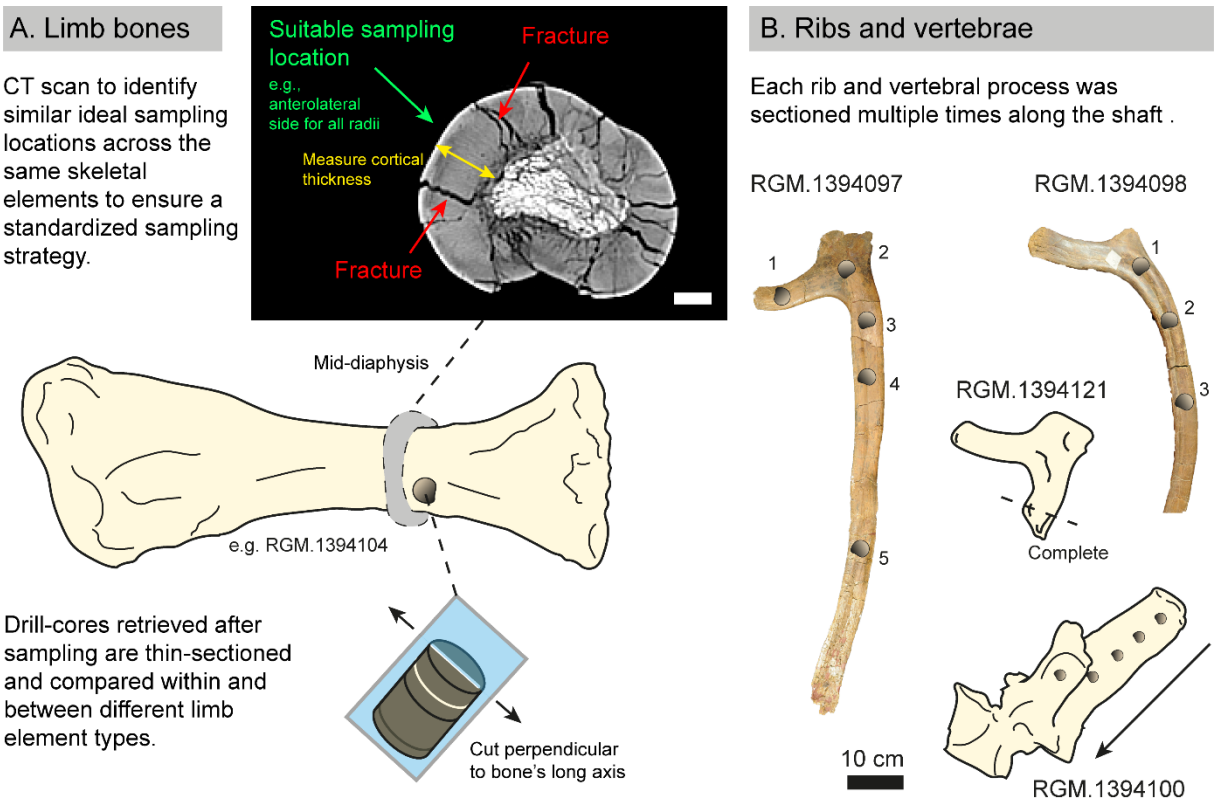

Figure 1. Overview of the applied methodology for limb and axial bones. Scale bar in the CT image is 1 cm.

of the rib, and the most distal sample reached approximately just over halfway of the total shaft length due to relatively poor preservation of rib elements (e.g., RGM.1394097, Figure 1). Core samples were retrieved centrally between the medial and lateral area of the shaft, intersecting both the anterior and posterior cortical surface. In addition, we made a complete thin-section of rib RGM.1394121 just distally from the tuberculum-capitulum junction to compare the medial- and lateral-most areas with samples from the HCM (Figure 1).

Thin-sections were prepared following standard methods (cf. Chinsamy and Raath, 1992, Lamm and Padian, 2013), where each sample was ground by hand until the desired thickness was reached. Sections were studied under normal transmitted and polarized transmitted light using a Leica DMR light microscope housed at Naturalis Biodiversity Center, the national natural history museum of the Netherlands. Photographs were taken using a Nikon DS-Ri2 digital microscope camera mounted on a Nikon Eclipse E600POL polarizing light microscope housed in the Dutch Gemmology Laboratory at Naturalis. Terminology for histological markers follows Buffrénil and Quilhac (2021).

4.2.5 Osteohistological analysis

In an effort to analyse the *Triceratops* histology beyond the description of basic histological markers, we focussed on additional methods to better constrain the growth patterns and age classes of the DTB *Triceratops*. First of all, we identified (annual) growth cycles in specific limb elements to evaluate the preservation of the primary growth record and potential for a skeletochronological analysis. Additionally, we applied the three-front model (Mitchell and Sander, 2014) to describe and better understand the observed histovariability between different types of limb elements. Although originally developed for sauropod dinosaurs, the three-front model can be applied to any histological description of the periosteal territory in amniotes (e.g., in plesiosaurs; Sander and Wintrich, 2021). The three-front model conceptualizes the observed patterns of cortical histology as the result of the interplay of three fronts. These simultaneously migrate from the centre of the bone outwards but differ in speed. Bone tissue is initially laid down by the apposition front (AF) which is followed by the Haversian substitution front (HSF), turning the primary tissue to secondary tissue. The HSF then is followed by the resorption front (RF) which turns compact tissue to cancellous tissue or an open medullary space (Mitchell and Sander, 2014).

The speed of the AF can be determined from histological indicators (e.g., parallel-fibered vs. woven bone, density and direction of vascular canals) but that of the HSF is considered constant, at least within a single low-level clade (Mitchell and Sander, 2014). For want of a method of speed determination of the HSF, constant speed is the most parsimonious assumption. The fact that the three-front model approach produced internally consistent results with its assumption of constant speed of the HSF (Mitchell and Sander, 2014) suggests that this assumption is reasonable. The speed of the RF is determined relative to the other two fronts. Note that the RF can overtake the HSF, resulting in a lack of remodelling, and that the HSF will overtake the AF when skeletal maturity is reached, resulting in a completely remodelled cortex (Mitchell and Sander, 2014).

Complementing the three-front model, we focussed on erecting histological ontogenetic stages (HOS, see Klein and Sander, 2008; Mitchell et al., 2017; Sander and Wintrich 2021) to establish a histological growth series for *Triceratops.* HOS were formulated based on the prevalence of different tissue types in any given section. Tissue types of use in defining HOS were described based mostly on characteristics of the bone matrix organisation, vascularity (primary osteons and simple vascular canals) and bone remodelling patterns.

In order to more accurately constrain the histological results of the skeletochronological analysis, the application of the three-front model and HOS, we calculated the percentage total lengths compared to estimated maximum lengths for each long bone (Table S1). First, we calculated limb to femur ratios for each limb bone based on associated *Triceratops horridus* skeleton RGM.1332500 from Naturalis Biodiversity Center, the Netherlands. While a detailed taphonomic description is outside the scope of this contribution and currently in preparation, RGM.1332500 preserves associated stylopodia and zeugopodia as suggested by the uniform preservation and relative association of the fossilised bones (see Figure S1 for the bonemap). Moreover, the lack of any duplicate elements as well as the presence of a narrow intraskeletal size range suggests that RGM.1332500 allows for accurate isometric scaling of the studied bones, at least for the want of published descriptions of associated skeletons. We acquired limb-to-femur ratios for all limb elements based on RGM.1332500, and applied this value to the largest femur available in this study, RGM.1394110 (Figure S4). This allowed us to obtain a reliable estimate of *Triceratops* limb bones of potentially maximum size. Measurements of the studied bones were then divided by the corresponding calculated maximum size to obtain percentage maximum size estimates of each long bone (Table 1).

To compare the results of the histologic ontogenetic stages between *T. horridus, T. prorsus* and *Torosaurus* (see section 4.7), we calculated values for bone circumference normalized to associated femur circumference. We opted for this approach as the *Torosaurus* specimen was too fragmentary for length measurements leaving circumference as the most ideal proxy for body size (Mallon et al., 2022). We first calculated limb-to-femur ratios for circumference measurements using RGM.1332500, and then applied the acquired ratios to calculate normalized circumference values for each sampled humerus, tibia and femur. This allowed us to visualize the relationship between potential body size and histologic ontogenetic stages for all three taxa (Figure 19).

4.3 Results

4.3.1 Humeri

The *Triceratops* humeri are represented by an ontogenetic series of small, medium-sized and large individuals (Table 1). Overall, histology of *Triceratops* humeri show large areas of parallel-fibred bone tissue, where it substitutes the woven bone in a mostly longitudinal woven-parallel complex (Figure 2B, D). They show cyclical patterns of parallel-fibred bone and woven bone, in which the parallel-fibred bone becomes increasingly more dominant towards the bone surface (Figure 2C). This cyclicity is more prominent in larger humeri (Figure 2). The smallest humerus (RSM P.2691) shows woven-parallel bone tissue containing a mixture of predominantly circumferential and longitudinal canals (Figure 2A), while the second smallest humerus (RSM P.3324.6.1) already has shifted to clear parallel-fibred bone tissue near the bone surface (Figure 2B). Among the larger humeri, the deeper cortex shows larger areas of woven-parallel bone tissue, but this quickly grades inwards into Haversian bone, and the primary tissue towards the bone surface shows an increase in bone tissue organisation (Figure 2C). Nevertheless, the periosteal surface still contains patches of organized and unorganized bone matrix. The predominant vascularity is characterized by longitudinal primary osteons accompanied by small amounts of randomly distributed circumferential osteons (with poorly defined laminae). However, the longitudinal osteons are relatively small, and are almost always positioned in circular rows parallel to the bone surface. These highly organized closely spaced longitudinal canals may resemble circumferential canals at lower magnification, thus the primary bone sometimes appears laminated (Figure 2C).

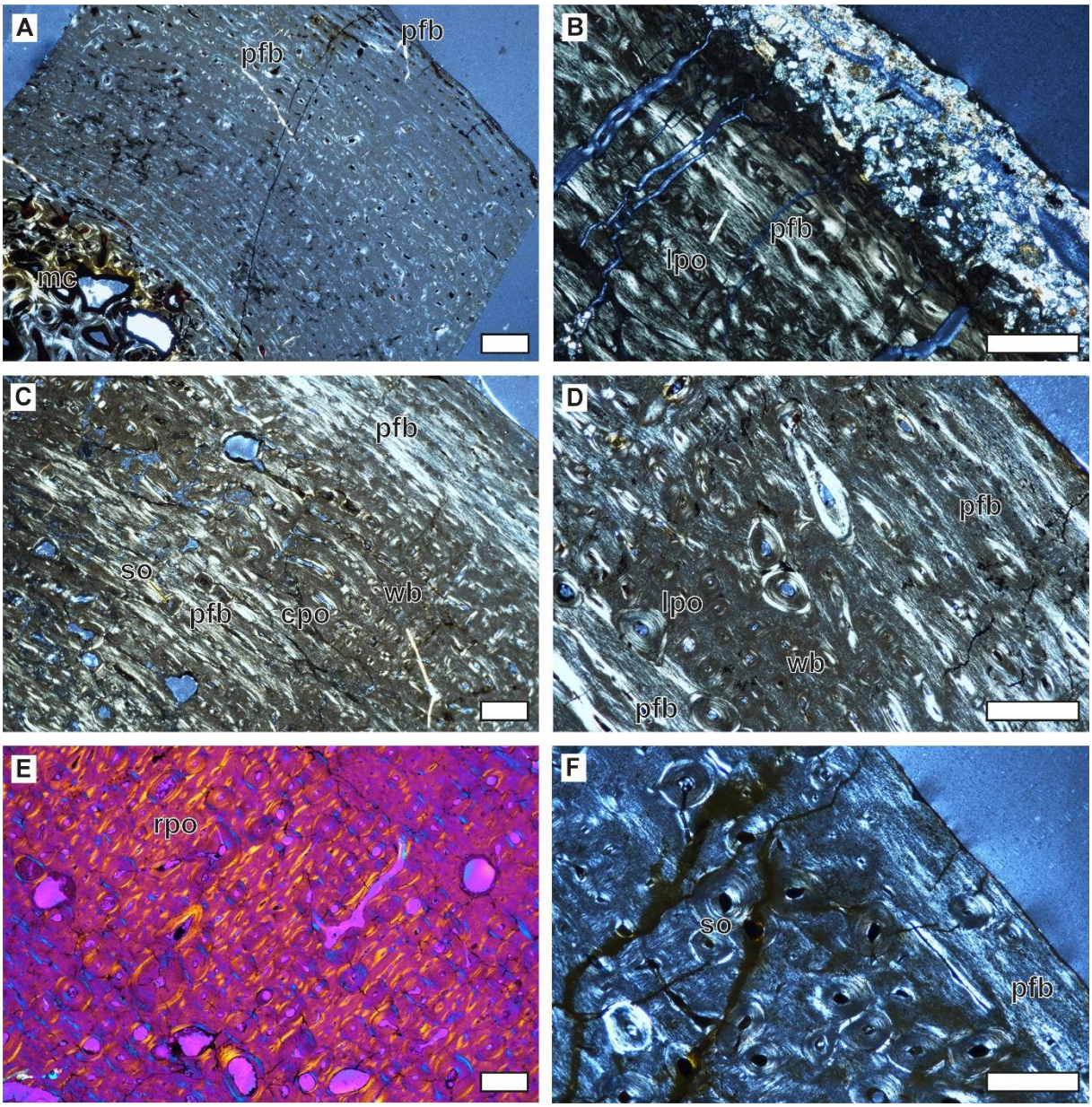

Figure 2. Overview of *Triceratops* humerus histology. Bone surfaces are towards the upper right corner for all images. All images are in cross-polarized light, and Figure 2E is with lambda-filter. A. Juvenile humerus RSM P.2691 (205 mm) showing a well-vascularized woven-parallel bone complex. The lower and upper parts of the cortex contain circumferential primary osteons while the mid-cortex represents a more conspicuous zone of longitudinal primary osteons. Overall, the lamellar centripetal infill of primary osteons is relatively weak. B. Humerus of early/late juvenile RSM P.3324.6.1 (550 mm) containing large zones of parallel-fibred bone tissue near the bone surface. There is a layer of sediment adhering to the bone surface. The primary osteons are relatively small and inconspicuous but are embedded in the parallel-fibred primary bone. C. Sub-adult humerus RGM.1394103 (651 mm) showing better defined zones of parallel-fibred and woven bone. Secondary osteons appear already closer to the bone surface. D. Adult humerus RGM.1394102 (761 mm) with larger zones of parallel-fibred bone and more advanced remodelling front. There are still randomly distributed areas of woven bone containing small longitudinal primary osteons. E. Same element as in D, but the upper mid-cortex showing a zone of radial woven-parallel bone tissue. F. Adult humerus CMN 9533 with increasing amounts of secondary osteons. All scale bars are 500 µm. cpo, circumferential primary osteon; lpo, longitudinal primary osteon; mc, medullary cavity; pfb, parallel-fibred bone; rpo, radial primary osteons; so, secondary osteon; wb, woven bone.

Vascularity follows the alternating patterns in bone tissue organisation, with parallel-fibred bone containing relatively fewer primary osteons than woven bone. The smallest humerus is significantly more vascularized than larger humeri (Figure 2D). However, the primary bone still shows occasional alternating cycles of longitudinal and circumferential vascularisation, as well as slight changes in bone tissue organisation, similar as in larger humeri. One humerus (RGM.1394103) has simple reticular vascular canals embedded in woven-parallel bone tissue that open at the bone surface, whereas the periosteal surface of larger humeri is underlain by a thin layer of poorly vascularized parallel-fibred bone tissue (Figure 2F). This most likely represents an incipient external fundamental system (EFS), and one humerus preserves inconspicuous lines of arrested growth (LAGs) (RGM.1394102). Otherwise, LAGs are not visible in plane- and cross-polarized light in the other humeri. Approximately halfway through the bone cortex, humerus RGM.1394102 shows an area of radial vascularisation with thin vascular canals that runs along the complete width of the thin-section, which is not observed in other humeri (Figure 2E).

Bone remodelling is evident in all but the two smallest humeri. In all but the largest humeri that show bone remodelling, there is still primary bone tissue preserved towards the bone surface, and dense Haversian bone is limited to only the deepest half of the cortex closer to the medullary cavity. The secondary osteons closer to the bone surface are less randomly distributed, but occasionally are aligned in circular rows parallel to the bone surface. More extensive remodelling in the form of resorption cavities is limited to the lower half of the bone cortex in larger humeri (Figure 2F). Osteocyte density is uniform across the primary bone, but flattened osteocytes occur near the bone surface as well as in zones of parallel-fibred bone, especially in larger humeri. Besides the random occurrences of alternating cycles containing parallel-fibred and woven bone, and corresponding cyclical shifts in vascular patterns, growth lines occur sporadically and inconspicuously in all studied humeri leaving a poor skeletochronological growth record.

4.3.2 Radii

The two radii sampled (RGM.1394104, 482 mm and RGM.1394105, 462 mm) have mostly matching histological patterns and are approximately the same size, but show some differences in age-related histological markers. The radii mostly show longitudinal woven-parallel bone tissue based on their isotropic primary bone tissue. Vascularity is characterized by relatively small simple vascular canals as well as longitudinal primary osteons. Both radii lack primary osteons at the outer bone surface, but radius RGM.1394104 shows sporadic vascular canals lacking lamellar bone opening up to the bone surface (Figure 3B). Radius RGM.1394105 shows nearly avascular bone tissue near the periosteum, but this is a relatively thin layer (Figure 3D). Secondary remodelling is extensive in both radii, but markedly higher in radius RGM.1394105 (Figure 3C, D). Nevertheless, secondary osteons do not reach the outermost part of the cortex but stay just below the bone surface. Primary bone tissue can still be observed between the secondary osteons all the way to the deepest cortex, where the onset of dense Haversian bone was just beginning. Larger resorption cavities lined with lamellar bone are limited to the deep cortex. Both radii show relatively high amounts of larger plump/rounded osteocytes uniformly distributed throughout the primary bone tissue, corroborating the presence of a predominantly woven-fibered bone matrix. Cyclical growth marks are absent throughout the cortex of both radii.

4.3.3 Ulnae

Similar to the radii, the three studied ulnae are fairly close in length and show the same histological characters, but differ in their age-related markers. Almost all of the primary bone is overprinted by

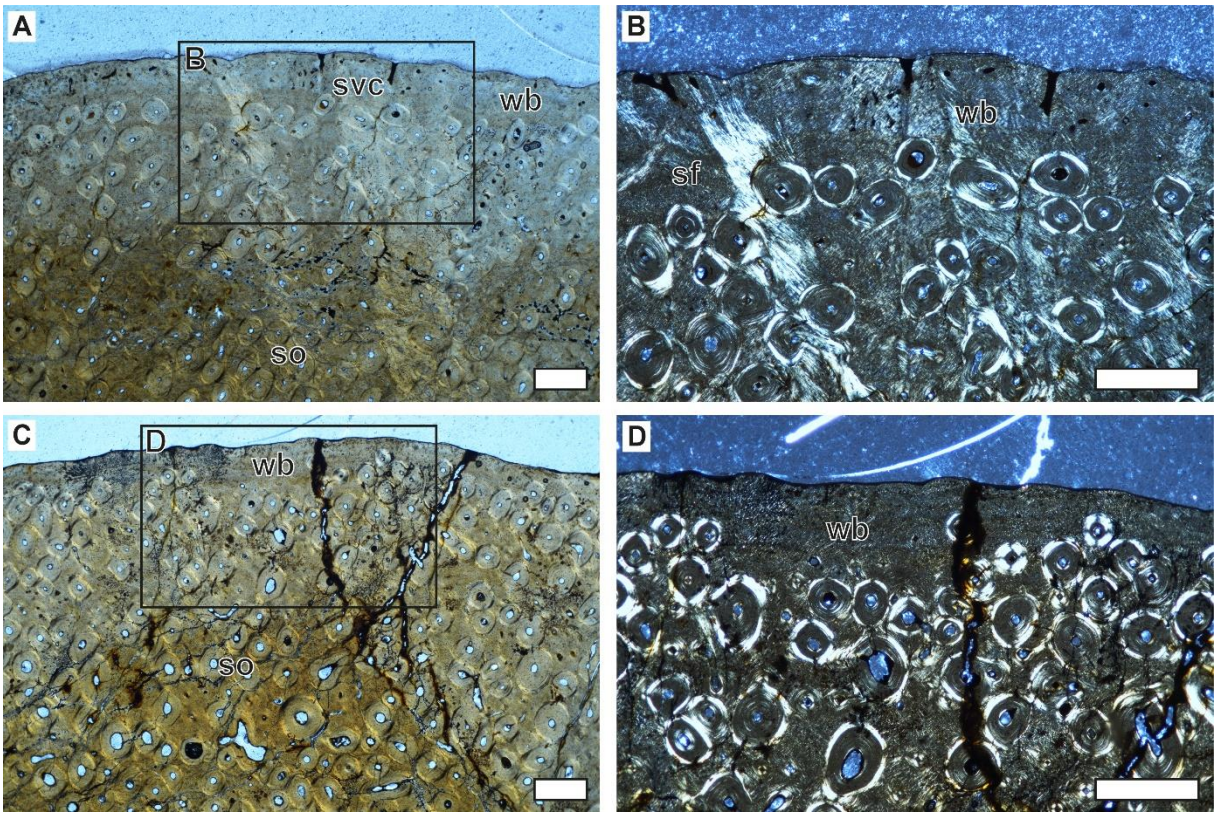

Figure 3. Overview of *Triceratops* radius histology. Bone surfaces are towards the top of the images. A. Sub-adult radius RGM.1394104 (482 mm) showing woven primary bone in plane-polarized light. Primary osteons are small and inconspicuous, but the bone surface contains numerous simple vascular canals that open up at the bone surface. Bone remodelling is advanced, and only the periosteum remains devoid of secondary osteons. B. Close-up of the same element in cross-polarized light. Sharpey's fibres become more visible. C. Adult radius RGM.1394105 (462 mm) showing woven bone with increased amounts of remodelling in plane-polarized light. This radius does not contain simple vascular canals near the bone surface. D. Close-up of the same element in cross-polarized light. The small longitudinal primary osteons become better visible between the larger secondary osteons. All scale bars are 500 µm. sf, Sharpey's fibres; svc, simple vascular canals; so, secondary osteon; wb, woven bone.

secondary osteons that quickly grade into dense Haversian tissue towards the deeper cortex, even in the smallest ulna (Figure 4B). The interstitial primary bone tissue is predominantly woven-parallel with longitudinally oriented primary osteons, similar to the radii. The primary osteons as well as the simple vascular canals are relatively small and in low abundance. Simple canals are mainly limited to the bone surface, but may occur randomly dispersed throughout the primary bone. The bone tissue near the periosteal surface changes to more parallel-fibred bone tissue, but still retains abundant primary osteons. In ulna RGM.1394107, this parallel-fibred bone tissue is also characterised by numerous simple vascular canals that occasionally open to the bone surface, as well as small numbers of primary osteons (Figure 4A). These canals are longitudinal but may show anastomosing canals connecting to neighbouring canals. Ulna RGM.1394106 shows avascular parallel-fibred bone just beneath the bone surface which is overprinted with secondary osteons. This indicates a distinctive decrease in the bone apposition front (AF) which is about to be overtaken by the Haversian substitution front (HSF) (Figure 4C). Ulna P.2095 shows a more advanced degree of remodelling with multiple generations of overlapping secondary osteons close to the bone surface (Figure 4D), i.e., the Haversian substitution front has progressed further than in RGM.1394106. Nevertheless, even the most heavily remodelled ulnae still preserve areas of primary (and active) bone. Osteocyte shape and abundance are uniform

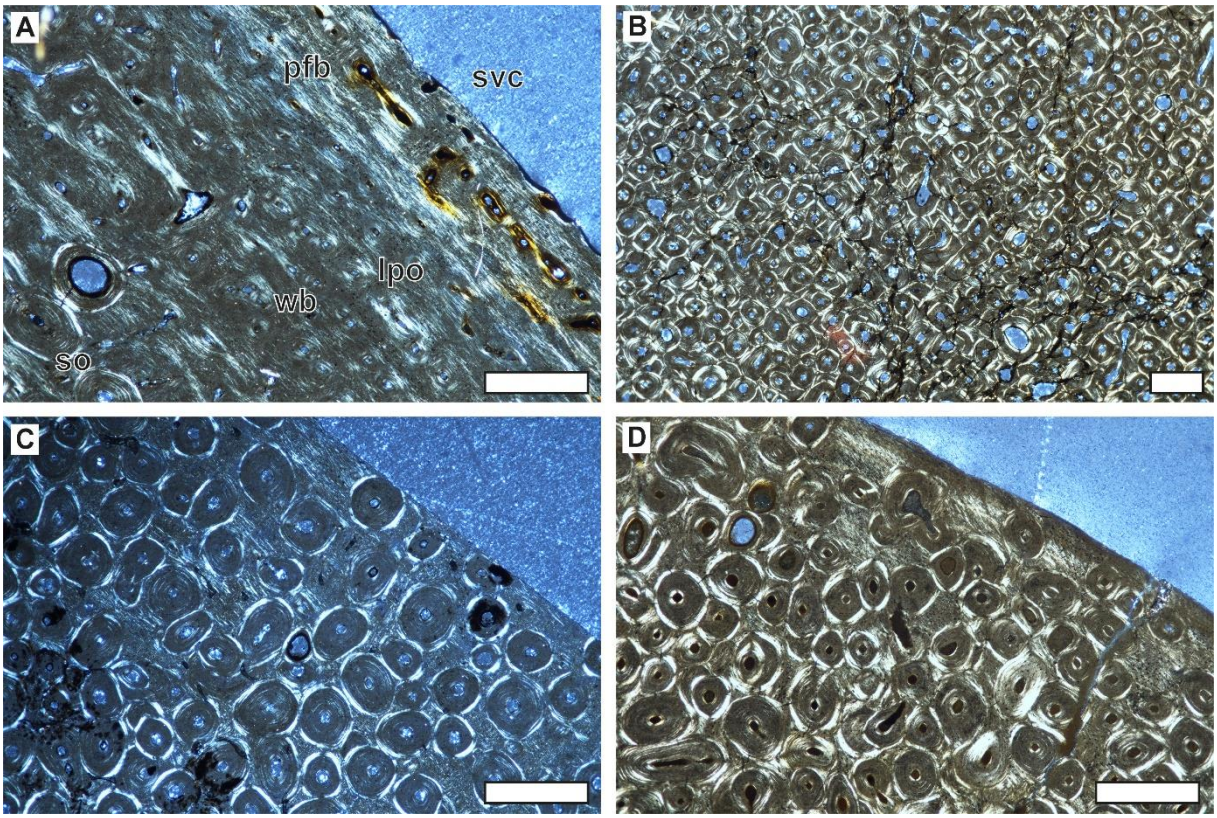

Figure 4. Overview of *Triceratops* ulna histology. Bone surfaces are towards the upper right corner in all images. All images are in cross-polarized light. A. Sub-adult ulna RGM.1394107 (649 mm) showing primarily woven bone with a bone surface of slightly more parallel-fibred bone tissue. The periosteum contains simple vascular canals that occasionally open up to the bone surface. Primary osteons are exclusively longitudinal. Bone remodelling is advancing towards the bone surface. B. Mid-cortex of the same element showing dense Haversian tissue. C. Adult ulna RGM.1394106 (680 mm) with only little preserved primary bone due to overprinting of secondary osteons. The primary tissue shows a mix of woven and more organized patches of bone. D. Adult ulna P.2095 (613 mm) with the highest rates of bone remodelling containing multiple generations of secondary osteons near the bone surface. The bone surface seems more organized than woven bone. All scale bars are 500 µm. lpo, longitudinal primary osteon; pfb, parallel-fibred bone; so, secondary osteon; svc, simple vascular canals; wb, woven bone.

across the entire primary bone cortex for all three ulnae, with only minor local differences in shape and size. None of the sections show clear resorption cavities, even in the dense Haversian bone of the deep cortex. However, we do note that the ulnae preserve the least amount of primary bone as determined from the CT images, and that the deep cortical bone is not represented here (Table 1.). The ulnae do not show any growth marks.

4.3.4 Femora

The four studied *Triceratops* femora represent relatively large individuals, but differ in their onset and pattern of specific histological markers. The majority of the primary bone tissue of all femora shows variations of parallel-fibred and woven tissue in a laminar woven-parallel complex, in which the vascularity is mainly characterized by small longitudinal primary osteons in circular rows mixed in with fewer amounts of circumferential canals. These variations in bone tissue type are sequential, and all femora show alternating layers of parallel-fibred and woven bone – a recurring phenomenon in the larger *Triceratops* limb elements studied here (Figure 5A). However, these cycles are mainly restricted

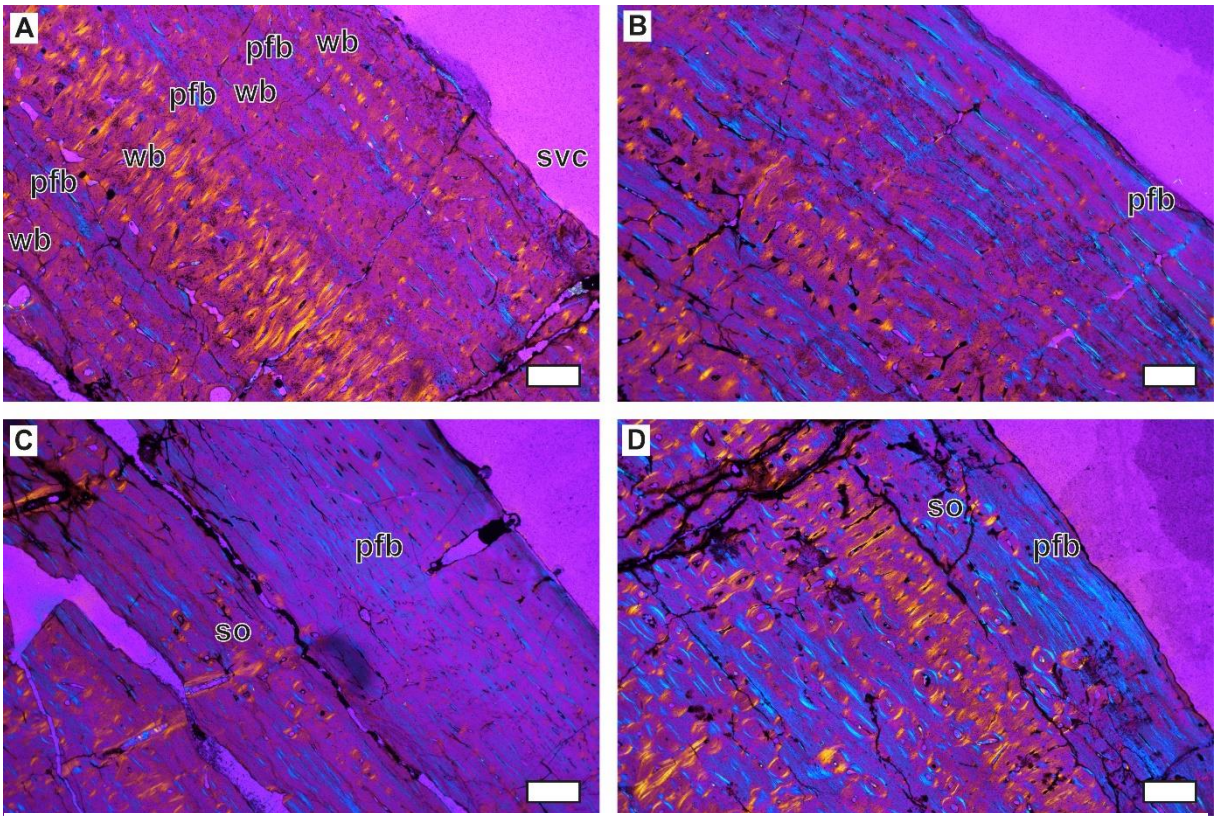

Figure 5. Overview of *Triceratops* femur histology. Bone surfaces are towards the upper right corner for all images. All images are in cross-polarized light with lambda filter. A. Sub-adult femur RGM.1394109 (1070 mm) showing distinct zones of parallel-fibred and woven bone towards the bone surface. The parallel-fibred zones are represented by the thin blue birefringent lines. Vascular organisation is variable in each zone of woven bone, containing a mix of longitudinal, circumferential, radial and reticular primary osteons. The bone surface contains simple vascular canals. B. Sub-adult femur RGM.1394111 (1020 mm) with woven primary tissue that grades into parallel-fibred bone towards the bone surface. Vascularity is predominantly circumferential, and the lamellar infill of the primary osteons are very clear. C. Adult femur RGM.1394108 with relatively high portions of parallel-fibred bone and overall lower vascular density. Primary osteons are predominantly circumferential and longitudinal in circular rows. Secondary osteons are advancing towards the bone surface. D. Adult femur RGM.1394110 (1120 mm) showing large areas of parallel-fibred bone close to the bone surface and high rates of bone remodelling. All scale bars are 500 µm. pfb, parallel-fibred bone; so, secondary osteon; svc, simple vascular canals; wb, woven bone.

to the outer cortex, and these growth cycles quickly disappear towards the medullary cavity. Nevertheless, the most pronounced differences between the femora are observed in the primary bone near the bone surface, in the extent of these alternating layers. Two femora (RGM.1394109 and RGM.1394111) contain significantly more areas of highly vascularized woven bone separated by thick layers of poorly vascularized parallel-fibred bone (Figure 5A, B). Other femora (RGM.1394108 and RGM.1394110) show contrasting patterns, with markedly thicker layers of parallel-fibred bone tissue separated by thinner layers of more vascularized woven bone (Figure 5C, D). Two femora (RGM.1394109 and RGM.1394110) also deposited radial primary osteons, but show otherwise contrasting primary tissue (Figure 5A, D).

Osteocyte shape and density correlate with bone tissue organisation. Parallel-fibred bone contains lower densities of mostly flattened osteocytes, while woven bone shows higher densities of mainly plumb and rounded osteocytes with clear canaliculi. Bone remodelling is extensive in all femora, but even the most remodelled elements still preserve large portions of primary bone (Figure 5D). The

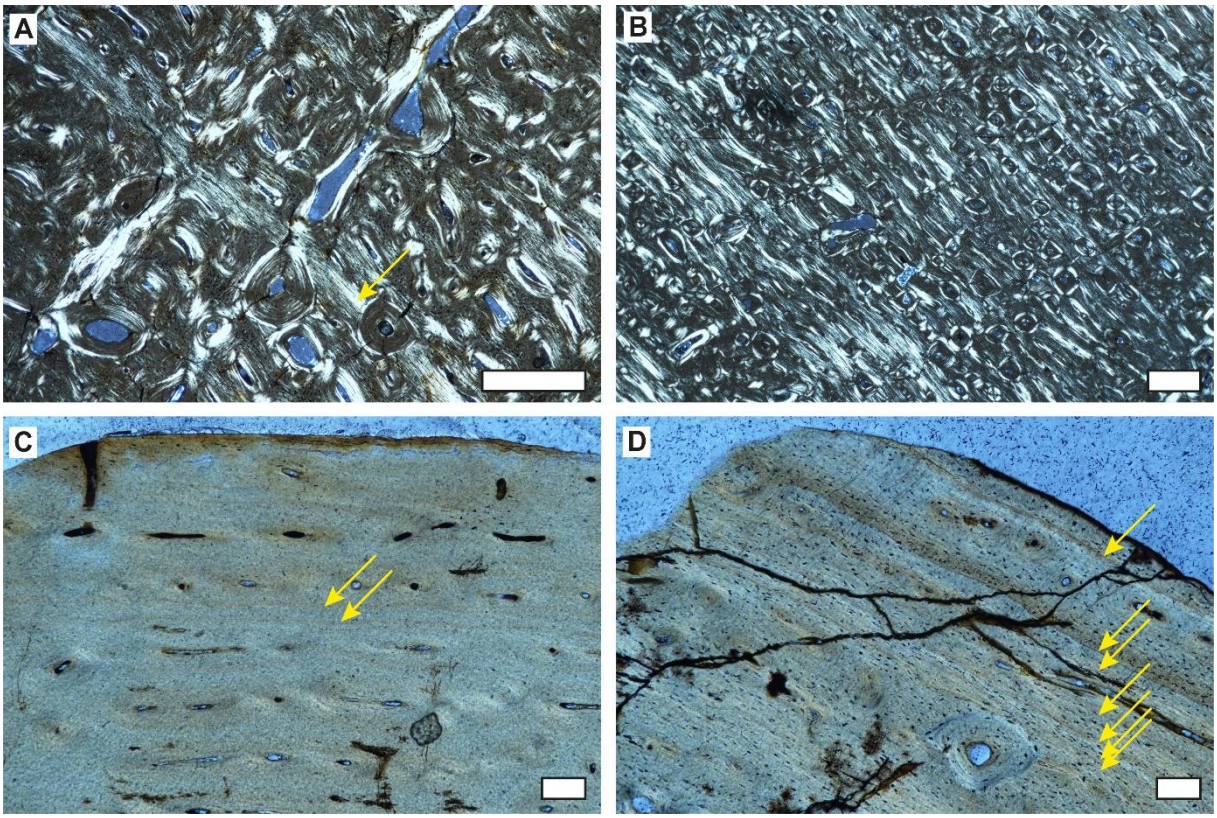

Figure 6. Overview of cyclical patterns in *Triceratops* femora. Bone surface is towards the top and upper right corner. A. Arrow indicating lines/zones of parallel-fibred bone in the mid-cortex of sub-adult femur RGM.1394109 (1070 mm) in cross-polarized light. These zones were counted for age estimations. Note the overlapping secondary osteons overprinting the primary tissue. B. Alternating zones of parallel-fibred and woven bone in adult femur RGM.1394108 as indicated by the marked changes in birefringence in cross-polarized light. C. Arrows indicating two closely spaced growth lines (LAGS) near the bone surface of the same femur in plane-polarized light. D. Arrows indicating seven closely spaced growth lines in the bone surface of adult femur RGM.1394110 (1120 mm). Scale bar for A and B is 500 µm and for C and D is 100 µm.

mid- to deep cortex of all femora is almost completely remodelled into Haversian tissue. Based on CT images, all femur cores were sampled up to the medullary border, except for RGM.1394110. However, larger resorption cavities are limited to the deeper cortex, and do not occur in all of the studied femora. In addition to the cyclical alternations in bone tissue type (Figure 6A, B), two of the studied femora also show growth lines close to the periosteum. Femur RGM.1394108 has two to three closely spaced growth lines (Figure 6C) and the outermost cortex is poorly vascularized. We interpret this feature as an incipient external fundamental system (EFS). Femur RGM.1394110, on the other hand shows a better defined EFS, consisting of up to seven growth lines which become increasingly more closely spaced towards the bone surface (Figure 6D). Curiously, the bone matrix deposited with the LAGs does not show a typical lamellar organisation but still contains a mixture of woven and parallel-fibred bone.

4.3.5 Tibiae

The six *Triceratops* tibiae studied here are all relatively close in size and represent large individuals, but they show distinct differences in histology (Figure 7). All tibiae have primary bone tissue displaying a mix of parallel-fibred and woven bone, in which the two bone matrix types occur in alternating layers. The increase in parallel-fibred bone follows a simultaneous decrease of woven bone towards the bone

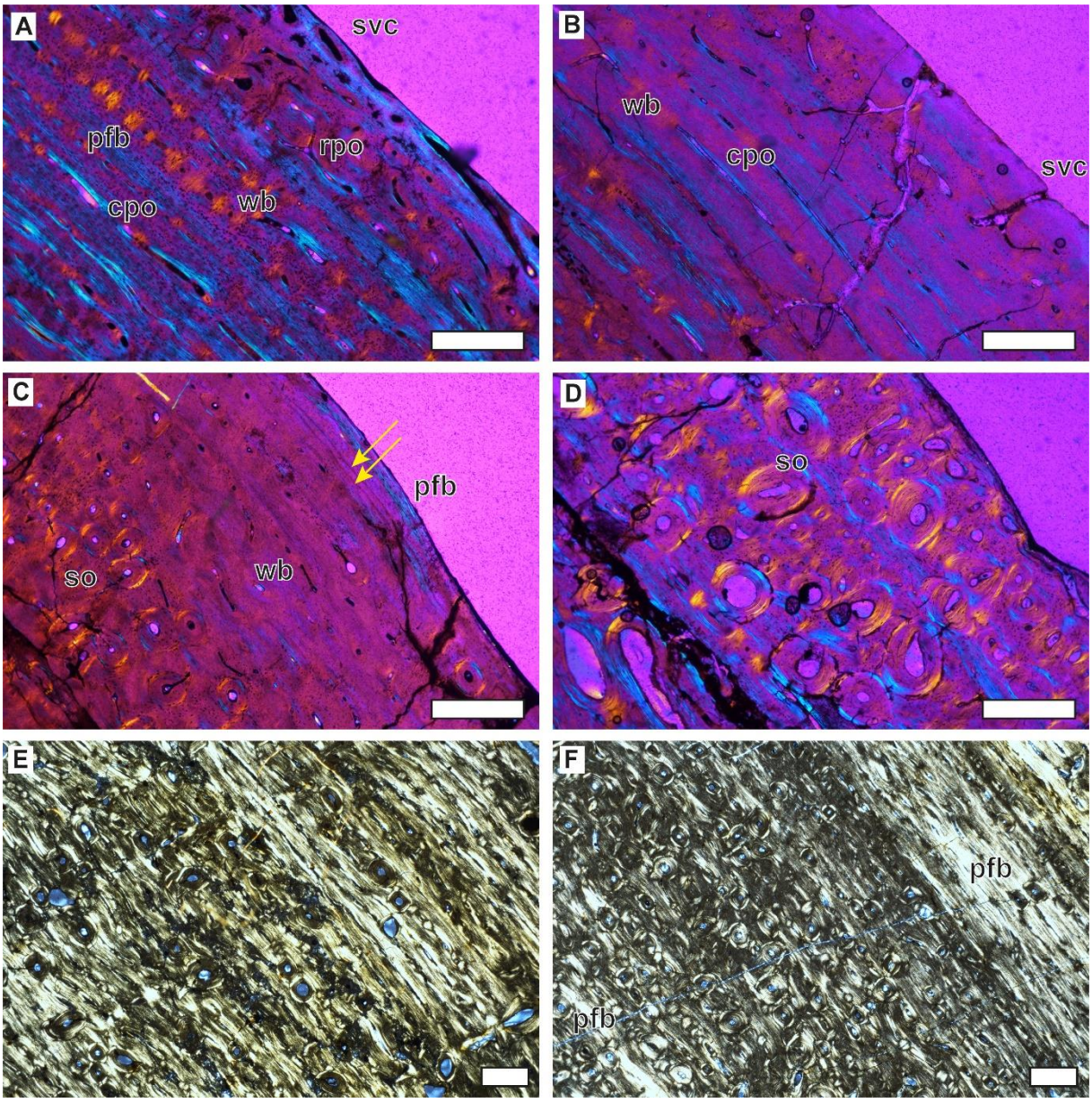

Figure 7. Overview of *Triceratops* tibia histology. Bone surfaces are towards the upper right corner for all images. All images are in cross-polarized light. A-D are taken with lambda filter. A. Sub-adult tibia RGM.1394117 (704 mm) showing large areas of woven bone and inconspicuous layers of parallel-fibred tissue. The predominant vascularity is circumferential, but there are longitudinal primary osteons mixed in (highly birefringent). Close to the bone surface is an area of reticular and oblique primary osteons and simple vascular canals. B. Sub-adult tibia RGM.1394116 (740 mm) with large area of circumferential woven-parallel bone tissue. Some of the laminar organisation is due to the longitudinal canals oriented in circular rows (compare with A). There are some vascular canals that open up at the bone surface. C. Adult tibia RGM.1394114 (781 mm) showing woven bone and a parallel-fibred bone surface. Overall, vascular density is lower and secondary osteons become more pronounced closer to the bone surface. The arrows indicate two LAGs. D. Adult tibia RGM.1394113 (785 mm) with advanced bone remodelling and few visible longitudinal primary osteons in the primary bone. E. The mid-cortex of sub-adult tibia RGM.1394117 showing continuous zones of parallel-fibred bone matrix. There is some inconspicuous layering, but overall zones are poorly defined. F. The mid-cortex of adult tibia RGM.1394115 showing better defined layers of parallel-fibred and woven bone matrix. All scale bars are 500 µm. cpo, circumferential primary osteon; pfb, parallel-fibred bone; rpo, reticular primary osteon; so, secondary osteon; svc, simple vascular canal; wb, woven bone.

surface, but the timing and preservation of this change in bone tissue ratio differs between tibiae. Vascular organisation of the primary tissue is almost exclusively characterized by small longitudinal primary osteons aligned in circular rows parallel to the bone surface, with occasional anastomosing canals (Figure 7C). However, one tibia (RGM.1394116) contains predominantly circumferential primary osteons except near the periosteal surface (Figure 7A). Tibia RGM.1394117 shows a mostly laminar organisation but has some reticular and oblique primary osteons near the bone surface (Figure 7B). The degree of vascularity follows the same alternating pattern as the bone matrix organisation, resulting in layers of either poorly vascularized parallel-fibred bone or well-vascularized woven bone (Figures 7A and 8). Based on Figure 8, these are interpreted as cyclical growth marks. However, these cyclical growth marks are not observed as clearly in all tibiae, and only RGM.1394114 preserves a considerable growth record (Figure 7E, F; Figure 8).

Similarly, osteocyte abundance and morphology show sequential differences in these alternating layers of parallel-fibred and woven bone. Osteocytes in parallel-fibred bone are mostly flattened and occur at a lower density, while the woven-fibred bone matrix has denser groupings of plump osteocytes. Other forms of cyclicity such as growth lines are observed only in the three largest tibiae in which up to two growth lines have been deposited just beneath the periosteal surface (Figure7C). These growth lines are preceded by small areas of parallel-fibred bone tissue.

Bone remodelling is evident in all studied tibiae, but the overall density of secondary osteons differs significantly among all elements. In smaller tibiae, the HSF is less advanced and the cortex shows

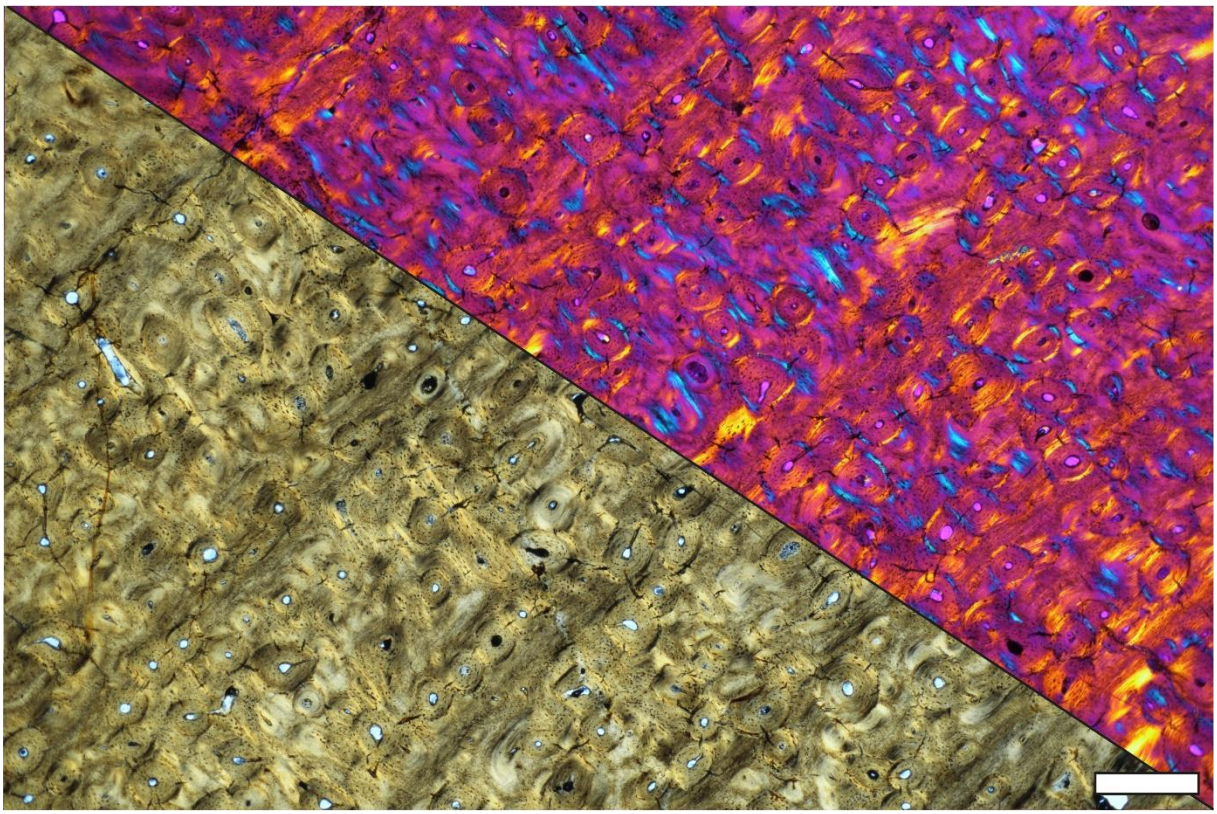

Figure 8. The mid to deep cortex of adult tibia RGM.1394114 (781 mm) showing distinct layers of parallel-fibred and woven bone. The bone surface is towards the upper left corner. The lower left half is in plane-polarized light and the upper right half is in cross-polarized light with lambda filter. The zones are of parallel-fibred bone are dark/black in plane-polarized light and orange in birefringent cross-polarized light. Despite the numerous secondary osteons, this tibia preserves a clear primary growth record. Scale bar is 500 µm.

lesser degrees of bone remodelling and preserves considerable amounts of original primary bone near the bone surface, while larger tibiae already form secondary osteons near the periosteal surface and contain dense Haversian tissue in the deeper cortex (Figure 7D). However, overall the remodelling pattern is diffuse, and primary bone may still be observed in deeper areas. Larger resorption cavities are extremely limited in all tibiae. While not all tibiae were sampled up to the medullary border as indicated by the CT images, the available cores that do represent a transect of the complete cortex also developed limited amounts of resorption cavities.

4.3.6 Fibulae

The four studied fibulae all represent relatively large individuals. Overall, the HSF has advanced close to the outer bone surface in all fibulae. Accordingly, bone remodelling is extremely high and they only preserve a relatively small amount of primary bone. This primary bone tissue is described as a woven-parallel complex with woven-fibred bone and small areas of parallel-fibred bone matrices (Figure 9). In general, the vascular organisation of the primary bone is limited to small longitudinal primary osteons

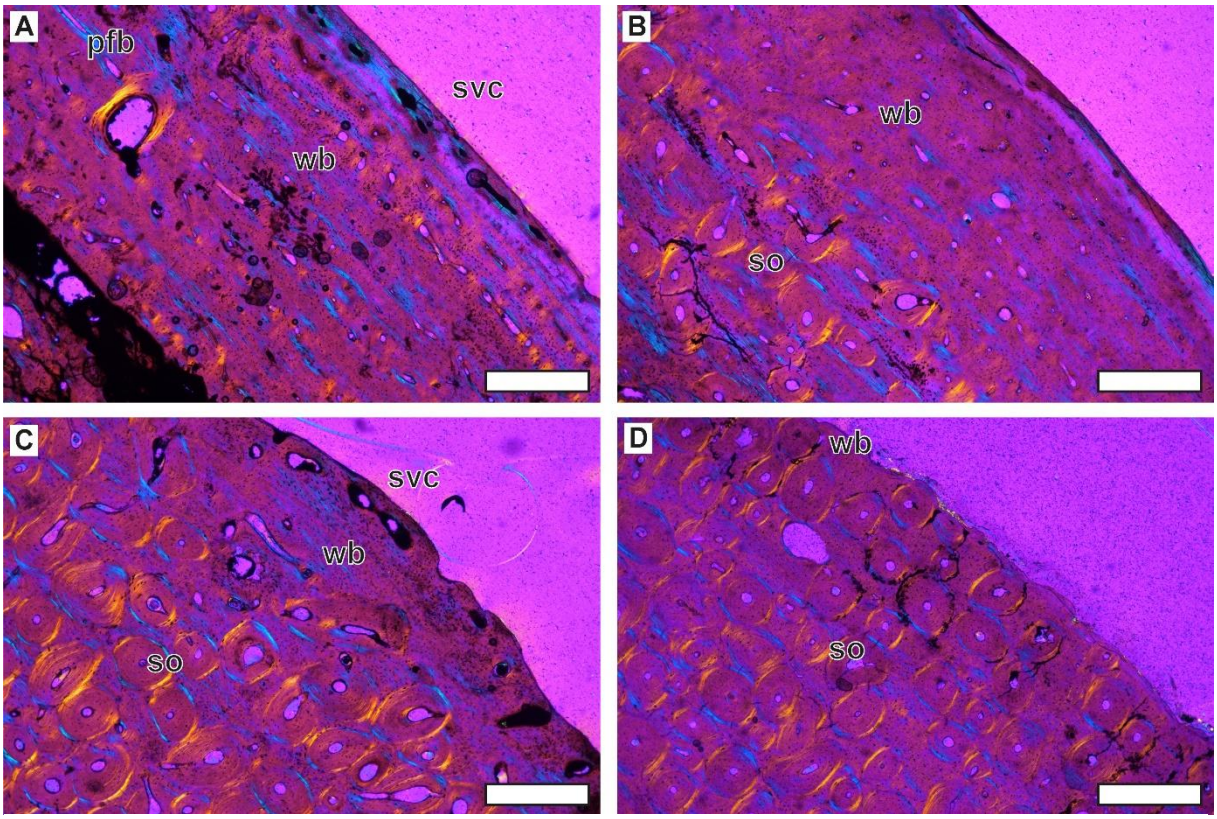

Figure 9. Overview of *Triceratops* fibula histology. All images are in cross-polarized light with lambda filter. Bone surface are towards the upper right corner of all images. A. Sub-adult fibula RGM.1394118 (645 mm) showing woven bone with random patches of parallel-fibred bone. Vascular density is high with mainly laminar woven-parallel bone deposited with circumferential primary osteons as well as circular oriented longitudinal ones. Bone surface contains simple vascular canals. B. Sub-adult fibula RGM.1394120 (637 mm) with woven bone and small patches of parallel-fibred bone. Vascular density is relatively lower than RGM.1394118, and bone remodelling is more advanced. C. Adult fibula RGM.1394119 (616 mm) with high degree of bone remodelling and low vascular density in the primary tissue. Nevertheless, the primary bone is primarily woven, and the bone surface still contains numerous simple vascular canals. D. Adult fibula CMN.57065 in which the primary bone is almost entirely overprinted by secondary osteons. The preserved primary tissue is woven. All scale bars are 500 µm. pfb, parallel-fibred bone; so, secondary osteon; svc, simple vascular canal; wb, woven bone.

(Figure 9A, B). In all fibulae, the vascular canals are relatively well-organized parallel to the bone surface. As with other studied *Triceratops* limb bones, the layers of parallel-fibred bone become thicker towards the bone surface. All fibulae show weakly expressed alternating zones of parallel-fibred tissue in their outer bone surface, but there is no clear pattern.

Fibula RGM.1394118 and RGM.1394119 still show simple vascular canals that occasionally open to the bone surface (Figure 9A, C), but the two other fibulae possess a near avascular periosteal surface. There is a marked difference in the advancement of remodelling, where two fibulae (RGM.1394118 and RGM.1394120) have significantly fewer secondary osteons. Nevertheless, all fibulae have a diffuse remodelling pattern towards the bone surface and possess dense Haversian bone in the deep cortex, especially the largest fibula CMNFV 57065 (Figure 9D). Resorption cavities in the deep cortex are limited across all studied fibulae, but fibula RGM.1394118 has numerous large immature secondary osteons.

4.3.7 Vertebrae

The *Triceratops* vertebrae show a high degree of secondary bone remodelling and the presence of growth lines (Figure 10). The most proximal area of the neural spine of the dorsal vertebra RGM.1394100 still shows some amount of primary bone (Figure 10A). The bone tissue is relatively well organized and contains numerous closely spaced growth lines that are overprinted by extensive

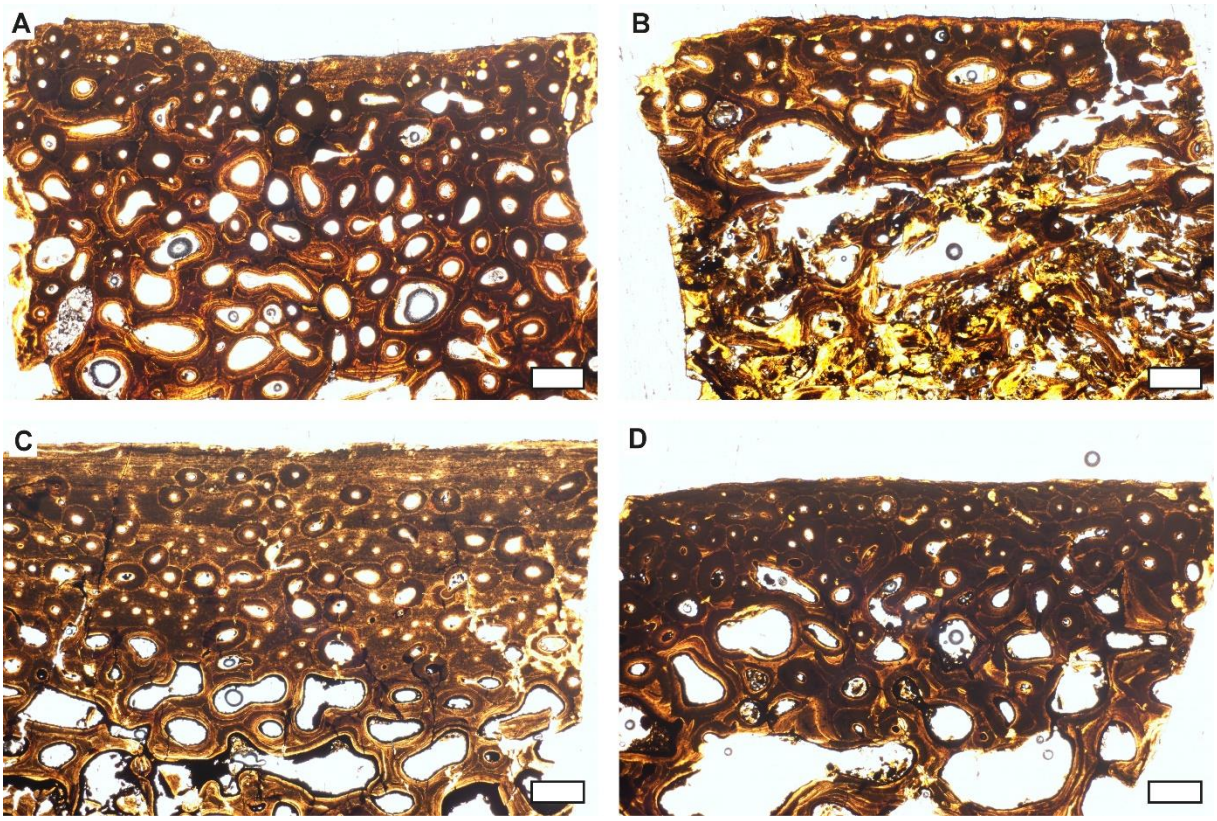

Figure 10. Overview of *Triceratops* vertebrae histology. All images are in plane-polarized light as this provides the most ideal visualisation of histological markers due to section thickness. Bone surfaces are towards the top for all images. A. Histology of the neural spine of dorsal vertebra RGM.1394100. Bone remodelling is advanced, but the primary bone is relatively avascular and contains inconspicuous growth marks. B. Transverse process of the same element, with higher rates of bone remodelling. C. Histology of the neural spine of cervical vertebrate RGM.1394101. Remodelling is less pronounced than in dorsal vertebrae, but the primary bone also contains inconspicuous growth marks. D. Highly remodelled transverse process of the same element. All scale bars are 500 µm.

remodelling. The vascularity consists of longitudinal primary osteons, but they occur in relatively low abundance throughout the primary bone. The amount of primary bone in the neural spine diminished greatly more distally as secondary osteons become more dominant and the medullary cavity covers relatively more area (Figure 10A). The transverse processes of dorsal vertebrae show even stronger degrees of bone remodelling and contain a high number of large overlapping secondary osteons (Figure 10B). The neural spine of the cervical vertebra produces a similar sequence in histological patterns but shows more extensive remodelling than the dorsal vertebra (Figure 10C). The transverse process, on the other hand, preserves relatively more primary bone than seen for dorsal vertebrae (Figure 10D). The small areas of preserved primary bone of cervical vertebrae are well-organised with only very few primary osteons. Bone remodelling is very extensive and large areas are remodelled into dense Haversian tissue.

4.3.8 Ribs

Rib sections from *Triceratops* are characterized by extensive bone remodelling (Figure 11). Where primary bone is still preserved, there is predominantly woven bone in a woven-parallel complex made up of dense longitudinal primary osteons. These osteons are generally more abundant larger in

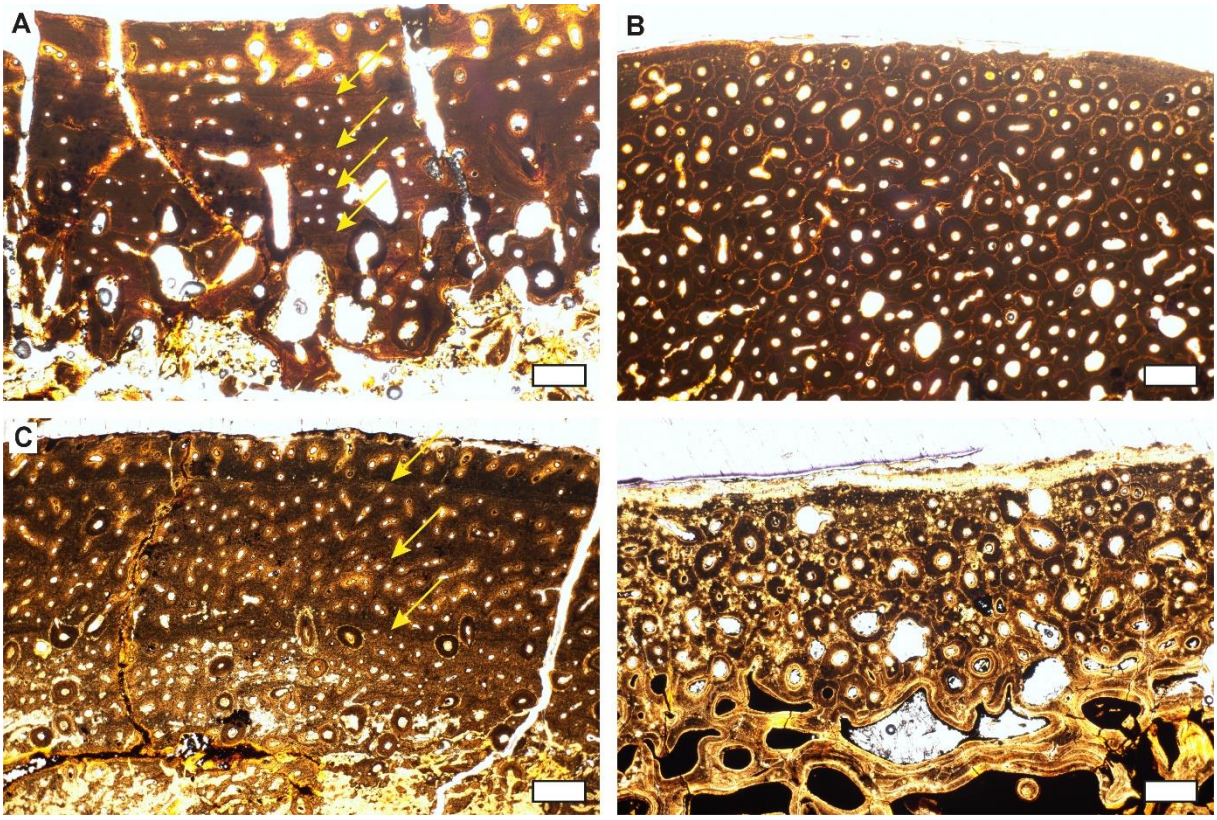

Figure 11. Overview of *Triceratops* rib histology. All images are in plane-polarized light as this provides the most ideal visualisation of histological markers due to section thickness. Bone surfaces of the anterior side are towards the top for all images. A. Histology of most proximal area of the main shaft of rib RGM.1394098 showing strong vascularity as well as bone remodelling and resorption in the lower half of the section. The arrows indicate possible growth lines. B. More distal area of rib RGM.1394098 showing dense Haversian bone. C. Most distal sample of rib RGM.1394098 showing only minor degrees of secondary remodelling. The arrows indicate three well-defined growth lines. Vascularity is relatively high. D. Capitulum of rib RGM.1394097 showing extremely dense Haversian bone turning into cancellous bone inwards. All scale bars are 500 µm.

diameter than those in limb elements. The primary bone of rib RGM.1394098 shows well-defined growth lines (Figure 11A, C), but their occurrence does not follow a regular pattern. The most proximal and most distal sample (Figure 1, sample #1 and #3) preserve clear growth lines, while the middle sample shows dense Haversian tissue (Figure 1). However, the relative amount of preserved primary bone diminishes towards the distal end, probably because the HSF is relatively more advanced than in the more proximal parts (Figure 11B). We do note that our sampling strategy for RGM.1394098 did not

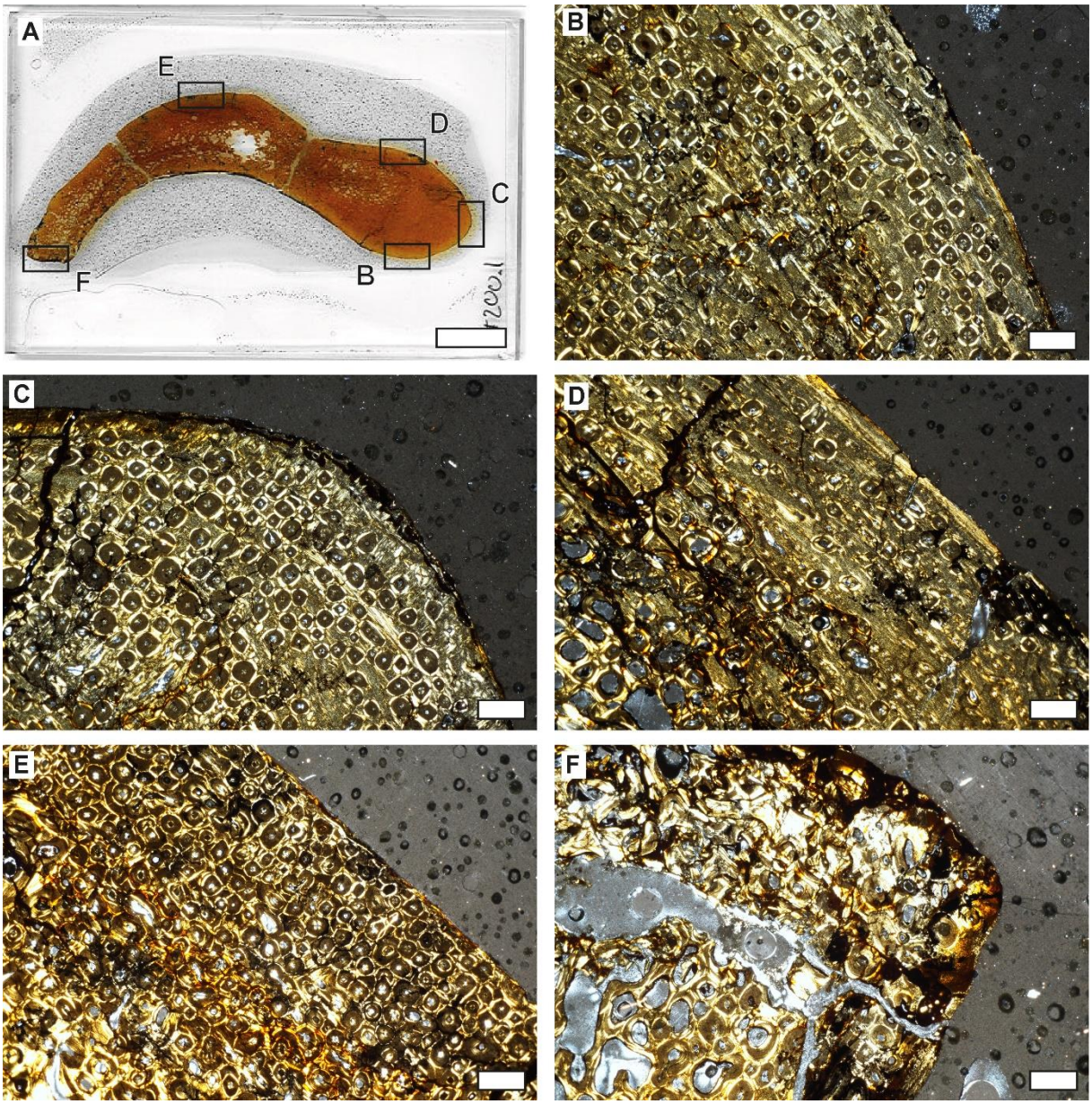

Figure 12. Histology of RGM.1394121, the complete rib section. Generally, most of the cortical bone is heavily remodelled. A. Overview of the section with insets for each image. B. Histology of the posterolateral side showing many secondary osteons and longitudinal woven-parallel bone. There are two growth marks of parallel-fibred bone in the primary cortex being overprinted by secondary osteons. C. Most lateral section showing one zone of parallel-fibred bone and heavy bone remodelling. D. Histology of the anterolateral side showing relatively less bone remodelling. The primary woven tissue does not preserve any growth marks. E. Anterior portion showing dense Haversian tissue with multiple generations of secondary osteons. F. The most medial portion showing medullary expansion and bone remodelling. Scale bar for A is 1 cm and scale bar for B to F is 500 µm.

cover the complete length of the rib. Rib RGM.1394097 did not show any significant variation in histological markers across the sampling transect. All five samples (Figure 1) showed very high degrees of remodelling with one or two inconspicuous growth marks. The relative abundance of secondary osteons was higher in more distal samples. Overall, the anterior regions of both ribs tend to show a lesser developed HSF and preserve more primary bone, including growth lines. The complete cross-section taken proximally reveals the same histological patterns (Figure 12). The thicker lateral margins (Figure 12A,B,C) show high numbers of secondary osteons and woven-parallel primary tissue with one or two growth lines consisting of more parallel-fibred bone tissue. More proximally, the capitulum shows a completely remodelled bone cortex of multiple generations of secondary osteons (Figure 11D). All ribs show dense Sharpey's fibres in the preserved primary bone, reflecting the insertion of the intercostal musculature.

4.3.9 Skeletochronology

Triceratops deposits mostly layers (annuli) of parallel-fibred tissue instead of well-defined LAGs. However, out of all the 25 sampled limb bones (16 when only including humeri, femora and tibiae), only four preserve considerable numbers of cyclical growth marks in their primary growth record (Figure 13). These include humeri RGM.1394102 and RGM.1394103, femur RGM.139414111 and tibia RGM.1394114. Thus, the majority of the larger limb elements (including humeri, femora, tibiae) as well as all smaller limb bones (including radii, ulnae, fibulae) do not preserve a cyclical growth record. The tibia sample preserves the highest number of growth cycles (16 combined zones and annuli), while the two humeri preserve very few growth marks (3 and 4 combined zones and annuli). The femur sample shows a total of 9 growth cycles. However, the preserved annuli of parallel-fibred bone are still poorly delineated from the surrounding faster-growing bone tissue. Moreover, the spacing of the recorded growth marks is irregular and does not follow the expected pattern of decreasing growth rates with ontogeny. Thus, the DTB *Triceratops* does not permit a detailed skeletochronological analysis given the limited preservation of

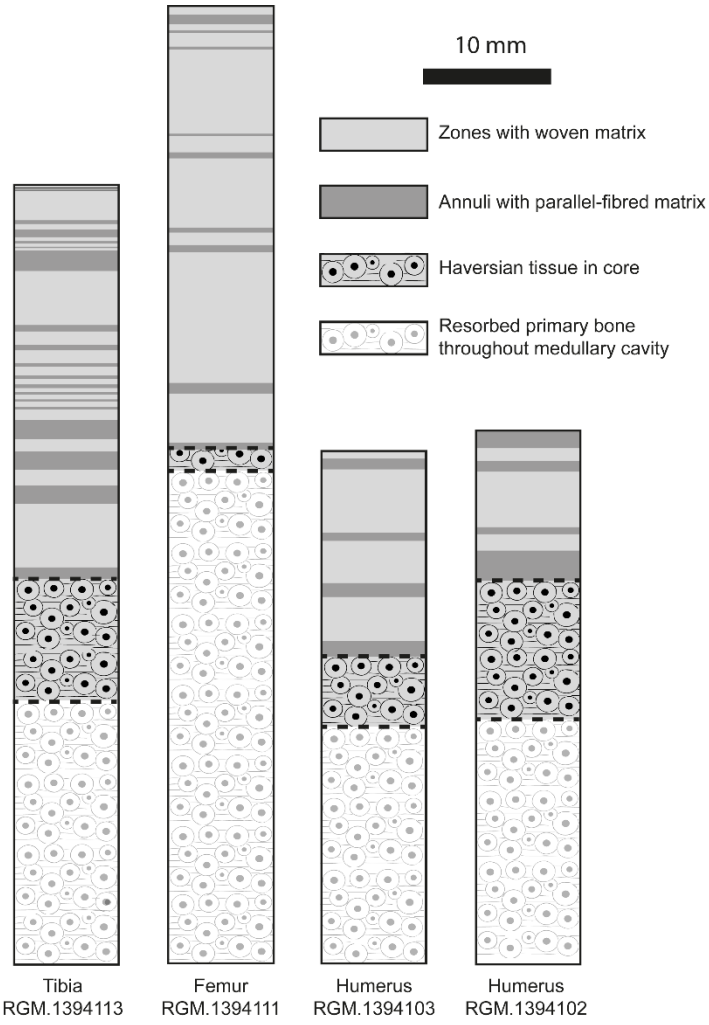

Figure 13. Schematic representation of the skeletochronological markers in the core samples of the elements that preserved the most complete growth records. Tibia RGM.1394113 shows the highest number of preserved growth cycles. Note that a large portion of the growth record is obliterated by the HSF and RF, and that growth cycle spacing is irregular. The medullary centre is to the left and the bone surface is to the right for each of the four core drawings. Black dotted lines represent the boundary between zones indicated in the legend.

a primary cyclical growth record in only a small number of elements as well as the inconsistent spacing of growth marks (see section 4.3).

4.3.10 Application of the Three-Front Model to limb bones

Figure 14 shows the three-front model applied to the histologically youngest and oldest *Triceratops* limb bones from the DTB. Note that these results are relative to each other and therefore can only be compared within the discussed framework of *Triceratops* histology. Nevertheless, these models provide a comprehensive overview of the observed histological patterns. The inter-elemental differences are most clearly expressed in the speed of the apposition front (AF) and resorption front (RF), because the relative cortical thickness seems the most defining characteristic for the observed histological patterns. The tibiae possess the thickest cortex, suggesting that the speed of the RF is relatively low compared to other limb bones. This explains the better preservation of primary bone in the deeper cortex of the tibiae, especially under the assumption of a constant speed of the Haversian substitution front (HSF, Mitchell and Sander, 2014) combined with a diffuse remodelling pattern seen

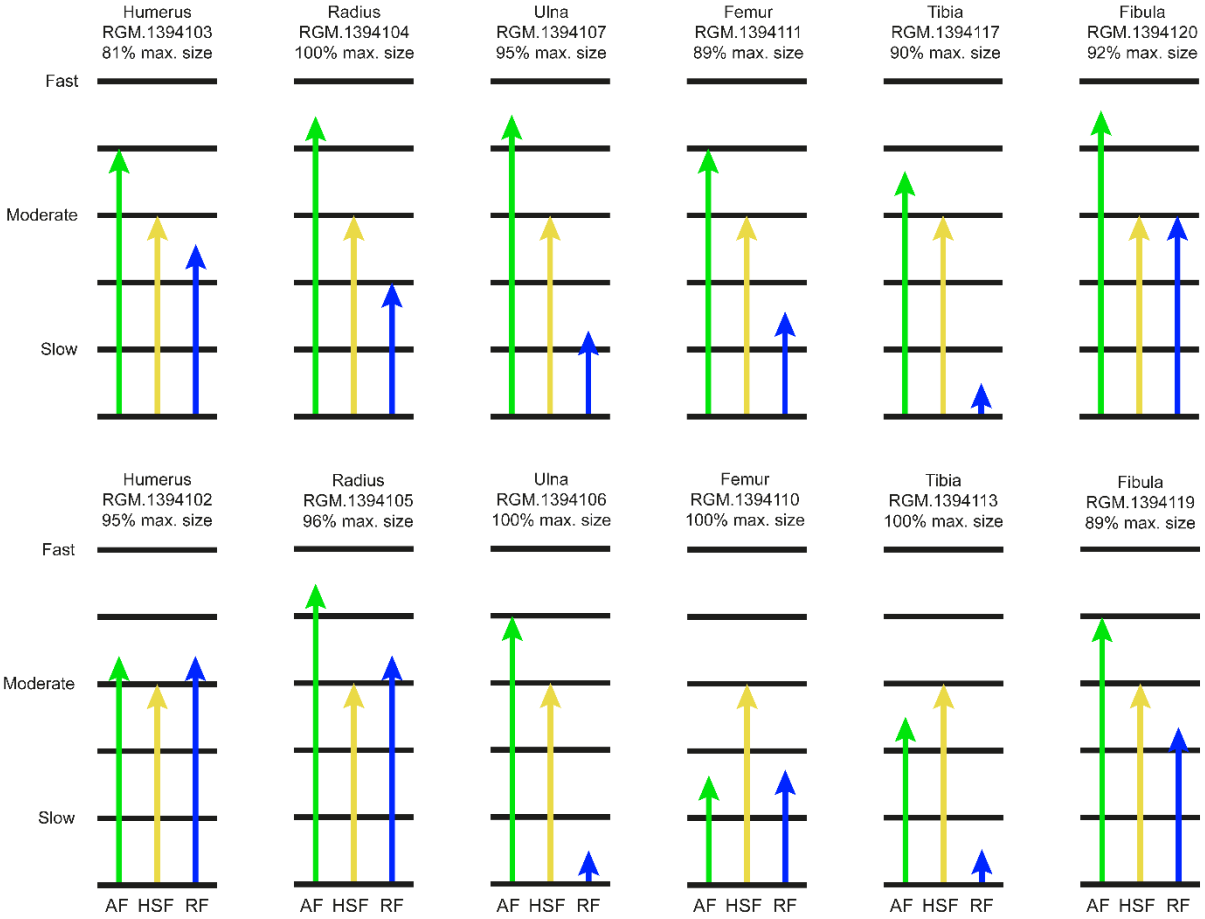

Figure 14. Three-front models of the histologically youngest and oldest limb bones of the DTB *Triceratops*. The upper row represents the youngest elements of each limb bone type, and the lower row represents the oldest elements. The arrows indicate the (relative) speed of each of the fronts. The percentages indicate the relative proportions compared to the largest element of that type across all available specimens described in this study. The larger elements such as the femora and tibiae show the strongest shifts in the three fronts with ontogeny, especially in the apposition front, which is also indicated by the larger variety of primary bone tissue types seen in the histology. Smaller elements only show minor changes in the three fronts, and the radii and fibulae even show older histology in smaller elements. AF, apposition front; HSF, Haversian substitution front; RF, resorption front.

in all limb bones. On the other hand, the humeri possess the thinnest cortex of all limb bone types, explaining our observation that the humeri show more advanced bone remodelling. In other words, constant remodelling rates across a thinner (i.e., resorbed) cortex will always result in relatively higher portions of secondary bone. Femora show the highest measured circumferences, but have intermediate cortical thickness compared to the humeri and tibiae. The smaller limb elements such as the radii, ulnae and fibulae show the fastest AF as indicated by the mostly woven bone at the periosteal surface. The greatest differences in the three-front models of the older limb bones are mostly expressed in the AF. Especially the larger limb bones such as the humeri, tibiae and femora show significant decreases in bone apposition rates. This agrees with the observed larger zones of parallel-fibred bone that occur at the periosteal surface of larger (and presumably older) limb bones. Moreover, some bones (e.g., femur RGM.1394110) also deposit inconspicuous LAGs (Figure 6 and 7) suggesting an even slower AF (Figure 14). Curiously, the ulnae, radii and fibulae that were interpreted as being older do not show this decrease in AF speed and retain the same primary bone tissue at the periosteal surface as their ontogenetically younger counterparts (Figure 14). This suggests some allometry between the different limb bones in *Triceratops*.

4.3.11 Histologic Ontogenetic Stages

The difficulties in quantifying the primary growth record in *Triceratops* limb bones via skeletochronology call for the use of 'histologic ontogenetic stages' (HOS) to better capture ontogenetic changes in *Triceratops* histology (Klein and Sander, 2008; Mitchell et al., 2017; Sander and Wintrich, 2021). *Triceratops* shows a wide range of different bone tissue types within any given section, but the majority of the observed primary tissue types are defined by a combination of circumferential and longitudinal primary osteons as well as a combination of woven and parallel-fibred bone matrix. Accordingly, we were able to differentiate between five major bone tissue types (Figure 15): circumferential woven-parallel bone (Type A), longitudinal woven-parallel bone (Type B), circumferential PFLC (Type C), longitudinal PFLC (Type D) and Haversian tissue (Type E). However, unlike in previous HOS studies (Klein and Sander, 2008; Sander and Wintrich, 2021), these tissues are not strictly laid down in an ontogenetic sequence except for Type E but are interspersed and repeat themselves. In other words, the proportions of multiple tissue types in a given element serve in defining the HOS. As both parallel-fibred and woven bone are observed in all elements and were already present in the smallest humerus RSM P.2691 (Figure 2A), we assume that this histology is typical for *Triceratops* and that ontogenetic series will show these bone tissues. We do note that our current histological dataset does not cover the full ontogenetic range known for this taxon from skeletal material, and the DTB *Triceratops* mostly encompass relatively old individuals such as subadults and adults. However, we had extended the size and presumably age range by adding the smaller humeri RSM P.2691 and RSM P.3324.6.1 from Canada to our histological sample. Nevertheless, the lowest stage (HOS 1)in our scheme remains hypothetical.

Using the five tissue types we described seven HOS corresponding to different biological ontogenetic stages (BOS) (Table 2). Each HOS is defined as a combination and sequence of each of the five tissue types (Table 2) and representative diagrams are found in Figure 16. While these stages describe the most dominant histological patterns, some bones preserve a unique combination of tissue types that fall outside the HOS scheme. For example, fibula RGM.1394119 is placed in HOS 7 based on the presence of dense Type E bone tissue, but still shows simple vascular canals with woven bone at the periosteal surface typical for lower HOS. As these tissue types do not represent true HOS 7, they could be considered as transitional stages (i.e., HOS 6.5). In addition, we sporadically observed areas

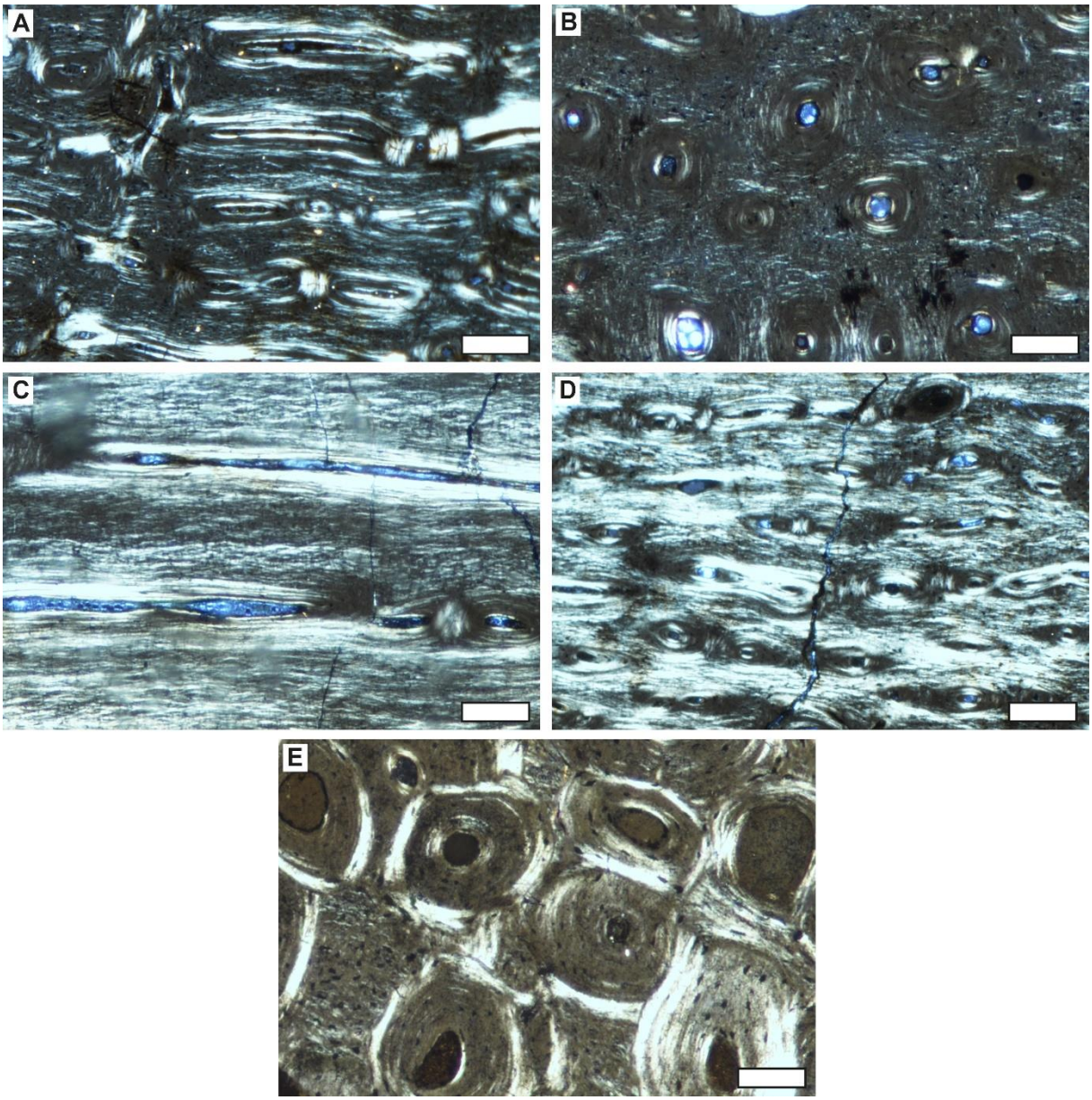

Figure 15. Representative photographs of each of the five tissue types used in the HOS definitions for *Triceratops*. All photographs are in cross-polarized light. A. Tissue type A consists of laminar woven-parallel bone tissue. B. Tissue type B consists of longitudinal woven-parallel bone tissue. C. Tissue type C consists of laminar parallel-fibred bone tissue ('PFLC'). D. Tissue type D defined as longitudinal parallel-fibred bone tissue ('PFLC'). E. Tissue type E consists of Haversian bone tissue, albeit with some primary bone remaining. Scale bar for A and D is 200 µm and scale bar for B, C and E is 100 µm.

of radial and reticular woven-parallel bone tissue substituting for either circumferential or longitudinal woven-parallel bone. However, the current histological dataset is too limited to allow for a more detailed HOS scheme.

HOS and body size are highly correlated. Figure 17 shows relative percentage maximum size (proxy for body size) plotted against their corresponding HOS for the humeri, femora and tibiae. The data shows the expected trend, where larger bones show higher HOS, and thus are considered ontogenetically older. However, it should be noted that elements that have the same HOS stage may still differ in number of secondary osteons, growth lines, simple vascular canals as well as local vascular organisation. Thus, while a general ontogenetic pattern exists, the proposed tissue types and HOS

stages should not be considered definitive, and their interpretation warrants some degree of flexibility. A refined HOS scheme with more HOS will require a substantial increase in sample size and body size range.

4.4 Discussion

4.4.1 Dominant primary histology and growth patterns

Like many non-avian dinosaurs and other fast-growing vertebrates (de Margerie et al., 2004, 2002), *Triceratops* shows typical woven-parallel bone tissue with a mixture of longitudinal and circumferential primary osteons. However, the bone matrix organization within the observed bone tissue type is not strictly fibrous/woven. Instead, the matrix surrounding the vascular network of primary osteons in cortical bone is often characterized by parallel-fibred bone tissue (e.g., Figure 8). Especially the larger limb elements such as humeri, tibiae and femora show this specific histological feature increasingly more towards the bone surface (e.g., Figure 5D). As a result, *Triceratops* long bones possess a distinct type of parallel-fibred 'fibrolamellar' bone tissue. A similar type of tissue has previously been described

Table 2. Description of the histologic ontogenetic stages (HOS) for *Triceratops*. A total of seven stages were developed based on the occurrence of dominant tissue types. HOS 1 was not available in the sample analysis but was extrapolated on the assumption that new-born animals have porous bone in general. HOS 3 was most likely available in humerus RSM P.3324.6.1, but the preservation was relatively poor. Thus the description for HOS 3 was partially based on extrapolation from HOS 2 to 4. For each HOS we assigned a biological ontogenetic stage (BOS). The HOS assigned to the studied material can be found in Table 1.

HOS	Tissue types	BOS
1	The bone tissue consists of woven bone with a high number of laminar simple vascular canals.	Hatchling
2	Cortex consists of Type A with small zones/patches of Type B. The primary osteons are relatively large and have a thin lining of lamellar bone. They often resemble simple vascular canals. No bone remodelling. Vascularity is relatively high and consistent.	Early juvenile
3	Mostly Type A with conspicuous layers of Type B. Inconspicuous zones of Type C that are mostly restricted to the periosteal surface. Lamellar bone of the primary osteons are well-defined, and primary osteons have become relatively small.	Late Juvenile
4	Type A with clear patches of Type B in the outer half of the cortex. Type C becomes more apparent as annuli throughout the primary bone, as well as occurring randomly within the zones of Type A and B. Bone remodelling in the form of secondary osteons is restricted to deeper parts of the cortex. Vascularity is high, but is generally lower close to the areas of Type C.	Early subadult
5	The majority of the cortex show thin zones of Type A and B, separated by thicker conspicuous areas of Type C. Bone remodelling is over halfway of the cortical bone, and the tissue close to the periosteal surface now shows immature secondary osteons. Type E is restricted to the very deep cortex. Vascularity remains constantly high, but slightly decrease in zones of Type C close to the bone surface. Type A and B may also sporadically show reticular or radial primary canals. Simple vascular canals may still be present and are restricted to the outermost periosteal surface, sometimes opening at the bone surface.	Late subadult
6	The preserved primary tissue shows higher numbers of layers of Type C and D of various thickness, and the primary cortex becomes more organized. Type A and Type B only occur as poorly vascularized layers, mostly near the periosteal surface, but even here the tissue is relatively more organized as parallel-fibred tissue is mixed in. When unorganized bone is present, Type B is than more dominant. There are no simple vascular canals. High numbers of secondary osteons appear close to the bone surface, but overall show a diffuse pattern. Type E progresses closer to the bone surface and covers more than half of the cortical thickness. Inconspicuous LAGs may form just beneath the periosteal surface indicating skeletal maturity.	Adult
7	Type E overtakes large portions of the cortical bone, and LAGs become more numerous, and may form an EFS. Primary tissue is limited to close to the periosteal surface, but may still show any tissue type depending on the element.	Mature

in limb bones of certain sauropod dinosaurs including *Ampelosaurus* and *Magyarosaurus,* in which the initially deposited scaffold of the primary bone is parallel-fibred instead of woven (Klein et al., 2012; Stein et al., 2010). Klein et al. (20120) proposed the term 'modified laminar bone' (MLB) to describe this unique histology of relatively slower bone apposition rates. However, the studied *Triceratops* primary bone is not characterized by a predominantly laminar organisation, but instead shows dense longitudinal vascularity. Therefore, we propose the more generalized term 'parallel-fibred lamellar complex' (PFLC) to discuss the dominant primary histological patterns observed here for *Triceratops*. The longitudinal primary osteons are almost always positioned in circumferentially oriented rows parallel to the bone surface, creating bone laminae similarly to those seen in true laminar woven-parallel bone (e.g., compare Figure 7A and 7B). So while the term 'modified laminar bone' might not accurately describe the tissue in *Triceratops*, there is a strong resemblance of PFLC with MLB. In addition to the longitudinal canals, the humeri and femora sporadically show zones of radial woven-parallel bone (Figure 2E and 5A, D).

Many large-bodied non-avian dinosaurs such as sauropods, theropods, and ornithopods predominantly show well-vascularized woven-parallel bone with limited growth marks throughout the primary cortex, indicating rapid uninterrupted growth (Buffrénil et al., 2021; Cullen et al., 2020; D'Emic et al., 2023; Horner et al., 2000; Sander et al., 2011). However, the ontogenetically increasing amount of parallel-fibred bone associated with flat osteocytes and lower vascularity suggests an overall slower growth rate for *Triceratops* (de Margerie et al., 2004, 2002). While this dataset only partially covers ontogenetically young *Triceratops* material, the presence of parallel-fibred 'fibrolamellar' bone in a medium-sized humerus (RSM P.3324.6.1 of 550 mm) suggests that the onset of these bone tissue changes already occurred at an early (ontogenetic) stage.

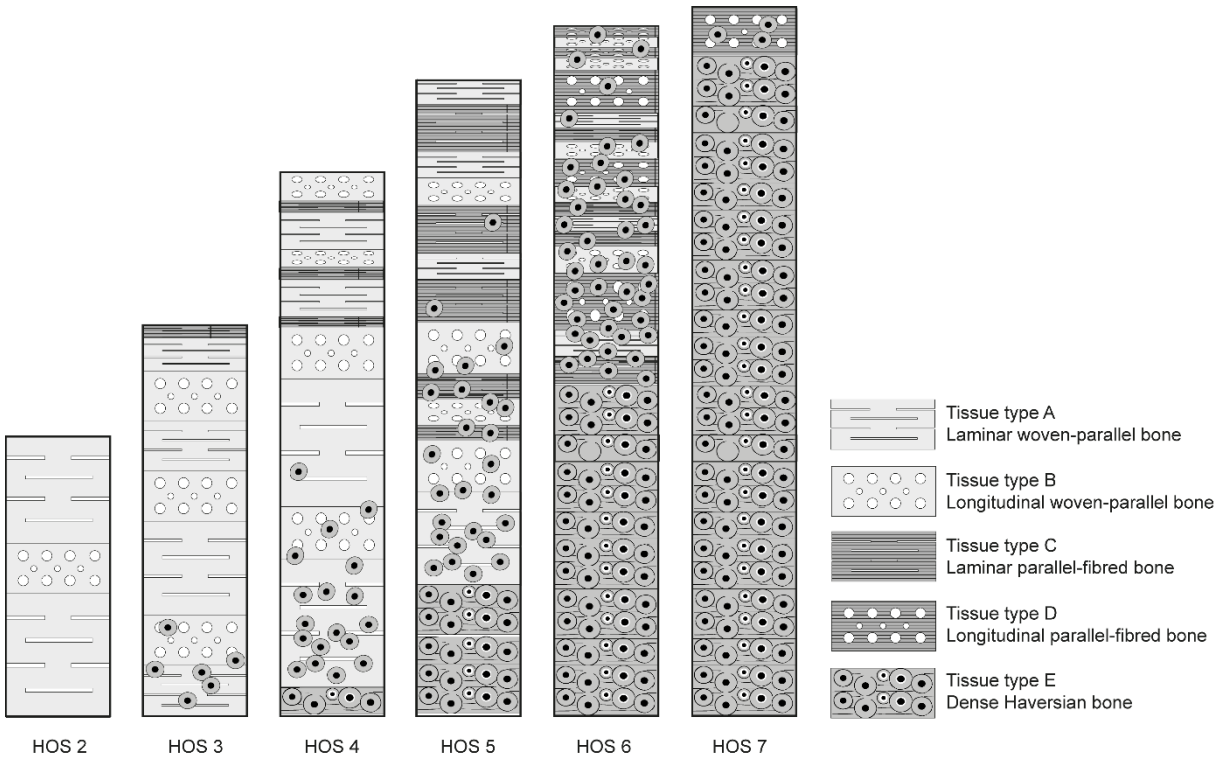

Figure 16. Diagrams showing the combination of bone tissue types defining HOS 2 to 7. Note that HOS 1 is currently hypothetical.

4.4.2 Patterns of bone remodelling explained by the Three-Front Model

All of the studied limb elements except for the two smallest humeri show extensive bone remodelling. The ulnae and radii preserve only very little amounts of primary bone close to the bone surface. This primary tissue mainly consists of longitudinal woven-parallel bone but is quickly overprinted by the advancing HSF, i.e., secondary osteons that grade into Haversian bone towards the medullary cavity, which apparently advances with a constant rate in all bones regardless of their size (Mitchel and Sander, 2014). Thus, the overall high degree of bone remodelling reflects the small size of elements including the radii and ulnae, as thinner bone cortices are more rapidly overtaken by the HSF. The larger limb elements conform to this same pattern of the size-independent advance of the HSF, and preserve more primary bone due to having thicker cortices. Fibulae preserve little primary bone but also lack dense Haversian tissue. Almost all humeri show larger areas of primary bone, except the largest – and presumably oldest – humerus P.1163.9, where remodelling has advanced to the bone surface (Figure 2F). The tibiae and femora also show lower amounts of secondary remodelling and have relatively high portions of preserved primary bone tissue. For all limb elements, extremely dense Haversian tissue is very limited, and large parts of cortical bone preserve interstitial primary tissue. In other words, *Triceratops* and presumably other ceratopsians differ from some other dinosaurs in that the HSF is diffuse and overlapping secondary osteons are often limited to two generations, even in the deepest cortical bone of complete core-samples. Taxon-specific differences in the HSF were already noted for sauropods by Sander (2000).

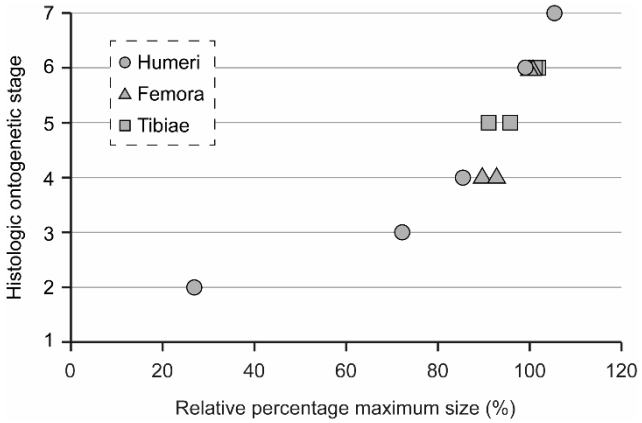

Figure 17. Relationship between size and HOS for the humeri, femora and tibiae. Element size is relative percentage to calculated maximum size (Table S1). Each bone type shows a predictable pattern where increased bone lengths correspond to higher HOS, and presumably older individuals. This pattern is best developed in the humeri because of the wide size range sampled. The close correlation between HOS and size is consistent with the sampled bones representing a single biological genus, i.e., *Triceratops*.

The observed inter-elemental differences in bone remodelling patterns can also be conceptualized by the three-front model. Humeri and tibiae that have overlapping bone dimensions (e.g., bone length and circumference at sampling location, Table 1) show an equally advanced HSF close to the periosteal surface. For example, the larger elements such as humerus RGM.1394102 (length 761 mm and circumference 382 mm) and tibia RGM.1394114 (length 781 mm and circumference 355 mm) from the DTB both show an HSF advanced close to the periosteal surface. These observations fall in line with the constant rate of bone remodelling, and thus constant speed of the HSF assumed by Mitchell and Sander (2014). However, tibiae (and femora) in general still preserve significantly thicker cortical bone than humeri (Table 1, Figure S1). This is also reflected in the three-front models, showing that the RF in humeri is significantly faster than in tibiae and femora (Figure 14 and 15). As a result, the humeri will always have higher portions of secondary bone and a larger medullary cavity compared to the tibiae and femora, despite a constant rate of the HSF. This pattern is even observed within the same individual. Thus, the observed bone remodelling patterns and distribution of histological markers are best explained by the analysis of the three-front model.

The proportionally large *Triceratops* cranium represents a relatively high volumetric percentage of the entire skeleton, especially in later ontogenetic stages, and must have exerted great biomechanical loading. Estimates of the centre of body mass and axial mass distributions in the chasmosaurine *Chasmosaurus* hinted towards an anteriorly inclined loading direction (Henderson, 2014). A similar loading regime in *Triceratops* should translate to relatively higher rates of remodelling in the forelimbs compared to the hindlimbs. This hypothesized pattern is observed in the *Triceratops* histological dataset presented here. The forelimbs show an overall more advanced remodelling front as evidenced by the multiple generations of secondary osteons as well as near-complete overprinting of the primary cortex in the radii and ulnae. We do note that possible size differences between different types of elements could also contribute to the observed remodelling patterns in fore- and hindlimbs as mentioned above. However, the lesser degree of remodelling in the cortex of the fibulae compared to the pronounced remodelling in radii with equally thick cortices (Table 1) suggests that additional factors such as biomechanical loading may play a role in *Triceratops* bone remodelling.

4.4.3 The absence of a primary growth record in appendicular and axial bones

Despite the extensive histological analysis performed on a large selection of *Triceratops* post-cranial material, we were able to retrieve only very limited skeletochronological data. Growth cycles were exclusively expressed as layers of parallel-fibred bone tissue and did not follow a predictable growth pattern with ontogeny (Figure 13). The elements that preserved the most complete primary growth record (e.g., tibia RGM.1394114) provided insufficient data for the calculation of realistic ages-at-death and annual bone apposition rates. The lack of a visible growth record in *Triceratops* is most likely not related to overprinting by secondary osteons. On the contrary, the bone remodelling patterns are relatively diffuse in many of the studied limb bones, and primary cortical bone often remains visible even in deeper areas of the cortex. Thus, it seems that *Triceratops* does not preserve a primary growth record in the first place, or at least complete enough for skeletochronological analyses. These same findings were obtained for large-bodied sauropods (Klein and Sander, 2008; Sander, 2000; Sander et al., 2011) where it is argued that cyclical growth marks are not deposited due to the high growth rates of the especially large limb bones. However, *Triceratops* shows relatively slower bone apposition rates as indicated by the large portions of parallel-fibred bone, but still does not preserve a clear primary growth record. More ontogenetically extensive datasets on *Triceratops* bone histology as well as other derived ceratopsians may reveal whether a lack of primary growth records is characteristic for the whole group.

In sauropods the ribs show a significantly more complete primary growth record and make up for the poor preservation in limb bones (Waskow and Sander, 2014; Waskow, 2019). It is argued that the absolute smaller sizes of ribs elicit lower growth rates and more periodical growth cessations. Considering the histological similarities between sauropods and *Triceratops,* it is expected that *Triceratops* may reveal similar discrepancies between limb and rib histology. However, the axial elements of *Triceratops* studied here show ambiguous results regarding the preservation of a primary growth record. The ribs that were sectioned proximal to distal reveal inconsistent patterns where distal samples show a more advanced HSF compared to proximal samples, despite the fact that distal rib regions represent younger bone tissue. The complete rib section from RGM.1394121 preserves a high number of secondary osteons that overprint the majority of the primary tissue. The primary cortex is limited to the periosteal surface and contains only a small number of inconspicuous growth lines. This observation is contrasting to the sauropod rib sections that show little remodelling and a high number of growth lines in the primary tissue (Waskow and Sander, 2014). Samples of the vertebrae show

equally ambiguous trends in sequential histological patterns along the proximal-distal transect. The primary tissue contains inconspicuous growth marks, but the Haversian bone overprints the majority of these markers, and does not enable accurate growth record reconstructions.

Thus, the remodelling front is more extensive in *Triceratops* ribs than in previously recorded non-avian dinosaurs (Waskow and Mateus, 2017; Waskow and Sander, 2014). Hedrick et al. (2020) reported similarly high remodelling patterns in the ribs of the centrosaurine dinosaur *Pachyrhinosaurus perotorum*. The authors argued that changes in rib shape as well as strong environmental influences resulted in increased remodelling rates of *Pachyrhinosaurus* ribs. The same lines of reasoning can be applied to the *Triceratops* ribs and vertebrae studied here, but it does not explain the differences seen between sauropods and ceratopsians. Overall, the current data on ceratopsian histology shows that ribs have equally inconsistent preservation of the primary growth record as limb elements, suggesting that the axial elements are poor candidates to study the growth and development of this group of dinosaurs. However, additional research on ceratopsian histology is needed to confirm if this pattern of rib growth also extends to a larger majority of the group.

4.4.4 Ontogenetic signal in *Triceratops* limb bone histology

Both the three-front models and the HOS follow an expected pattern consistent with an ontogenetic growth series of a single species. All limb bone samples lie on the same growth trajectory. For almost every element type (Figure 14), the three-front models show a decrease in the AF consistent with lower growth rates expected for older individuals. Along the same lines, the elements that show a faster AF were also assigned a lower (i.e., younger) HOS. However, the two methods show minor offsets in histological identification, especially when considering the putative associated elements in Figure 15. The three-front model indicates that there is a difference between the tibiae, femur and humerus – albeit small – specifically in the AF and RF. This would indicate that some elements may show a lower or higher growth rate. However, all four of the associated elements are assigned to the same HOS 6, suggesting that these elements have similar growth patterns.

The offset in growth pattern identification between both methods is most likely a result of the specific parameters used to describe the three-front models and HOS. In our three-front models, we only distinguished between bone matrix organisation to define the AF and did not consider the different types of vascularity observed in the sections (cf. Mitchell and Sander, 2014). In the HOS scheme, on the other hand, vascularity plays a major role in defining the histological position of the studied limb bones, but does not describe relative intra-bone variations seen in multiple fronts. For example, humerus RGM.1394102 shows a relatively poorly vascularized periosteal surface, but also possesses larger portions of woven-parallel bone tissue compared to the corresponding femur and tibia, giving it a relatively higher AF. However, the portions of woven-parallel bone show mostly longitudinal vascularisation, which would suggest a lower growth rate than laminar woven-parallel bone tissue when compared in the HOS scheme. Moreover, RGM.1394102 shows high densities of secondary osteons which is not defined by the three-front model, but is a determining factor in the HOS scheme. Thus, while the three-front models mostly describe specific relative histological differences within a set of samples, the HOS provide an alternative way of visualizing more general ontogenetic growth changes. Taken altogether, the ontogenetic placement of the *Triceratops* elements is most accurate when the three-front models and HOS are combined, and their analysis allow to better constrain the changes in *Triceratops* growth and ontogeny. While there are some minor deviations in age-size distributions, the overall pattern shows an expected relation between size and histology

(Figure 17) indicating that individuals with larger body mass represent ontogenetically older *Triceratops*.

4.4.5 Phylogenetic patterns of ceratopsian growth

The histology of non-ceratopsid ceratopsians has been studied more extensively than that of ceratopsids, and may provide insights on the evolution of ceratopsian growth patterns when combined with insights gained on *Triceratops* in this study (Figure 18). *Psittacosaurus* represents one of the most basal members of Ceratopsia, and a total of three *Psittacosaurus* species have been studied for their bone histology including (from most basal to most derived) *P. mongoliensis* (Erickson and Tumanova, 2000), *P. lujiatunensis* (Zhao et al., 2019) and *P. sibiricus* (Skutschas et al., 2021). While there are some marked differences in vascularisation and bone remodelling, many of the studied *Psittacosaurus* species show recurring histological patterns. All three *Psittacosaurus* species show predominant reticular vascular organisation and much woven bone in earlier ontogenetic stages, while the *Triceratops* juvenile humeri consisted of a mix of longitudinal and circumferential vascular canals. However, *P. lujiatunensis* and *P. sibiricus* deposit parallel-fibred bone and longitudinal canals only in the latest observed ontogenetic stage – markers that can already be seen in earlier stages in *Triceratops*. *P. mongoliensis* retains reticular woven-parallel bone tissue even in larger/older individuals. Bone remodelling is only evident in very late ontogeny in *P. lujiatunensis* and *P. sibiricus* but is not seen in *P.*

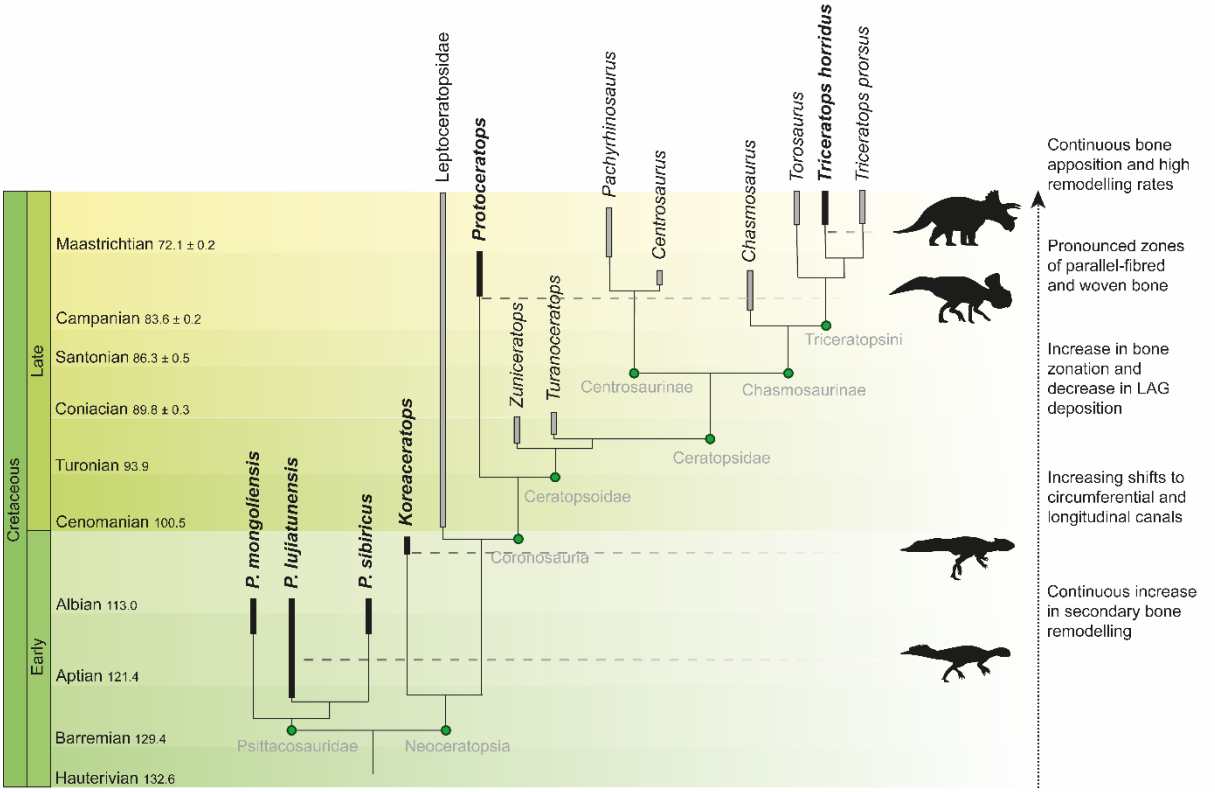

Figure 18. Phylogenetic tree of all major groups within Ceratopsia. Highlighted in black and by silhouette are the taxa of which extensive histological data is available and compared here. Phylogenetic relationships and age ranges for each group are based on literature data (Lee et al., 2011; Mallon et al., 2016; Sampson and Loewen, 2010; Sereno, 2010; Sues and Averianov, 2009; Wolfe et al., 2007; Zheng et al., 2015), and are broadly used to indicate the relationship between the highlighted taxa. Time periods are based on stratigraphy.org. Silhouette are from phylopic.com. *Psittacosaurus* silhouette by Skye McDavid; *Koreaceratops* silhouette based on work from Park Jin-Young and Son Minyoung; *Protoceratops* silhouette by Andrew A. Farke; *Triceratops* silhouette by Raven Amos.

mongoliensis, while *Triceratops* starts bone remodelling in an earlier ontogenetic stage. All *Psittacosaurus* species show LAGs starting from the juvenile stage suggesting that they expressed periodic growth stops already early in ontogeny. This contrasts with ceratopsids such as *Triceratops* that show continuous growth with LAGs only appearing very late in ontogeny. A similar trend is seen between more basal sauropodomorphs and derived sauropods (Botha et al., 2022; Sander et al., 2011).

Koreaceratops hwaseongensis – as a non-coronosaur neoceratopsian – is more derived than *Psittacosaurus* and shows markedly different bone histological patterns (Baag and Lee, 2022). The *Koreaceratops* tibiae show a mix of longitudinal and circumferential vascular canals throughout the entirety of the primary cortex. *Triceratops* shows the same two dominant vascular organisations in all of the studied limb elements, but may also show variable vascular patterns such as radial and reticular canals. The vascular density in *Koreaceratops* alternates between presumable zones and annuli (Baag and Lee, 2022). Unfortunately, the preservation of the studied *Koreaceratops* material did not allow for accurate estimates of bone tissue organisations, but the colour offsets and spacing of the different zones strongly suggest that the changes in vascular density coincide with shifts in bone tissue organisation (Baag and Lee, 2022). These cyclical patterns in woven and parallel-fibred bone tissue are also observed in *Triceratops* limb bones and are especially well-preserved in one tibia (Figure 8). Moreover, the degree of bone remodelling in the *Koreaceratops* tibiae was significantly lower than in the fibulae.

The similarity in histology between basal ceratopsians and ceratopsids becomes clearer when comparing *Protoceratops* to the *Triceratops* data here. *Protoceratops* is a member of the Coronosauria, falling just outside the more derived group of ceratopsoids, and shows clearer alternating zones of parallel-fibred and woven bone (Fostowicz-Frelik and Słowiak, 2018). These cyclical patterns are patchy in juvenile specimens, but become pronounced in the sub-adult stage. This sequence is also observed in *Triceratops,* where parallel-fibred bone is deposited in early ontogeny and becomes more abundant in later stages. However, there is no clear cyclicity observed in the *Triceratops* primary growth record. Nevertheless, as in *Triceratops*, the cyclical zones are most numerous and best preserved in the tibiae of *Protoceratops* and rarely culminate into a growth line. It is not stated whether the parallel-fibred bone matrix of *Protoceratops* is deposited in conjunction with primary osteons (similar as the PFLC) or remains purely avascular, but the illustrations in the paper showing centripetally infilled primary osteons suggests the former (Fostowicz-Frelik and Słowiak, 2018).

The histological characteristics in *Triceratops* can be traced back to more basal non-ceratopsid ceratopsians. Curiously, *Triceratops* – as one of the most derived ceratopsian – seems to preserve a relatively basal aspects regarding their growth regime, as the appearance of parallel-fibred growth zones is already evident in *Koreaceratops* (~103 Ma) and becomes more pronounced in *Protoceratops* (~73 Ma) and ultimately dominant in *Triceratops* (~67 Ma). We do note that the current taxonomic coverage may be too limited to extrapolate these findings. However, the currently available data suggests that – throughout the evolution of ceratopsian dinosaurs – species developed a more continuous growth pattern as indicated by the increasing absence of growth lines and ambiguity of a primary growth record in more derived taxa.

4.4.6 Comparison with other ceratopsids

Little has been published in the peer-reviewed literature on the histology of ceratopsids which makes it difficult to accurately compare the *Triceratops* histology to other closely related taxa. It has been suggested that centrosaurines and chasmosaurines mainly differ in skeletochronological preservation and degree of bone remodelling, with the latter preserving overall less growth marks and higher

remodelling rates (Hedrick et al., 2020; Levitt, 2013; Reizner, 2010). Within the centrosaurine data of Hedrick et al. (2020), the *Avaceratops* humerus preserved a single LAG in the mid-cortex of the humerus while *Yehuecauhceratops* showed up to five LAGs near the periosteal surface of the femur, corroborating their estimated ontogenetic position. However, the *Triceratops* adult femur RGM.1394111 preserves up to seven LAGs near the periosteal surface. Moreover, the described bone remodelling for *Yehuecauhceratops* is equivalent to that of late sub-adult *Triceratops*, and the current published data suggest that centrosaurines and chasmosaurines have more overlapping bone histological patterns than previously thought.

However, these previously published assumptions on ceratopsid histology are based on the study of fragmentary material which have not allowed for in-depth comparisons of ceratopsian histology along the lines of phylogeny and ontogeny. On the other hand, unpublished work on the centrosaurine *Einiosaurus procurvicornis* has provided novel insights into its growth regime (Reizner, 2010), but the sample set only comprises juveniles and sub-adults not older than six years (based on LAG count). Therefore, it is difficult to predict whether the lack of bone remodelling in this species is an effect of taxonomic differences or simply because these specimens represent ontogenetically young individuals that yet need to remodel. Likewise, previously unpublished thesis material on the chasmosaurines *Utahceratops gettyi* and *Kosmoceratops richardsoni* provided some of the first datasets on chasmosaurine limb bone histology (Levitt, 2013), but the sampled material was mainly from presumed juvenile or sub-adult individuals. Considering the very late appearances of growth lines in *Triceratops,* the absence of LAGs in the young adult *Utahceratops* femur could have been an ontogenetic signal and not necessarily a marked difference between centrosaurines and chasmosaurines. Additional ontogenetically well-constrained ceratopsid limb material is needed to better understand the taxonomic implications of the observed histological offsets. Especially the first large-bodied ceratopsians, such as the ceratopsoids (e.g., *Zuniceratops* and *Turanoceratops*), may yield valuable insights into the evolution of ceratopsid growth strategies.

4.4.7 *Triceratops* species and *Torosaurus*

The *Triceratops* sections presented here can be compared among the two different species as well as the available *Torosaurus* histology in the literature to provide additional context for potential species differences and for the taxonomic ambiguity between *Triceratops* and *Torosaurus*. Offsets between HOS and body size have previously been associated with potential taxonomic differences and/or sexual dimorphism (Klein and Sander, 2008; Redelstorff and Sander, 2010). For over a decade, there has been debated on whether *Torosaurus* is a valid genus or rather synonymous with *Triceratops* as its final ontogenetic stage (Longrich and Field, 2012; Maiorino et al., 2013; Mallon et al., 2022; Scannella and Horner, 2011, 2010). Previous hypotheses were mostly based on cranial characteristics including skull morphometrics, suture closing, transitional fossils and osteohistology of cranial elements. However, recently Mallon et al. (2022) provided first images on *Torosaurus* limb bone histology. Their femur sections allowed to determine the relative age of a *Torosaurus* specimen more accurately. Based on the lack of an EFS, widely spaced secondary osteons at the bone surface and overall woven-fibred bone tissue, Mallon et al. (2022) concluded that their *Torosaurus* specimen did not reach skeletal maturity, and most likely represents a sub-adult individual. Figure 19 shows the relationship between HOS and bone circumference normalized to femur circumference for the *Triceratops* bones of both species as well as the *Torosaurus* femur section. The *Torosaurus* specimen can be assigned to HOS 5 transitioning into HOS 6 based on the available histological description, while our oldest *Triceratops* femur shows advanced HOS 6. However, the *Torosaurus* femur does not strongly deviate from the observed

correlation between age and size for *Triceratops*, implying that both taxa are indistinguishable based on histology alone (Figure 19).

Similarly, our results do not find a clear difference in HOS and body size correlation between *T. horridus* and *T. prorsus*. We do observe that the *T. prorsus* specimens are larger than the *T. horridus* specimens, but they also show the highest HOS in the dataset (Table 1, Figure 19). Thus, it is still reasonable to assume that the *T. horridus* individuals in our dataset may grow slightly larger, reaching HOS 7 and skeletal maturity at approximately the same body size as *T. prorsus*. Overall, the presented *Triceratops* and *Torosaurus* histological database is currently too small to observe unequivocal taxonomic differences in ontogenetic growth patterns on the genus and species level.

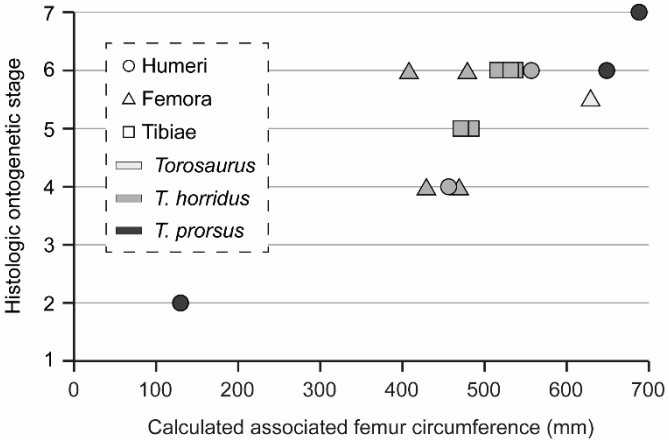

Figure 19. Relationship between body size and HOS for *T. horridus, T. prorsus* and *Torosaurus*. Bone size is represented by limb circumference normalized to femur circumference based on ratios of the associated *Triceratops* specimens RGM.1332500. Both *T. prorsus* and *Torosaurus* do not significantly deviate from the overall correlation for *T. horridus*.

4.4.8 Cranial ontogeny linked to skeletal maturity

The detailed taphonomic description of the DTB provided in **Chapter 2** may provide new insights on *Triceratops* ontogenetic development, as we can now assume that the DTB individuals represent an associated group with better constrained skeletal unity (i.e., association of skeletal elements to the correct individual; cf. Wiersma-Weyand et al., 2021). Following the naming convention of Horner and Goodwin (2006), the uncovered parietal and squamosal bones (and hence, the individuals) from the DTB were assigned to sub-adult and adult animals based on the presence and absence of epoccipital ornamentation, respectively (**Chapter 2: Figure 2**). Sub-adults with adorned frills represent younger individuals while the adults are considered to be mature and fully grown (Horner and Goodwin, 2006; in this case we do not consider *Torosaurus* to be the final ontogenetic stage of *Triceratops*). Younger *Triceratops* with sub-adult cranial morphologies should thus have relatively younger bone histology. Likewise, adult *Triceratops* displaying the final cranial ontogenetic stage should represent skeletally mature individuals based on their histology. Based on the taphonomic scenario reconstructed in **Chapter 2**, it is most parsimonious to conclude that the actively growing individuals (HOS 4 to 5) are associated with sub-adult frills and skeletally mature individuals (HOS 5 to 6, preserving an EFS) with adult frills in the DTB. Curiously, the DTB did not yield any fused cranial elements suggesting that cranial suture closing/fusion occurred later in development after attainment of skeletal maturity and/or that suture closing experienced higher developmental plasticity. Nevertheless, the apparent linkage of histological and cranial age classes of the DTB strongly suggests that the termination of the cranial ontogenetic trajectory coincides with that of somatic/skeletal growth (Figure 20). The histologically younger samples such as humeri RSM P.2691 and RSM P.3324.6.1 may be associated with the younger cranial ontogenetic stages (Figure 20). However, future efforts focussed on unravelling the histology of a ontogenetically more diverse dataset should provide more conclusive data on how cranial and skeletal development are linked for *Triceratops* and other horned dinosaurs.

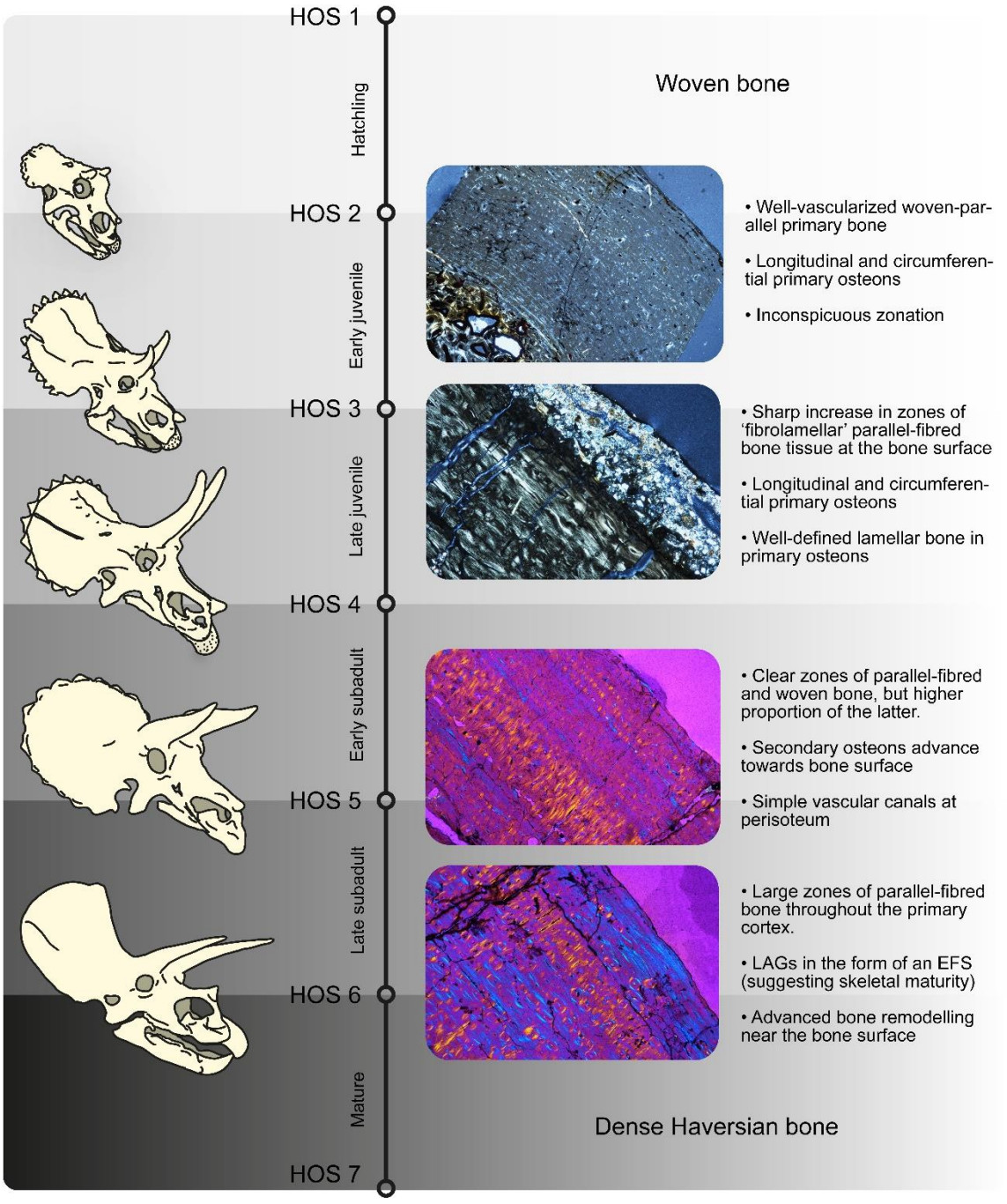

Figure 20. Overview of ontogenetic and associated histological stages for *Triceratops*. The cranial ontogeny is based on Horner and Goodwin (2006). The histological data from the DTB suggests that the attainment of the adult cranial ontogenetic stage coincides with the attainment of skeletal maturity. Hypothetically, the younger histological age classes observed in this study should represent younger cranial ontogenetic stages.

The established taphonomic scenario for the skeletal unity of the DTB (**Chapter 2**) as well as the newfound insights on the timing of cranial and skeletal maturity may help to clarify the taxonomic ambiguity between *Triceratops* and *Torosaurus*. The taphonomic analysis from **Chapter 2** has shown that the DTB is characterized as a monospecific catastrophic bonebed containing exclusively remains of *Triceratops*, and both sub-adult and adult parietal and squamosal elements that were recovered are not fenestrated nor show incipient fenestrae typical of *Torosaurus*. The adult *Triceratops* from the DTB described in this study shows ontogenetically older histology than *Torosaurus* as indicated by the presence of an EFS, a more advanced Haversian substitution front and higher proportions of parallel-

fibred over woven bone. Additionally, while not explicitly stated by the authors, the *Torosaurus* femur preserves sparse reticular canals (suggesting higher bone apposition rates) closer to the bone surface while our oldest *Triceratops* femur exclusively shows longitudinal and circumferential primary osteons. Based on histology, the *Torosaurus* specimen in Mallon et al. (2022) is younger than our described *Triceratops* adults. Thus, the presence of an adult – skeletally mature – *Triceratops* individual associated with an unfenestrated mature frill morphology older than known *Torosaurus* specimens strongly supports the two-genus hypothesis and rejects the synonymy between *Torosaurus* and *Triceratops*. One scenario exists in which fenestrae may form after cranial and skeletal maturity is reached or these taxa express such high levels of developmental plasticity that timing of cranial ontogeny is difficult to constrain altogether. However, the current body of knowledge on this topic does not provide such evidence (Longrich and Field, 2012; Maiorino et al., 2013; Mallon et al., 2022; Scannella and Horner, 2011, 2010).

4.5 Conclusion

Histological analyses of *Triceratops* limb bones plus auxiliary specimens revealed for the first time the growth pattern of this iconic ornithischian dinosaur. All limb bones of the stylopodium and zeugopodium show a consistent histology, with variations mainly due to cortical thickness as explained by the three-front model, and there is a clear relationship between body size and histologic ontogenetic stage. Ontogenetically young individuals – as represented by the small humerus RSM P.2691 – show a well-vascularized woven-parallel complex typical for actively growing endothermic juvenile animals and contains a mix of circumferential and longitudinal primary osteons. However, the dominant bone tissue type shifts into cycles of parallel-fibred bone and woven-fibred complex throughout ontogeny allowing to define the histological development through histologic ontogenetic stages. Sub-adult *Triceratops* limb bones are characterized by irregular alternating zones of thicker layers of woven and thinner layers of parallel-fibred bone tissue. Bone remodelling is only moderate, and simple vascular canals in the periosteal surface indicate active growth. As the animal approached skeletal maturity, the primary bone of adult *Triceratops* shows higher proportions of parallel-fibred bone tissue and increased bone remodelling. Skeletal maturity is indicated by an EFS near the periosteal surface.

Apart from the EFS in mature specimens, regular growth cycles are rare in the studied elements. A small number of elements preserve higher numbers of zones and annuli, but the majority of the sections show a poorly developed skeletochronological record, which we now consider typical for ceratopsid histology. Ribs and vertebrae preserve small numbers of LAGs, but the heavy remodelling combined with the significant influence of bone morphogenesis on growth mark spacing in ribs does not allow for accurate analysis of the primary growth record. Contrary to sauropod rib histology, *Triceratops* (and most likely other ceratopsids) show faster growing woven-parallel bone tissue in their ribs possibly hampering LAG deposition.

While the zones of parallel-fibred tissue in the limb bones are less vascularized than the zones of woven-parallel complex, they all contain primary osteons and form ‘fibrolamellar’ parallel-fibred bone (PFLC) similar to the modified laminar bone described for some sauropod taxa. In fact, *Triceratops* showed overall high vascularization throughout ontogeny across multiple different limb elements. The prevalence of parallel-fibred bone tissue relatively early in ontogeny combined with consistently high vascularisation suggests that *Triceratops* had a relatively fast and continuous growth rate, but not as rapid as is seen in many other groups of non-avian dinosaurs.

The zonation of parallel-fibred bone tissue is also observed in more basal ceratopsians, but becomes more pronounced in *Triceratops.* Comparisons with other ceratopsids provide equivocal

results due to lack of ontogenetically well-constrained material and warrants additional data on ceratopsid histology.

When combined with the bonebed data from **Chapter 2,** the clear transition of sub-adult and adult cranial ontogenetic stages associated with actively growing and skeletally mature individuals in the DTB suggest that cranial ontogeny follows the attainment of skeletal maturity. Consequently, the presented HOS scheme and ontogenetic ageing help resolving the taxonomic ambiguity between *Triceratops* and *Torosaurus*, as non-fenestrated *Triceratops* specimens from the DTB represent individuals that are histologically older (i.e., higher HOS) than published *Torosaurus* specimens. Our work adds to the rather limited ceratopsian histological database, being based on the most extensive dataset for any large-bodied neoceratopsian, and is beginning to unravel the evolution of ceratopsian growth strategies.

4.6 Supplementary data

Table S1. Limb measurements and limb-to-femur ratios of the associated *Triceratops horridus* skeleton RGM.1332500 at Naturalis Biodiversity Center, the Netherlands. The largest available femur on which the potential maximum sizes are based is femur RGM.1394110 (Figure S4). Measurements of RGM.1332500 were either based only on left (R) limb bones or based on left and right (L+R) limb bones when available. The maximum size values were used to calculate percentage maximum sizes for the sampled bones in Table 1 in the main text.

Limb bone	RGM.1332500 Length (mm)	RGM.1332500 Limb-to-femur ratio	Maximum size (mm) based on largest available femur
Humerus	708 (L+R)	0.68	762
Ulna	628 (R)	0.61	683
Radius	408 (L+R)	0.39	437
Femur	1038 (L+R)	1	1120
Tibia	720 (R)	0.69	773
Fibula	677 (L+R)	0.65	728

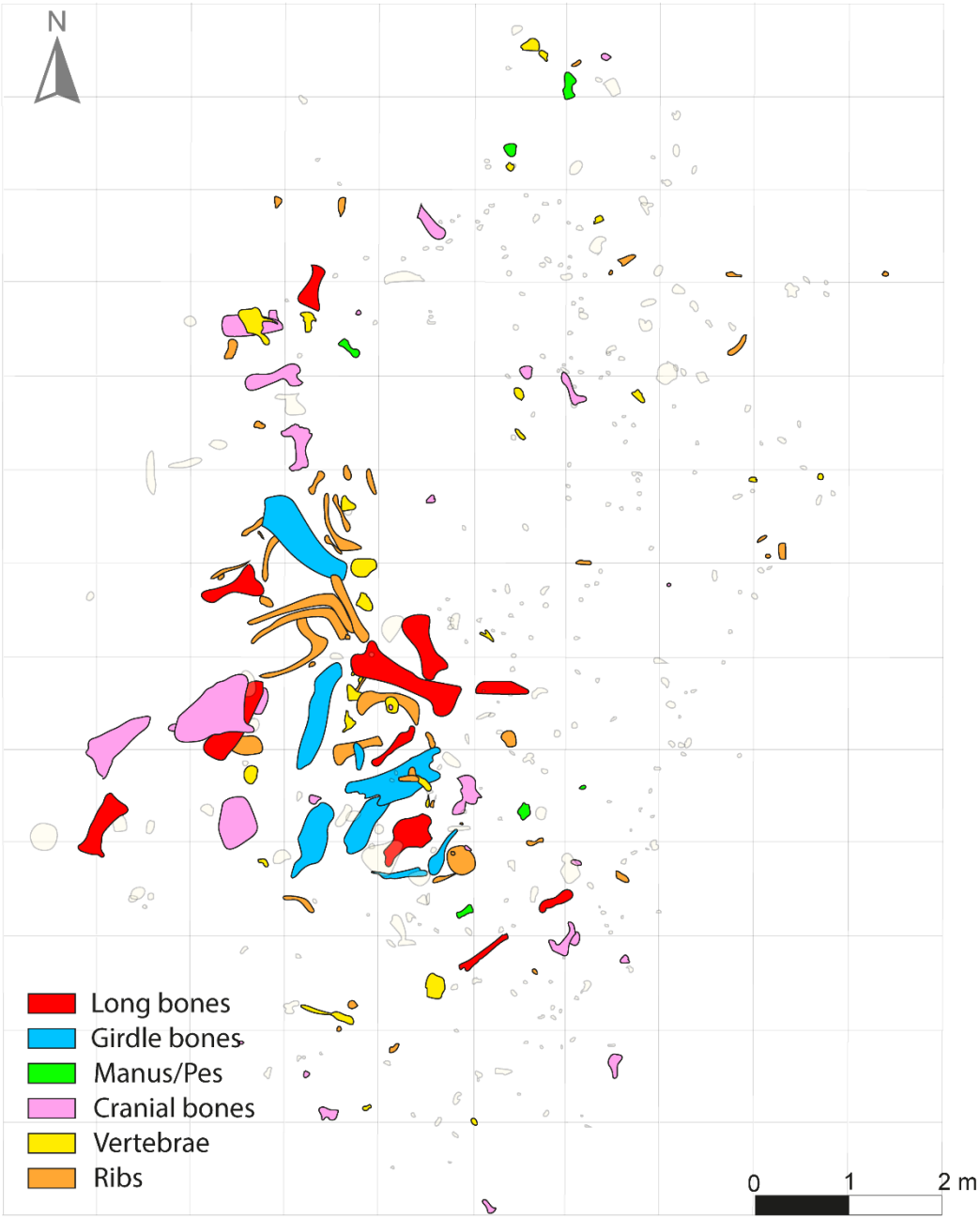

Figure S1. Bonemap of *Triceratops* RGM.1332500 on exhibit at Naturalis Biodiversity Center, the Netherlands. The bones are spatially constrained and each bone is unique, suggesting that the quarry preserves the remains of a single associated individual. The non-coloured pale outlines are unidentified bone fragments.

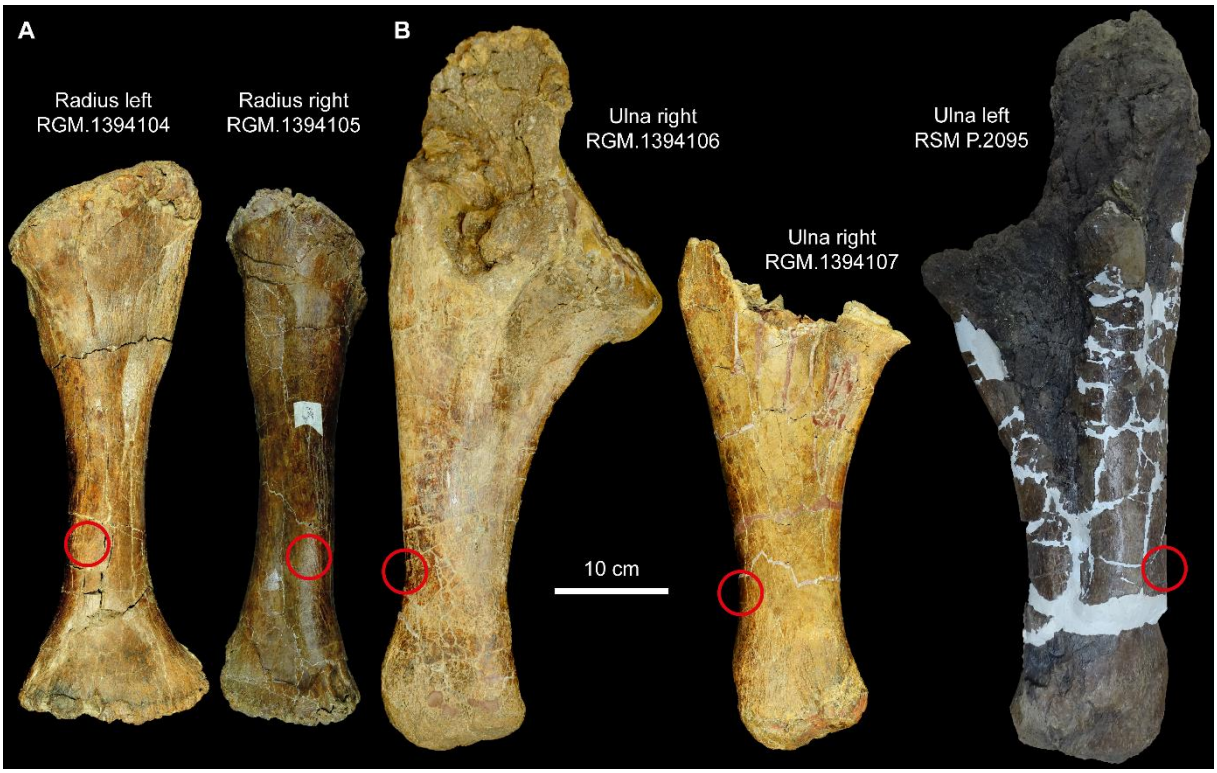

Figure S2. Overview of the radii (A) and ulnae (B) sampled in this study. The red circle indicates the sampling location for drill-coring (the anterolateral midshaft for the radii and the posterior ridge at midshaft of the ulnae).

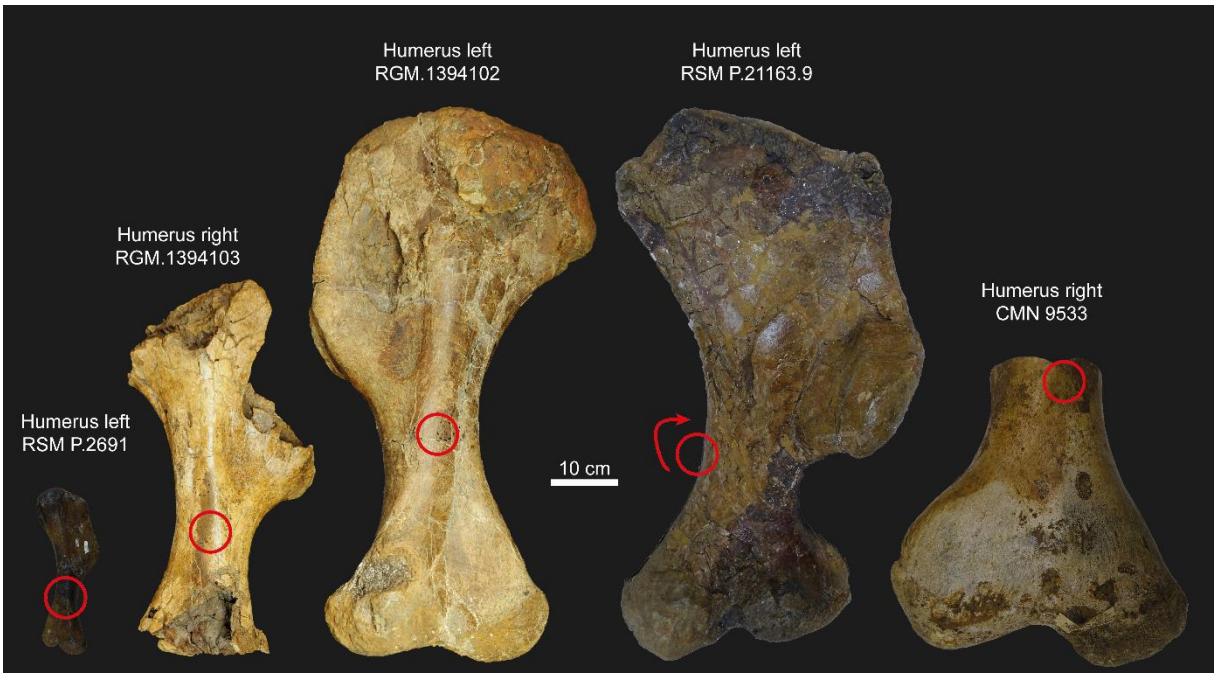

Figure S3. Overview of the humeri sampled in this study. The red circle indicates the sampling location for drill-coring (the central posterior midshaft). The red arrow indicates that the sampling location is located on the backside of the corresponding photograph.

Figure S4. Overview of the femora sampled in this study. The red circle indicates the sampling location for drill-coring (the medial midshaft just distally from the large muscle attachment site). The red arrow indicates that the sampling location is located on the backside of the corresponding photograph.

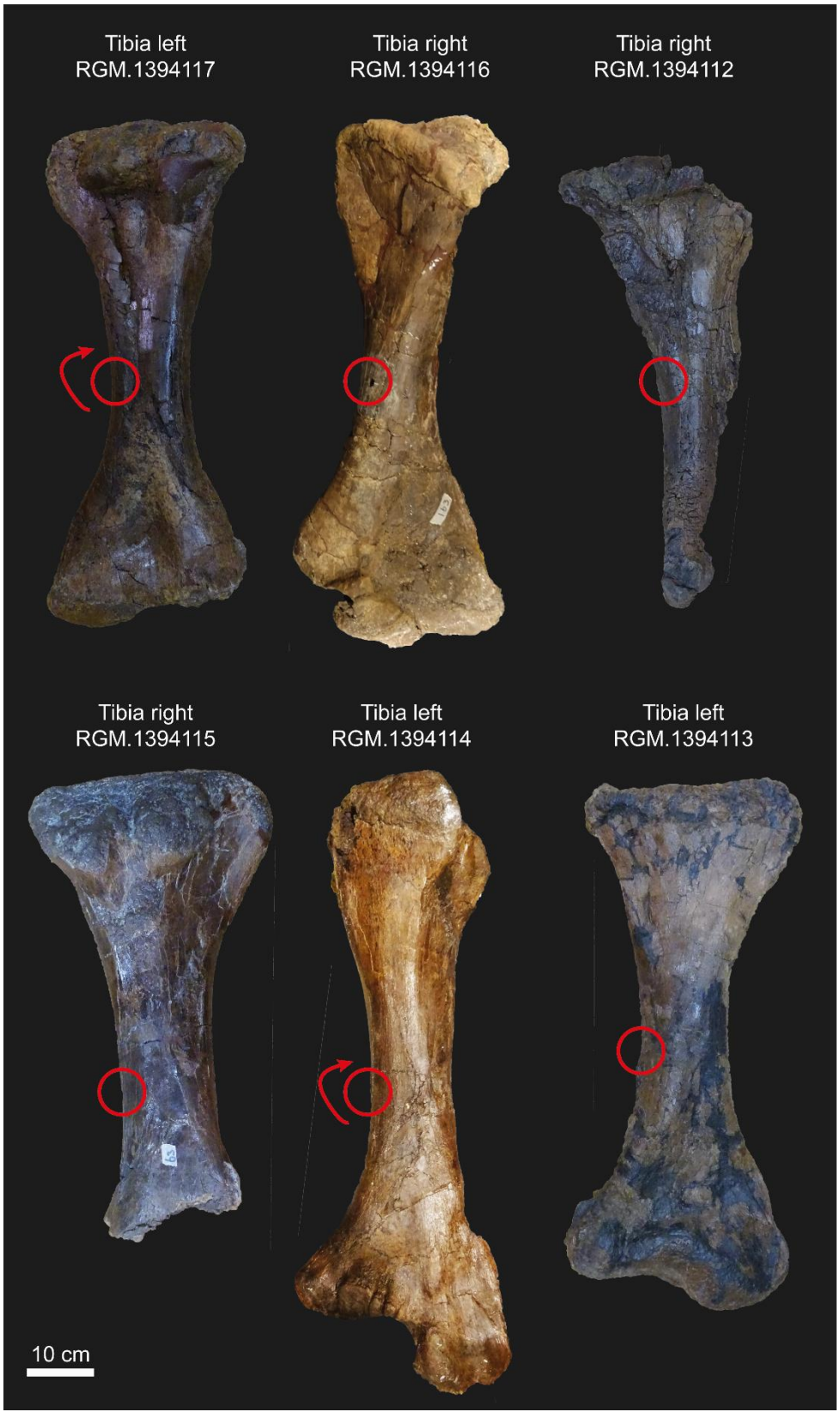

Figure S5. Overview of the tibiae sampled in this study. The red circle indicates the sampling location for drill-coring (the posteromedial midshaft). The red arrow indicates that the sampling location is located on the backside of the corresponding photograph.

Figure S6. Overview of the fibulae sampled in this study. The red circle indicates the sampling location for drill-coring (the lateral midshaft).

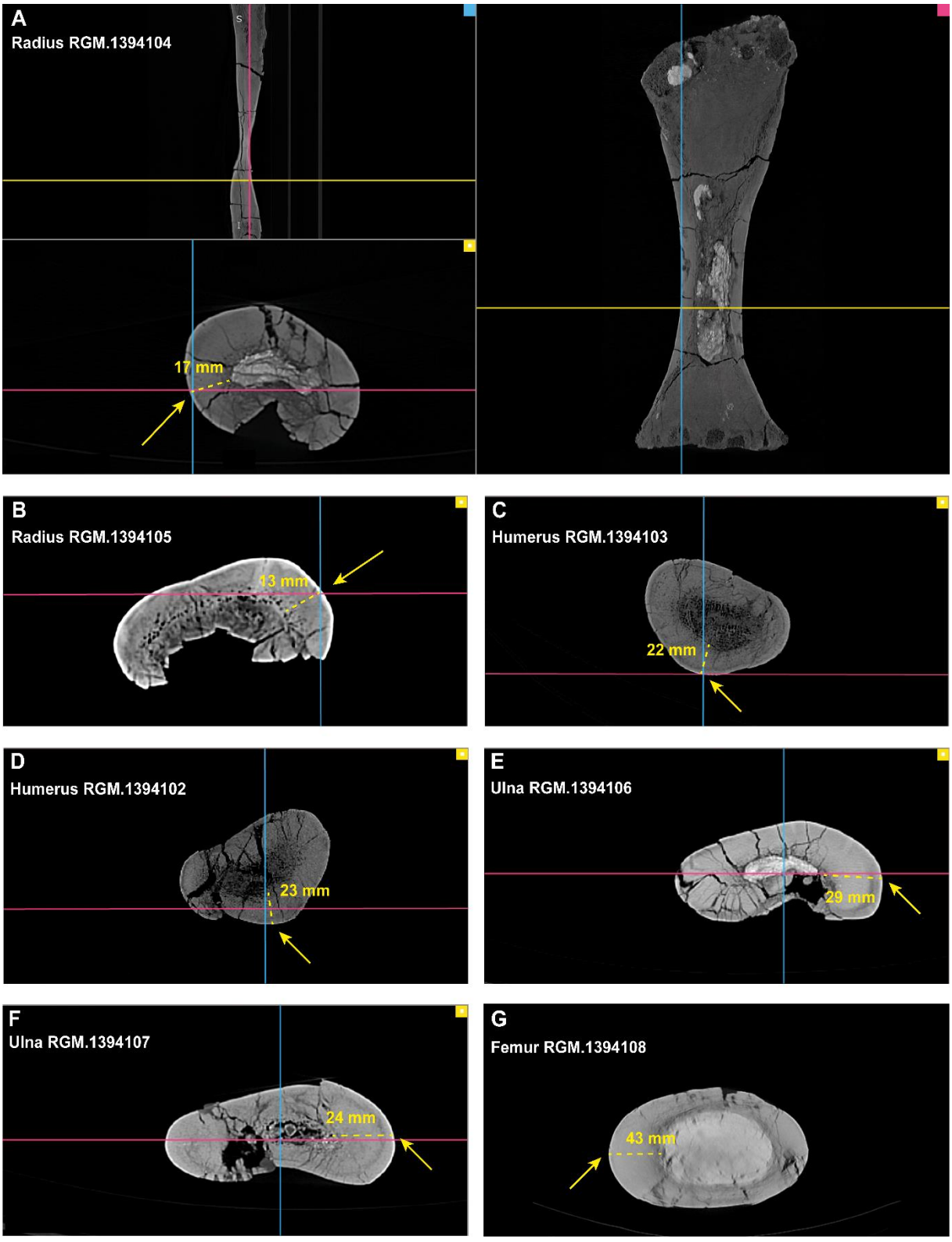
A
Radius RGM.1394104
17 mm
B
Radius RGM.1394105
13 mm
C
Humerus RGM.1394103
22 mm
D
Humerus RGM.1394102
23 mm
E
Ulna RGM.1394106
29 mm
F
Ulna RGM.1394107
24 mm
G
Femur RGM.1394108
43 mm

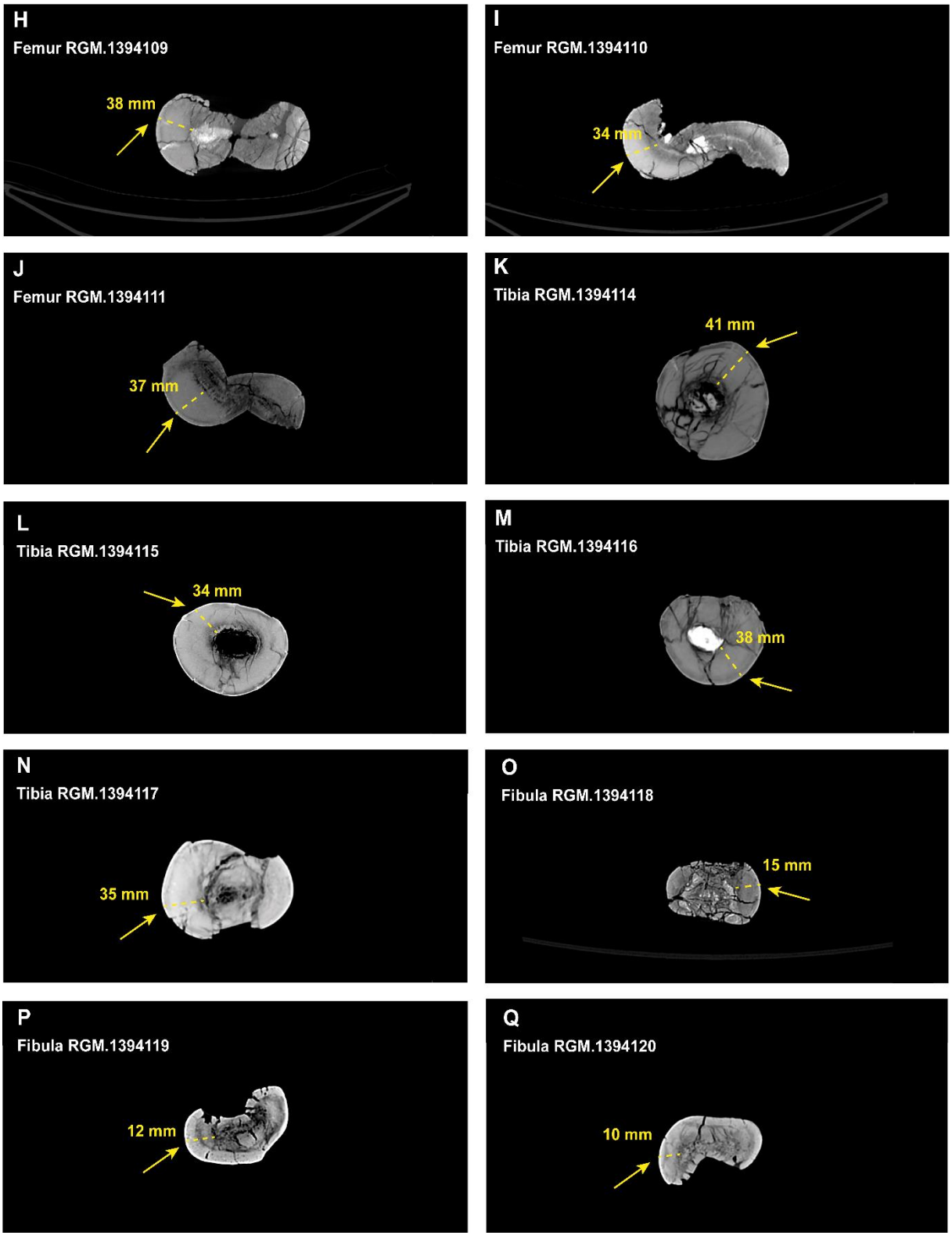
H
Femur RGM.1394109
38 mm
I
Femur RGM.1394110
34 mm
J
Femur RGM.1394111
37 mm
K
Tibia RGM.1394114
41 mm
L
Tibia RGM.1394115
34 mm
M
Tibia RGM.1394116
38 mm
N
Tibia RGM.1394117
35 mm
O
Fibula RGM.1394118
15 mm
P
Fibula RGM.1394119
12 mm
Q
Fibula RGM.1394120
10 mm

Figure S7. Overview of CT images for the available specimens from Naturalis Biodiversity Center, the Netherlands, showing variable degrees of preservation and diagenesis. For each limb element type, the ideal sampling location was pinpointed based on the thickest available intact cortical bone surrounding the midshaft area that was preserved across all the specimens. This resulted in a specific plane of sampling for each element type: the central posterior midshaft for the humeri (C, D), the anterolateral midshaft for the radii (A, B), the posterior ridge at midshaft of the ulnae (E, F), the medial midshaft of the femora (G, H, I, J), the posteromedial midshaft of the tibiae (K, L, M, N) and the lateral midshaft for the fibulae (O, P, Q). Images are not to scale but purely serve to clarify on the parameters used to assess the internal bone structure. The dashed line indicates the total measured cortical thickness (in mm) and the arrow shows point of insertion during core-sampling. Image A provides a more detailed print of applied viewing planes. All images were made by Radiant DICOM Viewer and Philips DICOM Viewer, both free viewing software.

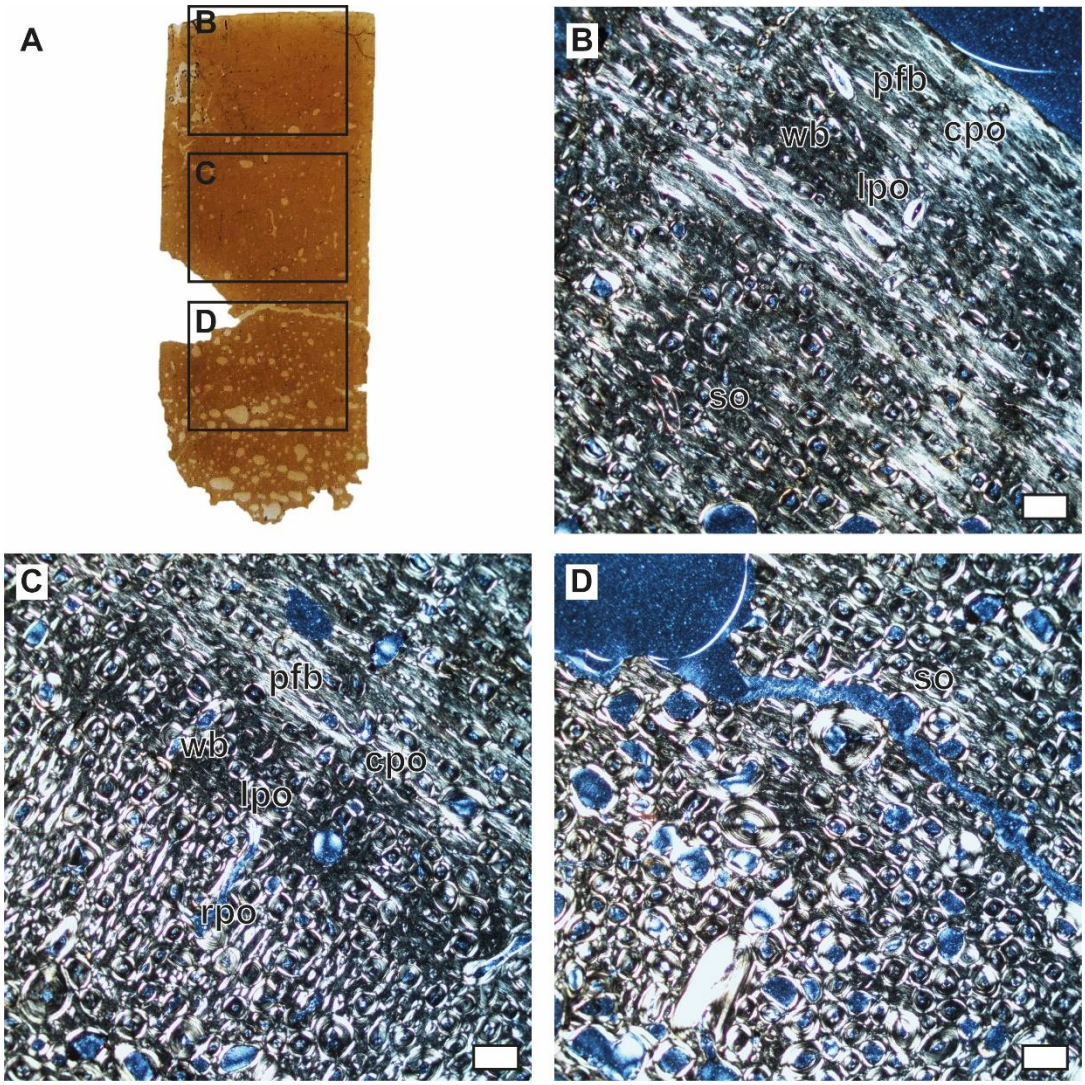

Figure S8. Overview of the histological patterns of humerus RGM.1394102, representing the oldest humerus from the DTB (HOS 6). All images are in cross-polarized light. All histological images have bone surfaces towards the upper right corner. A. Overview of the thin-section with corresponding sections annotated. B. Histology close to the bone surface showing portions of woven and parallel-fibred bone. The portions of woven bone most often have longitudinal osteons, while circumferential osteons are more common in parallel-fibred bone. Parallel-fibred bone is more widespread and may even be dispersed in layers of woven bone. Note the low number of secondary osteons, especially in the top half of the photograph. C. Overview of the histology in the mid-cortex showing thick layers of parallel-fibred bone with thinner layers of woven bone. There is a conspicuous layer of woven bone with radial vascularisation. Bone remodelling increases. D. Histology of cortical bone at the medullary border showing mostly woven bone, but with high numbers of secondary osteons and dispersed larger resorption cavities. All scale bars are 500 µm. cpo, circumferential primary osteon; lpo, longitudinal primary osteon; pfb, parallel-fibred bone; rpo, radial primary osteons; so, secondary osteon; wb, woven bone.

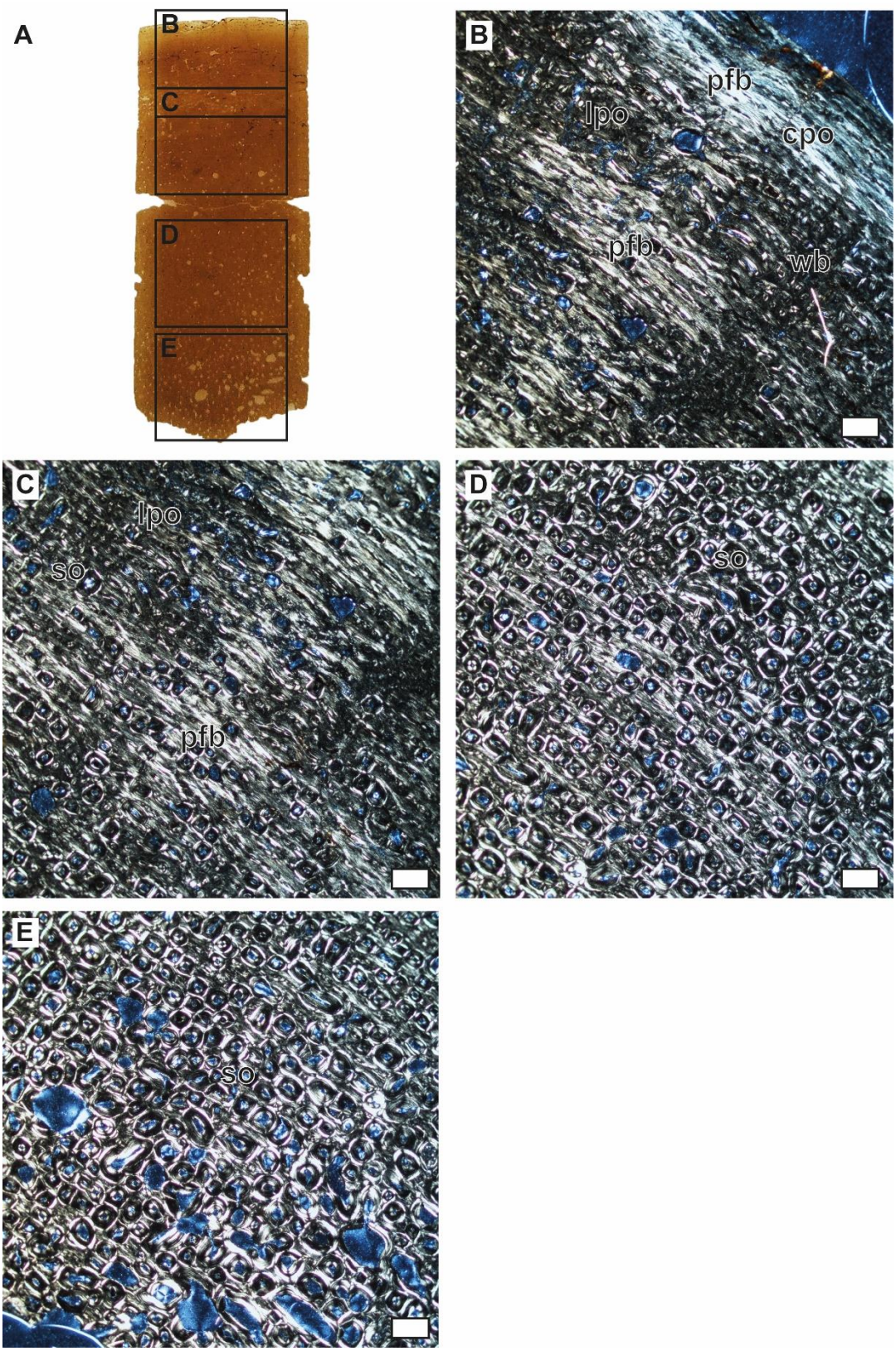
A
B
C
D
E
B
pfb
lpo
cpo
pfb
wb
C
lpo
so
pfb
D
so
E
so

Figure S9. Overview of the histological patterns of humerus RGM.1394103, representing the youngest humerus from the DTB (HOS 4). All images are in cross-polarized light. All histological images have bone surfaces towards the upper right corner. A. Overview of the thin-section with corresponding sections annotated. B. Histology of the bone surface showing relatively confined zones of parallel-fibred bones and larger zones of woven bone. The primary vascularity in the areas of woven bone is longitudinal, while circumferential osteons are mostly limited to the parallel-fibred bone tissue. However, these characteristics are interchangeable. Note the lack of secondary osteons in these parts. C. Upper part of the mid-cortex showing similar patterns as in B, but here the first secondary osteons start to appear. Woven bone is still more dominant than parallel-fibred bone. D. Lower part of the mid-cortex showing increased bone remodelling. The middle part of this section shows a layer of parallel-fibred bone tissue, but otherwise the interstitial primary cortex constitutes mainly woven bone. E. Cortical bone closely associated with the medullary cavity showing larger resorption cavities and dense Haversian tissue. All scale bars are 500 µm. cpo, circumferential primary osteon; lpo, longitudinal primary osteon; pfb, parallel-fibred bone; so, secondary osteon; wb, woven bone.

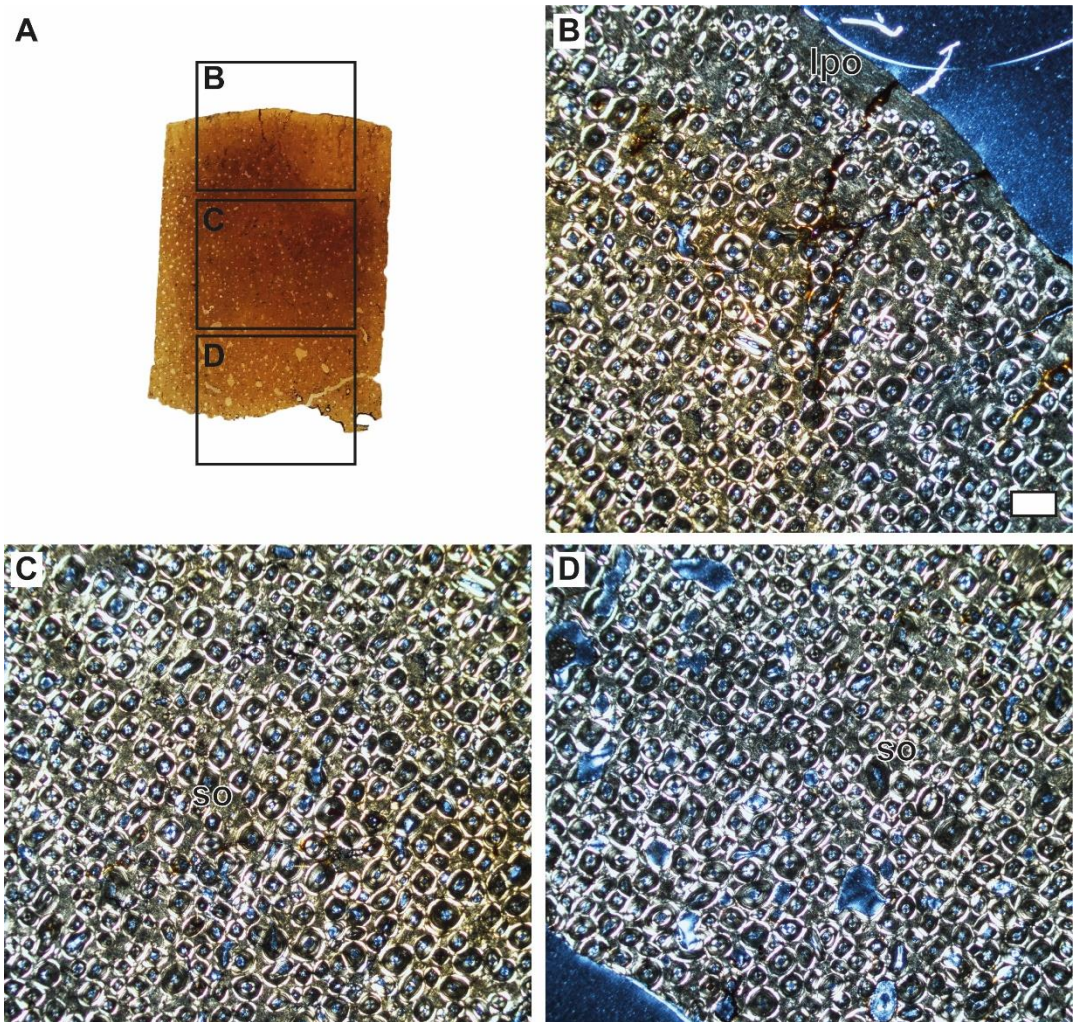

Figure S10. Overview of the histological patterns of radius RGM.1394105, representing the oldest radius from the DTB (HOS 7). All images are in cross-polarized light. All histological images have bone surfaces towards the upper right corner. A. Overview of the thin-section with corresponding sections annotated. B. Histology of the bone surface showing advanced bone remodelling. However, there is still considerable amounts of interstitial primary bone which is woven-parallel containing relatively small longitudinal primary osteons. C. Histology of the mid-cortex showing overlapping secondary osteons with only very little primary tissue. D. Histology close to the medullary cavity showing dense Haversian tissue and regular resorption cavities. All scale bars are 500 µm. lpo, longitudinal primary osteon; so, secondary osteon.

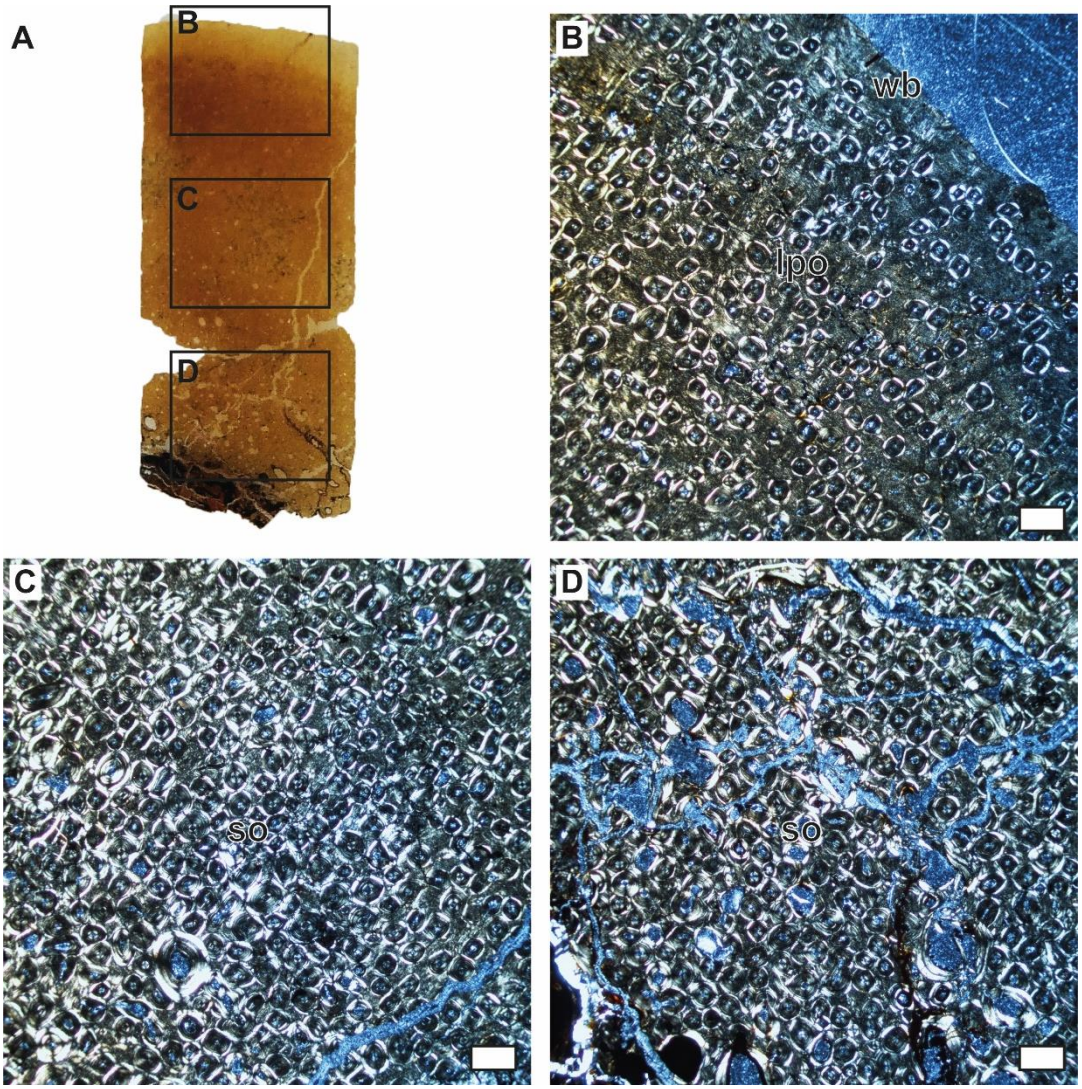

Figure S11. Overview of the histological patterns of radius RGM.1394104, representing the youngest radius from the DTB (HOS 6). All images are in cross-polarized light. All histological images have bone surfaces towards the upper right corner. A. Overview of the thin-section with corresponding sections annotated. B. Histology of the bone surface showing relatively large areas of primary (woven) bone and smaller longitudinal primary osteons. Secondary osteons are abundant, but are less dense than in RGM.1394105 (Figure S10). C. Histology of the mid-cortex showing high numbers of secondary osteons with smaller areas of interstitial primary tissue. D. Fractured bone cortex close to the medullary cavity showing mainly dense Haversian tissue. All scale bars are 500 µm. lpo, longitudinal primary osteon; so, secondary osteon; wb, woven bone.

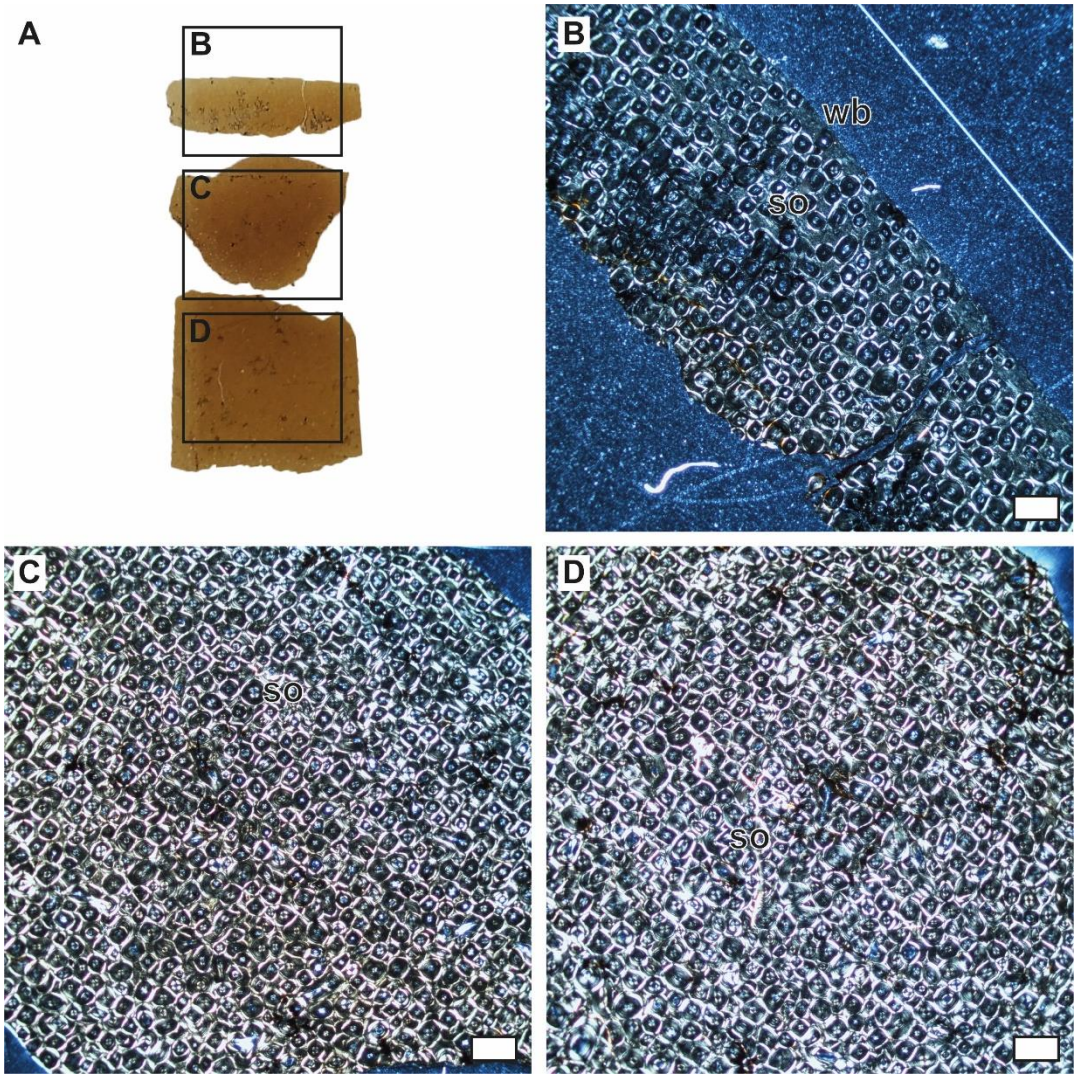

Figure S12. Overview of the histological patterns of ulna RGM.1394106, representing the oldest ulna from the DTB (HOS 7). All images are in cross-polarized light. All histological images have bone surfaces towards the upper right corner. Core was broken during sampling. A. Overview of the thin-section with corresponding sections annotated. B. Histology of the bone surface showing high numbers of secondary osteons with interstitial primary woven bone. Note the eroded secondary osteons at the upper bone surface indicating that the original bone surface has been abraded. C. Heavily remodelled mid-cortex with dense Haversian bone. D. Multiple generations of secondary osteons in dense Haversian bone close to the medullary cavity. All scale bars are 500 µm. lpo, longitudinal primary osteon; so, secondary osteon; wb, woven bone.

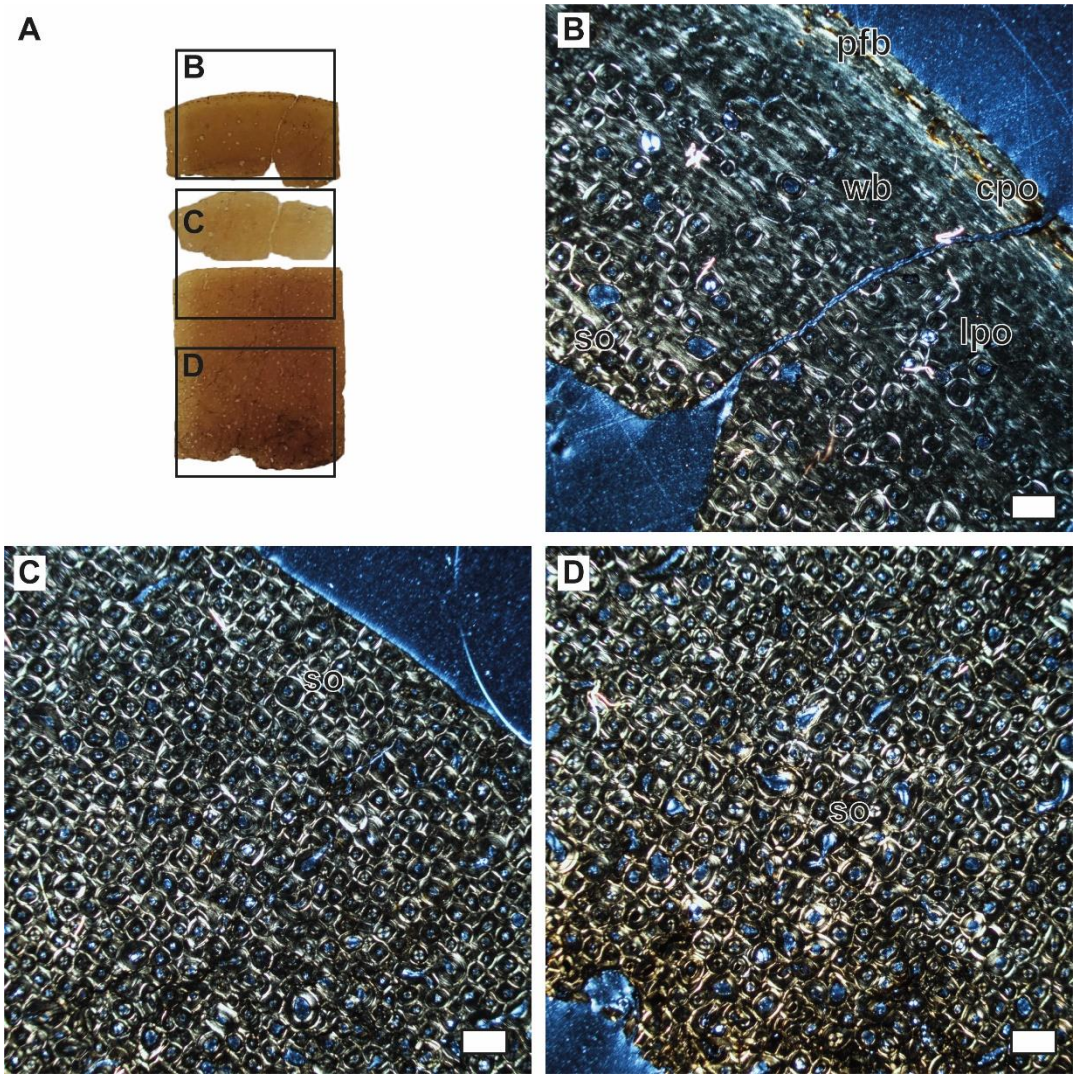

Figure S13. Overview of the histological patterns of ulna RGM.1394107, representing the youngest ulna from the DTB (HOS 5). All images are in cross-polarized light. All histological images have bone surfaces towards the upper right corner. Core was broken during sampling. A. Overview of the thin-section with corresponding sections annotated. B. Bone histology close to the bone surface showing large areas of woven bone with longitudinal primary osteons and thin layers of parallel-fibred bone containing elongated circumferential primary osteons. Bone remodelling is evident, but has not progressed to the outer bone surface. C. Mid-cortex showing high numbers of secondary osteons with only very little interstitial primary tissue. D. Completely overprinted deep cortex showing dense Haversian tissue. All scale bars are 500 µm. cpo, circumferential primary osteon; lpo, longitudinal primary osteon; pfb, parallel-fibred bone; so, secondary osteon; wb, woven bone.

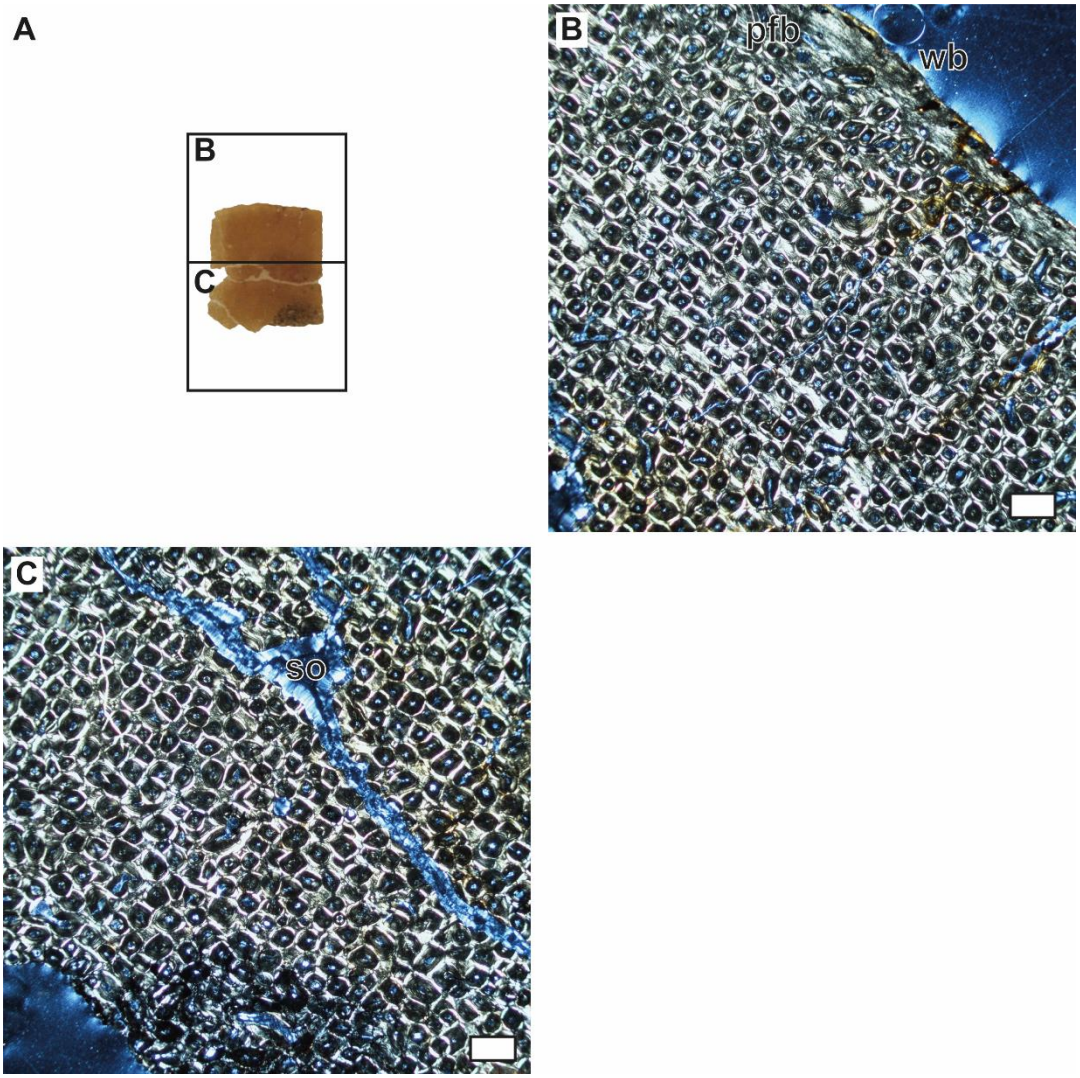

Figure S14. Overview of the histological patterns of fibula RGM.1394119, representing the oldest fibula from the DTB (HOS 7). All images are in cross-polarized light. All histological images have bone surfaces towards the upper right corner. A. Overview of the thin-section with corresponding sections annotated. B. Upper portion of the cortex showing dense Haversian tissue with a thin layer of parallel-fibred bone at the outer surface. There are small areas of woven bone present as well. C. Lower portion of the bone cortex bounding the medullary cavity showing dense Haversian tissue with multiple generations of secondary osteons. All scale bars are 500 µm. pfb, parallel-fibred bone; so, secondary osteon; wb, woven bone.

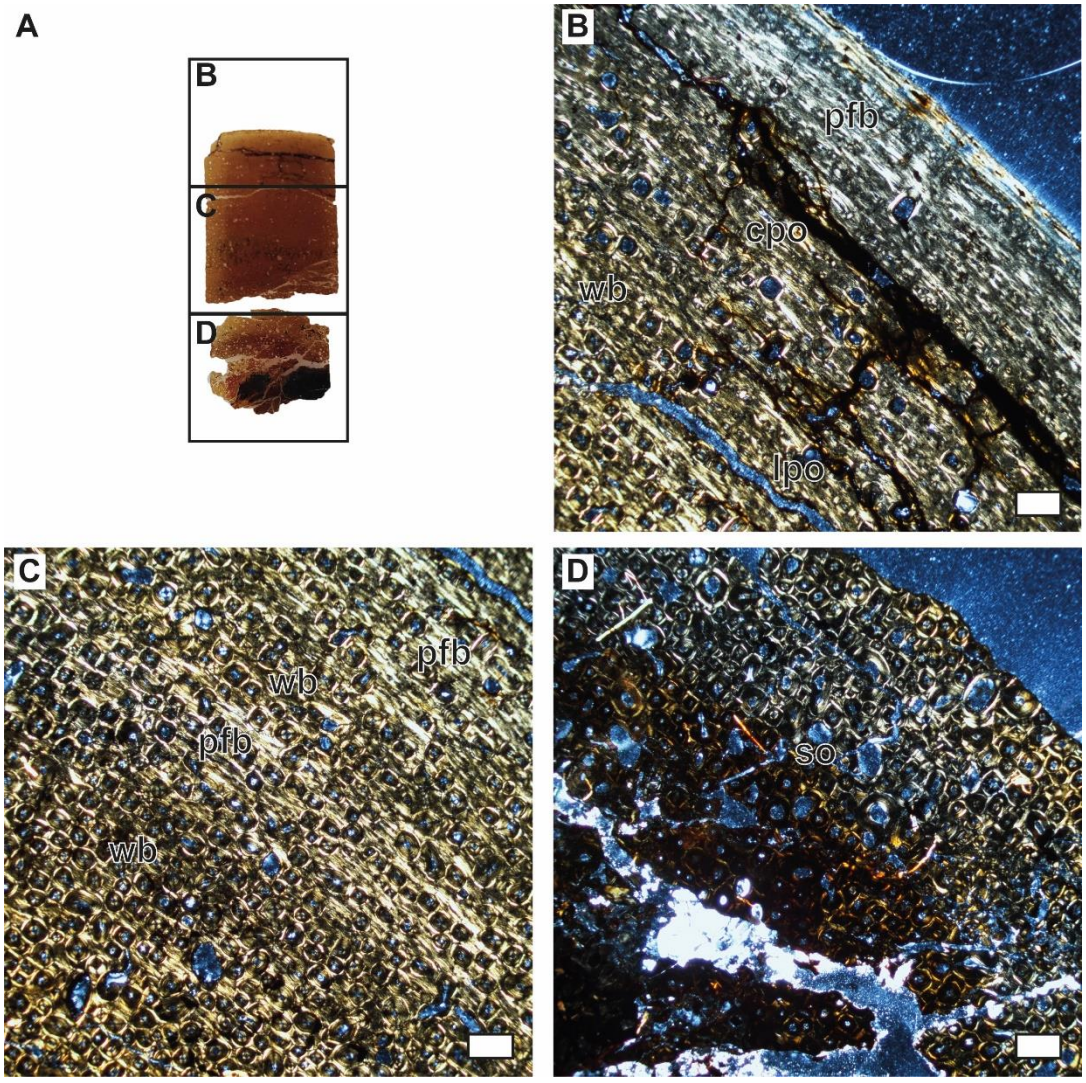

Figure S15. Overview of the histological patterns of fibula RGM.1394118, representing the youngest fibula from the DTB (HOS 5). All images are in cross-polarized light. All histological images have bone surfaces towards the upper right corner. A. Overview of the thin-section with corresponding sections annotated. B. Bone surface preserving primary bone predominantly showing woven bone with small areas of parallel-fibred tissue. Vascular canals are mainly orientated longitudinally, but circumferential primary osteons occur abundantly throughout the bone as well. Bone remodelling is advanced to the lower portion. C. Mid-cortex showing interchanging zones of parallel-fibred and woven bone. Bone remodelling is patchy but consistent throughout this part. Resorption cavities start to appear. D. Cortical bone close to the medullary cavity showing dense Haversian tissue en larger resorption cavities. All scale bars are 500 µm. cpo, circumferential primary osteon; lpo, longitudinal primary osteon; pfb, parallel-fibred bone; so, secondary osteon; wb, woven bone.

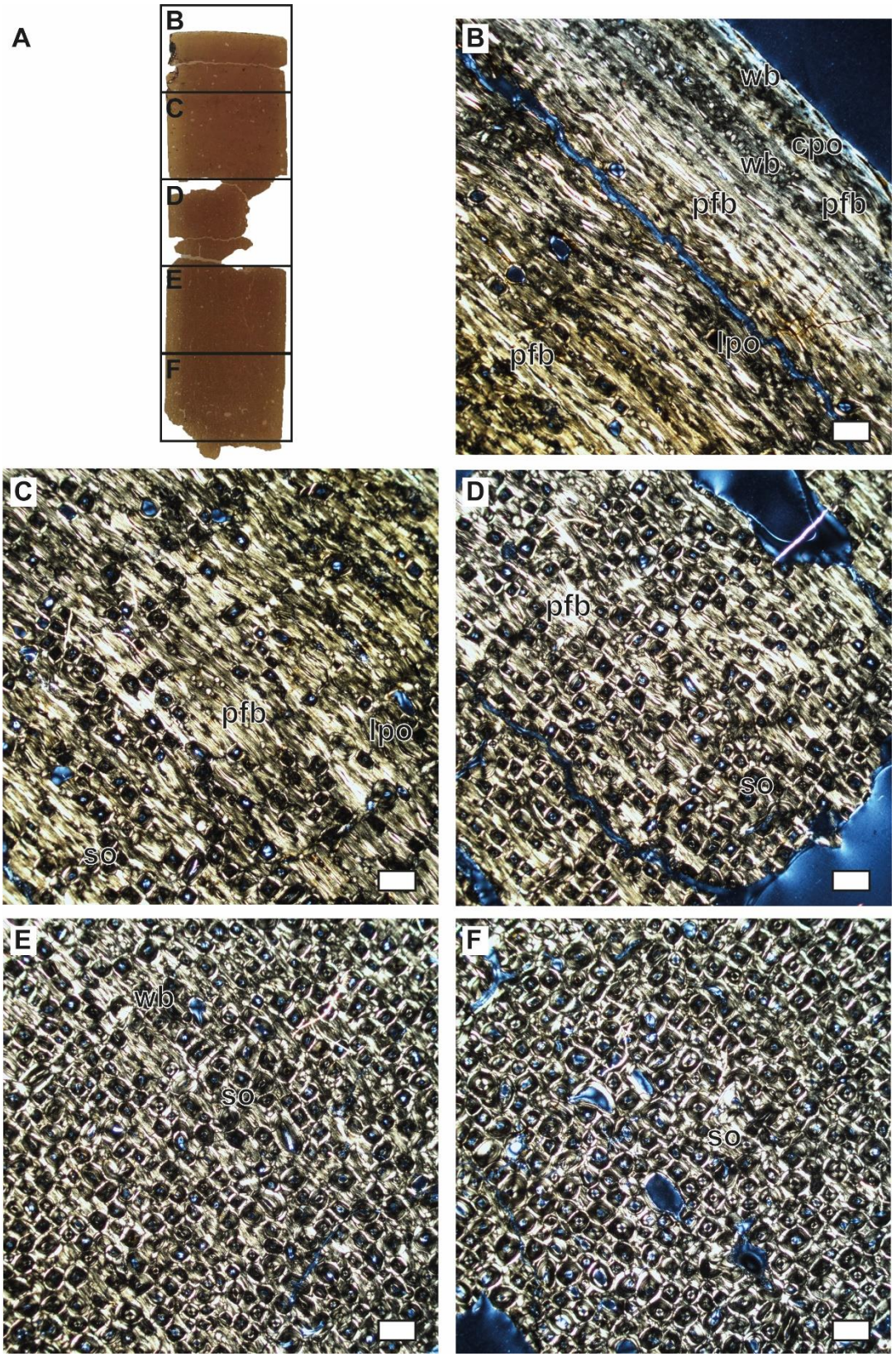
A
B
C
D
E
F
B
wb
cpo
wb
pfb
pfb
pfb
lpo
C
pfb
lpo
so
D
pfb
so
E
wb
so
F
so

Figure S16. Overview of the histological patterns of tibia RGM.1394117, representing the youngest tibia from the DTB (HOS 5). All images are in cross-polarized light. All histological images have bone surfaces towards the upper right corner. A. Overview of the thin-section with corresponding sections annotated. B. Bone surface showing conspicuous layers of parallel-fibred and woven bone. Vascularity is predominantly circumferential. Secondary osteons are rare. C. Upper mid-cortex showing large areas of parallel-fibred bone tissue. Circumferential canals are dominant, but small longitudinal primary osteons are still present. Secondary osteons become more consistent, but still occur in relatively low numbers. D. Mid-cortex with predominantly parallel-fibred bone. Bone remodelling becomes significantly more pronounced. E. Lower mid-cortex showing high numbers of secondary osteons and interstitial woven primary bone. F. Cortical bone close to the medullary cavity showing dense Haversian tissue and some resorption cavities. All scale bars are 500 µm. cpo, circumferential primary osteon; lpo, longitudinal primary osteon; pfb, parallel-fibred bone; so, secondary osteon; wb, woven bone.

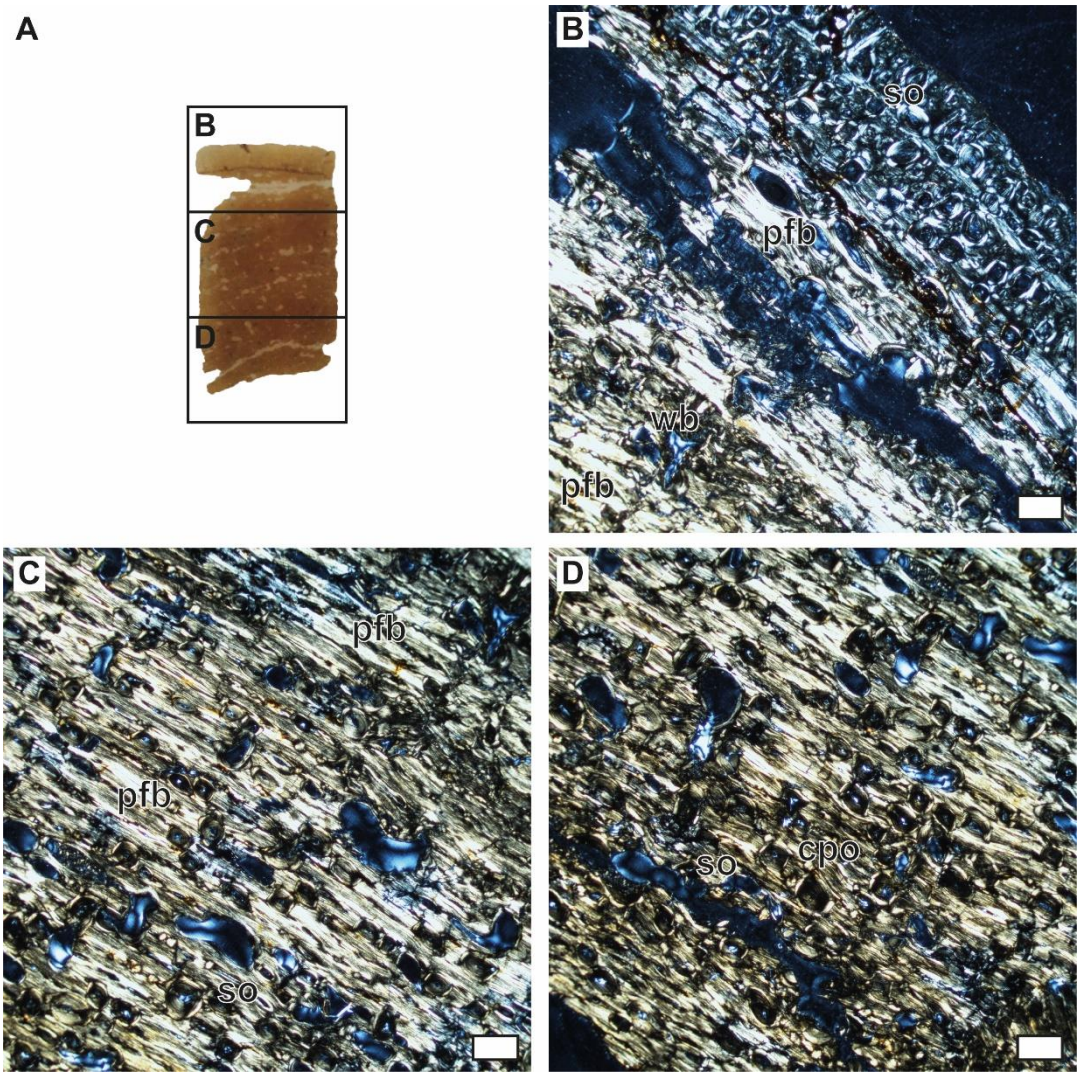

Figure S17. Overview of the histological patterns of tibia RGM.1394113, representing the oldest tibia from the DTB (HOS 6). All images are in cross-polarized light. All histological images have bone surfaces towards the upper right corner. A. Overview of the thin-section with corresponding sections annotated. B. Bone surface showing high numbers of overlapping secondary osteons and large areas of parallel-fibred bone. C. Mid-cortex dominated by parallel-fibred bone tissue and relatively large resorption cavities. D. Deep cortex dominated by parallel-fibred bone tissue and larger resorption cavities. All scale bars are 500 µm. pfb, parallel-fibred bone; so, secondary osteon; wb, woven bone.

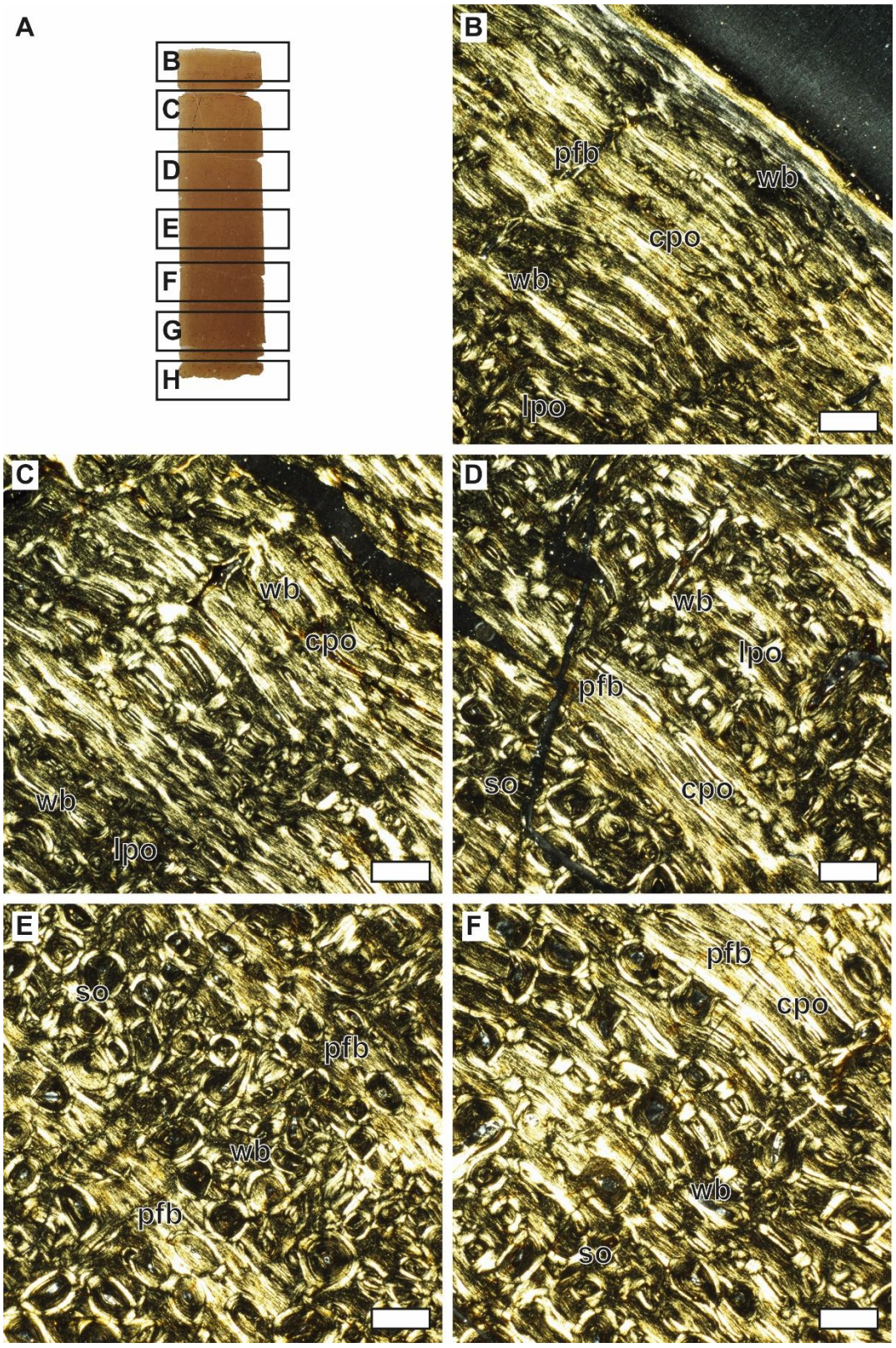
A
B
C
D
E
F
G
H
B
pfb
wb
cpo
wb
lpo
C
wb
cpo
wb
lpo
D
wb
lpo
pfb
so
cpo
E
so
pfb
wb
pfb
F
pfb
cpo
wb
so

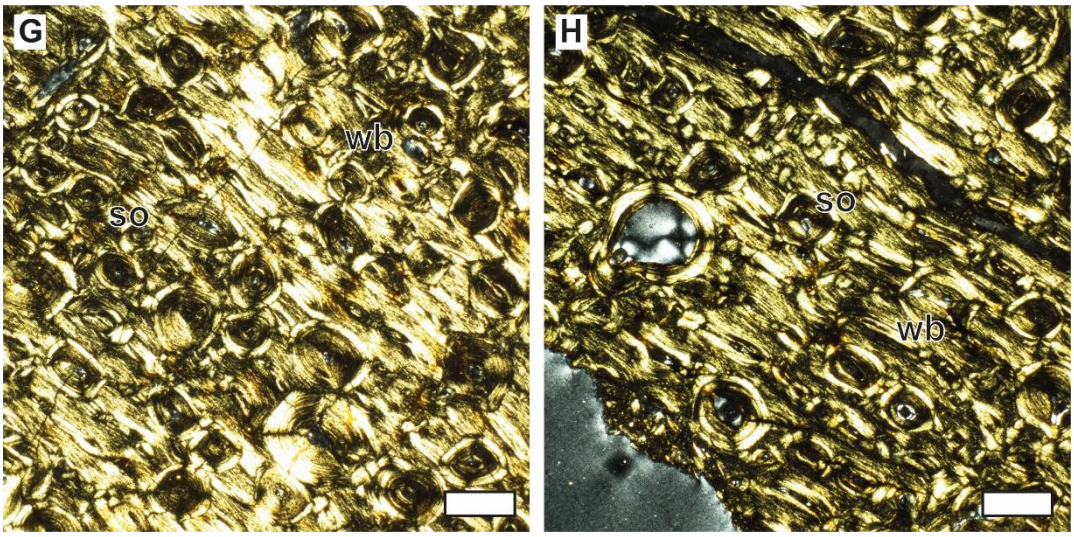

Figure S18. Overview of the histological patterns of femur RGM.1394111, representing the youngest femur from the DTB (HOS 4). All images are in cross-polarized light. All histological images have bone surfaces towards the upper right corner. A. Overview of the thin-section with corresponding sections annotated. B. Histology of the bone surface showing alternating zones of woven and parallel-fibred bone tissue. The vascularity is mostly circumferential. C. Histology of the bone subsurface showing circumferential and longitudinal primary osteons. Woven bone is generally associated with longitudinal canals. D. Large zones of woven longitudinal bone with thinner layers of parallel-fibred circumferential bone. The first secondary osteons start to appear. E. Thin layers of parallel-fibred bone with larger zones of woven bone overprinted by secondary osteons. F. Localised zones of parallel-fibred bone surrounded by larger areas of woven bone. G. High number of secondary osteons that overprint the primary tissue. H. Remodelled bone with resorption cavity close to the medullary region. All scale bars measure 500 µm. cpo, circumferential primary osteon; lpo, longitudinal primary osteon; pfb, parallel-fibred bone; so, secondary osteon; wb, woven bone.

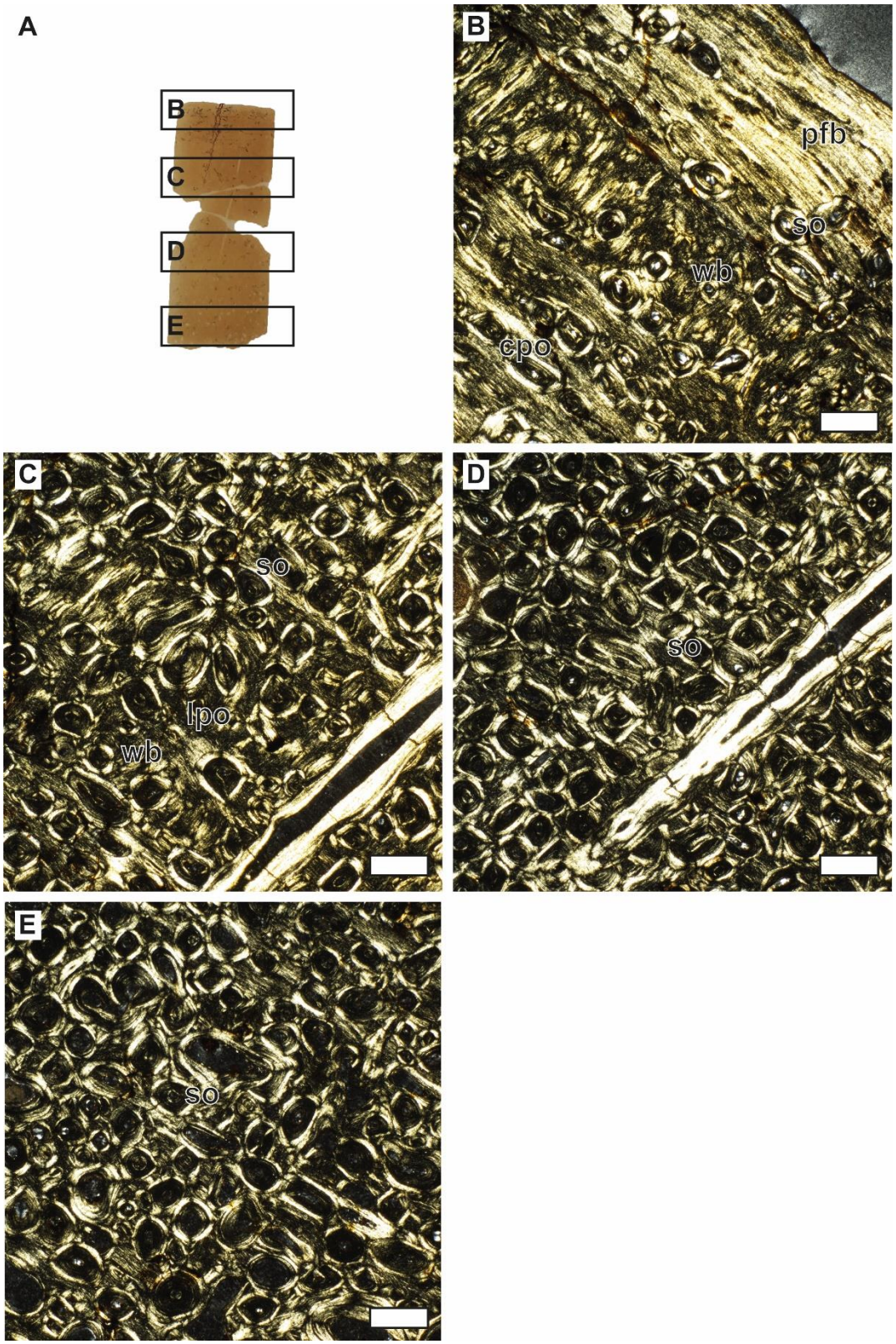
A
B
C
D
E
B
pfb
so
wb
cpo
C
so
lpo
wb
D
so
E
so

Figure S19. Figure S18. Overview of the histological patterns of femur RGM.1394110, representing the oldest femur from the DTB (HOS 6). All images are in cross-polarized light. All histological images have bone surfaces towards the upper right corner. A. Overview of the thin-section with corresponding sections annotated. B. Bone surface showing thick layers of parallel-fibred bone with low vascularity. There are alternating thinner layers of woven bone. Bone remodelling has advanced close to the bone surface as seen by the secondary osteons. C. Mid-cortex showing high numbers of secondary osteons. The small areas of interstitial primary tissue show woven bone and small longitudinal primary osteons. D. Lower mid-cortex with highly remodelled bone tissue. E. Cortical bone close to the medullary cavity showing overlapping secondary osteons. Note that interstitial primary tissue is still visible. All scale bars measure 500 µm. cpo, circumferential primary osteon; lpo, longitudinal primary osteon; pfb, parallel-fibred bone; so, secondary osteon; wb, woven bone.

Acknowledgements

We greatly appreciated the hospitality of Nancy and Donley Darnell and their help during the many field seasons on their property. In addition, many thanks go to our entire team of colleagues and volunteers for their enthusiasm and efforts in retrieving the fossil material. Special thanks go to preparators Yasmin Grooters, Martijn Guliker and their team of volunteers (Naturalis Biodiversity Center, the Netherlands) for handling and preparing the studied material for research. Additionally, many thanks go to Natasja den Ouden (Naturalis Biodiversity Center, the Netherlands) for streamlining access to the material and handling of the destructive sampling requests. We want to express our gratitude towards John van Gulik (Canon Medical Systems, the Netherlands) and Berend Stoel (Leids Universitair Medisch Centrum, the Netherlands) for access to CT scanners and their flexibility amidst the COVID outbreak. We like to thank Olaf Dülfer (Section Paleontology, Institute of Geosciences, University of Bonn, Germany) and Bouke Lacet (Faculty of Science, Vrije Universiteit, Amsterdam, the Netherlands) for making the thin-sections used in this study. For access to additional *Triceratops* material, we like to express our sincerest gratitude to Jordan Mallon (Canadian Museum of Nature, Ottawa, Canada) and Ryan McKellar (Royal Saskatchewan Museum, Regina, Canada). The project is funded by the Dutch Research Council (NWO) through ALW Open Programme (ALWOP.633). We like to acknowledge Dylan Bastiaans (PIMUZ, Switzerland) for his valuable contributions and input in developing the initial research plan. Furthermore, our gratitude goes towards the Mondriaan Fonds for their important contribution in sponsoring the field seasons. Lastly, many thanks to the two anonymous reviewers for their valuable and insightful comments that greatly improved this chapter.

References

Baag, S.J., Lee, Y.N., 2022. Bone histology on *Koreaceratops hwaseongensis* (Dinosauria: Ceratopsia) from the Lower Cretaceous of South Korea. Cretaceous Research 134, 105150. https://doi.org/10.1016/j.cretres.2022.105150

Bastiaans, D., Trapman, T., Guliker, M., Kaskes, P., Schulp, A., 2016. Multigenerational assemblage of Triceratops from the Newcastle area, Wyoming, USA – An in-depth analysis of cranial and post-cranial ontogenesis. In: Farke, A.A., MacKenzie, A., Miller-Camp, J. (Eds.), Journal of Vertebrate Paleontology, Program and Abstracts. p. 94

Botha, J., Choiniere, J.N., Benson, R.B.J., 2022. Rapid growth preceded gigantism in sauropodomorph evolution. Current Biology 32, 4501–4507.e2. https://doi.org/10.1016/j.cub.2022.08.031

Bartos, T.T., Galloway, D.L., Hallberg, L.L., Dechesne, M., Diehl, S.F., Davidson, S.L., 2021, Geologic and hydrogeologic characteristics of the White River Formation, Lance Formation, and Fox Hills Sandstone, northern greater Denver Basin, southeastern Laramie County, Wyoming. U.S.

Geological Survey Scientific Investigations Report 2021–5020, pp. 1–242. https://doi.org/10.3133/sir20215020.

Buffrénil, V. de, Quilhac, A., 2021. Bone tissue types: A brief account of currently used categories. In: Buffrénil, V. de, Ricqlès, A. de, Zylberberg, L., Padian, K. (Eds.), 2021. Vertebrate Skeletal Histology and Paleohistology. CRC Press, Boca Raton, pp. 147–190.

Buffrénil, V. de, Ricqlès, A. de, Zylberberg, L., Padian, K. (Eds.), 2021. Vertebrate Skeletal Histology and Paleohistology. CRC Press, Boca Raton.

Chiba, K., Ryan, M.J., Fanti, F., Loewen, M.A., Evans, D.C., 2018. New material and systematic re-evaluation of *Medusaceratops lokii* (Dinosauria, Ceratopsidae) from the Judith River Formation (Campanian, Montana). Journal of Paleontology 92, 272–288. https://doi.org/10.1017/jpa.2017.62

Chinnery, B., 2004. Morphometric analysis of evolutionary trends in the ceratopsian postcranial skeleton. Journal of Vertebrate Paleontology 24, 591-609. https://doi.org/10.1671/0272-4634(2004)024[0591:MAOETI]2.0.CO;2

Chinsamy, A., Raath., M.A., 1992. Preparation of fossil bone for histological examination. Palaeontologia Africana 29, 39–44.

Chinsamy, A., Thomas, D.B., Tumarkin-Deratzian, A.R., Fiorillo, A.R., 2012. Hadrosaurs were perennial polar residents. Anatomical Record 295, 610–614. https://doi.org/10.1002/ar.22428

Cullen, T.M., Brown, C.M., Chiba, K., Brink, K.S., Makovicky, P.J., Evans, D.C., 2021. Growth variability, dimensional scaling, and the interpretation of osteohistological growth data. Biological Letters 17, 20210383. https://doi.org/10.1098/rsbl.2021.0383

Cullen, T.M., Canale, J.I., Apesteguía, S., Smith, N.D., Hu, D., Makovicky, P.J., 2020. Osteohistological analyses reveal diverse strategies of theropod dinosaur body-size evolution. Proceedings of the Royal Society B 287, 20202258. https://doi.org/10.1098/rspb.2020.2258

D'Emic, M.D., O'Connor, P.M., Sombathy, R.S., Cerda, I., Pascucci, T.R., Varricchio, D., Pol, D., Dave, A., Coria, R.A., Curry Rogers, K.A., 2023. Developmental strategies underlying gigantism and miniaturization in non-avialan theropod dinosaurs. Science 379, 811–814. https://doi.org/10.1126/science.adc8714

Erickson, G.M., 2014. On dinosaur growth. Annual Review of Earth and Planetary Sciences 42, 675–697. https://doi.org/10.1146/annurev-earth-060313-054858

Erickson, G.M., Druckenmiller, P.S., 2011. Longevity and growth rate estimates for a polar dinosaur: a *Pachyrhinosaurus* (Dinosauria: Neoceratopsia) specimen from the North Slope of Alaska showing a complete developmental record. Historical Biology 23, 327–334. https://doi.org/10.1080/08912963.2010.546856

Erickson, G.M., Tumanova, T.A., 2000. Growth curve of *Psittacosaurus mongoliensis* Osborn (Ceratopsia: Psittacosauridae) inferred from long bone histology. Zoological Journal of the Linnean Society 130, 551–566. https://doi.org/10.1111/j.1096-3642.2000.tb02201.x

Forster, C. A., 1996a. New information on the skull of *Triceratops*. Journal of Vertebrate Paleontology, 16, 246–258. https://doi.org/10.1080/02724634.1996.10011312

Forster, C. A., 1996b. Species resolution in *Triceratops*: Cladistic and morphometric approaches. Journal of Vertebrate Paleontology, 16, 259–270. https://doi.org/10.1080/02724634.1996.10011313

Fostowicz-Frelik, L., Słowiak, J., 2018. Bone histology of *Protoceratops andrewsi* from the Late Cretaceous of Mongolia and its biological implications. Acta Palaeontologica Polonica 63, 503–517. https://doi.org/10.4202/app.00463.2018

Goldsmith, E.R., 2018. Bone Histology and Geochemical Taphonomy of Arctic Centrosaurine Ceratopsids from the Kikak-Tegoseak Quarry (North Slope, Alaska) (Unpubl. MSc thesis). Temple University, Philadelphia, 154 pp.

Goodwin, M.B., Clemens, W.A., Horner, J.R., Padian, K., 2006. The smallest known *Triceratops* skull: new observations on ceratopsid cranial anatomy and ontogeny. Journal of Vertebrate Paleontology 26, 103–112. https://doi.org/10.1671/0272-4634(2006)26[103:TSKTSN]2.0.CO;2

Hedrick, B.P., Goldsmith, E., Rivera-Sylva, H., Fiorillo, A.R., Tumarkin-Deratzian, A.R., Dodson, P., 2020. Filling in Gaps in the Ceratopsid Histologic Database: Histology of Two Basal Centrosaurines and an Assessment of the Utility of Rib Histology in the Ceratopsidae. Anatomical Record 303, 935–948. https://doi.org/10.1002/ar.24099

Henderson, D.M., 2014. Duck soup: the floating fates of hadrosaurs and ceratopsians at Dinosaur Provincial Park. Hadrosaurs. In: Eberth, D.A., Evans, D.C. (Eds). Hadrosaurs. Indiana University Press, Bloomington, pp. 459–466.

Holmes, R., Ryan, M.J., 2013. The postcranial skeleton of Styracosaurus albertensis. Kirtlandia 58, 5–37.

Horner, J.R., De Ricqlès, A., Padian, K., 2000. Long bone histology of the hadrosaurid dinosaur *Maiasaura peeblesorum* : growth dynamics and physiology based on an ontogenetic series of skeletal elements. Journal of Vertebrate Paleontology 20, 115–129. https://doi.org/10.1671/0272-4634(2000)020[0115:LBHOTH]2.0.CO;2

Horner, J.R., de Ricqlès, A., Padian, K., 1999. Variation in dinosaur skeletochronology indicators: implications for age assessment and physiology. Paleobiology 25, 295–304. https://doi.org/10.1017/S0094837300021308

Horner, J.R., Goodwin, M.B., 2008. Ontogeny of cranial epi-ossifications in *Triceratops*. Journal of Vertebrate Paleontology 28, 134–144. https://doi.org/10.1671/0272-4634(2008)28[134:OOCEIT]2.0.CO;2

Horner, J.R., Goodwin, M.B., 2006. Major cranial changes during *Triceratops* ontogeny. Proceedings of the Royal Society B 273, 2757–2761. https://doi.org/10.1098/rspb.2006.3643

Horner, J.R., Lamm, E.T., 2011. Ontogeny of the parietal frill of *Triceratops*: A preliminary histological analysis. Comptes Rendus Palevol 10, 439–452. https://doi.org/10.1016/j.crpv.2011.04.006

Horner, J.R., Padian, K., 2004. Age and growth dynamics of *Tyrannosaurus rex*. Proceedings of the Royal Society B 271, 1875–1880. https://doi.org/10.1098/rspb.2004.2829

Kaskes, P., Bastiaans, D., Verhage, O., De Rooij, J., Guliker, M., Schulp, A.S., 2019. Taphonomy of a unique multigenerational *Triceratops* bonebed from eastern Wyoming (USA): new insights from a multi-proxy perspective. In: Godefroit, P., Stein, K., Smith, T., Lambert, O., Olive, S. (Eds.), Program and Abstracts, European Association of Vertebrate Palaeontologists: XVII Annual Meeting, Brussels, Belgium, 2/07/19, vol. 17. p. 54.

Klein, N., Sander, M., 2008. Ontogenetic stages in the long bone histology of sauropod dinosaurs. Paleobiology 34, 247–263. https://doi.org/10.1666/0094-8373(2008)034[0247:OSITLB]2.0.CO;2

Klein, N., Sander, P.M., Stein, K., Le Loeuff, J., Carballido, J.L., Buffetaut, E., 2012. Modified Laminar Bone in *Ampelosaurus atacis* and other titanosaurs (Sauropoda): Implications for life history and physiology. PLoS ONE 7, e36907. https://doi.org/10.1371/journal.pone.0036907

Lamm, E.T., Padian, K., 2013. Preparation and sectioning of specimens. In: Padian, K., Lamm, E.T. (Eds.), Bone Histology of Fossil Tetrapods: Advancing Methods, Analysis, and Interpretation. University of California Press, Berkeley, pp. 55–160.

Lee, A., 2007. Bone microstructure reflects evolution of large size in horned dinosaurs. Microscopy and Microanalysis 13, 502–503. https://doi.org/10.1017/S1431927607078658

Lee, Y.N., Ryan, M.J., Kobayashi, Y., 2011. The first ceratopsian dinosaur from South Korea. Naturwissenschaften 98, 39–49. https://doi.org/10.1007/s00114-010-0739-y

Levitt. C.G., 2013. Bone histology and growth of chasmosaurine ceratopsid dinosaurs from the Late Campanian Kaiparowits Formation, southern Utah. (Unpubl. MSc Thesis). The University of Utah, Salt Lake City, p. 149.

Longrich, N.R., Field, D.J., 2012. *Torosaurus* is not *Triceratops*: Ontogeny in chasmosaurine ceratopsids as a case study in dinosaur taxonomy. PLoS ONE 7, e32623. https://doi.org/10.1371/journal.pone.0032623

Maidment, S.C.R., Barrett, P.M., 2011. A new specimen of *Chasmosaurus belli* (Ornithischia: Ceratopsidae), a revision of the genus, and the utility of postcrania in the taxonomy and systematics of ceratopsid dinosaurs. Zootaxa 2963, 1. https://doi.org/10.11646/zootaxa.2963.1.1

Maiorino, L., Farke, A.A., Kotsakis, T., Piras, P., 2013. Is *Torosaurus Triceratops*? Geometric morphometric evidence of Late Maastrichtian ceratopsid dinosaurs. PLoS ONE 8, e81608. https://doi.org/10.1371/journal.pone.0081608

Mallon, J.C., Holmes, R., 2010. Description of a complete and fully articulated chasmosaurine postcranium previously assigned to *Anchiceratops* (Dinosauria: Ceratopsia)., In: Ryan, M.J., Chinnery-Allgeier, B.J., Eberth, D.A. (Eds.), New Perspectives on Horned Dinosaurs. The Royal Tyrrell Museum Ceratopsian Symposium. Indiana University Press, Bloomington, pp. 189–202.

Mallon, J.C., Holmes, R.B., Bamforth, E.L., Schumann, D., 2022. The record of *Torosaurus* (Ornithischia: Ceratopsidae) in Canada and its taxonomic implications. Zoological Journal of the Linnean Society 195, 157–171. https://doi.org/10.1093/zoolinnean/zlab120

Mallon, J.C., Ott, C.J., Larson, P.L., Iuliano, E.M., Evans, D.C., 2016. *Spiclypeus shipporum* gen. et sp. nov., a boldly audacious new chasmosaurine ceratopsid (Dinosauria: Ornithischia) from the Judith River Formation (Upper Cretaceous: Campanian) of Montana, USA. PLoS ONE 11, e0154218. https://doi.org/10.1371/journal.pone.0154218

de Margerie, E., Cubo, J., Castanet, J., 2002. Bone typology and growth rate: testing and quantifying 'Amprino's rule' in the mallard (*Anas platyrhynchos*). Comptes Rendus Biologies 325, 221–230. https://doi.org/10.1016/S1631-0691(02)01429-4

de Margerie, E., Robin, J.-P., Verrier, D., Cubo, J., Groscolas, R., Castanet, J., 2004. Assessing a relationship between bone microstructure and growth rate: a fluorescent labelling study in the king penguin chick (*Aptenodytes patagonicus*). Journal of Experimental Biology 207, 869–879. https://doi.org/10.1242/jeb.00841

Mitchell, J., Sander, P.M., 2014. The three-front model: a developmental explanation of long bone diaphyseal histology of Sauropoda. Biological Journal of the Linnean Society 112, 765–781. https://doi.org/10.1111/bij.12324

Mitchell, J., Sander, P.M., Stein, K., 2017. Can secondary osteons be used as ontogenetic indicators in sauropods? Extending the histological ontogenetic stages into senescence. Paleobiology 43, 321–342. https://doi.org/10.1017/pab.2016.47

Prondvai, E., Godefroit, P., Adriaens, D., Hu, D.-Y., 2018. Intraskeletal histovariability, allometric growth patterns, and their functional implications in bird-like dinosaurs. Scientific Reports 8, 258. https://doi.org/10.1038/s41598-017-18218-9

Redelstorff, R., Hübner, T.R., Chinsamy, A., Sander, P.M., 2013. Bone histology of the stegosaur *Kentrosaurus aethiopicus* (Ornithischia: Thyreophora) from the Upper Jurassic of Tanzania. Anatomical Record 296, 933–952. https://doi.org/10.1002/ar.22701

Redelstorff, R., Sander, P.M., 2009. Long and girdle bone histology of *Stegosaurus* : implications for growth and life history. Journal of Vertebrate Paleontology 29, 1087–1099. https://doi.org/10.1671/039.029.0420

Reizner, J.A., 2010. An ontogenetic series and population histology of the ceratopsid dinosaur *Einiosaurus procurvicornis* (Unpubl. MSc Thesis). Montana State University, Bozeman, pp. 97.

Rooij, J. de, 2018. Discovery of a *Triceratops* bonebed: *Triceratops* long bone histology and implications on social behaviour (Unpubl. MSc thesis). Utrecht University, Utrecht, pp. 71.

Rooij, J. de, van der Lubbe, J.H.J.L., Verdegaal, S., Hulscher, M., Tooms, D., Kaskes, P., Verhage, O., Portanger, L., Schulp, A.S., 2022. Stable isotope record of *Triceratops* from a mass accumulation (Lance Formation, Wyoming, USA) provides insights into *Triceratops* behaviour and ecology. Palaeogeography, Palaeoclimatology, Palaeoecology 607, 111274. https://doi.org/10.1016/j.palaeo.2022.111274

Sampson, S.D., Loewen, M.A., 2010. Unraveling a radiation: a review of the diversity, stratigraphic distribution, biogeography, and evolution of horned dinosaurs (Ornithischia: Ceratopsidae). In: Ryan, M.J. Chinnery-Allgeier, B.J. Eberth, D.A. New Perspectives on Horned Dinosaurs: The Royal Tyrrell Museum Ceratopsian Symposium. Indiana University Press, Bloomington, pp. 405–427.

Sander, P.M., 2000. Longbone histology of the Tendaguru sauropods: implications for growth and biology. Paleobiology 26, 466–488. https://doi.org/10.1666/0094-8373(2000)026<0466:LHOTTS>2.0.CO;2

Sander, P.M., Klein, N., Stein, K., Wings, O., 2011. Sauropod bone histology and its implications for sauropod biology. In: Klein, N., Remes, C., Gee, C.T., Sander, P.M. (Eds.), Biology of the Sauropod Dinosaurs: Understanding the Life of Giants. Indiana University Press, Bloomington, pp. 276–302.

Sander, P.M., Wintrich, T., 2021. Sauropterygia: Histology of Plesiosauria. In: Buffrénil, V. de, Ricqlès, A. de, Zylberberg, L., Padian, K. (Eds.), Vertebrate Skeletal Histology and Paleohistology, CRC Press, Boca Raton, pp. 444–457.

Scannella, J.B., Horner, J.R., 2011. '*Nedoceratops*': An example of a transitional morphology. PLoS ONE 6, e28705. https://doi.org/10.1371/journal.pone.0028705

Scannella, J.B., Horner, J.R., 2010. *Torosaurus* Marsh, 1891, is *Triceratops* Marsh, 1889 (Ceratopsidae: Chasmosaurinae): synonymy through ontogeny. Journal of Vertebrate Paleontology 30, 1157–1168. https://doi.org/10.1080/02724634.2010.483632

Scannella, J.B., Fowler, D.W., Goodwin, M.B., Horner, J.R., 2014. Evolutionary trends in *Triceratops* from the Hell Creek formation, Montana. Proceedings of the National Academy of Sciences 111, 10245–10250. https://doi.org/10.1073/pnas.1313334111

Scott, S.H.W., Ryan, M.J., Evans, D.C., 2023. Postcranial description of *Wendiceratops pinhornensis* and a taphonomic analysis of the oldest monodominant ceratopsid bonebed. The Anatomical Record 306, 1824–1841. https://doi.org/10.1002/ar.25045

Sereno, P.C., 2010. Taxonomy, cranial morphology, and relationships of parrot-beaked dinosaurs (Ceratopsia: *Psittacosaurus*). In: Ryan, M.J., Chinnery-Allgeier, B.J., Eberth, D.A. (Eds.), New perspectives on horned dinosaurs: The Royal Tyrrell Museum ceratopsian symposium, Indiana University Press, Bloomington, pp. 21–58.

Skutschas, P., Morozov, S., Averianov, A., Leshchinskiy, S., Ivantsov, S., Fayngerts, A., Feofanova, O., Vladimirova, O., Slobodin, D., 2021. Femoral histology and growth patterns of the ceratopsian

dinosaur *Psittacosaurus sibiricus* from the Early Cretaceous of Western Siberia. Acta Palaeontologica Polonica 66, 437–447. https://doi.org/10.4202/app.00819.2020

Słowiak, J., Szczygielski, T., Ginter, M., Fostowicz-Frelik, Ł., 2020. Uninterrupted growth in a non-polar hadrosaur explains the gigantism among duck-billed dinosaurs. Palaeontology 63, 579–599. https://doi.org/10.1111/pala.12473

Stein, K., Sander, P.M., 2009. Histological core drilling: a less destructive method for studying bone histology. Methods in fossil preparation: proceedings of the first annual Fossil Preparation and Collections Symposium, 69–80.

Stein, K., Csiki, Z., Rogers, K.C., Weishampel, D.B., Redelstorff, R., Carballido, J.L., Sander, P.M., 2010. Small body size and extreme cortical bone remodeling indicate phyletic dwarfism in *Magyarosaurus dacus* (Sauropoda: Titanosauria). Proceedings of the National Academy of Sciences 107, 9258–9263. https://doi.org/10.1073/pnas.1000781107

Stein, M., Hayashi, S., Sander, P.M., 2013. Long bone histology and growth patterns in ankylosaurs: Implications for life history and evolution. PLoS ONE 8, e68590. https://doi.org/10.1371/journal.pone.0068590

Sues, H.D., Averianov, A., 2009. *Turanoceratops tardabilis*—the first ceratopsid dinosaur from Asia. Naturwissenschaften 96, 645–652. https://doi.org/10.1007/s00114-009-0518-9

Tokaryk, T. T., 1986. Ceratopsian dinosaurs from the Frenchman Formation (Upper Cretaceous) of Saskatchewan. Canadian Field-Naturalist 100, 192–196.

Vice, R.M., 2020. The forelimb and pectoral girdle of *Pachyrhinosaurus lakustai* (Ceratopsia, Centrosaurinae) (Unpubl. MSc Thesis). University of Alberta, Alberta, p. 162.

Waskow, K., 2019. Patterns of life history recorded in the dorsal rib histology of amniotes (PhD dissertation. University of Bonn, Bonn.

Waskow, K., Mateus, O., 2017. Dorsal rib histology of dinosaurs and a crocodylomorph from western Portugal: Skeletochronological implications on age determination and life history traits. Comptes Rendus Palevol 16, 425–439. https://doi.org/10.1016/j.crpv.2017.01.003

Waskow, K., Sander, P.M., 2014. Growth record and histological variation in the dorsal ribs of *Camarasaurus* sp. (Sauropoda). Journal of Vertebrate Paleontology 34, 852–869. https://doi.org/10.1080/02724634.2014.840645

Wiersma-Weyand, K., Canoville, A., Siber, H.-J., Sander, P.M., 2021. Testing hypothesis of skeletal unity using bone histology: The case of the sauropod remains from the Howe-Stephens and Howe Scott quarries (Morrison Formation, Wyoming, USA). Palaeontologia Electronica 24, a10. https://doi.org/10.26879/766

Wolfe, D.G., Kirkland, J.I., Smith, D., Poole, K., Chinnery-Allgeier, B., McDonald, A., 2007. *Zuniceratops christopheri*: An update on the North American ceratopsid sister taxon, Zuni Basin, west-central New Mexico. In: Braman, D.R., Brinkman, D. (Eds.), Ceratopsian Symposium: Short Papers, Abstracts, and Programs. Drumheller: Royal Tyrell Museum of Paleontology, pp. 159–167.

Woodward, H.N., Horner, J.R., Farlow, J.O., 2014. Quantification of intraskeletal histovariability in *Alligator mississippiensis* and implications for vertebrate osteohistology. PeerJ 2, e422. https://doi.org/10.7717/peerj.422

Woodward, H.N., Tremaine, K., Williams, S.A., Zanno, L.E., Horner, J.R., Myhrvold, N., 2020. Growing up *Tyrannosaurus rex*: Osteohistology refutes the pygmy "*Nanotyrannus*" and supports ontogenetic niche partitioning in juvenile *Tyrannosaurus*. Science Advances 6, eaax6250. https://doi.org/10.1126/sciadv.aax6250

Zhao, Q., Benton, M., Hayashi, S., Xu, X., 2019. Ontogenetic stages of ceratopsian dinosaur *Psittacosaurus* in bone histology. Acta Palaeontologica Polonica 64, 323–334. https://doi.org/10.4202/app.00559.2018

Zheng, W., Jin, X., Xu, X., 2015. A psittacosaurid-like basal neoceratopsian from the Upper Cretaceous of central China and its implications for basal ceratopsian evolution. Scientific Reports 5, 14190. https://doi.org/10.1038/srep14190

5

Chapter 5. Quantification of bone surface textures: exploring a new method of ontogenetic ageing

Published as:
de Rooij, J., Vintges, M. Q., Zuijdwijk, T., Heerkens, C. T. H., Schulp, A. S., 2023. Quantification of bone surface textures: exploring a new method of ontogenetic ageing. *Journal of Analytical Science and Technology, 14, 49*. DOI: https://doi.org/10.1186/s40543-023-00413-1

Abstract
Identification of ontogenetic age classes plays an important role in the fields of zoology, palaeontology and archaeology, contextualizing aspects of taxonomy, phylogeny, ecology and physiology. Textural ageing – the identification of age-related bone surface textures – provides a size-independent method for age assessment of vertebrate material. However, most of the work so far is limited to mostly qualitative results. While these works provided helpful insights on textural ageing patterns, they are heavily subject to observer bias and fall short of quantitative data relevant for detailed statistical analyses and cross-comparisons. Here, we present a pilot study on the application of digital microscopy to quantify bone surface textures on the long bones of the grey heron (*Ardea cinerea*) and the Canada goose (*Branta canadensis*) using internationally verified roughness parameters. Using a standardized measuring protocol, computed roughness values show a strong correlation with the qualitative textural patterns. Overall, higher roughness values correspond to increased numbers of grooves and pits and vice versa. Most of the roughness parameters allowed distinguishing between different ontogenetic classes and closely followed the typical sigmoidal animal growth curve. Our results show that bone texture quantification is a feasible approach in identifying ontogenetic age classes.

5.1 Introduction
Textural ageing is the analysis of bone surface textures of extant and extinct animal skeletal remains to define relative ontogenetic age classes (Tumarkin-Deratzian et al., 2006). Skeletal elements of specific taxa may develop different types of surface textures during ontogeny. The occurrence of specific texture types is controlled by the network of vascular canals penetrating the bone tissue and opening at the bone surface (Tumarkin-Deratzian et al., 2006). Bones of skeletally immature (i.e., younger) individuals have generally higher growth rates, thus producing a dense vascular network for nutrient transport which translates to increased bone surface roughness (Tumarkin-Deratzian et al., 2006). Contrastingly, skeletally mature individuals do not show active growth which results in relatively smooth bone surface textures. Based on these assumptions, skeletal elements of specific taxa may show (local) dynamic shifts in surface roughness related to ontogenetic stage (i.e., age). This provides an independent tool for ontogenetic ageing of animal skeletal remains, which would be especially useful in archaeological and palaeontological context where specimens can be preserved fragmentarily. The phenomenon of age-related changes in bone surface roughness has been qualitatively described for skeletal elements of several modern and extinct taxa, including the long bones of a small number of modern birds (Neognathae) (Acosta Hospitaleche and Picasso, 2020; Tumarkin-Deratzian et al., 2006; Watanabe, 2018), the American alligator (*Alligator mississippiensis*) (Tumarkin-Deratzian et al., 2007) and the long bones as well as the enigmatic parietosquamosal complex of horned dinosaurs

(*Centrosaurus, Einiosaurus* and *Pachyrhinosaurus*) (Brown et al., 2009; Sampson et al., 1997; Tumarkin-Deratzian, 2010, 2009). In addition, a single unpublished thesis project documented ontogenetic changes in bone textural patterns in modern post-Medieval humans (Wijngaarden, 2021). Thus, while the taxonomic resolution may be patchy at present, this approach provides a promising method for size-independent and non-destructive ontogenetic ageing of animal remains, which complements already established taxonomic, ecological and taphonomic toolkits in zoology, archaeology and palaeontology alike.

Almost all previous work in the study of bone textural ageing is limited to qualitative analyses, relying on categorical classes and descriptive terms to define changes in bone surface roughness. While these attempts have successfully established a classification scheme, it is difficult to conduct detailed statistical analyses. Moreover, this precludes reliable comparisons without introducing observer errors. Only a handful of studies attempted to quantify surface roughness on prehistoric material including taphonomic bone weathering stages (Vietti, 2016) and assessment of bone tool wear patterns in archaeology (Martisius et al., 2020).

Here we apply digital microscopy to test whether bone surface roughness can be quantified using verified surface roughness parameters. As taphonomic processes may significantly compromise the bone surface texture on fossil specimens, our dataset focusses first on modern taxa of which textural ageing patterns have already been established in previous studies (Tumarkin-Deratzian et al., 2006; Watanabe, 2018). This will allow for an accurate test of the quantification method without overprinting effects from taphonomy. Comparing the relation between roughness parameters and ontogeny for qualitative and quantitative datasets helps create a baseline for standardisation of textural ageing methods.

5.2 Material and methods

5.2.1 Digital microscopy

A Keyence VHX-6000 digital microscope housed at the Department of Imaging Physics, Faculty of Applied Sciences of the Delft University of Technology was used for the analysis of bone surface roughness. This setup allows for high resolution 2D and 3D measurements to register small variations in surface topography. We performed roughness analyses by quantifying 2D and 3D surface topography following ISO 4287 and ISO 25178 standards, respectively. While these ISO standards provide a wide range of parameters quantifying surface textures, we chose to mostly focus on the most relevant roughness parameters including the 'average roughness' ('Ra' for 2D surfaces and 'Sa' for 3D surfaces). Ra and Sa values are calculated as the arithmetical mean deviation of valleys and peaks in a measured surface profile. Higher Ra/Sa values correspond to more pronounced valleys and peaks, and thus a rougher surface topography. Likewise, we incorporate peak (Rp) and valley (Rv) heights as well as their difference (Rz) when analysing the different roughness patterns to provide an accurate quantification of bone surface roughness.

5.2.2 Specimen selection

Roughness analyses were performed on the humeri, femora and tibiotarsi of the grey heron (*Ardea cinerea)* and the Canada goose (*Branta canadensis*) as the long bones of these taxa are known to show age-related shifts in bone surface texture (Tumarkin-Deratzian et al., 2006; Watanabe and Matsuoka, 2013). Moreover, these taxa show insignificant sexual dimorphism that otherwise could influence ontogenetic growth patterns. All individuals of both taxa belong to local populations located in the

Netherlands, thus any inter- or intraspecific variation introduced due to mixing of different populations is not expected. Specimens of *Branta canadensis* were collected from independent hunting organisations responsible for population control. As these specimens were mainly acquired through targeted culling, they exclusively represent skeletally mature individuals. The restricted ontogenetic classes of the *B. canadensis* samples provide an ideal dataset to evaluate the consistency and robustness of the applied techniques tested here. Specimens of *Ardea cinerea* were housed at the natural history museum of Rotterdam, the Netherlands, and were field collected after natural death. The heron specimens represent an ontogenetic series of differently sized individuals (Figure 1). Individual birds were dissected and the left and right humeri, femora and tibiotarsi were removed and subsequently macerated. Maceration entails the removal of organic soft tissue through controlled putrefaction/decomposition in a closed container. As such, this approach allows for the extraction of bones without compromising bone surfaces through potential cut marks.

5.2.3 Measuring protocol

Figure 1 shows a complete overview of the followed research protocol. Firstly, a qualitative assessment using visual images of the bone textural patterns acquired through the Keyence VHX-6000 (equipped with the VH-ZST 20x to 2000x objective) was made for both taxa following similar strategies applied in the literature. The microscope photographs allowed for comparison with the quantitative data. Using the microscope, the mid-diaphysis of each bone was analysed to avoid potential confounding effects of attachment sites for joint cartilage as well as possible changes in surface texture due to bone morphogenesis of proximal and distal joints. Additionally, we avoided areas that contained muscle attachment sites. Following these criteria, the surface roughness of the humeri and tibiotarsi were measured on the anterior and posterior mid-diaphysis, and the surface roughness of the femora was measured on the medial and lateral mid-diaphysis. To obtain a representative image of the bone surface for the surface roughness measurements (Sa), we standardized the size of the sampling area for both *Ardea cinerea* and *Branta canadensis*. Limb bones pertaining to *Ardea cinerea* were smaller than *Branta canadensis* and the large absolute size differences between ontogenetically different grey heron specimens required standardized proportions of the sampling area on the mid-diaphysis. This resulted in a mid-diaphyseal sampling area of 2 by 0.5 mm at 300x magnification for the grey heron and 20 by 5 mm at 50x magnification for the Canada goose.

We used the analytical tool associated with the Keyence VHX-6000 microscope to quantify bone surface roughness. Table S1 provides all the microscope settings, and no specific filters were used during the analysis. A high-resolution 3D image of the bone surface was rendered for each bone using image-stitching under coaxial light. Specific light settings were unique for each specimen, but we experienced that medium light intensity combined with a variable use of polarizing filter is best practise to improve image quality and reduce glare. Depending on the size of the sampled bone, we demarcated the area of interest (2 or 20 mm apart) on the mid-diaphysis using a pencil to provide reference during image acquisition, and a series of images were stitched along the mid-diaphysis until the preferred sampling area was captured. The lowest and highest points of focus were chosen along the Z-axis for the first and last image, respectively, and a 10 µm vertical pitch guaranteed that the entire stitched image was in focus. The slope and convexity were filtered out in the rendered 3D surface image using step-wise corrections associated with the Keyence software to ensure that the observed variations in surface topography were limited to roughness parameters only (Figure S1). An ISO-verified built-in line (2D) and areal (3D) roughness analysis was then performed across the indicated surface area to acquire roughness data (Figure S2). To account for possible errors introduced by different sampling directions,

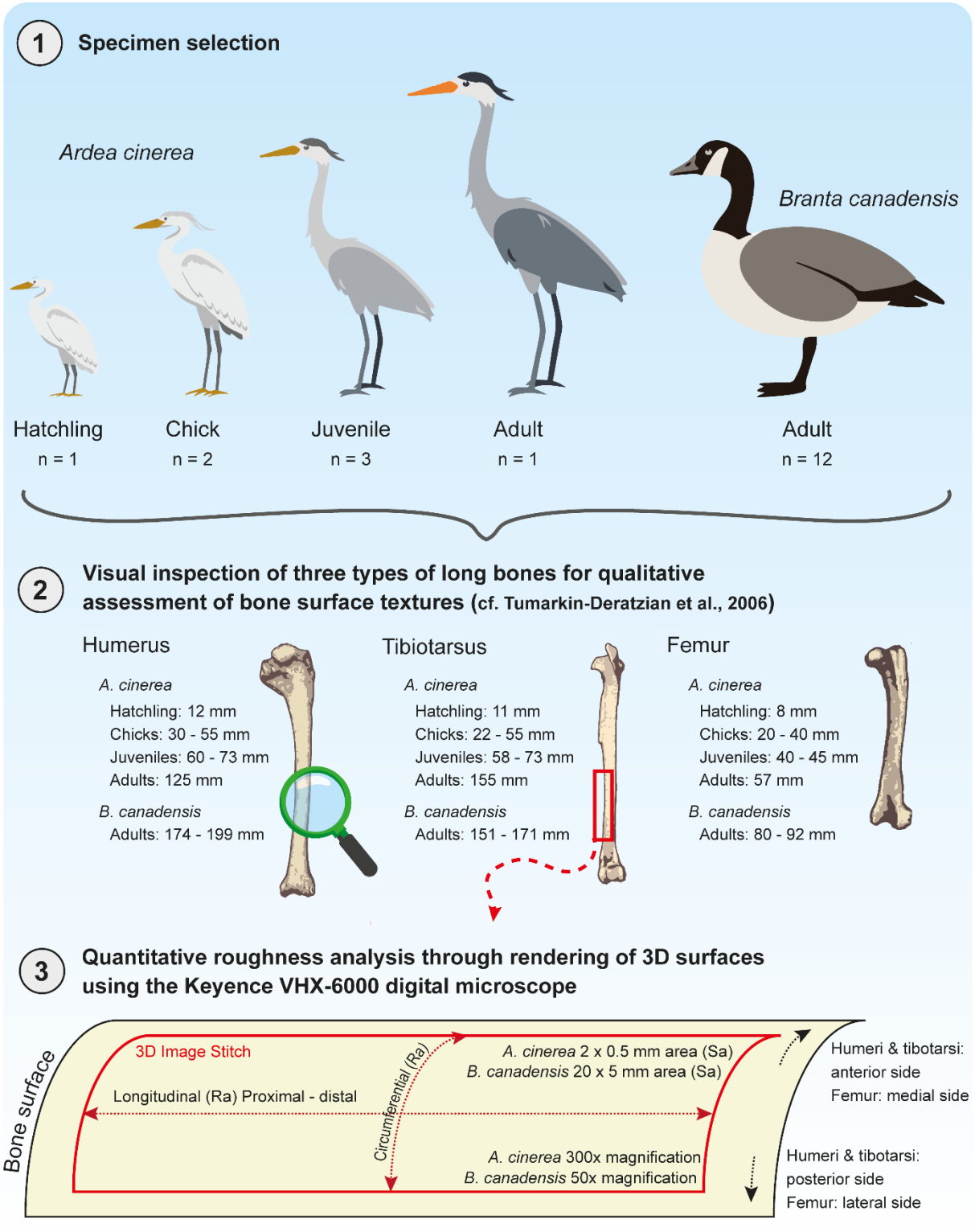

Figure 1. Overview of the material and methods used in this study. Firstly, relevant taxa and their ontogenetic stages were chosen for sampling. The humeri, tibiotarsi and femora were removed and processed. After a qualitative analysis, each bone was studied using digital microscopy yielding quantitative roughness values. The measurement values in section 2 indicate the size range of each corresponding sampled bone for all four ontogenetic classes for both taxa.

we performed the 2D line analysis longitudinally (in the proximal-distal direction) (2 or 20 mm) as well as circumferentially (perpendicular to that direction) (0.5 or 5 mm) on opposite sides for each bone type (Figure 1).

5.3 Results

5.3.1 Grey heron (*Ardea cinerea*)

Qualitative assessment of the bone surface textures of the grey heron revealed similar structures as previously observed for this taxon (Figure 2) (Watanabe and Matsuoka, 2013). All three limb bones show strong shifts in overall surface texture throughout ontogeny. The adult form is characterized by a relatively smooth bone surface that lacks any kind of large pits, pores or grooves, confirming the ontogenetic position as a skeletally mature adult. On the other hand, heron chicks display the highest roughness based on the higher amounts of relatively large pores and grooves along the mid-diaphyseal surface. Visual inspection of juvenile bones show a roughness intermediate between chicks and adults, where the abundance and depth of grooves and pits significantly start to diminish with ontogeny. Of note, the heron hatchlings do not conform to the expected trend of increased porosity in younger individuals (Sibly and Brown, 2020), and show relatively less roughness than juveniles. Instead, the bone surface shows a larger number of more superficial fine-grained anastomosing grooves (Figure 2).

Detailed statistical analyses and data exploration are provided in the Supplements. Non-parametric paired Mann-Whitney U tests as well as Kruskal-Wallis tests did not reveal a significant

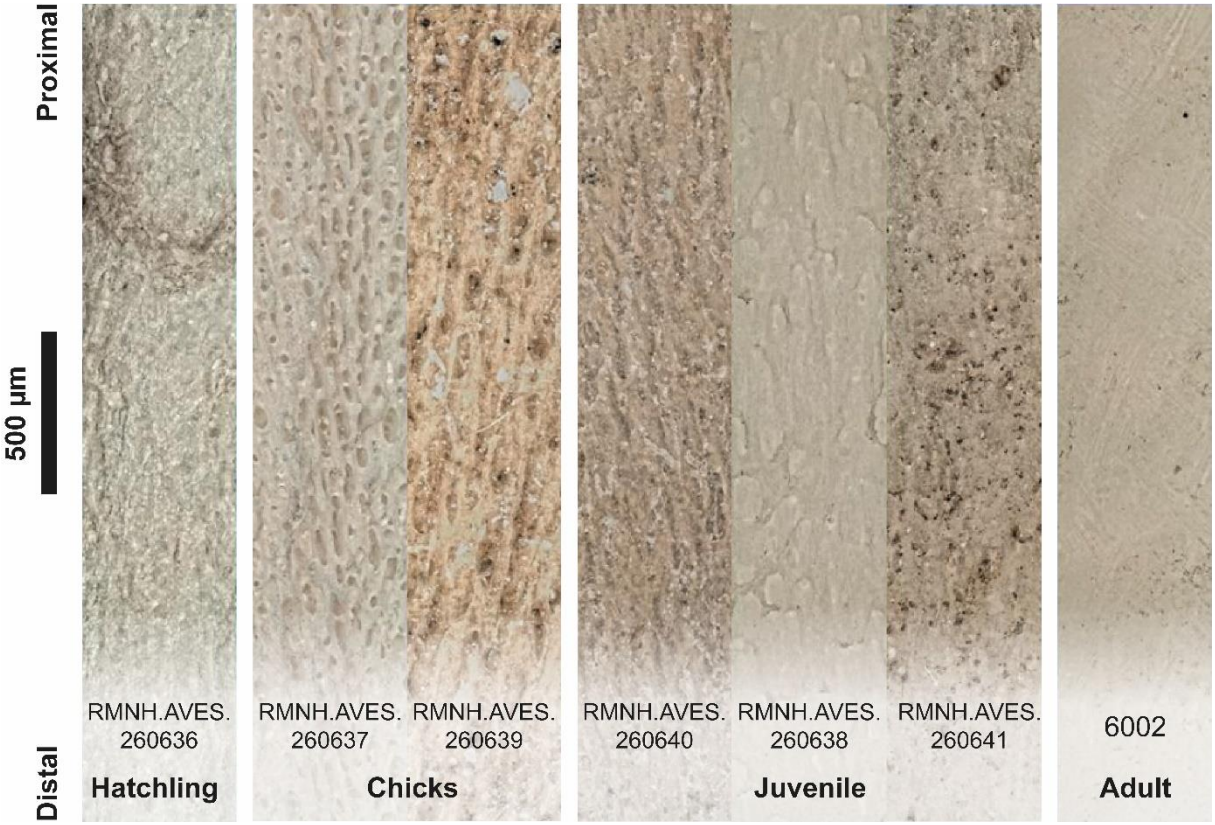

Figure 2. Qualitative roughness data for *Ardea cinerea* of different ontogenetic stage. Images are from the tibiotarsi, and are taken along the bone's long axis in distal to proximal direction. Chicks show the highest number of large and deep grooves and pits. Hatchlings and juveniles show clear roughness patterns, but only very few penetrating pores. Adults are almost completely smooth.

difference between the applied measuring procedures for *Ardea cinerea*. In other words, neither the bone area (e.g., anterior or posterior) nor the measuring direction (longitudinal or circumferential) influenced the roughness parameters, and both strategies produced similar data (Table S2 and S3). Additionally, we found very limited effects of bone type (humeri, tibiotarsi, femora) on roughness values across the studied bird specimens (Table S5). Thus, considering the major overlap in roughness values within individual birds, we opted to calculate the average values for each roughness parameter and use those for data interpretation and discussion (Table S6). Figure 3 shows the relationship between average Ra values and ontogenetic age. Similar trends are observed in almost all other roughness parameters including Rv, Rp and Rz (Figure 4). A paired t-test ($p < 0.05$) shows that Rv values are greater than Rp values for *Ardea cinerea* specimens (See Supplements, $p = 0.01$). Ra and Sa values are significantly different ($p = 0.03$), but they show similar relationships with ontogenetic age (Figure 4). Overall, the roughness parameters all show a predictable pattern that decreases with ontogenetic age, and are in agreement with the qualitative data. Chicks have the highest average Ra (11.5 µm) and adults the lowest (3.4 µm). Hatchlings and juveniles both have intermediate Ra values (5.4 and 8.8 µm, respectively).

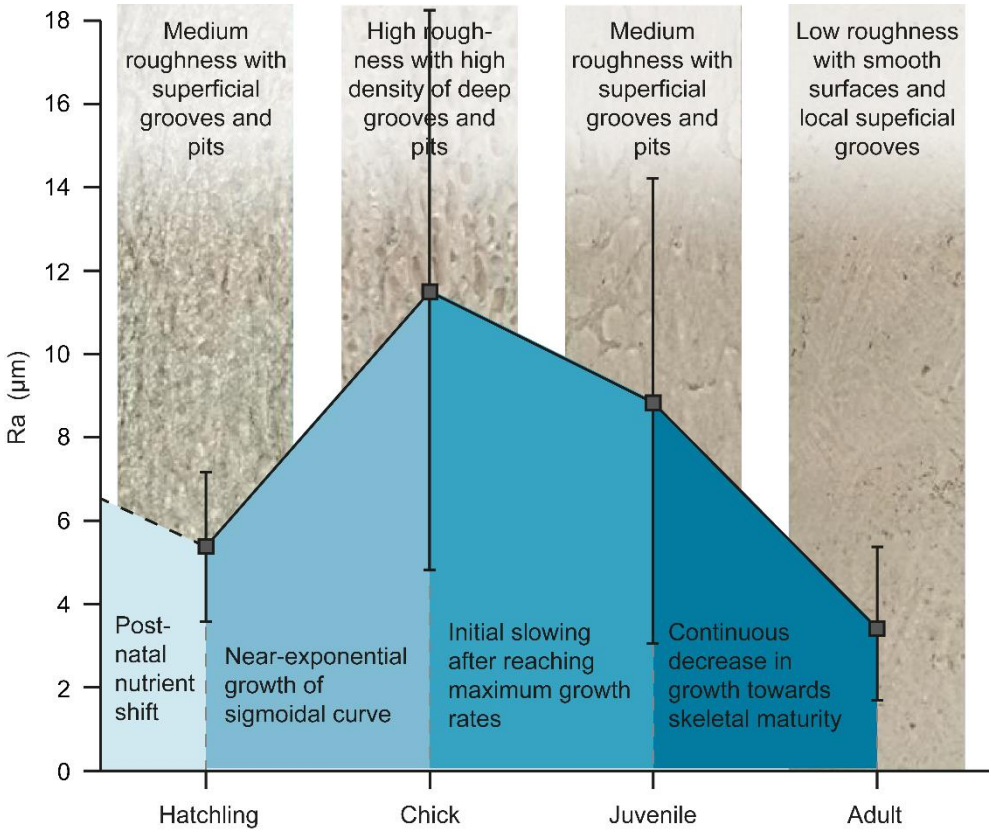

Figure 3. Graph showing the relationship between roughness (Ra) and ontogenetic stage. The observed qualitative roughness patterns are positively correlated with the Ra values, and coincide with the proposed shifts in growth rate known for modern birds. The dashed line corresponding to the post-natal nutrient shift is hypothetical. The error bars represent 2σ and show relatively high ranges most likely due to the chosen ontogenetic classes still containing relatively variable roughness values (especially the intermediate classes such as chicks and juveniles, see Discussion).

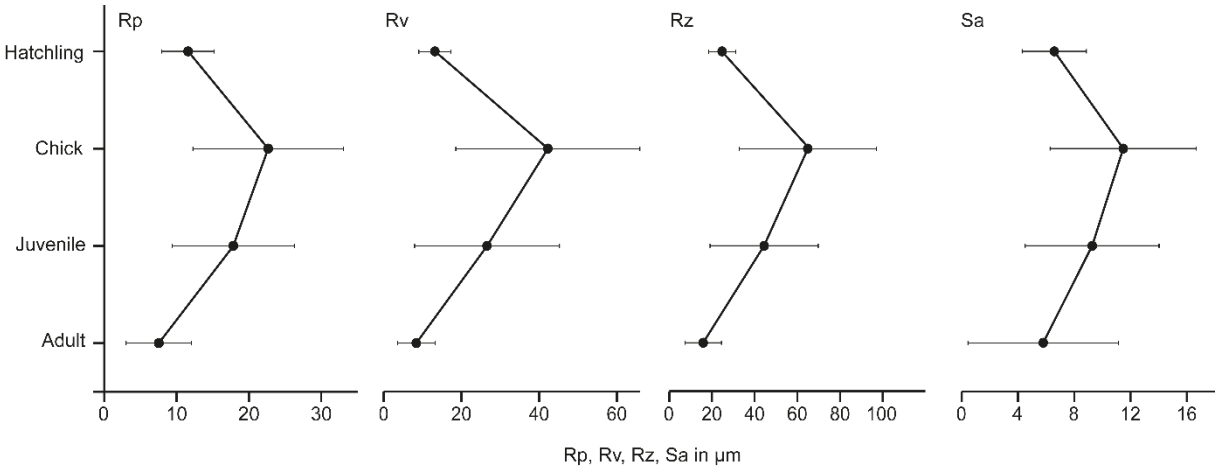

Figure 4. Relationship between Rp, Rv, Rz, Sa and ontogenetic stage for *Ardea cinerea*. All other major roughness parameters show similar trends as seen in Ra. The error bars represent 2σ.

5.3.2 Canada goose (*Branta canadensis*)

The ontogenetically restricted *Branta canadensis* samples allow testing of the robustness of bone surface quantification through digital microscopy by repeated measurements of limited ontogenetic age classes. The qualitative assessment of the *Branta canadensis* specimens show very little variation in bone surface textures, corroborating the ontogenetically restricted sample size (Figure 6A). Bone surfaces are all relatively smooth, with only minor local variations in size and abundance of grooves and pits across all the studied samples. They most closely resemble the adult specimens of *Ardea cinerea* as well as previously recorded adult *Branta canadensis* (Tumarkin-Deratzian et al., 2006). The quantitative roughness analysis showed significant differences between Ra values obtained through longitudinal and circumferential measuring directions (Table S2 and S4). The data obtained from circumferential sampling showed greater spread and higher values that were more randomly distributed (Figure 5). Thus, we only used the roughness values obtained from longitudinal sampling for our data interpretation. When compared with only the longitudinal data, there is no significant difference in Ra values between the three limb bone types ($p = 0.07$, Table S6). The *Branta canadensis* dataset was limited to adult specimens only, thus we plotted the average (longitudinal only) Ra values per specimen against bone length, as we assumed that bone length was a general indicator for overall body mass and presumably age. We opted for humerus length to represent body size as the humerus shows the highest size ranges and is thus expected to more accurately visualize the relationship between Ra values and body size. The ontogenetically restricted dataset does not allow for detailed statistical analyses, but the relationship between humerus length and Ra values follow a predictable pattern of decreasing roughness with presumable age (Figure 6B). Average Ra values per specimen range from 13.9 µm to 45.2 µm, in which the smallest individual shows the highest Ra value while the largest individual shows the smallest. A paired two sample t-test ($p < 0.05$) indicates that the Rp values for *Branta canadensis* are significantly larger than the Rv values ($p = 0.00$), and the Rz values are significantly larger than those of *Ardea cinerea* ($p = 0.00$).

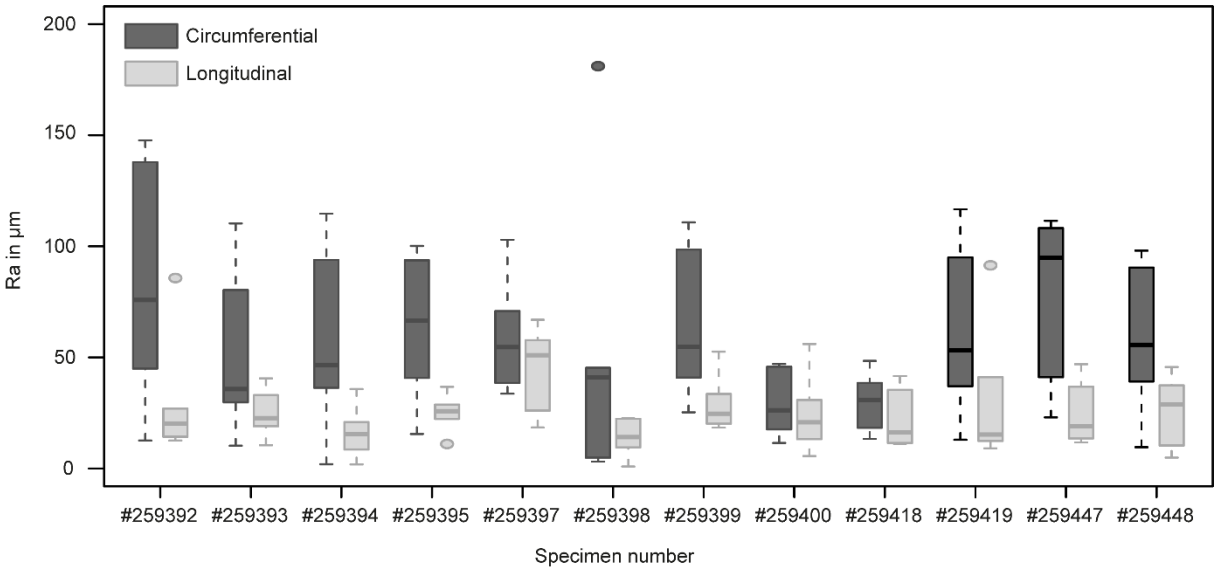

Figure 5. Comparison between Ra values acquired through longitudinal and circumferential measuring strategies on *Branta canadensis*. Note the consistently higher offsets for circumferential data as well as the higher spread.

5.4 Discussion

5.4.1 Comparison of quantitative and qualitative inspection

The general pattern in textural ageing produced through digital microscopy indicates a decrease in surface roughness values with ontogeny. This observed decrease coincides with the loss of superficial grooves and pits during the attainment of skeletal maturity. This pattern is not only observed in the ontogenetic series of *Ardea cinerea* (Figure 3 and 4), but it even shows within the adult stage of *Branta canadensis* (Figure 6) where qualitative inspection fails to distinguish the subtle roughness differences. Despite the limited sample sizes, the overlap of both the quantitative and qualitative patterns as well as the consistent output across specimens within both taxa strongly suggest that the digital roughness analyses accurately captured patterns of textural ageing and reflect ontogenetic changes in roughness due to changes in bone vascularity. We do note that the relationship between roughness parameters and ontogenetic stage (Figure 3 and 4) present relatively large standard deviations, which is most likely a result of the chosen ontogenetic grouping as well as the limited sample sizes. Vertebrate ontogeny is defined by a continuous increase in body sizes and future attempts should define more diverse ontogenetic classes. Additionally, the different intrabone measuring strategies compared here revealed little to no effects on the multiple roughness parameters, and where two roughness parameters showed strong significant differences, they still showed similar biological relationships (e.g., Ra and Sa, Figure 3 and 4).

This work further highlights the importance of following a standardized measuring protocol when analysing quantitative roughness data, at least when using digital microscopy. For example, while most values generated through different measuring strategies showed no differences, the roughness parameters from longitudinal and circumferential sampling on *Branta canadensis* showed strongly diverging values (Figure 5). The circumferential measurements resulted in extremely high and scattered Ra values, while in theory these bone surfaces are not expected to show different average roughness within the same area. The current dataset only provides limited explanation on this offset in measuring strategies, but it most likely represents introduced errors as a result of magnification, light intensity

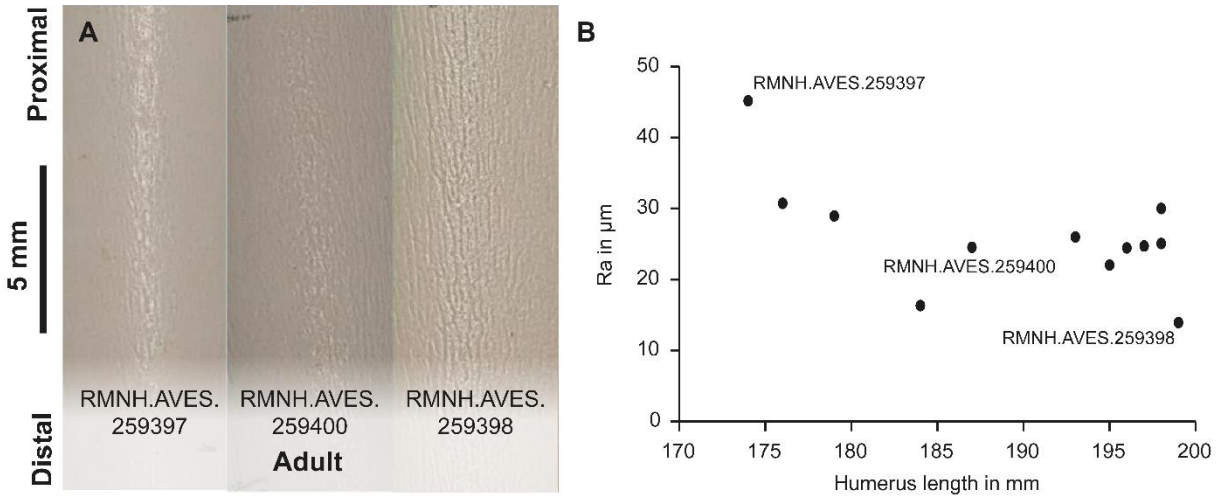

Figure 6. Qualitative and quantitative roughness data of *Branta canadensis*. A. Overview of bone textural patterns of the smallest, medium-sized and largest specimens. B. Plot of longitudinally acquired Ra values and associated humerus size. The specimen numbers represent the ones in image A. Note the gradual decrease in Ra with larger size.

and/or post-stitching image transformation and processing. Filtering out the convexity often preserved deformed extremities that overlap with circumferential sampling (e.g., Figure S1). These confounding factors do not occur along longitudinal transect parallel to the bone's long axis. As such, following the long axis of long bones produce the most reliable roughness data and is considered best practise in our analysis. In addition, the current dataset is too limited to exclude any potential effects of local bone roughness variations within specific age classes. Expansion of the quantitative roughness dataset across local bone areas and more discrete ontogenetic classes should reveal how local bone topography and measuring standards affect roughness values.

Moreover, the strong differences in roughness values between *Ardea cinerea* and *Branta canadensis* also warrants extra scrutiny. Average Ra values of *Branta canadensis* specimens were an order of magnitude higher than *Ardea cinerea*, including ontogenetically younger individuals, despite the qualitative inspection of chick *Ardea cinerea* showing more textured bone surfaces than adult *Branta canadensis*. This most likely represents a measuring artefact introduced by using widely diverging microscope magnifications, as intra-species values acquired using the same magnification still follow the expected ontogenetic trend. Different magnifications may ultimately affect the resolution of the rendered 3D image, thereby potentially altering the threshold of observable microstructures within the surface topography. Thus, our work strongly recommends the use of standardized magnifications when examining the same animal taxon, and care should be taken when comparing multiple taxa.

5.4.2 Ontogenetic changes in bone surface texture

In general, ontogenetically younger animals are expected to show higher growth rates as rapid attainment of adult sizes favours access to limited resources (Sibly and Brown, 2020). However, both the qualitative and the quantitative roughness data show the same ontogenetic pattern in which hatchling long bones have a lower roughness compared to the older chick stage. This most likely reflects the typical three phase sigmoidal growth curve of animal development, where initial body mass increases during early ontogeny are relatively low, but increase rapidly during ontogeny after which the growth rate ultimately plateaus (Emmans, 2022; Sibly and Brown, 2020). The same pattern is observed in the Ra values presented here (Figure 4) as well as in other parameters including Rv, Rp, Rz and Sa of

Ardea cinerea. The hatchlings represent the earliest ontogenetic stage after birth, and experience a brief lag phase most likely related to the pre- and postnatal shift in nutrient sources. This corresponds to moderate Ra values, and thus a relatively lower roughness. Subsequently, the higher juvenile Ra values correspond to the extended period of rapid near-exponential growth rates, manifested by increased roughness. Growth rates than significantly decrease again and level off nearing adulthood and skeletal maturity indicated by lower Ra values and smooth surfaces. Similarly, the Ra values for *Branta canadensis* adults still follow the expected trend of decreasing growth rates close to skeletal maturity (Figure 6). Thus, the close affinity between measured bone surface roughness parameters (e.g., Ra and Sa) and growth rate further corroborates the validity of quantifying bone textures as conducted in this study.

The data also suggests that *Ardea cinerea* show significantly higher ($p < 0.05$) Rv values (i.e., show deeper valleys) than Rp values ($p = 0.01$). It is reasonable to assume that the blood vessels opening at the bone surface of ontogenetically younger individuals results in deeper grooves creating higher Rv values. Specimens of *Branta canadensis* on the other hand have higher Rp (i.e., higher peaks) than Rv values ($p = 0.00$), which may be a result of sampling a large set of adult specimens that have completely closed bone surfaces creating bone topography mostly defined by peaks. Further analyses on more ontogenically diverse specimens should reveal such patterns more unambiguously.

5.4.3 Implications and future research

This pilot study shows the positive correlation between quantitative roughness data and ontogenetic stage, and provides a foundation and directions for future studies aiming to better quantify and understand patterns in bone surface roughness, with applications in biology, archaeology and palaeontology alike. As data acquisition is completely non-destructive this method may be applied to a large selection of modern and fossil bone material, enabling more thorough collection-based research. As such, it serves as an accurate size-independent proxy for ontogenetic maturity, where it may complement other ageing methods. In order to make this method an established technique, it is necessary to compare qualitative and quantitative bone textural patterns across a larger taxonomic and ontogenetic range. Furthermore, future applications of this technique may help identify to what extent taphonomy (e.g., erosion and weathering) affects the quantitative roughness values (Martisius et al., 2020; Vietti, 2016). This enables more accurate identification and ageing of poorly constrained and often fragmentary fossil bones. This way, quantitative surface texture analyses may improve our understanding of aspects of depositional settings and fossil provenance in archaeological and palaeontological context.

5.5 Conclusion

The data presented in this pilot study show that quantitative bone surface roughness measurements allow for textural ageing. Preliminary surface topography data conforming to ISO 4287 and 25178 on *Ardea cinerea* and *Branta canadensis* revealed corresponding patterns in ontogenetic shifts between quantitative and qualitative inspection. The Ra, Rv, Rp, Rz and Sa values were positively correlated to the hypothesized changes in growth rate coinciding with the gradual attainment of skeletal maturity. Sampling strategies should adhere to standardized protocols but these can be developed on a case-by-case basis based on the available material as well as taxa. Future research should reveal to what extent the proposed textural ageing method can be applied to the fossil record.

5.6 Supplementary data

5.6.1 Check for normality and statistical analyses

All statistical analyses were carried out in R and R Studio (R Core Team, 2020). We conducted multiple analyses to explore the effects of sampling strategies on the roughness values. These comparisons include the effects of bone element type, bone side and measuring direction. Additionally, we explored the relationship between Ra (2D linear) and Sa (3D areal) values, as well as the differences between Ra, Rv, Rp and Rz values among taxa and ontogenetic stage. Each set of roughness values pertaining to these strategies was treated as a separate dataset and was tested for normality using Shapiro-Wilk tests for normality (test statistic: W = 0 to 1, significance level: $p < 0.05$). Almost all datasets showed a significant deviation from normality, so the majority of the statistical analyses were non-parametric. We applied Mann-Whitney U tests (test statistic: $U = n_{max} - n_{min}$, significance level: $p < 0.05$) and Kruskal-Wallis tests (test statistic H, significance level: $p < 0.05$). Only the Rv, Rp and Rz values were normally distributed and analysed by parametric two sample t-tests (test statistic: t, significance level: $p < 0.05$).

5.6.2 Bone area and measuring direction

Ra values grouped and compared per bone area location showed a strong deviation from normality. Thus, we applied non-parametric paired Mann-Whitney U tests to identify possible differences between Ra values measured on either the anterior/medial or posterior/lateral side of the three elements per taxon. The statistical tests did not show any significant differences between Ra values for the three bone elements in both *Ardea cinerea* and *Branta canadensis* (Table S2). Ra values grouped by measuring direction also deviated from normality and were analysed by paired Mann-Whitney U tests. The tests for *Ardea cinerea* long bones showed no significant difference between the Ra values obtained through either longitudinal or circumferential sampling directions (Table S2). The Ra values of longitudinal and circumferential sampling values for *Branta canadensis* were significantly different for all three limb bone types (Table S2). In addition, a Kruskal-Wallis rank test combined with post-hoc paired Mann-Whitney U tests using Bonferroni corrections was applied to better understand the relationships between bone area and measuring direction for each limb bone type. The combined tests did not return any significant differences between bone area or bone measuring direction for all three limb bone types in *Ardea cinerea* (Table S3). For *Branta canadensis*, however, the tibiotarsi showed two out of six significant differences between combinations of bone area and measuring direction and the femora showed four out of six significant differences, consistent with the single paired Mann-Whitney U tests (Table S4).

Table S1. Settings of the Keyence VHX-6000 for the roughness analysis in this study.

Measurement type	Roughness
Lighting	Coaxial
Ls filter	None
Lc filter	None
Lf filter	None
End effect correction	On
Double Gaussian	Off
Filter type	Gaussian
S-filter	None
L-filter	None
Vertical Pitch Z-axis	10.0 µm

Table S2. Overview of the p-values from the Mann-Whitney U paired tests for the relationship between R values of the specific bone sides and measuring directions. The bone sides are identified as anterior or posterior for the humeri and tibiotarsi, while for the femora they are identified as medial and lateral. The measuring directions are compared between longitudinal (parallel to the bone's long axis) and circumferential (perpendicular to that axis) directions.

Taxon	Bone element	Anterior/medial vs. posterior/lateral (p < 0.05)	Longitudinal vs. circumferential (p < 0.05)
Ardea cinerea	Humerus	0.30	0.74
Ardea cinerea	Tibiotarsus	0.95	0.50
Ardea cinerea	Femur	0.22	0.59
Branta canadensis	Humerus	0.42	0.00
Branta canadensis	Tibiotarsus	0.26	0.00
Branta canadensis	Femur	0.29	0.00

5.6.3 Interbone comparison

We performed non-parametric Kruskal-Wallis tests with post-hoc Bonferroni-corrected pairwise Mann-Whitney U tests to explore the difference in Ra values between the three limb bone types for each ontogenetic stage of *Ardea cinerea* and *Branta canadensis*. As there was no consistent difference in Ra values between bone side and measuring direction for *Ardea cinerea*, we opted to group all the Ra values and compared them between humeri, tibiotarsi and femora per ontogenetic stage. The measuring direction on *Branta canadensis* bones did seem to influence the measured Ra values (Figure 5), thus to avoid the potential confounding effects of the highly spread circumferentially measured Ra values for *B. canadensis,* we performed a similar analysis but incorporating only the Ra values acquired using the longitudinal measuring protocols. In both cases we attempted to use as many datapoints as possible for robust statistical testing. For *Ardea cinerea*, each ontogenetic stage did not show a significant difference between the Ra values for the three limb elements except for the potential difference between humerus and tibiotarsus of chick herons (Table S5). Similarly, the subset of

Table S3. Results of the Kruskal-Wallis tests and post-hoc pairwise Mann-Whitney U tests with Bonferroni corrections for each possible combination of bone side and measuring direction in *Ardea cinerea*. The p-value of the Kruskal-Wallis tests are shown in the first row. The remaining numbers are the p-values of the pairwise Mann-Whitney U tests per possible combination. Each abbreviations specifies a comparison between bone side and measuring direction. AL, anterior-longitudinal; AC, anterior-circumferential; LL, lateral-longitudinal; LC; lateral-circumferential; ML, medial-longitudinal; MC, medial-circumferential; PL, posterior-longitudinal; PC, posterior-circumferential.

	***Ardea cinerea* humeri Kruskal-Wallis p-value = 0.99**			***Ardea cinerea* tibiotarsi Kruskal-Wallis p-value = 0.86**			***Ardea cinerea* femora Kruskal-Wallis p-value = 0.82**		
Combi.	AL/LL	AC/LC	PL/ML	AL/LL	AC/LC	PL/ML	AL/LL	AC/LC	PL/ML
AC/LC	1.00	-	-	1.00	-	-	1.00	-	-
PL/ML	1.00	1.00	-	1.00	1.00	-	1.00	1.00	-
PR/MC	1.00	1.00	1.00	1.00	1.00	1.00	1.00	1.00	1.00

Table S4. Results of the Kruskal-Wallis tests and post-hoc pairwise Mann-Whitney U tests with Bonferroni corrections of Ra values for each possible combination of bone side and measuring direction in *Branta canadensis*. The p-value of the Kruskal-Wallis tests are shown in the first row. The remaining numbers are the p-values of the pairwise Mann-Whitney U tests per possible combination. Each abbreviations specifies a comparison between bone side and measuring direction. AL, anterior-longitudinal; AC, anterior-circumferential; LL, lateral-longitudinal; LC; lateral-circumferential; ML, medial-longitudinal; MC, medial-circumferential; PL, posterior-longitudinal; PC, posterior-circumferential.

	***Branta canadensis* humeri Kruskal-Wallis p-value = 0.11**			***Branta canadensis* tibiotarsi Kruskal-Wallis p-value = 0.00**			***Branta canadensis* femora Kruskal-Wallis p-value = 0.00**		
Combi.	AL/LL	AC/LC	PL/ML	AL/LL	AC/LC	PL/ML	AL/LL	AC/LC	PL/ML
AC/LC	1.00	-	-	0.03	-	-	0.01	-	-
PL/ML	1.00	1.00	-	1.00	0.01	-	1.00	0.00	-
PR/MC	0.15	1.00	0.31	1.00	1.00	0.15	0.07	1.00	0.02

longitudinal *Branta canadensis* Ra values showed insignificant differences between the humeri, tibiotarsi and femora of adult specimens (Table S6).

5.6.4 Ra (2D linear) and Sa (3D areal) values

To accurately compare corresponding Ra an Sa values per bird specimen, we averaged the Ra and Sa values for each bird as the various statistical analyses showed ambiguous effects at best regarding different sampling strategies including values for specific bone element, bone side and measuring direction. Moreover, as the comparison between corresponding Ra and Sa values rely purely on methodology, we did not separate according to ontogenetic stage and we performed a paired Mann-Whitney U test on the complete averaged Ra dataset and corresponding Sa values for both *Ardea cinerea* and *Branta canadensis*. Both *A. cinerea* ($p = 0.03$) and *B. canadensis* ($p = 0.00$) show a significant difference between Ra and Sa values.

5.6.5 Rv, Rp and Rz values

Paired two sample t-tests on the Rv and Rp values show that *Ardea cinerea* have significantly higher Rv values than Rp ($p = 0.01$), while *Branta canadensis* show significantly lower Rv values than Rp values ($p = 0.002$). Rz values were compared between *A. cinerea* and *B. canadensis* and a two sample t-test

Table S5. Results of the Kruskal-Wallis tests and post-hoc pairwise Mann-Whitney U tests with Bonferroni corrections for interbone comparison of Ra values within the four age classes of *Ardea cinerea*. Except for the humerus and tibiotarsus of chick grey herons, there is no significant difference in Ra values between different types of bone element.

	***Ardea cinerea* hatchling Kruskal-Wallis p-value = 0.05**		***Ardea cinerea* chick Kruskal-Wallis p-value = 0.10**		***Ardea cinerea* juvenile Kruskal-Wallis p-value = 0.15**		***Ardea cinerea* adult Kruskal-Wallis p-value = 0.21**	
	Femur	Humerus	Femur	Humerus	Femur	Humerus	Femur	Humerus
Humerus	0.69	-	1.00	-	0.28	-	1.0	-
Tibiotarsus	0.17	0.60	0.99	0.04	0.38	1.00	0.6	0.8

(unpaired) revealed that the Rz values for *A. cinerea* were significantly smaller than *B. canadensis* (p = 0.00).

Table S6. Results of the Kruskal-Wallis tests and post-hoc pairwise Mann-Whitney U tests with Bonferroni corrections for interbone comparison of longitudinal Ra values between different limb bone types of *Branta canadensis*.

***Branta canadensis* adult Kruskal-Wallis p-value = 0.07**		
	Femur	Humerus
Humerus	0.09	-
Tibiotarsus	0.41	1.00

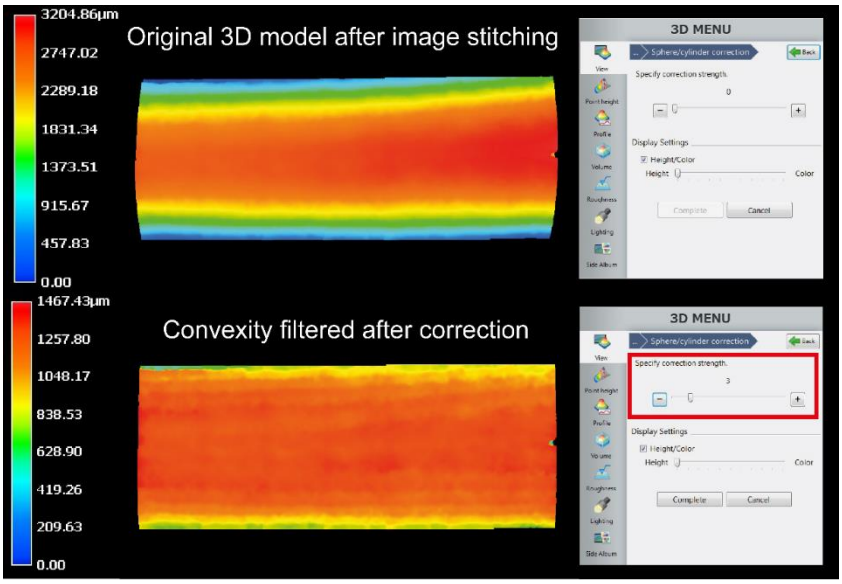

Figure S1. Heatmap output showing the height distribution of the 3D model. By specifying the correction strength (red square), it becomes possible to reduce the convexity step-wise until the desired shape is reached. This often required two to three correction steps.

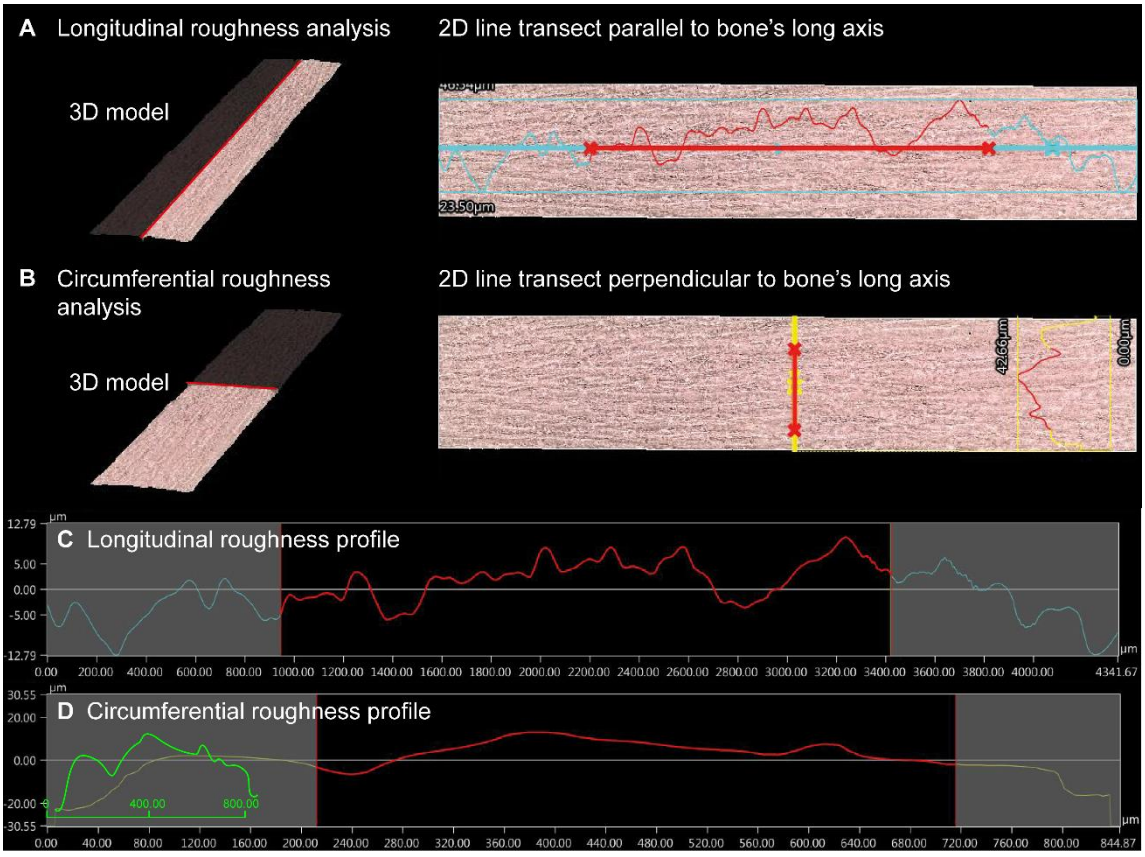

Figure S2. Example of the output of the roughness analysis showing longitudinal and circumferential sampling strategies and corresponding roughness profiles. We used the built-in roughness tool to produce a roughness profile for each bone. A. Longitudinal sampling strategy. B. Circumferential sampling strategy. C. Roughness profile of the longitudinal transect. D. Roughness profile of the circumferential transect. The graph in green represents the same data but is standardized to the x-axis of the longitudinal data graph in C.

Acknowledgements

We want to thank Wim van den Assem and Boris Temming for providing us with the *Branta canadensis* specimens and Bram Langeveld and Erwin Kompanje (Natural History Museum Rotterdam, the Netherlands) for access to *Ardea cinerea* specimens. Many thanks to Becky Desjardins (Naturalis, the Netherlands) and Ydnas Louisa for helping with the preparation of the material. We are grateful to Frans Rodenberg (Leiden University, the Netherlands) for his help in setting up the statistical analyses and to Silvania Pereira (Department of Imaging Physics, Delft University of Technology, the Netherlands) for her feedback on the manuscript and discussion on the applied methodology. Lastly, many thanks to the two anonymous reviewers for their time and comments that greatly improved the chapter.

References

Acosta Hospitaleche, C., Picasso, M.J.B., 2020. Textural ageing in *Pygoscelis antarctica* (Aves, Sphenisciformes): a new comparative scale for penguin bones. Vertebrate Zoology 70, 125–139. https://doi.org/10.26049/VZ70-2-2020-03

Brown, C.M., Russell, A.P., Ryan, M.J., 2009. Pattern and transition of surficial bone texture of the centrosaurine frill and their ontogenetic and taxonomic implications. Journal of Vertebrate Paleontology 29, 132–141. https://doi.org/10.1671/039.029.0119

Emmans, G.C., 2022. The potential post-hatching growth of domestic birds is sufficiently described by the Gompertz function. British Poultry Science 63, 701–719. https://doi.org/10.1080/00071668.2022.2083941

Martisius, N.L., McPherron, S.P., Schulz-Kornas, E., Soressi, M., Steele, T.E., 2020. A method for the taphonomic assessment of bone tools using 3D surface texture analysis of bone microtopography. Archaeological and Anthropological Sciences 12, 251. https://doi.org/10.1007/s12520-020-01195-y

Sampson, S.D., Ryan, M.J., Tanke, D.H., 1997. Craniofacial ontogeny in centrosaurine dinosaurs (Ornithischia: Ceratopsidae): taxonomic and behavioral implications. Zoological Journal of the Linnean Society 121, 293–337. https://doi.org/10.1111/j.1096-3642.1997.tb00340.x

Sibly, R.M., Brown, J.H., 2020. Toward a physiological explanation of juvenile growth curves. Journal of Zoology 311, 286–290. https://doi.org/10.1111/jzo.12770

Tumarkin-Deratzian, A.R., 2010. Histological evaluation of ontogenetic bone surface texture changes in the frill of *Centrosaurus apertus*, in: Ryan, M.J., Chinnery-Allgeier, B.J., Eberth, D.A. (Eds.), New Perspectives on Horned Dinosaurs: The Royal Tyrrell Museum Ceratopsian Symposium. Indiana University Press, Bloomington, pp. 251–263.

Tumarkin-Deratzian, A.R., 2009. Evaluation of long bone surface textures as ontogenetic indicators in centrosaurine ceratopsids. Anatomical Records 292, 1485–1500. https://doi.org/10.1002/ar.20972

Tumarkin-Deratzian, A.R., Vann, D.R., Dodson, P., 2007. Growth and textural ageing in long bones of the American alligator *Alligator mississippiensis* (Crocodylia: Alligatoridae). Zoological Journal of the Linnean Society 150, 1–39. https://doi.org/10.1111/j.1096-3642.2007.00283.x

Tumarkin-Deratzian, A.R., Vann, D.R., Dodson, P., 2006. Bone surface texture as an ontogenetic indicator in long bones of the Canada goose *Branta canadensis* (Anseriformes: Anatidae). Zoological Journal of the Linnean Society 148, 133–168. https://doi.org/10.1111/j.1096-3642.2006.00232.x

Vietti, L.A., 2016. Quantifying bone weathering stages using the average roughness parameter Ra measured from 3D data. Surface Topography: Metrology and Properties 4, 034006. https://doi.org/10.1088/2051-672X/4/3/034006

Watanabe, J., 2018. Ontogeny of surface texture of limb bones in modern aquatic birds and applicability of textural ageing. Anatomical Records 301, 1026–1045. https://doi.org/10.1002/ar.23736

Watanabe, J., Matsuoka, H., 2013. Ontogenetic change of morphology and surface texture of long bones in the gray heron (*Ardea cinerea*, Ardeidae). In: Göhlich, U.B., Kroh, A. (Eds.), Paleornithological Research 2013, pp. 279–306.

Wijngaarden, C.L., 2021. Bone surface texture and age-at-death of post-Medieval adult skeletal remains from Middenbeemster, the Netherlands: Testing the textural ageing method on human remains (Unpublished MSc Thesis). Leiden University, Leiden.

6

Chapter 6. Synthesis

Palaeontology is based on the study of often fragmentary fossil remains. Even when material is exceptionally preserved or abundantly available, testing of hypotheses always requires extrapolation of palaeontological data. This thesis presents a holistic approach to the study of dinosaur bonebeds, applying multiple lines of evidence to contextualize taphonomic, palaeoecological and ontogenetic signals within a single local mass death assemblage. Accordingly, this work provides an example of how a unique toolkit helps to approximate the scientifically most accurate reconstruction of dinosaur behaviour. Here, the results of the formulated Bonebed Toolkit are reviewed in the framework of the DTB, and the novel insights gained on *Triceratops* palaeobiology are discussed in the context of ceratopsid bonebeds and gregariousness.

6.1 Combining multiple independent lines of evidence to reveal the behaviour of extinct animals

First of all, the sedimentological and taphonomic context of the DTB investigated in **Chapter 2** reconstructs possible scenarios for the depositional environment and reveals the taphonomic history of the fossil assemblage. High-resolution grain size analyses performed on the bone-bearing layer returned very fine-grained sediments, suggesting that initial deposition of the *Triceratops* material occurred in extremely low energetic (hydrodynamic) environments (i.e., near-stagnant water). In other words, the *Triceratops* material neither experienced long-distance transport or highly energetic flooding events during deposition, nor during the time of death and initial burial. It is thus most likely that all five *Triceratops* individuals were associated with each other and formed a potential aggregation at their time of death. This is further supported by the taphonomic signals from the DTB. Semi-quantitative analysis of bone modifications revealed uniform degrees of fossilisation across the entire DTB, strongly suggesting that all the *Triceratops* material – and hence all individuals – have the same taphonomic history and do not represent reworked material. The same conclusions can be drawn from the µXRF data, which show similar incorporation and preservation of trace elements in the fossil material across the DTB. Moreover, the DTB is a monodominant assemblage and thus by definition only deposited the remains of a single taxon, namely *Triceratops horridus*. As such, the absence of remains of other dinosaur taxa provides evidence against long distance transport and argues in favour of a local rapid burial event that instantaneously killed and buried all five *Triceratops* individuals. Additionally, thorough inspection for potential bite marks did not reveal any signs of scavenging on the DTB material, further strengthening the hypothesis of a single rapid burial event.

Secondly, the results of the stable carbon and oxygen isotope analyses performed in **Chapter 3** offer additional insights on the provenance of the *Triceratops* individuals while contributing to a better understanding of *Triceratops* palaeoecology. The isotopic preservation in *Triceratops* tooth enamel was equal across the DTB and showed consistent offsets compared to tooth dentine, hinting towards equal taphonomic modifications of the material. Moreover, the carbon and oxygen isotope signatures of *Triceratops* enamel show large overlap with those of the *Champsosaurus* and lepisosteids, both taxa being indicators of the local water conditions at the time when the DTB was deposited. In other words, transported material could (isotopically) deviate from the local environment – while there is no deviation here. Consequently, the geochemical data presented in this thesis provided an alternative line of reasoning to verify that the DTB represents a single deposition rather than an accumulation over time. Additionally, comparison of carbon and oxygen isotope ratios between multiple *Triceratops* individuals from the DTB yielded overlapping values showing relatively weak cyclicity. These

incremental samples thus indicate that most likely none of the DTB *Triceratops* originated from a geographically different reworked assemblage, which is in agreement with the single origin of the DTB as also proposed by the sedimentological analyses. In accordance with the incremental isotope data, the DTB *Triceratops* all showed limited migratory behaviour approximately three to twelve months prior to their death, further corroborating the isotopic overlap and limited transport of the material.

Lastly, the histological data presented in **Chapter 4** has provided new information on *Triceratops* growth and ontogeny. While this chapter did not discuss the results in the larger framework of bonebed analyses, the observed age classes – combined with available data on cranial ontogeny – will help to establish mortality profiles for the DTB *Triceratops*. The DTB preserves two distinct age classes based on cranial ontogeny and histological markers. The younger age group is represented by actively growing subadults associated with an ornamented parietosquamosal frill complex, while the older age group represents adults that have attained skeletal maturity and lack epoccipital frill ornamentation. Accordingly, the acquired age profile of the DTB can be compared between profiles belonging to attritional or catastrophic fossil assemblages. The DTB cannot be identified as attritional as it did not preserve the more vulnerable individuals susceptible to background mortality such as juveniles or very old adults. Instead, the DTB closely resembles a catastrophic age profile where the preserved individuals are restricted to subadults and early adults. These catastrophic age profiles will more likely resemble that of the (presumable) living population, indicating that a single higher-impact event killed off the group of *Triceratops* indiscriminately of age classes. Again, this hypothesis is supported by the sedimentological, taphonomic and geochemical data of the DTB.

While behavioural patterns are extremely difficult to reconstruct using the fossil record, mass death assemblages have often provided a unique window into the paleobiology of extinct taxa. However, fossil bonebeds require detailed taphonomic scrutiny to define them as true mass death events and previous studies focused on a combination of conditions to identify such events including taxonomic exclusivity, high numbers of densely clustered skeletal elements and shared taphonomic history among the preserved individuals (Botfalvai et al., 2021; Capaldo and Peters, 1995; Eberth and Getty, 2005; Haynes, 1988; Mclain et al., 2021; Qi et al., 2007; Snyder et al., 2020; Turnbull and Martill, 1988). This thesis expanded the range of methods to include sedimentological, osteohistological and geochemical data providing additional support in the framework of bonebed interpretations. As such, each dataset presented in this thesis has defined the DTB as a true mass death assemblage representing a catastrophic bonebed in which all five *Triceratops* individuals were rapidly killed and buried in a single local mortality event. The available taphonomic data of the two previously reported *Triceratops* bonebeds indicate possible log-jam scenarios (Mathews et al., 2009) and asynchronous deposition of multiple individuals (Keenan and Scannella, 2014), thus providing equivocal evidence for true mass death assemblages which has left current inferences on *Triceratops* social behaviour ambiguous at best. However, the DTB described here in detail presents an extremely robust dataset to reconstruct the most parsimonious scenario for *Triceratops* behaviour, and provides strong support for *Triceratops* gregariousness.

What follows is a set of five plates (by Nadia de Waal) that depicts the possible scenarios that led to the preservation of the Darnell *Triceratops* Bonebed. This hypothetical reconstruction is based on the most parsimonious interpretation of the bonebed data presented in this thesis.

Prolonged rain seasons and wet environments make miring
the most likely cause of death for a small herd of *Triceratops*
Nadia de Waal

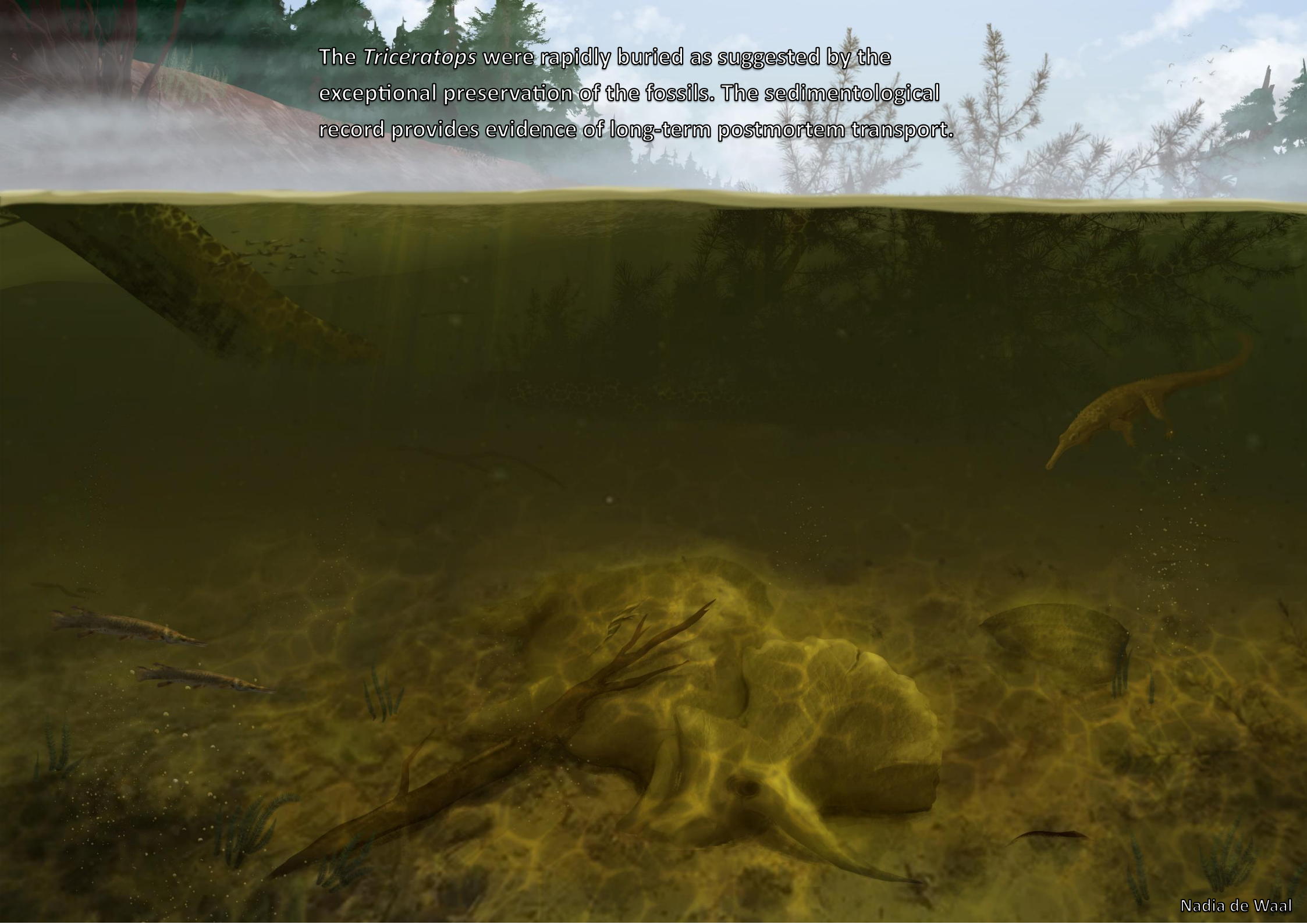
The *Triceratops* were rapidly buried as suggested by the exceptional preservation of the fossils. The sedimentological record provides evidence of long-term postmortem transport.
Nadia de Waal

Skeletons started to decompose and the first stages of fossilization may have begun. The initial depositional environment changed over time
Nadia de Waal

Increased waterflows in rivers may lead to crevasse splays. These sediment spills redistribute and disarticulate the *Triceratops* skeletons
Nadia de Waal

The herd of *Triceratops* was initially preserved as one associated group, but became more disarticulated over time before their final burial and its discovery 66 million years later.
Nadia de Waal

6.2 Potential mechanisms for bonebed preservation and gregarious behaviour in ceratopsids

Monospecific bonebeds have been reported for numerous other centrosaurine and chasmosaurine taxa including *Achelousaurus* (Sampson, 1995a), *Albertaceratops* (Ryan, 2007), *Centrosaurus* (Chiba et al., 2015; Currie and Dodson, 1984; Eberth and Getty, 2005; Ryan et al., 2001; Ryan and Russell, 2005), *Coronosaurus* (Ryan et al., 2012; Ryan and Russell, 2005), *Einiosaurus* (Reizner, 2010; Rogers, 1990; Sampson, 1995b, 1995a), *Medusaceratops* (Chiba et al., 2018), *Pachyrhinosaurus* (Fanti et al., 2015; Fiorillo and Gangloff, 2003; Langston Jr., 1975; Ryan et al., 2010; Tanke, 1988), *Spinops* (Farke et al., 2011), *Styracosaurus* (Ryan, 2003; Sampson et al., 1997; Visser, 1986), *Wendiceratops* (Evans and Ryan, 2015; Scott et al., 2023), *Xenoceratops* (Ryan et al., 2012), *Agujaceratops* (Lehman, 2006, 1989; Lucas et al., 2006), *Anchiceratops* (Brown, 1914; Sternberg, 1926), *Coahuilaceratops* (Loewen et al., 2010), *Torosaurus* (Gilmore, 1946), *Triceratops* (Keenan and Scannella, 2014; Mathews et al., 2009) and *Utahceratops* (Sampson et al., 2010). In general, centrosaurine bonebeds are more abundant than chasmosaurine bonebeds and often preserve higher numbers of individuals, despite no clear other geographical, temporal or taphonomic differences between the two groups (Eberth et al., 2010). While the DTB represents the largest *Triceratops* bonebed, the general assemblage data is still consistent with previously described chasmosaurine bonebeds, and therefore the discrepancy between the number and composition of centrosaurine and chasmosaurine bonebeds most likely represents an inherent biological signal and is not related to taphonomic biases. Furthermore, the currently available ceratopsid bonebed data suggests that gregarious behaviour evolved relatively early in ceratopsian evolution (Fastovsky et al., 2011; Meng et al., 2004; Qi et al., 2007; Scott et al., 2023), and that more derived ceratopsids were characterized by unique social behavioural patterns (Eberth et al., 2010; Lehman, 2006; Scott et al., 2023; Wolfe and Kirkland, 1998).

Current assumptions on ceratopsid social behaviour are also largely based on observations on extant taxa (Sampson, 2009). Gregarious and social behavioural strategies in extant animals are often defined by an interplay of environmental and ecological factors including predation pressure (Avila et al., 2022; Childress and Lung, 2003; Shannon et al., 2022; Sorato et al., 2012), landscape vegetation (Gómez et al., 2022; Iribarren and Kotler, 2012; Koger et al., 2023; Lesmerises et al., 2018), resource distribution (Iribarren and Kotler, 2012; Johnson et al., 2002; Monaghan and Metcalfe, 1985; Sorato et al., 2012), home range size (Campos et al., 2014; Gehrt and Fritzell, 1998; Pough et al., 2013) and mate accessibility for reproductive success (Dougherty, 2021; Gehrt and Fritzell, 1998; Roth et al., 2021). Alternatively, many extant taxa are considered facultatively social, participating in social hierarchies only during specific seasons, using different sensory cues, or showing completely different social structures per generation or population altogether (Brashares and Arcese, 2002; Jędrzejewski et al., 2022; Jenikejew et al., 2020; Menz et al., 2017; Réale and Dingemanse, 2010). Moreover, temporary aggregations of animals may form due to environmental stresses such as food scarcity or prolonged drought periods. In this case, conspecifics may tolerate each other's presence irrespective of preferred social behaviour. On the other end of the spectrum, animals may form permanent herds, here defined as a monospecific socially cohesive group of (related) individuals, with a possible complex hierarchal structure of dominance. Sampson (2009) provided a comprehensive overview of possible scenarios for ceratopsid social behaviour. By correlating these to a suite of characters observed in extant analogues, Sampson (2009) hypothesized that the majority of ceratopsids likely formed small to large, nonterritorial (i.e., moving between food sources), hierarchically structured, mixed-sex herds, at least periodically, in which potential predator defence dictated the actual group size (Fortin et al., 2009; Fortin and Fortin, 2009; MacNulty et al., 2014; Mooring et al., 2006).

The newly acquired dataset on *Triceratops* palaeobiology presented in this thesis enables more accurate testing of specific mechanisms that would promote grouping behaviour. First of all, sexual dimorphism has not been observed in *Triceratops* – or any other ceratopsian – despite the high number of available skulls bearing elaborate cranial ornamentation (Knell and Sampson, 2011; Mallon, 2017; Mallon and Holmes, 2006; Padian and Horner, 2011). Additionally, the histological analysis conducted in Chapter 4 did not reveal a dichotomy in growth patterns within same-age individuals, a phenomenon otherwise used as evidence for possible sexual dimorphic growth strategies in some sauropod taxa (Klein and Sander, 2008; Sander, 2000). Thus, the currently available data suggests that *Triceratops* most likely did not evolve sexual dimorphism, at least not expressed in cranial morphology or ontogenetic growth strategies. Secondly, the ontogenetic changes in bone histology revealed that growth termination coincided with the attainment of the final cranial ontogenetic stage, suggesting that *Triceratops* reached relatively delayed cranial maturity, similar as group-living bovids (Goodwin et al., 2006; Horner and Goodwin, 2006). This is in agreement with the earlier proposed hypothesis stating that subadult and adult cranial morphologies most likely signalled sexual maturity as appropriate body sizes were reached (Horner and Goodwin, 2006). Lastly, the carbon and oxygen isotope data presented in Chapter 3 revealed that *Triceratops* habitats were less restricted than previously hypothesized, and they most likely inhabited open coastal floodplains as well as more vegetated fluvial systems (Cullen et al., 2020). While the current isotope datasets provide limited insights on *Triceratops* migratory behaviour, it is reasonable to assume that (groups of) *Triceratops* were forced to move between these areas for foraging to sustain their large body sizes, instead of being permanently confined to relatively smaller territories. Accordingly, the niche occupation and relatively large home range of *Triceratops* would promote grouping behaviour. While current *Triceratops* bonebeds consist of three to five individuals, estimates of true group sizes in *Triceratops* herds remain speculative at best, especially considering the diverging group sizes between and within ceratopsids as well as extant taxa (Fortin et al., 2009; Fortin and Fortin, 2009; MacNulty et al., 2014; Mathews et al., 2009; Ryan et al., 2001). Group size is most likely defined by boundaries set by the landscape environment, intraspecific interactions and/or predator-prey interactions. *Tyrannosaurus rex* represented the apex predator during the Late Maastrichtian of North America and reports of *Triceratops* pathologies suggest that both taxa interacted with each other (Happ, 2008). As such, gregariousness may provide an extremely efficient defence mechanism against predation. Moreover, while the *Triceratops* horns and frill may not have been used as direct weapons, they may have played a crucial role to intimidate and deter potential predators. This notion is further supported by the lack of sexual dimorphism, as predator defence is advantageous for both male and female, especially against large predators such as *T. rex*.

Considering all the available data on *Triceratops* palaeobiology so far, the potential for gregariousness in *Triceratops* is controlled by similar parameters as in modern analogues, and fits in the proposed scheme of ceratopsid socioecology defined by Sampson (2009). In other words, for at least a period of their life, *Triceratops* likely formed relatively small herds that provided sufficient defence against potential predators while moving from different patches of food resources within a given home range. *Triceratops* group sizes most likely expressed some plasticity conforming to multiple external factors such as predation pressure, food availability or mating seasons. More specific insights on potential social structures such as dominance hierarchies, mating strategies or parental care in *Triceratops* remain purely hypothetical at present (Hunt and Farke, 2010; Sampson, 2009), but monospecific habitual gatherings, as herein argued is found in the DTB, would have enabled more complex social interactions among conspecifics. This is further supported by the development of the elaborate parieto-squamosal frill complex of *Triceratops* (and other ceratopsids), which is hypothesized

to serve in socio-sexual signalling, species recognition and/or intraspecific combat (D'Anastasio et al., 2022; Farke et al., 2009; Farlow and Dodson, 1975; Hone et al., 2016, 2012; Knapp et al., 2018; Nabavizadeh, 2023; Padian and Horner, 2011; Sampson, 2009).

6.3 Future perspectives

The 'Bonebed Toolkit' assembled, tested and presented in this thesis provides a novel, multipronged approach to study large mass death assemblages in archaeology and palaeontology. Not only does it provide insights on the origin and provenance of the bonebed material, but it also helps to create a thorough understanding of the taxa that are present. An exciting and important next step is implementing the Bonebed Toolkit in research of bonebeds from other extinct taxa. For example, many reported ceratopsid bonebeds have not been analysed in such detail (Ryan et al., 2010), and revealing behavioural patterns in related taxa may shed light on the evolution of growth strategies, living environments or gregarious and social behaviour. Needless to say, the use of the Bonebed Toolkit extends beyond the study of horned dinosaurs and can be applied to a plethora of taxa as long as relevant material is preserved. Moreover, the results presented here highly recommend the use of a multidisciplinary framework to better understand mass death assemblages. Bonebed analyses that lack such scrutiny may be limited to ambiguous interpretations, while bonebeds otherwise contain a wealth of information. Perhaps most importantly, while this thesis has presented a specific approach tailored for the DTB, the Bonebed Toolkit is not limited to the techniques discussed in this thesis. The Bonebed Toolkit approach essentially provides a framework to combine multiple lines of evidence in archaeological and palaeontological research, making the Bonebed Toolkit a highly flexible and continuously innovating strategy.

References

Avila, A.B., Corriale, M.J., Donadio, E., Di Bitetti, M.S., Ponzio, M.F., Cantarelli, V., De Angelo, C., 2022. Capybara responses to varying levels of predation risk. Animal Behaviour 190, 1–9. https://doi.org/10.1016/j.anbehav.2022.05.008

Botfalvai, G., Prondvai, E., Ősi, A., 2021. Living alone or moving in herds? A holistic approach highlights complexity in the social lifestyle of Cretaceous ankylosaurs. Cretaceous Research 118, 104633. https://doi.org/10.1016/j.cretres.2020.104633

Brashares, J.S., Arcese, P., 2002. Role of forage, habitat and predation in the behavioural plasticity of a small African antelope. Journal of Animal Ecology 71, 626–638. https://doi.org/10.1046/j.1365-2656.2002.00633.x

Brown, B., 1914. *Anchiceratops*, a new genus of horned dinosaurs from the Edmonton Cretaceous of Alberta ; with Discussion of the origin of the ceratopsian crest and the brain casts of *Anchiceratops* and *Trachodon*. Bulletin of the American Museum of Natural History 33.

Campos, F.A., Bergstrom, M.L., Childers, A., Hogan, J.D., Jack, K.M., Melin, A.D., Mosdossy, K.N., Myers, M.S., Parr, N.A., Sargeant, E., Schoof, V.A.M., Fedigan, L.M., 2014. Drivers of home range characteristics across spatiotemporal scales in a Neotropical primate*, Cebus capucinus*. Animal Behaviour 91, 93–109. https://doi.org/10.1016/j.anbehav.2014.03.007

Capaldo, S.D., Peters, C.R., 1995. Skeletal inventories from wildebeest drownings at Lakes Masek and Ndutu in the Serengeti Ecosystem of Tanzania. Journal of Archaeological Science 22, 385–408. https://doi.org/10.1006/jasc.1995.0039

Chiba, K., Ryan, M.J., Braman, D.R., Eberth, D.A., Scott, E.E., Brown, C.M., Kobayashi, Y., Evans, D.C., 2015. Taphonomy of a monodominant *Centrosaurus apertus* (Dinosauria: Ceratopsia)

bonebed from the upper Oldman formation of southeastern Alberta. Palaios 30, 655–667. https://doi.org/10.2110/palo.2014.084

Chiba, K., Ryan, M.J., Fanti, F., Loewen, M.A., Evans, D.C., 2018. New material and systematic re-evaluation of *Medusaceratops lokii* (Dinosauria, Ceratopsidae) from the Judith River Formation (Campanian, Montana). Journal of Paleontology 92, 272–288. https://doi.org/10.1017/jpa.2017.62

Childress, M.J., Lung, M.A., 2003. Predation risk, gender and the group size effect: does elk vigilance depend upon the behaviour of conspecifics? Animal Behaviour 66, 389–398. https://doi.org/10.1006/anbe.2003.2217

Cullen, T.M., Longstaffe, F.J., Wortmann, U.G., Huang, L., Fanti, F., Goodwin, M.B., Ryan, M.J., Evans, D.C., 2020. Large-scale stable isotope characterization of a Late Cretaceous dinosaur-dominated ecosystem. Geology 48, 546–551. https://doi.org/10.1130/G47399.1

Currie, P.J., Dodson, P., 1984. Mass death of a herd of ceratopsian dinosaurs. In: Reif, W.-E, Westphal, F. (Eds.), Third Symposium on Mesozoic terrestrial ecosystems, Short Papers, pp. 61–66.

D'Anastasio, R., Cilli, J., Bacchia, F., Fanti, F., Gobbo, G., Capasso, L., 2022. Histological and chemical diagnosis of a combat lesion in *Triceratops*. Scientific Reports 12, 3941. https://doi.org/10.1038/s41598-022-08033-2

Dougherty, L.R., 2021. Meta-analysis shows the evidence for context-dependent mating behaviour is inconsistent or weak across animals. Ecology Letters 24, 862–875. https://doi.org/10.1111/ele.13679

Eberth, D.A., Brinkman, D.B., Barkas, V., 2010. A centrosaurine mega-bonebed from the Upper Cretaceous of Southern Alberta: Implications for behavior and death events. In: Ryan, M.J., Chinnery-Allgeier, B.J., Eberth, D.A. (Eds.), New Perspectives on Horned Dinosaurs: The Royal Tyrrell Museum Ceratopsian Symposium. Indiana University Press, Bloomington, pp. 495–508.

Eberth, D.A., Getty, M.A., 2005. Ceratopsian bonebeds: occurrence, origins, and significance. In: Currie, P.J., Koppelhus, E.B. (Eds.), Dinosaur Provincial Park. A Spectacular Ancient Ecosystem Revealed. Indiana University Press, Bloomington, pp. 501–536.

Evans, D.C., Ryan, M.J., 2015. Cranial Anatomy of *Wendiceratops pinhornensis* gen. et sp. nov., a Centrosaurine Ceratopsid (Dinosauria: Ornithischia) from the Oldman Formation (Campanian), Alberta, Canada, and the Evolution of Ceratopsid Nasal Ornamentation. PLoS ONE 10, e0130007. https://doi.org/10.1371/journal.pone.0130007

Fanti, F., Currie, P.J., Burns, M.E., 2015. Taphonomy, age, and paleoecological implication of a new *Pachyrhinosaurus* (Dinosauria: Ceratopsidae) bonebed from the Upper Cretaceous (Campanian) Wapiti Formation of Alberta, Canada. Canadian Journal of Earth Sciences 52, 250–260. https://doi.org/10.1139/cjes-2014-0197

Farke, A.A., Ryan, M.J., Barrett, P.M., Tanke, D.H., Braman, D.R., Loewen, M.A., Graham, M.R., 2011. A new centrosaurine from the Late Cretaceous of Alberta, Canada, and the evolution of parietal ornamentation in horned dinosaurs. Acta Palaeontologica Polonica 56, 691–702. https://doi.org/10.4202/app.2010.0121

Farke, A.A., Wolff, E.D.S., Tanke, D.H., 2009. Evidence of combat in *Triceratops*. PLoS ONE 4, e4252. https://doi.org/10.1371/journal.pone.0004252

Farlow, J.O., Dodson, P., 1975. The behavioral significance of frill and horn morphology in ceratopsian dinosaurs. Evolution 29, 353. https://doi.org/10.2307/2407222

Fastovsky, D.E., Weishampel, D.B., Watabe, M., Barsbold, R., Tsogtbaatar, Kh., Narmandakh, P., 2011. A nest of *Protoceratops andrewsi* (Dinosauria, Ornithischia). Journal of Paleontology 85, 1035–1041. https://doi.org/10.1666/11-008.1

Fiorillo, A.R., Gangloff, R.A., 2003. Preliminary notes on the taphonomic and paleoecologic setting of a *Pachyrhinosaurus* bonebed in northern Alaska. Journal of Vertebrate Paleontology 23, 50A.

Fortin, D., Fortin, M.-E., 2009. Group-size-dependent association between food profitability, predation risk and distribution of free-ranging bison. Animal Behaviour 78, 887–892. https://doi.org/10.1016/j.anbehav.2009.06.026

Fortin, D., Fortin, M.-E., Beyer, H.L., Duchesne, T., Courant, S., Dancose, K., 2009. Group-size-mediated habitat selection and group fusion–fission dynamics of bison under predation risk. Ecology 90, 2480–2490. https://doi.org/10.1890/08-0345.1

Gehrt, S.D., Fritzell, E.K., 1998. Resource distribution, female home range dispersion and male spatial interactions: group structure in a solitary carnivore. Animal Behaviour 55, 1211–1227. https://doi.org/10.1006/anbe.1997.0657

Gilmore, C.W., 1946. Reptilian fauna of the North Horn formation of central Utah. United States Geological Survey Professional Papers, 210C.

Gómez, J.M., Schupp, E.W., Jordano, P., 2022. The ecological and evolutionary significance of effectiveness landscapes in mutualistic interactions. Ecology Letters 25, 264–277. https://doi.org/10.1111/ele.13939

Goodwin, M.B., Clemens, W.A., Horner, J.R., Padian, K., 2006. The smallest known *Triceratops* skull: new observations on ceratopsid cranial anatomy and ontogeny. Journal of Vertebrate Paleontology 26, 103–112. https://doi.org/10.1671/0272-4634(2006)26[103:TSKTSN]2.0.CO;2

Happ, J., 2008. An analysis of predator-prey behavior in a head-to-head encounter between *Tyrannosaurus rex* and *Triceratops*. In: Larson, P.L., Carpenter, K. (Eds.), *Tyrannosaurus Rex*: The Tyrant King. Indiana University Press, Bloomington, pp. 355–370.

Haynes, G., 1988. Mass deaths and serial predation: Comparative taphonomic studies of modern large mammal death sites. Journal of Archaeological Science 15, 219–235. https://doi.org/10.1016/0305-4403(88)90064-7

Hone, D.E., Wood, D., Knell, R., 2016. Positive allometry for exaggerated structures in the ceratopsian dinosaur *Protoceratops andrewsi* supports socio-sexual signaling. Palaeontologia Electronica 19.1.5A, 1–13. https://doi.org/10.26879/591

Hone, D.W.E., Naish, D., Cuthill, I.C., 2012. Does mutual sexual selection explain the evolution of head crests in pterosaurs and dinosaurs?: Ornithodiran mutual sexual selection. Lethaia 45, 139–156. https://doi.org/10.1111/j.1502-3931.2011.00300.x

Horner, J.R., Goodwin, M.B., 2006. Major cranial changes during *Triceratops* ontogeny. Proceedings of the Royal Society B. 273, 2757–2761. https://doi.org/10.1098/rspb.2006.3643

Hunt, R.K., Farke, A.A., 2010. Behavioral interpretations from ceratopsid bonebeds, in: Ryan, M.J., Chinnery-Allgeier, B.J., Eberth, D.A. (Eds.), New Perspectives on Horned Dinosaurs: The Royal Tyrrell Museum Ceratopsian Symposium. Indiana University Press, Bloomington, pp. 447–455.

Iribarren, C., Kotler, B.P., 2012. Foraging patterns of habitat use reveal landscape of fear of Nubian ibex *Capra nubiana*. Wildlife Biology 18, 194–201. https://doi.org/10.2981/11-041

Jędrzejewski, W., Hoogesteijn, R., Devlin, A.L., Tortato, F., Concone, H.V.B., Azevedo, F., Eriksson, C.E., Fragoso, C.E., Abarca, M., Morato, R.G., Giordano, A.J., Hoogesteijn, A., Rampim, L., Gamarra,

G., Carreño, R., Velásquez, G., Schmidt, K., 2022. Collaborative behaviour and coalitions in male jaguars (*Panthera onca*)—evidence and comparison with other felids. Behavioral Ecology and Sociobiology 76, 121. https://doi.org/10.1007/s00265-022-03232-3

Jenikejew, J., Chaignon, B., Linn, S., Scheumann, M., 2020. Proximity-based vocal networks reveal social relationships in the Southern white rhinoceros. Scientific Reports 10, 15104. https://doi.org/10.1038/s41598-020-72052-0

Johnson, D.D.P., Kays, R., Blackwell, P.G., Macdonald, D.W., 2002. Does the resource dispersion hypothesis explain group living? Trends in Ecology & Evolution 17, 563–570. https://doi.org/10.1016/S0169-5347(02)02619-8

Keenan, S.W., Scannella, J.B., 2014. Paleobiological implications of a *Triceratops* bonebed from the Hell Creek Formation, Garfield County, northeastern Montana. In: Wilson, G.P., Clemens, W.A., Horner, J.R., Hartman, J.H. (Eds.), Through the End of the Cretaceous in the Type Locality of the Hell Creek Formation in Montana and Adjacent Areas. Geological Society of America Special Papers 503. Pp. 349–364. https://doi.org/10.1130/2014.2503(14)

Klein, N., Sander, M., 2008. Ontogenetic stages in the long bone histology of sauropod dinosaurs. Paleobiology 34, 247–263. https://doi.org/10.1666/0094-8373(2008)034[0247:OSITLB]2.0.CO;2

Knapp, A., Knell, R.J., Farke, A.A., Loewen, M.A., Hone, D.W.E., 2018. Patterns of divergence in the morphology of ceratopsian dinosaurs: sympatry is not a driver of ornament evolution. Proceedings of the Royal Society B. 285, 20180312. https://doi.org/10.1098/rspb.2018.0312

Knell, R.J., Sampson, S., 2011. Bizarre structures in dinosaurs: species recognition or sexual selection? A response to Padian and Horner. Journal of Zoology 283, 18–22. https://doi.org/10.1111/j.1469-7998.2010.00758.x

Koger, B., Deshpande, A., Kerby, J.T., Graving, J.M., Costelloe, B.R., Couzin, I.D., 2023. Quantifying the movement, behaviour and environmental context of group-living animals using drones and computer vision. Journal of Animal Ecology 1365-2656.13904. https://doi.org/10.1111/1365-2656.13904

Langston Jr., W., 1975. The ceratopsian dinosaurs and associated lower vertebrates from the St. Mary River Formation (Maestrichtian) at Scabby Butte, Southern Alberta. Canadian Journal of Earth Sciences 12, 1576–1608. https://doi.org/10.1139/e75-142

Lehman, T.M., 1989. *Chasmosaurus mariscalensis* , sp. nov., a new ceratopsian dinosaur from Texas. Journal of Vertebrate Paleontology 9, 137–162. https://doi.org/10.1080/02724634.1989.10011749

Lehman, T.M., 2006. Growth and population age structure in the horned dinosaur *Chasmosaurus*. In: Carpenter, K. (Ed.), Horns and Beaks: Ceratopsian and Ornithopod Dinosaurs, Indiana University Press, Bloomington, pp. 259–317.

Lesmerises, F., Johnson, C.J., St-Laurent, M.-H., 2018. Landscape knowledge is an important driver of the fission dynamics of an alpine ungulate. Animal Behaviour 140, 39–47. https://doi.org/10.1016/j.anbehav.2018.03.014

Loewen, M.A., Sampson, S.D., Lund, E.K., Farke, A.A., Aguillón-Martínez, M.C., De Leon, C.A., Rodríguez-de la Rosa, R.A., Getty, M.A., Eberth, D.A., 2010. Horned dinosaurs (Ornithischia: Ceratopsidae) from the Upper Cretaceous (Campanian) Cerro del Pueblo Formation, Coahuila, Mexico, in: Ryan, M.J., Chinnery-Allgeier, B.J., Eberth, D.A. (Eds.), New Perspectives on Horned Dinosaurs: The Royal Tyrrell Museum Ceratopsian Symposium, Indiana University Press, Bloomington, pp. 99–116.

Lucas, S.G., Sullivan, R.M., Hunt, A.P., 2006. Re-evaluation of *Pentaceratops* and *Chasmosaurus* (Ornithischia: Ceratopsidae) in the upper Cretaceous of the western interior. New Mexico Museum of Naturalis History and Science Bulletin, Late Cretaceous Vertebrates from the Western Interior 35.

MacNulty, D.R., Tallian, A., Stahler, D.R., Smith, D.W., 2014. Influence of group size on the success of wolves hunting bison. PLoS ONE 9, e112884. https://doi.org/10.1371/journal.pone.0112884

Mallon, J.C., 2017. Recognizing sexual dimorphism in the fossil record: lessons from nonavian dinosaurs. Paleobiology 43, 495–507. https://doi.org/10.1017/pab.2016.51

Mallon, J.C., Holmes, R.B., 2006. A reevaluation of sexual dimorphism in the postcranium of the chasmosaurine ceratopsid *Chasmosaurus belli* (Dinosauria: Ornithischia). Canadian Field Naturalist 120, 403. https://doi.org/10.22621/cfn.v120i4.347

Mathews, J.C., Brusatte, S.L., Williams, S.A., Henderson, M.D., 2009. The first *Triceratops* bonebed and its implications for gregarious behavior. Journal of Vertebrate Paleontology 29, 286–290. https://doi.org/10.1080/02724634.2009.10010382

Mclain, M.A., Ullmann, P.V., Ash, R.D., Bohnstedt, K., Nelsen, D., Clark, R.O., Brand, L.R., Chadwick, A.V., 2021. Independent confirmation of fluvial reworking at a Lance Formation (Maastrichtian) bonebed by traditional and chemical taphonomic analyses. Palaios 36, 193–215. https://doi.org/10.2110/palo.2020.064

Meng, Q., Liu, J., Varricchio, D.J., Huang, T., Gao, C., 2004. Parental care in an ornithischian dinosaur. Nature 431, 145–146. https://doi.org/10.1038/431145a

Menz, C.S., Goldizen, A.W., Blomberg, S.P., Freeman, N.J., Best, E.C., 2017. Understanding repeatability and plasticity in multiple dimensions of the sociability of wild female kangaroos. Animal Behaviour 126, 3–16. https://doi.org/10.1016/j.anbehav.2017.01.012

Monaghan, P., Metcalfe, N.B., 1985. Group foraging in wild brown hares: effects of resource distribution and social status. Animal Behaviour 33, 993–999. https://doi.org/10.1016/S0003-3472(85)80033-6

Mooring, M.S., Patton, M.L., Reisig, D.D., Osborne, E.R., Kanallakan, A.L., Aubery, S.M., 2006. Sexually dimorphic grooming in bison: the influence of body size, activity budget and androgens. Animal Behaviour 72, 737–745. https://doi.org/10.1016/j.anbehav.2006.02.006

Nabavizadeh, A., 2023. How *Triceratops* got its face: An update on the functional evolution of the ceratopsian head. The Anatomical Record ar.25196. https://doi.org/10.1002/ar.25196

Padian, K., Horner, J.R., 2011. The evolution of 'bizarre structures' in dinosaurs: biomechanics, sexual selection, social selection or species recognition? Journal of Zoology 283, 3–17. https://doi.org/10.1111/j.1469-7998.2010.00719.x

Pough, F.H., Janis, C.M., Heiser, J.B. (Eds.), 2013. Vertebrate life, 9th ed. Pearson, Boston.

Qi, Z., Barrett, P.M., Eberth, D.A., 2007. Social behaviour and mass mortality in the basal ceratopsian dinosaur *Psittacosaurus* (early Cretaceous, people's republic of China): social behaviour and mass mortality in ceratopsian dinosaur. Palaeontology 50, 1023–1029. https://doi.org/10.1111/j.1475-4983.2007.00709.x

Réale, D., Dingemanse, N.J., 2010. Personality and individual social specialization. In: Székely, T., Moore, A.J., Komdeur, J. (Eds.), Social Behaviour: Genes, Ecology and Evolution, Cambridge University Press, Cambridge.

Reizner, J.A., 2010. An ontogenetic series and population histology of the ceratopsid dinosaur *Einiosaurus procurvicornis* (Unpubl. MSc thesis). Montana State University, Bozeman, pp. 97.

Rogers, R.R., 1990. Taphonomy of three dinosaur bone beds in the Upper Cretaceous Two Medicine Formation of Northwestern Montana: Evidence for drought-related mortality. PALAIOS 5, 394. https://doi.org/10.2307/3514834

Roth, A.M., Dingemanse, N.J., Nakagawa, S., McDonald, G.C., Løvlie, H., Robledo-Ruiz, D.A., Pizzari, T., 2021. Sexual selection and personality: Individual and group-level effects on mating behaviour in red junglefowl. Journal of Animal Ecology 90, 1288–1306. https://doi.org/10.1111/1365-2656.13454

Ryan, M.J., 2007. A new basal centrosaurine ceratopsid from the Oldman Formation, southeastern Alberta. Journal of Paleontology 81, 376–396. https://doi.org/10.1666/0022-3360(2007)81[376:ANBCCF]2.0.CO;2

Ryan, M.J., 2003. Taxonomy, systematics and evolution of centrosaurine ceratopsids of the Campanian western interior basin of North America (Unpubl. MSc thesis). University of Calgary, Calgary, pp. 424–460

Ryan, M.J., Chinnery-Allgeier, B.J., Eberth, D.A. (Eds.), 2010. New perspectives on horned dinosaurs: the Royal Tyrrell Museum Ceratopsian Symposium. Indiana University Press, Bloomington.

Ryan, M.J., Evans, D.C., Shepherd, K.M., 2012. A new ceratopsid from the Foremost Formation (middle Campanian) of Alberta. Canadian Journal of Earth Sciences 49, 1251–1262. https://doi.org/10.1139/e2012-056

Ryan, M.J., Russell, A.P., 2005. A new centrosaurine ceratopsid from the Oldman Formation of Alberta and its implications for centrosaurine taxonomy and systematics. Canadian Journal of Earth Sciences 42, 1369–1387. https://doi.org/10.1139/e05-029

Ryan, M.J., Russell, A.P., Eberth, D.A., Currie, P.J., 2001. The taphonomy of a *Centrosaurus* (Ornithischia: Certopsidae) bone bed from the Dinosaur Park Formation (Upper Campanian), Alberta, Canada, with comments on cranial ontogeny. PALAIOS 16, 482–506. https://doi.org/10.1669/0883-1351(2001)016<0482:TTOACO>2.0.CO;2

Sampson, S.D., 2009. Speculations on the socioecology of ceratopsid dinosaurs (Ornithischia: Neoceratopsia) In: Tanke, D.H., Carpenter, K. (Eds.), Mesozoic Vertebrate Life. Indiana University Press, Bloomington, pp. 263–276.

Sampson, S.D., 1995a. Two new horned dinosaurs from the upper Cretaceous Two Medicine Formation of Montana; with a phylogenetic analysis of the Centrosaurinae (Ornithischia: Ceratopsidae). Journal of Vertebrate Paleontology 15, 743–760. https://doi.org/10.1080/02724634.1995.10011259

Sampson, S.D., 1995b. Horns, herds, and hierarchies. Natural History 104, 36–40.

Sampson, S.D., Loewen, M.A., Farke, A.A., Roberts, E.M., Forster, C.A., Smith, J.A., Titus, A.L., 2010. New horned dinosaurs from Utah provide evidence for intracontinental dinosaur endemism. PLoS ONE 5, e12292. https://doi.org/10.1371/journal.pone.0012292

Sampson, S.D., Ryan, M.J., Tanke, D.H., 1997. Craniofacial ontogeny in centrosaurine dinosaurs (Ornithischia: Ceratopsidae): taxonomic and behavioral implications. Zoological Journal of the Linnean Society 121, 293–337. https://doi.org/10.1111/j.1096-3642.1997.tb00340.x

Sander, P.M., 2000. Longbone histology of the Tendaguru sauropods: implications for growth and biology. Paleobiology 26, 466–488. https://doi.org/10.1666/0094-8373(2000)026<0466:LHOTTS>2.0.CO;2

Scott, S.H.W., Ryan, M.J., Evans, D.C., 2023. Postcranial description of *Wendiceratops pinhornensis* and a taphonomic analysis of the oldest monodominant ceratopsid bonebed. The Anatomical Record 306, 1824–1841. https://doi.org/10.1002/ar.25045

Shannon, G., Cordes, L.S., Slotow, R., Moss, C., McComb, K., 2022. Social disruption impairs predatory threat assessment in african elephants. Animals 12, 495. https://doi.org/10.3390/ani12040495

Snyder, K., McLain, M., Wood, J., Chadwick, A., 2020. Over 13,000 elements from a single bonebed help elucidate disarticulation and transport of an *Edmontosaurus thanatocoenosis*. PLoS ONE 15, e0233182. https://doi.org/10.1371/journal.pone.0233182

Sorato, E., Gullett, P.R., Griffith, S.C., Russell, A.F., 2012. Effects of predation risk on foraging behaviour and group size: adaptations in a social cooperative species. Animal Behaviour 84, 823–834. https://doi.org/10.1016/j.anbehav.2012.07.003

Sternberg, C.M., 1926. Notes on the Edmonton Formation of Alberta. Canadian Field Naturalist 40, 102–104.

Tanke, D.H., 1988. Ontogeny and dimorphism in *Pachyrhinosaurus* (Reptilia: Ceratopsidae), Pipestone Creek, N.W. Alberta, Canada. Journal of Vertebrate Paleontology 8, 41A.

Turnbull, W.D., Martill, D.M., 1988. Taphonomy and preservation of a monospecific titanothere assemblage from the Washakie formation (Late Eocene), southern Wyoming. An ecological accident in the fossil record. Palaeogeography, Palaeoclimatology, Palaeoecology 63, 91–108. https://doi.org/10.1016/0031-0182(88)90092-2

Visser, J., 1986. Sedimentology and taphonomy of a *Styracosaurus* bonebed in the late cretaceous Judith River Formation, Dinosaur Provincial Park, Alberta (Unpubl. MSc thesis). University of Calgary, Calgary, pp. 144–150.

Wolfe, D.G., Kirkland, J.I., 1998. *Zuniceratops christopheri* n. gen. & n. sp., a ceratopsian dinosaur from the Moreno Hill Formation (Cretaceous, Turonian) of west-central New Mexico. In: Lucas, S.G., Kirkland, J.I., Estep, J.W. (Eds.), Lower and Middle Cretaceous terrestrial ecosystems. New Mexico Museum of Natural History and Science Bulletin 14, 303–317.

Acknowledgements

First and foremost, I am extremely grateful to my promotor Anne Schulp. I think I may call myself an exception regarding the amount of time spent with a single supervisor. Anne, in 2015 you were crazy enough to let a young Bachelor student with zero skill in dinosaur palaeontology handle some of the world's most unique fossil material. I still remember my excitement when I got the official green light to start my own dinosaur project. Apparently, you were happy with the results and before I knew it, I was doing a Master's project under your supervision. Fast forward to 2023, and you are still stuck with me. Over the course of these eight years, you have always believed in my skills, and allowed me to fulfil the childhood dream of many, many people including myself: becoming a dinosaur scientist. I often forget how privileged I have been, when I was sitting in the train again with a *Triceratops* horn or touring the country with half a dinosaur skeleton in my car, sharing my excitement with others. Thanks for making everything possible.

I am also grateful to Martin Sander and Jeroen van der Lubbe. My PhD programme was filled to the brim with many interesting, but very different, techniques and methods, many of which were completely new to me. My visits to you in Bonn, Martin, were paramount to my understanding of bone histology and I appreciate your time for our discussions. Jeroen, our joint role as student supervisor during the stable isotope project introduced me to the world of stable isotope systematics. Many thanks for guiding me in uncharted territory. I believe I learned at least as much as the students.

Many thanks to all the wonderful people from the Dinolab. They say fieldwork is the best part of any project, and that is absolutely true. I have thoroughly enjoyed every single day out in the field accompanied by an amazing group of people. I will always remember the awesome fossils that we discovered, the tents that were lost to the Wyoming winds or the endless layovers and cancelled flights. A special thanks to Martijn Guliker and Yasmin Grooters for making the lab and material open and accessible for my projects. My apologies for continuously stealing your fossils.

I would like to extend my sincere gratitude to all the other members of research project including Pim Kaskes, Oeki Verhage, Dylan Bastiaans and all the amazing students that contributed to the final results. I truly appreciate all the in-depth discussions that we had which were invaluable for my progress. Pim and Oeki, you have proven to me that rocks also play a crucial role in palaeontology, not just the (cooler looking) fossil bones. Dylan, in a way it could have been you writing this thesis, but my deepest thanks for occasionally taking the role as daily supervisor, and discussing with me my ideas and results on the project. I will never forget the adventurous drive on the highway in sub-zero temperatures during a blizzard in the winter of northern Canada. At least we got our samples. Megan, Sybrand, Charlotte, Nadia, Marleen, Ydnas, Colijn and Koen, I hope you enjoyed your internships with me as much as I enjoyed all your enthusiasm.

Thanks should also go to all the members of the reading committee for their time, energy and interest in reading my PhD thesis. I sincerely hope the story makes sense.

And finally, where would I have been if it was not for my lovely girlfriend Carlijne. Thank you (and sorry…) for taking on the role of my personal psychologist for the last four and a half years. You can send me the bill, but I would not have wanted anyone else to share my setbacks and celebrate my successes with.

Curriculum vitae

Relevant work experience

2019 – 2023 **PhD candidate Vertebrate Palaeontology**
Naturalis Biodiversity Center & Utrecht University, Faculty of Geosciences

2018 – 2019 **Fossil preparator**
Naturalis Biodiversity Center

2017 – 2018 **Collection employee Invertebrates**
Naturalis Biodiversity Center

School and study career

2016 – 2018 **MSc Earth, Life and Climate (Biogeology)**
Utrecht University, Faculty of Geosciences

2013 – 2016 **BSc Biology**
Vrije Universiteit Amsterdam, Faculty of Science

2007 – 2013 **VWO, profile 'Natuur en Gezondheid'**
Lyceum Sancta Maria, Haarlem

Outreach

TV and radio

17-09-2022 **NPO Radio 1**
'Oudste hart aller tijden gevonden'

21-10-2021 **NOS Jeugdjournaal**
'Dino Big John verkocht voor 5,5 miljoen'

21-10-2021 **BNR Nieuwsradio**
'Veiling *Triceratops* Big John'

Podcasts

2022 **Podcast 'Moet Jij Weten'**

2021 **'Dinocast' – Award winning podcast series on Dutch palaeontology**

Public engagement

2023 **'Hoe?Zo! Show'**
Science show for children (*Utrecht University*)

2022 **'Operatie Breinbreker'**
Science fair for children (*Utrecht University*)

Publications

Articles

de Rooij, J., van der Lubbe, J. H., Verdegaal, S., Hulscher, M., Tooms, D., Kaskes, P., Verhage, O., Portanger, L., Schulp, A. S. (2022). Stable isotope record of *Triceratops* from a mass accumulation (Lance Formation, Wyoming, USA) provides insights into *Triceratops* behaviour and ecology.

Palaeogeography, Palaeoclimatology, Palaeoecology, 607, 111274. https://doi.org/10.1016/j.palaeo.2022.111274

de Rooij, J., Lucassen, S. A. N., Furer, C., Schulp, A. S., Sander, P. M., 2023. Exploring the ceratopsid growth record: comprehensive osteohistological analysis of *Triceratops* (Ornithischia: Ceratopsidae) and its implications for growth and ontogeny**.** Cretaceous Research, 154, 105738. https://doi.org/10.1016/j.cretres.2023.105738

de Rooij, J., Vintges, M. Q., Zuijdwijk, T., Heerkens, C. T. H., Schulp, A. S., 2023. Quantification of bone surface textures: exploring a new method of ontogenetic ageing. Journal of Analytical Science and Technology, 14, 49. https://doi.org/10.1186/s40543-023-00413-1

Conference abstracts

de Rooij, J., Lucassen, S. A. N., Sander, P. M., Schulp, A. S. (2022). Osteohistology of *Triceratops* fore- and hindlimb: implications for growth, development and taxonomy. In Society of Vertebrate Paleontologists 82nd Annual Meeting, Toronto, Canada.

de Rooij, J., van der Lubbe, H. J. L., Hulscher, M., Tooms, D., Schulp, A. S. (2022). Stable isotope record of *Triceratops* from a mass accumulation (Lance Formation, Wyoming, USA) provides insights into *Triceratops* behaviour and ecology. In European Association of Vertebrate Palaeontologists 19th Annual Meeting, Benevento, Italy.

Lucassen, S. A. N., **de Rooij, J.**, Schulp, A. S. (2022). New insights into *Triceratops* limb bone histology: Revealing skeletal unity through patterns in histovariability. In European Association of Vertebrate Palaeontologists 19th Annual Meeting, Benevento, Italy.

Vintges, M. Q., **de Rooij, J.**, Schulp, A. S. (2022). Quantifying bone surface roughness in *Branta canadensis* using 3D digital microscopy: Implications for textural ageing of extant and extinct species. In European Association of Vertebrate Palaeontologists 19th Annual Meeting, Benevento, Italy.

de Rooij, J., Kaskes, P., Bastiaans, D., Verhage, O., Portanger, L. A., Schulp, A. S. (2020). Solving the mystery of a 66 million year old *Triceratops* mass death assemblage. In Nederlands Aardwetenschappelijk Congres 2020.

de Rooij, J., Schulp, A. S., Reumer, J. W. F., Stein, K. (2019). Discovery of a *Triceratops* bonebed: *Triceratops* long bone histology and the latitudinal gradient hypothesis. In European Association of Vertebrate Palaeontologists 16th Annual Meeting, Caparica, Portugal.

Kaskes, P., Bastiaans, D., Verhage, O., **de Rooij, J.**, Guliker, M., Schulp, A. S. (2019, July). Taphonomy of a unique multigenerational *Triceratops* bonebed from eastern Wyoming (USA): New insights from a multi-proxy perspective. In European Association of Vertebrate Palaeontologists: 17th Annual Meeting (p. 54).